3D Reconstruction of
Cerebral Blood Flow and Vessel Morphology
from X-Ray Rotational Angiography

Irina Wächter

Department of Medical Physics and Bioengineering

University College London

2009

I, Irina Wächter, confirm that the work presented in this thesis is my own. Where information has been derived from other sources, I confirm that this has been indicated in the thesis.

Abstract

Three-dimensional (3D) information on blood flow and vessel morphology is important when assessing cerebrovascular disease and when monitoring interventions. Rotational angiography is nowadays routinely used to determine the geometry of the cerebral vasculature. To this end, contrast agent is injected into one of the supplying arteries and the x-ray system rotates around the head of the patient while it acquires a sequence of x-ray images. Besides information on the 3D geometry, this sequence also contains information on blood flow, as it is possible to observe how the contrast agent is transported by the blood. The main goal of this thesis is to exploit this information for the quantitative analysis of blood flow.

I propose a model-based method, called flow map fitting, which determines the blood flow waveform and the mean volumetric flow rate in the large cerebral arteries. The method uses a model of contrast agent transport to determine the flow parameters from the spatio-temporal progression of the contrast agent concentration, represented by a flow map. Furthermore, it overcomes artefacts due to the rotation (overlapping vessels and foreshortened vessels at some projection angles) of the c-arm using a reliability map.

For the flow quantification, small changes to the clinical protocol of rotational angiography are desirable. These, however, hamper the standard 3D reconstruction. Therefore, a new method for the 3D reconstruction of the vessel morphology which is tailored to this application is also presented.

To the best of my knowledge, I have presented the first quantitative results for blood flow quantification from rotational angiography. Additionally, the model-based approach overcomes several problems which are known from flow quantification methods for planar angiography.

The method was mainly validated on images from different phantom experiments. In most cases, the relative error was between 5% and 10% for the volumetric mean flow rate and between 10% and 15% for the blood flow waveform. Additionally, the applicability of the flow model

was shown on clinical images from planar angiographic acquisitions. From this, I conclude that the method has the potential to give quantitative estimates of blood flow parameters during cerebrovascular interventions.

Acknowledgements

Contents

List of Figures

List of Tables

Nomenclature

Symbol	Explanation	Page of definition
α	Baseline flow parameter	72
β	Waveform shape parameter	72
γ	Waveform shape parameter	72
δ	Waveform shape parameter	72
η	Dynamic viscosity	33
Λ	Line integral	104
Λ_μ	Line integral of attenuation	104
Λ_ρ	Line integral of iodine density	108
μ	Attenuation	104
ν	Kinematic viscosity	33
ω	Angular frequency	34
Π	Projection function	102
ρ	Density	33
χ	Flow division factor of bifurcation	79
A	Cross-sectional area	34
a_n	Cross-sectional area of lamina n	75

1

Introduction

1.1 Motivation

For diagnosis, treatment planning, and treatment outcome assessment of cerebrovascular diseases, it is beneficial to obtain three-dimensional (3D) information on vessel morphology and haemodynamics. Possible applications are the following: For a stenosis, the vessel lumen is an indication for the degree of the stenosis, but the blood flow through the stenosis is the parameter which really determines the severity of the stenosis. For an arteriovenous malformation, it is important to locate the feeding and draining vessels. For an aneurysm, it would be desirable to determine the risk of rupture. Important factors for this are the morphology and the haemodynamics of the aneurysm. Additionally, it is of general interest to quantify blood flow, as abnormal blood flow rates or abrupt velocity changes indicate a pathology.

Rotational angiography enables 3D information about the vessel morphology to be obtained during an intervention and is nowadays used routinely at the beginning of aneurysm and AVM interventions. For a cerebral rotational angiography acquisition, iodine-based contrast agent is injected into one of the carotid or vertebral arteries and a sequence of x-ray images is acquired, while the x-ray source and detector, mounted on a c-arm, rotate around the head of the patient. Some systems also acquire a second sequence without contrast agent injection to enable mask subtraction.

Besides the information about 3D morphology, the rotational angiographic sequence contains information about haemodynamics, as it is possible to see how the contrast agent is transported by the blood between successive images in the sequence. This information, however, is not yet exploited in current angiographic systems. The goal of this work was to extract haemodynamic information, namely the mean volumetric flow rate and the waveform, from rotational angiography.

The extraction of haemodynamic information from planar angiographic images has been a topic of research for over 30 years. The basic idea is to determine blood flow by analysing

variations in the x-ray image intensity due to changes of the contrast agent concentration. It is a difficult problem for several reasons:

- the images do not show the blood flow, but only how the contrast agent is transported by the blood;

- the blood flow velocity varies temporally (during the cardiac cycle) and spatially (changes of the velocity across the blood vessel and changes due to a change in radius or at a bifurcation);

- the x-ray images only show a projection view of the variations of the contrast agent concentrations.

1.2 Statement of contribution

In this thesis, I introduce the concept of the flow map fitting, which is a new method for the quantification of blood flow. A flow map represents the spatial and temporal progression of the contrast agent concentration. During the flow map fitting, a simulated flow map is fitted to the flow map which was extracted from angiographic image data. In this process, the mean volumetric flow rate and the blood flow waveform are determined. A flow model is used for the simulation of the flow map. The design of the flow map fitting allows all available information to be used and missing information to be estimated.

The flow map fitting was designed for flow quantification from rotational angiography. On the one hand, this has the advantage that the 3D geometry can be determined from the same sequence. On the other hand, this has the disadvantage that the rotation introduces artefacts in the flow map because of overlapping vessels and foreshortening of vessels. I have introduced the reliability map to overcome these problems. The reliability map gives the reliability of each entry of the flow map. To the best of my knowledge, I have presented the first quantitative results for flow estimation from rotational angiography.

Although the method was designed for rotational angiography, it can also be applied to planar angiography. In the cerebral case, the reliability map does not change with time, but it is still useful to automatically select which vessel segments should be used for flow quantification. The reliability map would also be beneficial in the cardiac case: Here, foreshortening and overlapping changes because of the motion of the heart. All other advantages of the flow map fitting also hold for the planar case. I have successfully applied my method to clinical datasets, where the geometry was determined from unsubtracted rotational angiography and the flow quantification utilized planar angiography.

The idea to use an explicit flow model to support the flow quantification is based on Philips internal results from Weese and Bredno. I started with their convection model and I have added the diffusion model, the waveform model, the injection model and the mixing model. I also incorporated a model of the vessel geometry which allows for tapering and branching vessels so

that the method can handle information from several vessel segments. For validation, I have added Womersley profiles and non-uniform mixing at the injection site. Most parts of the model were previously published; I have collected them and used them in a new way.

A main advantage of my method is that it can use densitometric and kinematic information from the angiographic images at the same time. The convection model enables the use of kinematic information, whereas the model of the mixing at the injection site enables the use of densitometric information. Relative densitometric information is used to determine the shape of the waveform. Absolute densitometric information can be used to determine the mean volumetric flow rate, but if this is not available, the kinematic information can be used to determine it. To the best of my knowledge, this is the first method which allows both kinds of information to be used concurrently.

Further advantages are: The method is very robust against noise and artefacts because the whole flow map is used at once. This is particularly important in the case of rotational angiography. The method can be adapted to different scenarios. For example, if information from an attenuation calibration or information about the timing of the injection is available, this can be used to support the flow quantification. As a convective dispersion model is used, the flow estimate should not depend on the distance from the injection site and overestimation during the inflow phase and underestimation during the outflow phase that has been reported elsewhere can be prevented. Because of the model of the vessel geometry, variations of the radius and bifurcations can be handled. Therefore, observations from several vessel segments can be used.

For the flow quantification from rotational angiography, it is beneficial if the rotational sequence shows inflow and outflow of contrast agent. This, however, hampers the standard 3D reconstruction. I have proposed a method for 3D vessel reconstruction, which uses flow information to overcome this problem. To achieve this, I have introduced the concept of the rotational time intensity curve, which can be used to determine flow information and to decide whether or not a voxel lies inside a vessel.

1.3 Structure of Thesis

In Chapter 2, an introduction to several topics which are related to this thesis is given: The clinical motivation, the physics of blood flow and contrast agent transport, other methods to determine cerebral blood flow and the principles of rotational angiography are introduced. Further, a literature review on the extraction of morphologic and haemodynamic information from angiographic images with an emphasis of the extraction of 3D information is given.

Chapters 3 to 5 introduce the basis for the algorithms presented later. In Chapter 3, the models for blood flow and contrast agent transport are explained, which are subsequently used for the computer simulation in Chapter 4 and for the flow quantification in Chapter 7. In Chapter 4, two different ways for the generation of synthetic, but realistic rotational angiographic images are explained. These images were used for the development and validation of the algorithms

described in this thesis. Before x-ray images can be used in a quantitative way, a geometric and an attenuation calibration must be performed. These are explained in Chapter 5.

Chapters 6 and 7 present the main part of this thesis. In Chapter 6, the reconstruction of the 3D centreline and radii from a rotational angiographic sequence are described. This information and the results of all previous chapters are used for the flow quantification described in Chapter 7.

In Chapter 8, preliminary results for clinical images are presented. My conclusions and ideas for future work are presented in Chapter 9.

2

Background and literature review

In this chapter, I first introduce medical terms related to cerebrovascular disease, the basics of x-ray angiography, and the physics of blood flow and contrast agent transport. After that, I describe which non-angiographic methods exist for measuring cerebral blood flow. Then, I review the literature on how information on vessel morphology and haemodynamics can be determined from x-ray angiography with a special emphasis on the extraction of 3D information.

2.1 Cerebrovascular disease

Cerebrovascular disease is the third commonest cause of death in western countries. The ultimate effect of cerebrovascular disease is to reduce the supply of oxygen to the brain (hypoxia). The cells most vulnerable to hypoxia are neurons. They become irreversibly damaged after 5-7 minutes of insufficient oxygen supply (Underwood, 2004).

2.1.1 Anatomy

Before the different types of cerebrovascular disease are introduced, an overview of the cerebral vasculature, or more precisely the main arteries which supply the brain, should be given.

The left common carotid artery branches off the aortic arch directly, whereas the right common carotid artery and the right and left vertebral arteries are connected to the aortic arch through the subclavian arteries (see Figure 2.1(a)). The common carotid artery bifurcates into the internal and external carotid artery (see Figure 2.1(b)). Both vertebral arteries merge into to basilar artery. The internal carotid and the basilar artery supply the circle of Willis (see Figure 2.1(c)). The circle of Willis is a circle of arteries and it consists of: left and right internal carotid arteries, left and right anterior cerebral arteries, left and right posterior cerebral arteries, left and right posterior communicating arteries, and anterior communicating artery (see Figure 2.1(d)).

The circle of Willis creates redundancies in the cerebral circulation. If one part of the circle or one of the arteries supplying the circle becomes blocked or narrowed, blood flow from

(a) Frontal view

(b) Lateral view

(c) Frontal-inferior view

(d) Inferior view
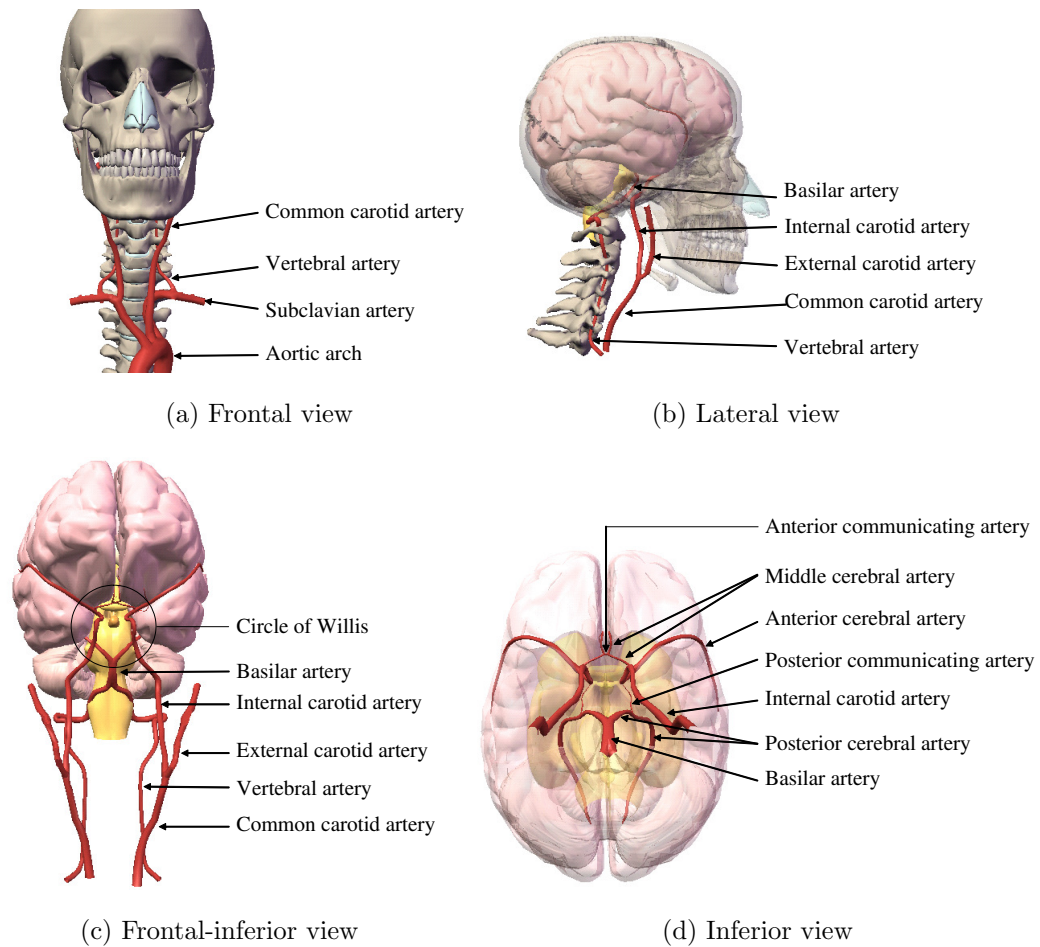
Figure 2.1: Overview of the main arteries which supply the brain, generated with the help of the software 'The visible body' (Argosy Publishing, 2008).

the other blood vessels can often preserve the supply of the brain. The anterior, middle, and posterior cerebral arteries lead from the circle of Willis to the brain.

2.1.2   Stroke

The term stroke denotes a sudden event in which a disturbance to the function of the central nervous system occurs due to cerebrovascular disease. A stroke can be ischaemic or haemorrhagic, as explained below.

2.1.3   Carotid stenoses

A stenosis is a narrowing of a vessel lumen, which in most cases is caused by atherosclerotic plaque (Underwood, 2004). A common site for a stenosis is the carotid bulb, a characteristic widening of the internal carotid artery just after the carotid bifurcation. The narrowing can result in a reduction of blood flow, it can even cause an occlusion of the artery.

The narrowing usually builds up gradually, but it can also happen that a piece of plaque breaks off and obstructs a smaller artery in the brain. Both result in an undersupply of parts of the brain with oxygen - an ischaemic stroke.

(a) Pre-angioplasty.   (b) Post-angioplasty.
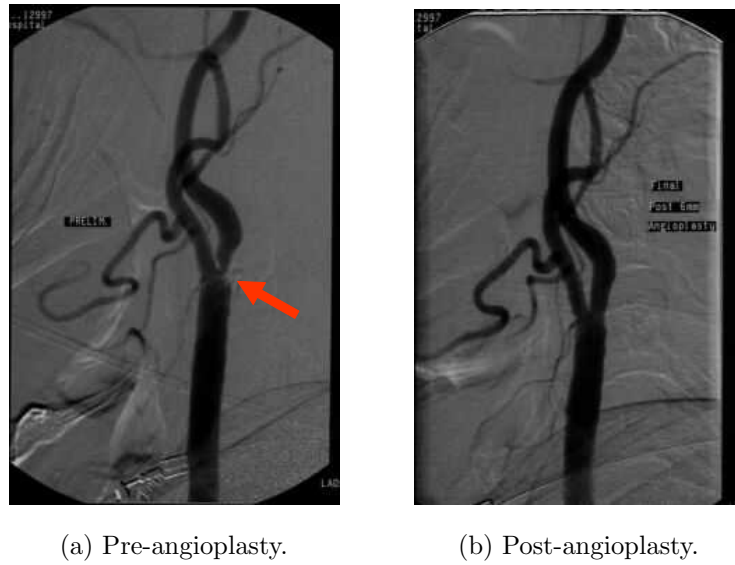
Figure 2.2: Left internal carotid artery stenosis (Department of Health Western Australia, 2007).
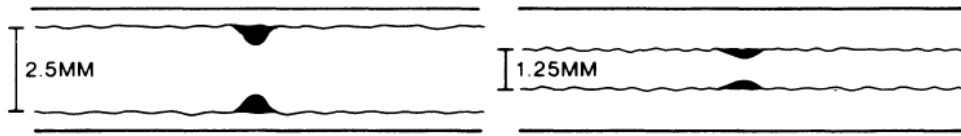
Figure 2.3: Local and diffuse stenosis: The left images shows a local stenosis whereas the right image shows a diffuse stenosis with a local stenosis. Both correspond to a 50% stenosis measure. The right stenosis is actually more severe than the left stenosis because the reference radius is reduced as well (Harrison et al., 1984).

The detected stenosis can be treated with drug therapy or it can be treated with endarterectomy, angioplasty, or stenting. Endarterectomy is a surgical procedure where the atherosclerotic plaque on the inside of the artery is removed. Angioplasty is the mechanical widening of stenosed blood vessel, typically by expanding a balloon delivered by a catheter. Stenting is the application of a metal-mesh tube which extends the vessel. Angioplasty and stenting are often applied together during an endovascular intervention under angiographic guidance. Angiographic images of a stenosis before and after angioplasty are shown in Figure 2.2.

For decisions on treatment, knowledge of the severity of the stenosis is crucial. International standards still propose to evaluate stenoses by manual estimation of the relative diameter reduction from angiographic images and various trials have shown that a stenosis of more than 70% is correlated with a significantly higher risk of stroke (Fox, 1993). For example, in the North American Syptomatic Carotid Enarterectomy Trial (NASCET, 1991), patients with symptoms caused by carotid stenosis where either assigned to medical therapy or surgical treatment. The follow-up after 24 month for patients with a stenosis of 70% or greater showed that 26% of the medical group had a stroke (13.1% fatal) and only 9% of the surgical group (2.5% fatal).

However, it was shown that studies have a high intra- and inter-observer variability (DeR-

ouen et al., 1977) and that manual estimations do not correlate very well with post-mortem measurements (Alperin et al., 1991). Additionally, it is known that for estimation of the severity of a stenosis the relative diameter change is not sufficient (Brown et al., 1977). In particular in the case of a diffuse stenosis, the knowledge of the local reduction of the radius is not sufficient (see Figure 2.3). The stenosis increases the resistance, which can lead to a decreased blood flow rate. In addition to that, a sudden increase of the radius after the stenosis can lead to turbulent flow, which in increases the risk of embolus. In both cases, angiographic flow measurements could provide crucial, additional information.

The stenosis normally increases the resistance of the vessel. A treatment which removes the stenosis reduces this resistance. This might lead to cerebral hyperperfusion, which can result in a haemorrhagic stroke. Clinically, cerebral hyperperfusion is arbitrarily defined as hypertension with symptoms of severe headache, seizures, and confusion. Physiologically, it is defined as a doubling of intraoperative cerebral blood flow values (Bass, 2004). Angiographic flow measurements could provide a comparison of the blood flow before and after the intervention in order to detect cerebral hyperperfusion.

2.1.4 Cerebral aneurysms

An aneurysm is a weak spot in an artery wall which balloons out because of the pressure of the blood circulating inside the affected artery. More than 90% of all aneurysms occur at bifurcations in the arterial system (Rubin, 2001).

The risk of an aneurysm is that the internal pressure becomes too high and the aneurysm ruptures. Asymptomatic aneurysms rupture at a rate of 3% per year; so the risk of rupture increases over time (Edvinsson et al., 1993). However, some aneurysms never rupture. When rupture does occur, the leaking blood increases the pressure on the brain or produces a haematoma, either of which can result in a haemorrhagic stroke.

Treatment can reduce the risk, but it also carries considerable risks. For the decision on treatment, it is important to evaluate the risk of rupture. The larger the aneurysm is, the more likely it is to rupture. Therefore, the 3D morphology of the aneurysm must be determined for diagnosis. Also the aneurysm's location as well as previous haemorrhage are important factors in the prediction of aneurysmal rupture (Caplan, 1998). Haemodynamic factors, however, are probably crucial for the explanation of growth and rupture of an aneurysm. Insight into the haemodynamics might lead to improved risk management and treatment planning (Ford et al., 2005).

For aneurysms with a low risk of rupture, periodic monitoring is often recommended as the best approach. Aneurysms with higher risk of rupture can be treated with clipping or coiling (Johnston et al., 1999). Clipping is a surgical procedure where a small clip is placed across the base or neck of the aneurysm to block the blood flow from entering. Coiling is an endovascular intervention with angiographic guidance where the aneurysm is filled with tiny platinum coils to cause a stable blood clot and prevent blood flow from entering. Angiographic images of an

(a) Pre-coiling.   (b) Post-coiling.
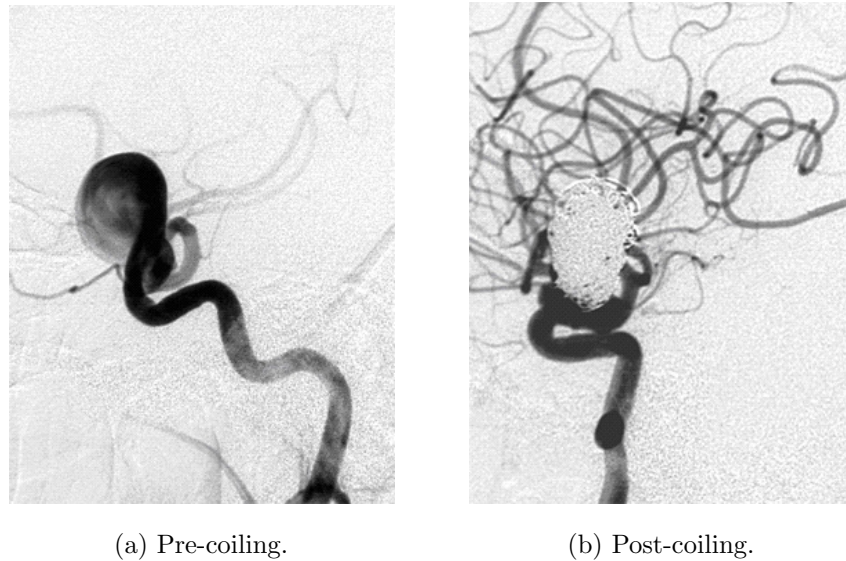
Figure 2.4: Cerebral aneurysm (University of Arkansas for Medical Science, 2008).

aneurysm before and after coiling are shown in Figure 2.4.

In the case of an aneurysm treated with coiling or clipping, abnormal haemodynamics can lead to regrowth (Grass et al., 2002) and the haemodynamics determine the stability of the coils (Graves et al., 1992). Again, a haemodynamic assessment of the intervention might be helpful.

A haemodynamic assessment could be given by a computational fluid dynamics simulation. Rotational angiography can be used to determine the patient specific geometry (Steinman et al., 2003; Castro et al., 2006). Angiographic flow measurements could potentially provide flow boundary conditions. Flow modelling could help to predict the risk of aneurysm rupture without treatment or during treatment, and the risk of causing a haemodynamic stroke by transient or permanent occlusion of the vessels adjacent to the aneurysm during treatment.

2.1.5 Arteriovenous malformations

In the circulatory system, arteries are normally connected to veins by tiny capillary vessels. An arteriovenous malformation (AVM) is a congenital vascular defect in which an artery is connected directly to a vein without the intervening capillary network (Leeds and Kieffer, 2000).

As veins are not prepared to bear the pressure which exists in an artery, there is a risk that these start to haemorrhage, which results in a haemorrhagic stroke. The risk of haemorrhage for an AVM is 2-4% per year (The Arteriovenous Malformation Study Group, 1999). AVMs are normally detected while patients are young (10 to 30 years) and in 66% of these cases they lead to learning disorders (The Arteriovenous Malformation Study Group, 1999).

AVMs are usually treated. Possibilities for treatment include surgical removal, stereotactic radiosurgery, and endovascular embolization. During endovascular embolization a glue-like substance is injected under angiographic guidance to block the vessel and reduce the blood flow into the AVM. For large AVMs, multiple embolization procedures may be required to avoid changing blood flow patterns in the brain too rapidly or drastically. Surgical removal or stereotactic

(a) Pre-embolization.　　　　　　　(b) Post-embolization.
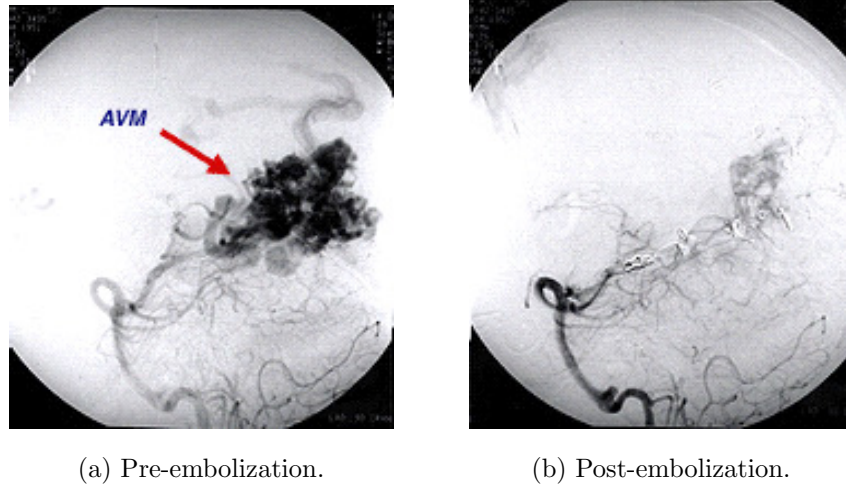
Figure 2.5: Arteriovenous malformations (Center for Endovascular and Exovascular Therapy, 2008).

radiosurgery is normally carried out after embolization (Hartmann et al., 2007). Angiographic images of an AVM before and after embolization are shown in Figure 2.5.

For the planning of an intervention on an AVM, it is necessary to know its 3D geometry. Knowledge of the 3D vessel geometry can be used for guidance during the intervention. Additionally, it would be very helpful to reconstruct the flow in the vessel tree as it can indicate which vessels feed the AVM (Schmitt et al., 2005).

For the assessment of an intervention it is beneficial to know how the flow division at the carotid bifurcation changes due to the intervention. The AVM treatment changes the downstream resistance. This changes the flow division at the upstream bifurcations. Therefore, it is interesting to monitor how the flow division changes. This could potentially be done by angiographic means.

2.2　X-ray, angiography, and rotational angiography

X-rays were discovered by Röntgen in 1895. He discovered accidentally that this form of radiation could penetrate opaque objects and cast ghostly images on a photographic plate. Soon x-rays were used to diagnose broken bones. This is only possible because different materials have different x-ray attenuation coefficients; for example bone has a higher attenuation than soft tissue.

The current standard method for examining blood vessels is angiography. In 1927 Moniz introduced cerebral angiography by opacification of the carotid artery in x-ray images with a contrast agent (Leeds and Kieffer, 2000). After Seldinger (1953) introduced his catheterisation method, angiography became widely used in clinical practice. In this method, a catheter is brought into a feeding vessel of the tree or the segment which should be examined and contrast agent is injected. Then, a sequence of x-ray images is recorded. As the contrast agent, for example an iodine based solution, has a much higher attenuation than soft tissue or bone, it

can be distinguished on the x-ray image. When a contrast agent is injected into a vessel, the vessel lumen becomes visible on the x-ray image. In many cases an x-ray image without contrast agent, called the mask image, is subtracted from the images with contrast agent. The resulting images are called digitally subtracted angiographic (DSA) images. In a DSA image, it is easier to examine blood vessels because they are not overlapped by other structures.

At the same time, the so-called c-arm – a new geometry for x-ray systems – was introduced. It gets its name from its shape: the x-ray detector and the x-ray tube are connected by a c-shaped arc. It can be moved around the patient to acquire x-ray images from different directions. A c-arm system is used during most endovascular interventions today.

Since the 1970s angiographic images can be digitised and processed by computer, making DSA possible (Ovitt et al., 1980). Since then, the automatic extraction of morphologic and haemodynamic information about the vessel system has been a major goal of medical image processing research.

In their original form, x-ray images only give 2D projective information. However, if x-ray images of the vessel system are available from two or more orientations, it is possible to reconstruct the 3D geometry of the vessel system. In early applications, the user exploited biplane images to determine the 3D path of a vessel manually. This tedious procedure is no longer necessary following the advent of rotational angiography.

For the acquisition of rotational angiography, a long contrast agent injection is given. When the whole vessel tree is filled with contrast agent, the acquisition of x-ray images starts and simultaneously the c-arm rotates around the patient. This gives the rotational angiographic sequence. Under certain circumstances this sequence can be used to reconstruct a CT-like volume dataset, the 3DRA dataset.

Rotational angiography was first described in the 1970s (Voigt et al., 1975), but it was not until the late 1990s that it has become used in routine clinical practice. Several technical problems had to be solved: The reconstruction requires distortion-free projection images and precise knowledge of the trajectory of the c-arm, but the c-arm was not developed with these requirements in mind. A calibration procedure to solve this problem and first clinical images were presented by Koppe et al. (1995). Once these problems had been solved, rotational angiography became a great success. Today, it is used to guide most aneurysm and AVM interventions.

2.3 Underlying physics and physiology

2.3.1 Physics of blood flow

Several great mathematicians and physicists made the current understanding of blood flow possible: Newton introduced the concept of fluid viscosity; Euler established the equations of inviscid fluid motion; Poiseuille's equation describes flow in a capillary tube; Bernoulli's equation is used to determine velocities by means of pressure measurements; and finally the Navier-Stokes equations give the general equations for fluid motion. Nevertheless, the understanding of blood

flow is still incomplete (Nichols and O'Rouke, 2005).

Newton postulated that the shear stress between two layers of a fluid is proportional to the velocity gradient. The constant of proportionality is the dynamic viscosity η. Fluids satisfying this law, such as water, are called Newtonian fluids. Blood is a solution of solid particles (such as red blood cells) in a fluid (the plasma). The plasma itself behaves like a Newtonian fluid, but in contrast, the whole blood does not have a constant viscosity and therefore it is a non-Newtonian fluid. The viscosity of blood depends on: the haematocrit (proportion of blood volume that is occupied by red blood cells), the velocity of the blood, and the radius of the blood vessel (Ku, 1997). Nevertheless, it is often assumed that blood is a Newtonian fluid.

Poiseuille's equation describes steady, incompressible, laminar flow in a straight tube of infinite length and constant cross section (Hughes, 1979). The relationship between volumetric flow rate Q, pressure drop along the tube $\partial P/\partial x$ and radius R is given by

$$Q = \frac{\pi R^4}{8\eta} \frac{\partial P}{\partial x}. \tag{2.1}$$

It is important to note that volume flow rate depends on the fourth power of the radius. The velocity v at a point in the tube depends on its distance r from the centre of the tube

$$v(r) = \frac{(R^2 - r^2)}{4\eta} \frac{\partial P}{\partial x}. \tag{2.2}$$

So, the velocity profile can be described as a parabola and the average velocity $\overline{v}$ across the tube is

$$\overline{v} = \frac{R^2}{8\eta} \frac{\partial P}{\partial x} = \frac{Q}{\pi R^2}. \tag{2.3}$$

Not all of the conditions for Poiseuille's equation are fulfilled by the circulation of blood: As the heart works like a pulsatile pump, the flow in the arteries near to the heart is not steady. Furthermore, the flow in larger arteries is not always laminar. Whether the flow is laminar or not, is determined by its Reynolds number,

$$Re = \frac{\overline{v}L}{\nu}, \tag{2.4}$$

where $\nu = \eta/\rho$ is the kinematic viscosity, $\overline{v}$ is the mean velocity, and L is the characteristic length (for a pipe L the diameter). It can be interpreted as the ratio of the inertial forces to the viscous forces. If the Reynolds number is lower than 2000, the flow usually is laminar. The Reynolds number in the brain is approximately 100, whereas the Reynolds number in the aorta is approximately 1000. Physiological flow is mainly laminar, but flow in the aorta or after a stenosis can be turbulent.

In addition to this, Poiseuille's equation assumes that the tube is long compared to the region of interest and the diameter, since the flow profile at the inlet is not fully developed, i. e. not yet parabolic. The length after which the flow is fully developed is called inlet length L_I and it is given by (Nichols and O'Rouke, 2005)

$$L_I = \frac{2k\overline{v}R^2}{\nu}, \tag{2.5}$$

where $k = 0.08$ is a derived constant. In most blood vessels, the distances between bifurcations are too small to fulfil this condition. For example, the inlet length at the right common carotid artery can be calculated to be about 13 cm (assuming a radius of 4 mm and a mean flow velocity of 20 cm/s), which is more than the length of the artery.

Finally, blood vessels are not straight tubes due to bifurcations, tortuous vessels, asymmetric plaque, and tapering radii and compliance. Although blood flow does not fulfil all conditions for Poiseuille's equation, the model was still an important step in understanding blood flow (Nichols and O'Rouke, 2005) and it can be used to get an approximate description of blood flow.

An extension of Poiseuille's equation for pulsatile flow was given by Womersley (1955). His solution can be used to determine the flow profile for pulsatile flow in a straight tube from the flow waveform. The shape of the profiles is determined by the Womersley number

$$Wo = R\sqrt{\frac{\omega}{\nu}}, \tag{2.6}$$

where R is the radius, ω is the angular frequency of the pulsatile signal and ν is the kinematic viscosity. The Womersley number can be interpreted as the ratio of the unsteady, pulsatile forces to the viscous forces. For larger arteries, the Womersley number takes values between 2 and 5.

Bernoulli's equation, also called flow conservation equation, is based on the continuity equation, which can be used to determine the impact of a changing cross sectional area on the velocity. It states that for an incompressible fluid the product of velocity v and cross sectional area A stays constant in a tube with changing cross sectional area

$$Q = v_1 A_1 = v_2 A_2. \tag{2.7}$$

This can be used to evaluate the influence of a stenosis and it is a basic assumption for some flow extraction algorithms which are explained later. Furthermore, it helps to understand why the velocity of the blood decreases with the distance from the heart: because the total cross sectional area of all vessels increases with the distance.

For a more general description of flowing fluids, the Navier-Stoke equations can be used. These are a set of non-linear partial differential equations which combine the mass conservation equation and the momentum conservation equation. They are valid for all fluids, but only for simple cases can an analytic solution be found. Blood flow can be modelled mathematically using the time-dependent Navier-Stokes equations for incompressible fluids (Xu, 2001):

$$\nabla \cdot v = 0, \tag{2.8}$$

$$\rho \left[\frac{\partial v}{\partial t} + v \cdot \nabla v \right] = -\nabla P + \nabla \cdot (\eta \nabla v), \tag{2.9}$$

where ρ is the density, v is the velocity, η is the viscosity of the fluid, and ∇P is the pressure gradient.

However, as blood flow is non-Newtonian, pulsatile, and determined by a complex geometry, the Navier-Stokes equations cannot be solved analytically. Nevertheless, it is possible to obtain approximate numerical solutions, which is the subject matter of the field of computational fluid dynamics (CFD).

The strategy of CFD is to replace the continuous problem domain with a discrete domain using a grid. The governing equations are then solved for relevant flow variables at the grid points in an iterative way. In the case of blood flow through an artery, the relevant flow variables are blood velocity, blood pressure and wall shear stress.

The first CFD studies used artificial models of blood vessels, which idealised the patient geometry (Perktold and Peter, 1990; Lou and Yang, 1991). The next generation of CFD studies worked on post-mortem casts of blood vessels (Perktold et al., 1998). As it is not possible to study patient-specific haemodynamics using a general geometrical model, more recent studies have extracted the patient-specific geometry from medical images. In most cases the geometry is extracted from magnetic resonance imaging (Zhao et al., 2000; Redaelli et al., 2002; Ford et al., 2005), but three dimensional rotational angiography (Hassan et al., 2003; Steinman et al., 2003), computer tomography(Groden et al., 2001) and ultrasound (Glor et al., 2004) may also be used for this purpose.

With a CFD simulation even complex vascular structures can be modelled. Examples are the following: healthy carotid bifurcations with the characteristic widening at the Internal Carotid artery (Delfino et al., 1997; Xu, 2001; Redaelli et al., 2002), stenosed carotid bifurcations (Steinman et al., 2000; Marshall et al., 2004), the circle of Willis (Cebral et al., 2003; Moore et al., 2005), all major arteries of the cerebral vasculature (Manos et al., 2008), different types of cerebral aneurysms (Hassan et al., 2003; Steinman et al., 2003; Ford et al., 2005; Cebral et al., 2005), and arteriovenous malformations (Orlowski et al., 2008).

Even if the geometry is realistic and patient specific, many generalising or simplifying assumptions must be made to make CFD simulations computationally feasible. For almost every simulation, it is assumed that the flow is homogeneous, incompressible and Newtonian, although blood flow is definitely non-Newtonian. Other issues are pulsatility, elastic vessel walls (Zhao et al., 2000; Cebral et al., 2002), and the accurate determination of the inlet flow. In many cases the inlet flow was determined from a sex-and age-matched volunteer (Steinman et al., 2003; Castro et al., 2006). A patient-specific inlet flow can be determined using phase contrast MR (Xu, 2001; Cebral et al., 2002) or US (Zhao et al., 2000; Hassan et al., 2003).

As there is no gold standard to measure complex flow fields in a high resolution, it is difficult to validate the results of a CFD simulation. Ford et al. (2005) have introduced a CFD system that generates a sequence of virtual angiographic images, which can be compared to the angiography of the patient for validation purpose.

2.3.2 Physics of contrast agent transport

Besides the physics of blood flow, the physics of contrast agent transport are of interest in the context of this thesis. The transport of the contrast agent by the blood is determined by two phenomena: convection and diffusion. Convection is the active transport of contrast agent due to the movement of the blood and diffusion is the passive transport due to concentration differences.

In most cases, the transport of a soluble substance in a moving medium can be described by the convection-diffusion equation (Cebral et al., 2003)

$$\frac{\partial C}{\partial t} + v\nabla C = d\nabla^2 C, \tag{2.10}$$

where C is the concentration, v the velocity and d the diffusivity constant. This assumes that the molecular diffusion coefficient is independent of the concentration, that the density difference between both fluids is negligible and that there are no chemical reactions between both fluids.

The convection-diffusion equation can also be solved numerically. The solution of the convection diffusion equation depends on the underlying flow. Ideally, this would involve the simultaneous, but computationally expensive solution of the coupled Navier-Stokes and transport equations. Ford et al. (2005) assumed passive scalar transport to decouple the solution of contrast agent transport from that of the blood flow as follows: first a solution for the blood flow is determined and used as input for the solution of the contrast agent transport problem.

For laminar, axially symmetric flow in a tube, the concentration $C(r,l,t)$ of the solute can be described as a function of longitudinal distance l, radial distance r and time t. The convection-diffusion equation is then (Aris, 1960)

$$\frac{\partial C(r,l,t)}{\partial t} = d \cdot \left(\frac{\partial^2 C(r,l,t)}{\partial r^2} + \frac{1}{r} \cdot \frac{\partial C(r,l,t)}{\partial r} + \frac{\partial^2 C(r,l,t)}{\partial l^2} \right) - v(r)\frac{\partial C(r,l,t)}{\partial l} \tag{2.11}$$

with the boundary conditions

$$\frac{\partial C(0,l,t)}{\partial r} = \frac{\partial C(R,l,t)}{\partial r} = 0, \tag{2.12}$$

$$C(r,l,0) = C_0(r,l), \tag{2.13}$$

where $v(r)$ is the velocity, d is the molecular diffusion coefficient, R is the radius of the vessel, and $C_0(r,l)$ is the initial distribution of contrast agent. The first and second term of the right-hand side of Equation 2.11 describe radial diffusion, the third term describes longitudinal diffusion and the last term describes longitudinal convection.

In the field of chemical engineering, many approaches were proposed to solve Equation 2.11. In these approaches usually, the longitudinal distribution of the concentration averaged over the cross section for a given point in time is determined. In particular earlier solutions considered special cases by making assumptions about the underlying flow, the Peclet number or the point in time. The Peclet number

$$Pe = \frac{R \cdot \overline{v}}{d} \tag{2.14}$$

relates the rate of convection of a flow to its rate of diffusion. The point in time is characterised by the dimensionless time

$$\tau = \frac{d \cdot t}{R^2}. \tag{2.15}$$

Ekambara and Joshi (2004) give an overview over many different approaches and state for which range of Pe and τ these are valid and which additional assumptions were made.

Taylor (1953) was the first to give a solution of the transport of a soluble substance introduced into a fluid flowing in a small tube. For his analytical solution, he assumed that the flow is steady, parabolic and laminar, that longitudinal diffusion is negligible, and that a specific initial distribution of the concentrations is given. He gave a solution for the mean concentration over the cross section, first for convection only and then for convection and diffusion. His solution can be applied for $Pe > 500$ and $\tau > 0.5$. Aris (1960) extended the work of Taylor to pulsatile flow, he included longitudinal diffusion and he extended the applicability range to $Pe > 100$ and $\tau > 0.2$.

Bailey and Gogarty (1962) further developed a numerical method to solve the equation by superimposing convective and diffusive effects alternately. They first solved the convection part by shifting the concentration values and then they applied radial diffusion. Their approach can be used for arbitrary initial values of C_0 and it was validated for $Pe > 600$ and $\tau > 0.1$. Takahashi et al. (1990) extended the work of Bailey and Gogarty: They implemented longitudinal and radial diffusion and they showed that their approach is valid at all points in time and for arbitrary Peclet numbers.

In the scope of this thesis, the distribution of the contrast agent concentrations has to be simulated for many points in time (for each frame). Therefore, a numerical method would be more applicable than an analytical solution. For the application of contrast agent transport in a blood vessel the Peclet number is in the order of 10^4 (assuming $D \approx 10^{-7}$ m²/s, $R \approx 10^{-3}$ m, $v \approx 1$ m/s) and the dimensionless time is in the order of 10^{-2} (assuming $t \approx 1$ s). Therefore, the Peclet number would allow the application of all mentioned approaches. Whereas, the point in time prohibits the application of the analytical solutions of Taylor (1953) and Aris (1960). For the numerical approaches, Takahashi et al. (1990) state the following: If a numerical method is valid for $\tau = \tau_0$, it must be valid for $\tau < \tau_0$ because of its iterative property. Therefore both numerical methods should be applicable. Overall, I conclude that a numerical approach should be used for the work of this thesis.

2.3.3 Influence of the injection on the blood flow

In general, the contrast agent injection can have the following effects on the blood flow (Schröder et al., 1981; Morris et al., 1982; Stoeter et al., 1984; Schalij et al., 1994): First of all, the injection increases the total volumetric flow rate at the injection site. This effect only takes place during the injection and it will be called the 'direct effect' from now on. Secondly, the higher viscosity of the contrast agent (compared to blood) can increase the vascular resistance downstream and therefore decrease the volumetric blood flow rate. The viscosity effect will be apparent for a few

heart cycles until most of the contrast agent is washed out again. Thirdly, the contrast agent can act as a vasodilator. This means that the diameter of the downstream vessels increases and therefore the resistance decreases and the volumetric blood flow rate increases. This is the pharmacological effect and it takes place over a longer time scale.

The description of the intensity and the timescale of these effects vary substantially within the literature. The reason for this probably is that they depend on the duration and volumetric flow rate of the injected contrast agent and on the chosen contrast agent. The most important differences between contrast agents seem to be the osmolality (Hilal, 1966; Almén, 1987) and the viscosity (Pugh, 1996). An overview of different iodine-based contrast agents and their osmolality and viscosity is given in Table 2.1. Furthermore, the effects could vary between humans and animals, between healthy and diseased vessels (Zwaan et al., 1999), and for different organs.

Early studies deployed ionic contrast agents: Kagstrom et al. (1958) used Diatrizoate for their study and they reported that blood flow remained elevated for 15 min after the injection. Hilal (1966) conclude that the increase is caused by vasodilatation due to the high osmolality of their contrast agent. Huber and Handa (1967) showed that the downstream vessels dilate after injection of contrast agent. As the vasodilatation can cause pain for the patient (Kallehauge and Praestholm, 1982), substantial effort was made to create non-ionic and low osmolality contrast agents.

Almén (1987) compared contrast agents of different osmolality on dogs. They concluded that less hypertonic contrast agents, created a lesser and shorter increase in blood flow. However, they also showed that this is not the only factor for the pharmacological effect as two contrast agents with the same osmolality, had different effects. Diatrizoate had the greatest and longest effect: In the first 30 s after the injection, the blood flow was increased by 132% ± 40%, after 1 min and 3 min it was still increased by 20% ± 24% and 18% ± 18%, respectively. Metrizamide had the smallest and shortest effect: In the first 30 s after the injection, the blood flow was increased by 25% ± 16%, after 1 min and 3 min it was only increased by 6% ± 10% and 1% ± 7%, respectively.

Stoeter et al. (1984) conducted a study with 55 patients with cerebrovascular disease injecting the ionic but low osmolality contrast agent Ioxaglate and saline solution. They report a threefold response: during the Ioxaglate injection the flow is increased or even turbulent, followed by 3-8 s of depressed flow and then by 10-15 s of increased flow. Saline solution was injected at different rates (1 ml/s up to 10 ml/s). The results show an immediate increase of the flow rate which depends on the flow rate of the injection. For the injection of saline solution, the flow rate always returned to the baseline value within a few seconds.

Pugh et al. (1992) analysed the reaction of 15 patients towards Iodixanol, which is a contrast agent which can be made isotonic. Although the contrast agent has the same osmolality as blood, still an increase of blood flow at 5 to 30 s after the injection was reported.

Contrary results were presented by Zwaan et al. (1999). They analysed the influence of

Official name	Product name	Iodine concentration [mg/ml]	Osmolality @ 37° [mOsm/kg H2O]	Viscosity @ 37° [mPa s]
Ionic, high osmolality:				
Diatrizoate	Angiografin, Hypaque, Urografin, Renografin	300	1500	5.2
Ionic, low osmolality:				
Ioxaglate	Hexabrix	320	600	7.5
Non-ionic, low osmolality:				
Metrizamide	Amipaque	170-300	300-484	Not known
Iopamidol	Niopam, Solutrast, Iopamiro	250-370	524-796	3.0-9.4
Iopromide	Ultravist	150-370	330-770	1.5-10.0
Iohexol	Omnipaque	140-350	322-844	1.5-10.4
Non-ionic, isotonic:				
Iodixanol	Visipaque	270-320	290	6.3-11.8
Iotrolan	Isovist	240-300	270-290	3.9-8.5
For comparison:				
Blood			280	2.3 - 3.0

Table 2.1: Osmolality and viscosity of different contrast agents (mainly obtained from Kipshidze et al. (2007))

different contrast agents with low osmolality on 55 patients with peripheral arterial occlusive disease. Like most others, they report an increase of flow during the time of injection, but in contrast to most other studies, they report a reduction in blood flow for about one minute after the injection of Iopromide or Iopamidol. They speculate that diseased endothelial cells might be the reason for vasoconstrictive instead of vasodilating effects. They also report that the blood flow remained unchanged after the injection of Iodixanol and state that this is probably due to its isotonic nature.

Several studies concentrated on the viscosity effect. Morris et al. (1982) injected saline solution of different viscosity. They showed that the magnitude and duration of the decrease depend on the viscosity of the injection and they conclude that the resistance increases when the viscous media reaches the microcirculation. Padayachee et al. (1983) reported that ionic contrast agents with a viscosity only slightly higher than blood produce little or no decrease. Nauert et al. (1989) reported Iotrolan (high viscosity) produces a significantly higher initial decrease than Diatrizoate (low viscosity). When Diatrizoate was mixed with gelatine to increase viscosity, similar results as with Iotrolan were observed. The duration of the viscosity effect is difficult to analyse: it starts when the contrast agent reaches the microcirculation but until the end of

injection it is outweighed by the direct effect; it ends when the contrast agent has been washed out but after 8 s to 12 s after the start of injection it is outweighed by the pharmacological effect.

Few studies concentrated on the direct effect of the injection. In these studies, arterial blood is injected to avoid effects of different osmolality and different viscosity. Levin et al. (1977) injected heparinised blood at a rate much higher than the blood flow to analyse only the direct effect of the injection. They reported a significant increase of blood flow which sustained throughout the duration of the injection. They also suggest that the magnitude of the increase is directly related to the injection rate. Wolf et al. (1978) reported that the relation between injection rate and flow increase is non-linear. Jacobson et al. (1981) also analysed the direct effect. They injected arterial blood at a flow rate below, equal, and above the rate of blood flow. From their graphs it can be read how the blood flow is changed by the injection: The average control blood flow rate was approximately 4 ml/s. At an injection of 2 ml/s, 4 ml/s, 6 ml/s, and 8 ml/s the flow in the artery increased by 18%, 29%, 33%, and 40% respectively. This corresponds to 36%, 29%, 22%, and 20% of the flow rate of the injection.

In the work of this thesis, the flow is quantified from observations made during the time of injection. Therefore, the effects which take place during the time of injection are most important, but in addition to that, the pharmacological effect of previous contrast agent injections has to be considered. From the results presented in literature, I conclude that the pharmacological effects can be neglected if a contrast agent of low osmolality is used and if the time since the last injection is at least 3 min. The effects of viscosity can be neglected, if a contrast agent of low viscosity is used or observations are made within few seconds after the start of the injection. Unfortunately, the contrast agents with low osmolality have a high viscosity. The osmolality and viscosity increase with the iodine concentration. Therefore, a contrast agent with low to medium iodine concentration should be used to minimise both the pharmacological and the viscosity effect, although the lower concentration might reduce image quality. For example, Isovist 240 (3.9 mPa s, 270 mOsm/kg H2O) or Ultravist 240 (2.8 mPa s, 480 mOsm/kg H2O) have a similar osmolality and viscosity as blood. The direct effects of the contrast agent injection cannot be neglected if observations are made during the time of injection. These will be discussed further throughout this thesis.

2.4 Measuring cerebral blood flow

During the last century many methods and devices to determine blood flow have been proposed. Ideally, a method to measure blood flow should be non-invasive. Less ideally, the method is minimally invasive. This is the case if, for example, a catheter has to be introduced or continuous blood samples have to be taken. Still less ideally, blood vessels are exposed and a measuring device is put around them. Even less ideally, exposed blood vessels are cut and the volume of the haemorrhage is measured. Unfortunately, the more invasive techniques tend to be more accurate (Wyatt, 1984; Colchester et al., 1986).

This thesis is concerned with blood flow measurements during an endovascular intervention. Therefore, it is acceptable if the method is minimally invasive, meaning that a catheter has to be introduced. In the following, different methods are described. A special emphasis is put on the question of whether the method is applicable in the brain and whether it is applicable during an endovascular intervention.

2.4.1 Fick's principle

The first blood flow measurements were based on Fick's principle. Fick (1870) postulated that the uptake of a marker substance by an organ per unit of time must be equal to the blood flow through that organ multiplied by the difference of its arterial and venous concentration. More generally, Fick's principle is expressed as

$$V(t) = Q_a(t) \cdot C_a(t) - Q_v(t) \cdot C_v(t), \tag{2.16}$$

where $V(t)$ is the volume uptake rate, $Q_a(t)$ and $Q_v(t)$ are the arterial and venous blood flow rate, and $C_a(t)$ and $C_v(t)$ are the arterial and the venous concentration of the marker substance. If one assumes that the arterial blood flow is the same as the venous blood flow

$$Q_v(t) = Q_a(t) = Q(t) \tag{2.17}$$

then the principle can be used to determine blood flow by

$$Q(t) = \frac{V(t)}{C_a(t) - C_v(t)}. \tag{2.18}$$

Fick applied his principle to estimate the cardiac output and his marker substance was oxygen. The uptake of oxygen should be estimated from the breathing of the subject. He had no apparatus to actually measure the required variables. He used values from literature to compute that the cardiac output is 77ml per heart beat. Grehant and Quiniquand (1886) made the first experimental test of Fick's method.

Kety and Schmidt (1945) were the first to apply Fick's principle to measure cerebral blood flow. An illustration of their setup is given in Figure 2.6. They used nitrous oxide (N_2O) as a marker substance and Fick's principle integrated over time

$$\overline{Q} = \frac{M(T)}{\int_0^T (C_a(t) - C_v(t)) dt}, \tag{2.19}$$

where $M(T)$ is the quantity of N_2O taken up by the brain in the time T since the beginning of the application of the marker substance. The denominator in Equation 2.19 can be measured from arterial and venous blood samples; the numerator cannot be determined directly in humans. Kety and Schmidt assumed that after sufficient time, an equilibrium will be established between the brain and the venous blood. The cerebral blood flow per unit weight of the brain (CBF) is then given by

$$\text{CBF} = \frac{s \cdot C_v(T)}{\int_0^T (C_a(t) - C_v(t)) dt}, \tag{2.20}$$
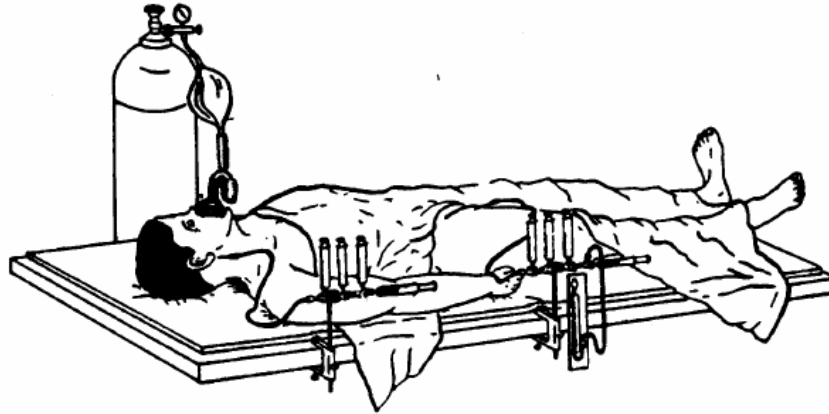
Figure 2.6: Illustration of setup from Kety and Schmidt (1945) for measuring cerebral blood flow according to Fick's principle.

where s represents a partition coefficient which is close to 1. Although this method cannot provide the total flow for a specific artery, it was still an important development and it is the basis for first pass distribution methods which will be explained in the section about angiographic flow measurements (Section 2.6).

Fritts and Cournand (1958) evaluated the accuracy of Fick's method. They observed the following limitations: In general, the venous blood flow does not equal the arterial blood flow due to the compliance of the blood vessels; concentrations cannot be measured instantaneously; the uptake of oxygen on the capillary level does not have to equal the measured uptake at the mouth, as the lung can act as an oxygen reservoir.

2.4.2 Indicator dilution

Stewart (1893) introduced the idea of indicator dilution. He proposed to inject saline solution to alter the electrical conductivity of blood. This alteration will travel with the blood and the arrival can be detected with a galvanometer. The transit time could be measured with a stopwatch. Hamilton et al. (1928) extended this method. They continuously took samples of the blood so that they could determine the temporal variation of the indicator concentration, which when plotted form a so-called dilution curve. From this, they could determine the cardiac output.

Meier and Zierler (1954) described the theory and assumptions of the indicator solution. When the indicator is introduced it mixes with the blood. If the blood flow is high, it mixes with a large amount of blood and the resulting concentration is low. If it can be assumed that each particle of the indicator passes the recording site exactly once, the total injected amount M must equal the amount which passes by at the recording site:

$$M = \int_0^\infty c(t)Q(t)dt. \tag{2.21}$$

To determine the flow, it has to be assumed that the flow is steady

$$Q = \frac{M}{\int_0^\infty c(t)dt}.$$

(2.22)

This means that the indicator dilution theory is actually not valid for pulsatile blood flow. Doriot et al. (1997) showed that it is also not valid if the indicator diffuses in the blood.

Nevertheless, indicator dilution has played an important role in the cardiovascular field and many people still believe that it is an adequate way to measure blood flow. Several derivations of the technique have been proposed, like the thermodilution technique or the angiographic dilution technique.

In the angiographic dilution technique, an iodine-based contrast agent is injected and then a sequence of x-ray images is acquired. The dilution curve is determined from the x-ray images. In general, the x-ray images only give relative information about the contrast agent concentration. If absolute flow should be measured, an accurate attenuation calibration of the x-ray system is required.

The angiographic dilution technique has an even weaker theoretical basis than the standard indicator dilution theory: Doriot et al. (1997) conclude in their theoretical analysis that the indicator dilution theory is not applicable for angiographic techniques because of the way the contrast agent concentrations are averaged over the cross section. This technique also belongs to the group of angiographic methods to determine blood flow. However, as its limitations are already described here, it will not be considered further in the section on angiographic flow measurements.

2.4.3   Electromagnetic flow meters

The electromagnetic flow meter (EMF) is based on the phenomenon of electromagnetic induction discovered by Faraday (1832). When a charged particle moves in a magnetic field, an electric field is induced. Williams (1930) realized that this phenomenon could be used to measure velocities in a pipe. Fabre (1932) was the first to propose that electromagnetic induction could be used to measure blood flow. He described a measurement device, but did not present any evidence that he actually built the device.

If a magnetic field B is established around the blood vessel, a magnetic force F_M is applied to the ions in the blood:

$$F_M = e \cdot v \cdot B,$$

(2.23)

where e is the electric charge and v is the velocity of the ion. The positive and negative ions are separated and an electric field with voltage U_H is induced. The electric field applies an opposing force F_E to the ions:

$$F_E = \frac{e \cdot U_H}{d},$$

(2.24)

where d is the diameter of the vessel. The equilibrium voltage, known as the Hall voltage U_H, depends on the velocity of the ions and can be used to determine the velocity which is given by

$$v = \frac{U_H}{B \cdot d}.$$

(2.25)

(a) Scheme of electromagnetic flow meter.

(b) Exposed artery with electromagnetic flow meter.
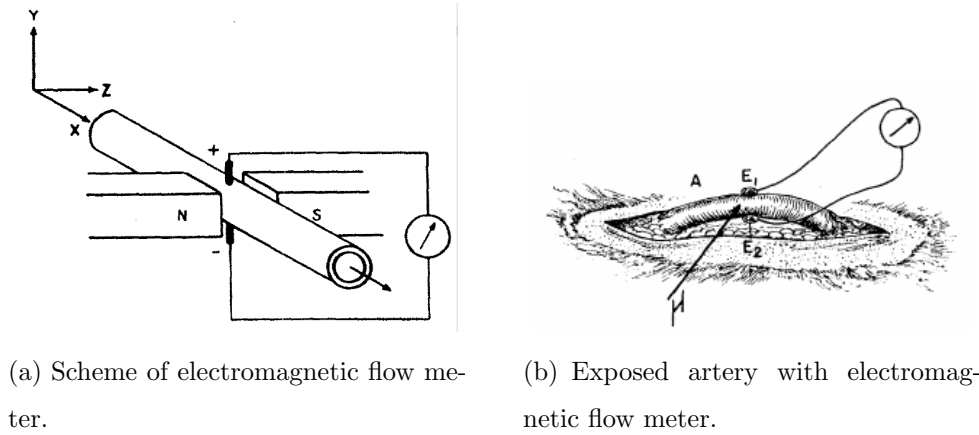
Figure 2.7: Illustrations of electromagnetic flow meter from Kolin et al. (1957).

Kolin (1936) built the first EMF for blood flow measurements and demonstrated the linear relationship between the volumetric flow rate and the Hall voltage. He applied the method to measure flow in the carotid artery of a dog. An illustration of his device is shown in Figure 2.7. Many practical issues associated with creating the magnetic field around the artery and measuring the Hall voltage had to be solved, but today the method is very accurate and has a good temporal resolution. Concerning the accuracy Wyatt (1968) reported the following: When properly calibrated, the EMF can be 2% accurate. Two manufacturers offer pre-calibrated devices with an accuracy of 10%. Partial breakdown of the insulation can lead to serious errors in the EMF measurements.

Unfortunately however, it is too invasive to be widely used in clinical practice. In particular, as the device must be put around the vessel, it cannot be used during endovascular interventions but only during open surgery. Because of its accuracy and its good temporal resolution, it is often used to determine the ground truth during experiments with phantoms.

2.4.4 Ultrasound

Ultrasound imaging uses reflected sound waves to image tissue structures in a patient. The sound wave is produced by the transducer and transmitted into the body. It is partially reflected at boundaries between different tissues when these tissues have different acoustical impedance. Some of these reflections return to the transducer and can be used to form an image. In B-mode ultrasound, a linear array of transducers simultaneously scans a plane through the body that can be viewed as a two-dimensional image on screen. This will be called grey-scale imaging in the following.

Measuring blood flow velocities with ultrasound became feasible when Satomura et al. (1960) suggested that the Doppler effect could be used. If the ultrasound wave is reflected from a particle, like a red blood cell, which is moving with the blood, the frequency of the reflected ultrasound wave changes. This change, the so-called Doppler shift, can be used to determine the velocity of the blood.

The ultrasound transducer emits an ultrasound wave with the emission frequency $f_{E,T}$.

(a) Doppler spectral waveform. (b) Colour Doppler Image.
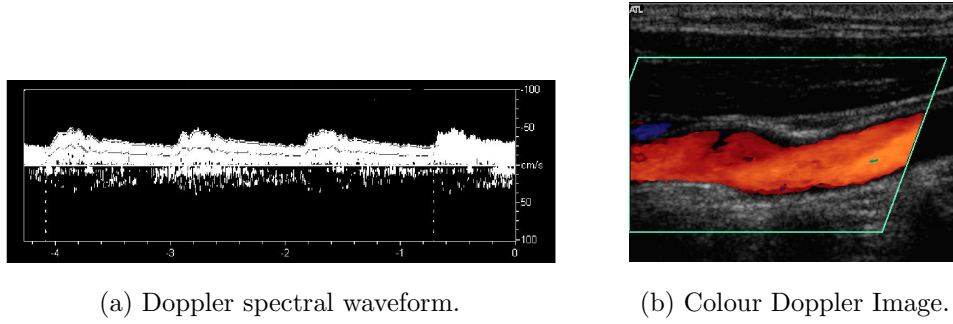
Figure 2.8: Flow analysis based on the Doppler effect.

The wave hits a blood particle, which is moving relatively to the transducer with a speed v_B and the velocity component in direction of the ultrasound beam is $v_B \cdot \cos(\alpha)$. If the particle is moving away from the transducer, the wave is received with a smaller frequency $f_{R,B} < f_{E,T}$ by the blood particle and reflected with the same frequency $f_{E,B} = f_{R,B}$. It is received by the ultrasound transducer with the frequency $f_{R,T} < f_{E,B}$. The Doppler frequency f_D is given by

$$f_D = f_{E,T} - f_{R,T} = 2 f_E \frac{v_B}{c} \cos(\alpha), \qquad (2.26)$$

where c is the speed of sound in the medium. The velocity of the blood particle can be determined by rearranging Equation 2.26 to give:

$$v_B = \frac{f_D c}{2 f_E \cos(\alpha)}. \qquad (2.27)$$

The Doppler frequency can be measured. The determination of the insonation angle α, however, is more difficult, as it will be discussed in the following. If the ultrasound transducer emits perpendicular to the vessel, the shift is reduced to zero and no measurements are possible.

The blood flow velocity varies within the blood vessel. Therefore, the Doppler signal is a combination of signals with different frequencies. A spectral analysis is used to recover the different velocities. The velocities also vary during the cardiac cycle. The Doppler spectral waveform represents both variations. An example is given in Figure 2.8(a).

The Doppler velocity measurements can be combined with grey-scale imaging of the blood vessel. This is called Duplex ultrasound. A further advance is Colour Doppler imaging. It combines grey-scale imaging with a two dimensional mapping of flow information. Stationary structures are assigned a grey value, whereas moving structures are assigned a colour value according to the velocity and orientation detected by the Doppler. Typically, red indicates motion in one direction, whereas blue indicates motion in the opposite direction. The magnitude of the velocity is indicated by the saturation of the colour. The range has to be selected by the user. Overall the blood flow acts as a contrast agent and it improves the imaging of blood vessels. An example image is shown in Figure 2.8(b).

Planiol and Pourcelot (1973) reported first blood flow measurements in the carotid arteries with ultrasound. Since then, ultrasound is increasingly used to examine the extracranial

carotids, particularly to examine stenoses in the proximal internal carotid. The different types of ultrasound examinations are applicable in different situations (Carroll, 1991): Grey-scale imaging provides more accurate quantification of low-grade stenoses and it can also be used for plaque characterisation. Doppler spectral analysis provides more accurate information for high-grade occlusive stenoses. The better the agreement between both assessments, the more reliable is the diagnosis. Colour Doppler can explain discrepancies between both assessments and it is the best way to find the point of maximal stenosis (Polak et al., 1989). At a more recent consensus conference it was concluded that for the quantification of a carotid stenosis all three examinations should be conducted (Grant et al., 2003).

The application of ultrasound in the brain is largely limited by the skull because the bones of the skull block the transmission of ultrasound. However, regions with thinner walls or small gaps – so-called insonation windows – can be used for transcranial ultrasound. The first transcranial Doppler (TCD) measurement was reported in 1982, when the blood flow velocities in the middle cerebral artery were measured through a window in the temporal area (Aaslid et al., 1982). Today many of the larger cerebral vessels can be examined with TCD, including the circle of Willis and the vertebral and basilar arteries. The main limitation of TCD is the sonographer's inability to determine the insonation angle. In clinical practice, the insonation angle is assumed to be relatively small so that the introduced error should be small. However, errors up to 50% in the velocity measurement have been reported (Krejza et al., 2001).

Transcranial colour Doppler (TCCD) allows outlining and visualization of the vessel. This allows reliable identification of the insonated vessel and measurement of the insonation angle. Then, the angle corrected velocity can be determined (Baumgartner et al., 1994; Seidel et al., 1995). The intra-observer variability of this method was reported to be between 5% and 13% (Baumgartner et al., 1994).

Measuring blood flow velocities with ultrasound is a non-invasive, bedside method. It has very small risk and side effects for the patient and it is relatively inexpensive. Disadvantages of ultrasound are the limited spatial resolution of the ultrasound images and for transcranial measurements the drop-out rate because of insufficient acoustic bone window in 20% of the patients (Seidel et al., 1995). Further problems are various artefacts, which might lead to a misinterpretation (Hedrick et al., 2004), a lack of standardized procedures (Grant et al., 2003), and substantial variability in equipment from machine to machine, from manufacturer to manufacturer and between older and newer equipment (Grant et al., 2003). Although blood flow velocities can be determined quite accurately, the determination of the volumetric blood flow rate is more problematic because an accurate diameter estimation is required.

During our clinical study, we used TCCD measurements for comparison. Although TCCD measurements can be obtained during an intervention, this proved to be tedious. It was very difficult to have the sonographer present during the intervention: in several cases it was impossible and in other cases the measurements had to be done 30 min before the intervention. Also a

considerable amount of user interaction was required to determine quantitative flow information from the ultrasound images. Additionally, repeated measurements on the same patient gave 30% difference in the resulting volumetric mean flow rate. The reason for this was probably the lack of precision of the diameter estimation.

2.4.5 Magnetic resonance angiography

It was known long before the advent of magnetic resonance imaging (MRI) that flow can change the MR signal. Suryan (1951) noted a variation of the MR signal with the velocity of a fluid. From the start of MR imaging, it was noted that blood flow produces artefacts in MR images: for example, fast moving flow produces a signal void. These artefacts can be used to image blood vessels (MR angiography) or to quantify blood flow. Two main techniques are possible: time of flight (TOF) MRI and phase contrast (PC) MRI.

The first in vivo flow measurements using MRI were done by Singer (1978) using the TOF technique. For the TOF technique, a thin slice perpendicular to the blood flow direction is subjected to excitation pulses. The signal of the spins decreases with an increasing number of excitation pulses until a saturation level is reached. The contrast in the image is based on the saturation of stationary tissue and fully magnetised spins in the flowing blood. More details on flow measurements with the TOF technique are given by Smith (1990). Today TOF-MRI is mainly used for vessel imaging.

In 1988 the foundations of the current method for measuring blood flow with MRI were laid: Walker et al. (1988) proposed to use PC MR angiography. The PC technique is based on a phase shift in the signal between stationary tissue and moving tissue. In normal images this can be seen as artefact. The phase shift is proportional to the blood velocity and it depends on the applied field gradients. To determine the phase shift, two measurements are taken: a reference measurement and a flow encoded measurement. Unfortunately, only one component of the velocity vector can be determined with one measurement. By acquiring flow encoded measurements in three orthogonal directions, a complex 3D flow field can be determined. The signal directly represents the velocity of the blood flow.

Non-invasive volumetric blood flow measurements are possible with PC-MR, but there are still some problems: PC methods are sensitive to a user specified range of velocities. The user chooses a velocity encoding value (v_{enc}) taking into account the expected value of the peak systolic velocity. Blood velocities higher than v_{enc} will cause a phase wrapping and might be misinterpreted in the image. However, the higher v_{enc} is chosen the lower is the signal to noise ratio (Marshall et al., 2004), which is a problem for low velocities during diastole. Misalignment between the true direction of flow and the direction of flow encoding introduces errors in the flow measurements (Mostbeck et al., 1992). Partial volume effects introduce errors for flow measurements in smaller vessels (Mostbeck et al., 1992). One normal flow measurement using this technique takes about 5 min (Marshall et al., 2004). Complex 4D visualisations are possible (Frydrychowicz et al., 2007), but the long acquisition time and the required motion

control still pose a problem for the clinical routine. PC-MR is used increasingly for diagnosis, but it is rarely used to guide interventions as interventional MRI is not yet widespread. It is questionable whether it might replace the x-ray guidance during endovascular interventions and it will certainly take a long time until it will be available at smaller clinical sites.

2.4.6   X-ray angiography

The measurement of blood flow using x-ray angiography will be explained in detail in Section 2.6. Measuring blood flow with angiographic images is minimally invasive. The main disadvantage is the radiation exposure during the examination. Therefore, angiographic sequences should be used for the flow estimation, which are acquired anyway during an intervention. Its main advantage is that angiographic systems are readily available in intervention rooms and that it is used during all cerebrovascular interventions. Additionally, it has a superior spatial and temporal resolution and signal-to-noise ratio compared to other image modalities(Shpilfoygel et al., 2000). Nevertheless, no method for quantifying blood flow based on angiographic images has been established in the clinical routine yet.

2.5   Extraction of morphological information from angiographic images

The main goal of this thesis is to develop a method for the quantification of blood flow from rotational angiography. As most algorithms for blood flow quantification from angiographic images, including the one which is proposed in this thesis, assume that the vessel geometry is known, methods for the extraction of morphological information are reviewed in this section.

Since the introduction of digital medical images, researchers have been interested in obtaining representations of the vessel geometry from these images. Kirbas and Quek (2004) presented a comprehensive review of vessel extraction methods that are currently available concluding that there is no generic method that fits all tasks. Which method is suitable depends on the image modality and the required output. Here, I will concentrate on methods for angiographic images and on the question of how 3D information can be determined from projection images.

The geometry of a blood vessel can basically be described in two different ways: either by a voxel- or surface-based representation of its lumen or by its centreline and either radius or cross-sectional area (CSA). To determine volume blood flow from the blood velocity, the knowledge of CSA or the radius is required and to establish an analytic representation of the vessel tree, the knowledge of the centreline is helpful. Thus, for the purpose of flow extraction, this review is focused on the centreline-radius representation.

Most methods to extract the vessel centreline and radius were developed in the field of quantitative coronary angiography (QCA). The goal of a QCA system is to assess the severity of a coronary artery stenosis. Brown et al. (1977) presented the first QCA system. It was followed by the QCA system from Reiber et al. (1978). The components of these systems and many similar systems will be discussed below. Although most of the methods presented

here, were intended for the evaluation of coronary arteries, they are also applicable for cerebral arteries.

2.5.1 Centreline

The definition of the term centreline is problematic. In particular at a bifurcation or at a non-elliptical vessel the centreline is not well defined. Brown et al. (1977) gives one possibility for the definition of a centreline determined from angiographic images: The centreline is mathematically defined such that its perpendicular at any point intersects both vessel edges at equal distance from itself . There are different approaches to determine it:

- manually by the user (Brown et al., 1977; Reiber et al., 1978; Kooijman et al., 1982; Hawkes et al., 1985; Selzer et al., 1989; Fleagle et al., 1989; Büchi et al., 1990; Movassaghi et al., 2004);

- automatically, in a clearly defined region of interest (Spears et al., 1983; LeFree et al., 1985; Wankling et al., 1990);

- automatically from a given start point and possibly several end points (Hoffmann et al., 1986; Eichel et al., 1988; Sun, 1989; Alperin et al., 1989; Haris et al., 1999);

- fully automatically (Nguyen and Sklansky, 1986; Guo and Richardson, 1998).

In the method of Brown et al. (1977), the user had to trace the borders of the vessel and then the centreline was computed according to the definition above. This is the system which required most user interaction. In the system from Kooijman et al. (1982), points on the centreline were selected manually. Then, the complete centreline was determined by interpolation. Particularly for tortuous vessels, where the distance between subsequent points must be small, this could still be a tedious procedure. Additionally, the results might not be reproducible. A method to improve the reproducibility is to recompute the centreline after the border detection (Selzer et al., 1989).

In the system from Spears et al. (1983), the user had to define a small rectangular region of interest around a small vessel segment. Then, the vessel edge points were determined automatically and the centreline was computed according to the definition above. In the method from LeFree et al. (1985), the user had to select a circular region which had to be centred around the lesion. Then, circular profiles of decreasing radius were used to determine the angular position of the centreline. In the approach from Wankling et al. (1990), a rectangular region of interest had to be given and the vessel segment was rotated such that its long axis is horizontal. The centreline was determined by connection of the pixels with maximum intensity of each column. The main limitation of methods in this category is that they are normally restricted to quite small regions of interest.

One possibility to determine the centreline between two given points is to use an iterative tracking algorithm. Such tracking algorithms typically find the path of maximum intensity in

an image or they are based on continuity constraints of vessel position, curvature, diameter or image intensity.

Hoffmann et al. (1986) developed the "double-square-box region-of-search" method: the perimeter of a box around the current point is searched for the maximum value. If the direction deviates by less than 25° from the current direction, the point is selected as the next centreline point. Otherwise, the procedure is repeated for a smaller box.

Eichel et al. (1988) proposed a method called sequential edge linking. As input, the start point and the initial direction are provided. All potential paths are associated with a metric value (based on the probability of whether each element of the path is an edge element) and were stored in a stack data structure. In each step of the method, the best path was removed and extended in three possible ways. The metrics of the descendent paths were calculated and they were inserted into the stack according to the value of the metric. The main limitation of this method was that it was computationally expensive. This should be less of a problem today.

General problems with tracking algorithms are as follows: The tracking might stop too early (for example at a stenosis); or the tracking might cross over to another vessel; or the tracking might leak into an area without any vessels. Sun (1989) tried to improve tracking by exploiting spatial continuity of the vessels centreline, orientation, diameter and density. The radius and orientation of the current centreline point is used to extrapolate the vessel centreline. In the 'look-ahead' distance, which corresponds to the current radius, a density profile is determined along a scanline perpendicular to the current orientation. Matched filtering is used to determine the next centreline point and radius from the density profile. Sen et al. (1999) evaluated different methods to restrict the tracking and they found that backward tracking (from distal to proximal) improved the results substantially. There are numerous variations of these iterative tracking methods, but all known methods fail in the case of a severe stenosis (Wink et al., 2004).

Front propagation or minimal cost path methods have the potential to cope with this problem. Sethian (1996) proposed the fast marching method, which is a fast wavefront propagation method and is a special case of the level set method (Malladi and Sethian, 1995). In contrast to other level set methods, the fast marching algorithm uses the assumption that the propagation speed is always positive to determine the propagation very efficiently. The propagation is analogous to the propagation of a wavefront in a supporting medium: The wavefront propagates outwards from a point source with a speed depending on the supporting medium. Deschamps and Cohen (2002) applied this method to the segmentation of blood vessels. The centreline of the blood vessel can be determined by backtracking on the results of the fast marching algorithm. This results in a minimum cost path that connects the start and end points, which are normally identified manually by a user. The costs are given by the inverse of the speed function. If the cost function is constant in an area, the path with the smallest Euclidean distance is found. This will have the effect that the minimum cost path does not go through the centre of a large and curved vessel. Deschamps (2001) proposed a centering strategy to solve this problem. In

original versions of the algorithm, the speed function was determined directly by the image intensities. Wink et al. (2004) proposed to use the vesselness, as described by Frangi et al. (1998), to improve the speed function. Later, they stated that situations such as the proximity or crossing of vessels cause problems for these methods and proposed to penalise radius changes to reduce this problem.

Fully automatic solutions generally involve two steps: First, potential centreline points are detected over the complete image, which are then combined to determine the vessel tree structure. Fully automatic methods are often not as reliable as methods which use a start point. Additionally, the root of the vessel tree should be known with certainty for the purpose of flow quantification. Therefore, fully automated methods will not be considered further here.

2.5.2 Radius and cross sectional area

For the estimation of the radius or the CSA from angiographic images, there are also several different approaches available:

- manual tracing of the vessel contour (Brown et al., 1977; Harpen and Lecklitner, 1984);

- methods based on automatic edge detection (geometric methods) (Kooijman et al., 1982; Spears et al., 1983; Hawkes et al., 1985; Mancini et al., 1987; Fleagle et al., 1989; Selzer et al., 1989; Büchi et al., 1990; Beier et al., 1992);

- densitometric methods (Crawford et al., 1977; Kruger, 1981; Colchester and Brunt, 1983; Nichols et al., 1984; Colchester et al., 1986; Hawkes et al., 1992);

- model-based methods (Shmueli, 1983; Fujita et al., 1987; Pappas and Lim, 1988; Alperin et al., 1989).

In the first QCA system from Brown et al. (1977), the user had to trace vessel contours manually. This was a very tedious process, which took at least 10 min for one image. Also, the results depended on the user detecting the vessel edges reliably. Nevertheless this approach was used in numerous clinical systems (Hermiller et al., 1992).

Most later systems are based on automatic edge detection. In most cases, the centreline or at least the local vessel direction is given beforehand. This information is used to determine the image intensity profile, also called densitometric profile, along a scanline perpendicular to the local vessel direction. The borders of the vessel are determined from the edges of this profile. The vessel radius is given by half of the distance between the right and the left border. The edge detection can be based on the first derivative, the second derivative or a combination of both. Beier et al. (1992) reported that using the first derivative systematically overestimated the radius, whilst using the second derivative systematically underestimated the radius. But they also stated that it is not necessary to determine both derivatives as a combination of the first derivative with an adequate correction is much faster and leads to a similar accuracy. Kooijman et al. (1982) reduced the influence of noise by averaging each scanline with its adjacent

scanlines. Spears et al. (1983) fitted a polynomial to the profile and determined the derivatives from the polynomial. Selzer et al. (1989) introduced an exponential weighting to reduce the influence of nearby vessels. Fleagle et al. (1989) did not use scanlines, instead they determined 2D derivatives of the complete image. To determine the CSA, an assumption about the shape of the vessel is required. If the CSA is determined from a single radius, the vessel cross section must be assumed to be circular and the CSA is determined from the squared radius. Thus, any errors in the radius estimation are exaggerated. Brown et al. (1977) used two radius estimations from perpendicular views assuming an elliptical vessel cross section.

An alternative approach to characterize the vessel lumen is the densitometric approach which was first outlined by Kruger (1981). In this approach, it is necessary to have background subtracted images, and image intensities should be calibrated so that a linear relationship exists between the image intensities and the amount of iodine in the blood vessels. When the blood vessel is parallel to the detector plane, the integral of the densitometric profile depends linearly on the concentration of iodine in the blood vessel and the CSA of the blood vessel. If this is repeated at several locations along the vessel with the same contrast agent concentration, the relative increase or decrease of the CSA can be calculated and, in particular, a relative stenosis measure can be determined. Absolute diameters can be determined by comparing with densitometric profiles of calibration tubes of known size and equal contrast agent concentration. The problem of this is that in general the contrast agent concentration is not known. This is addressed by the approach of Hawkes et al. (1992). They calibrate for the product of the iodine concentration and an attenuation calibration factor using the assumption of circular cross section at a healthy vessel segment. The resulting calibration factor is used to determine the cross sectional area of a diseased segment which must be nearby to have the same concentration of contrast agent. The radius is normally determined from the CSA under the assumption of a circular cross section.

Shmueli (1983) proposed a model-based approach for the vessel radius estimation from DSA images. Pappas and Lim (1988) extended this method for non-subtracted images by also modelling the background. The vessel is modelled by a general cylinder with elliptical cross section and the background is modelled by a low order polynomial. The model is used to compute an ideal densitometric profile. The parameters of the model, in particular the radius of the cylinder, are fitted to the measured densitometric profile in an iterative manner. Fujita et al. (1987) proposed a variation which also takes the point spread function of the x-ray system into account and which is known as the iterative deconvolution method. The actual densitometric profile is compared to model profiles, which are generated by convolution of a cylinder profile with the point spread function. The radius of the cylinder is then adapted until the difference between both profiles is minimised.

The main advantage of edge-based approaches compared to densitometric approaches is that they depend less on the concentration of contrast agent and that the image intensities do

not have to be calibrated. From densitometric flow measurements it is known that the contrast agent concentration in the vessel varies temporally and spatially. These variations are used for the flow quantification. Therefore, the assumption of constant contrast agent concentration is questionable. In general, the image intensities are not linearly proportional to the attenuation due to beam hardening and scatter. This results in the effect that vessels behind bones appear to be less dense than others. It is possible to account for these variations with an analytical model or with an attenuation calibration. However, it still limits the clinical applicability. Another limitation of the densitometric approaches is that the vessel should not be foreshortened in the projection image. Moderate foreshortening can be corrected if the vessel orientation is known. This, however, is not always the case. The main limitation of edge-based approaches is that the vessel edge is often not clearly defined in the image because of the inherent blurring by the x-ray system. This is not an issue for densitometric approaches. Another advantage of the densitometric approach is that the vessel CSA can also be computed correctly for vessels with irregular cross sectional areas. This is particular important at a stenosis.

Doriot et al. (1992) compared the accuracy of the edge-based and the densitometric approaches. They concluded that the densitometric approach is more accurate for quantification of the cross sectional area from a single view. For biplane views, results were similar for both approaches. Hoffmann et al. (2002) evaluated the accuracy of all three automatic approaches. They concluded that for larger vessels good results could be obtained with all three approaches, but for smaller vessels only the densitometric and the model-based approaches gave accurate results. The main limitation of both studies was that they were based on static phantoms and not on contrast agent injections into a circulation. So they could not evaluate the effects of variations in the contrast agent concentrations. This should be mainly a problem for the densitometric approach. However, during my experiments, I have also seen that the edge-based radius estimation gave lower results when the contrast agent was injected into a circulation compared to constant filling with approximately the same concentration of contrast agent. Additionally, Hoffmann et al. did not consider different orientations of the vessel. Dorsaz et al. (1995) reported high discrepancies in densitometric measurements from biplane views. These could be reduced but not resolved, if a correction for orientation was introduced.

2.5.3   Obtaining absolute vessel size and 3D vessel geometry

Without any additional information or calibration, it is not possible to determine the absolute size of a vessel from single plane angiographic images because no information about the magnification is available. It is also not possible to reconstruct the 3D vessel geometry from single plane angiographic images because no information about the depth of the vessels is available. The following approaches tackle the problem of absolute radii:

- usage of the catheter as scaling device (Brown et al., 1977; Kooijman et al., 1982; Mancini et al., 1987; Selzer et al., 1989; Fleagle et al., 1989);

- densitometric methods with an attenuation calibration as explained in the previous section.

The following approaches tackle both problems

- point-based reconstruction (Kim et al., 1982; Bresler and Macovski, 1984; Wollschlager et al., 1985; Hawkes et al., 1985; Kitamura et al., 1988; Fencil et al., 1988; Metz and Fencil, 1989; Guggenheim et al., 1991; Wahle et al., 1996; Blondel et al., 2002; Movassaghi et al., 2004; Blondel et al., 2006);

- 3D fast marching based on 2D information (Young et al., 2003; Law et al., 2003);

- CT-like reconstruction (Feldkamp et al., 1984; Niki et al., 1993; Koppe et al., 1995; Schmitt et al., 2005).

Brown et al. (1977) proposed to use the catheter as a scaling device to determine absolute vessel size. For a catheter of known size, the radius is determined from the x-ray image. The 'real' radius and the 'image' radius are used to compute the magnification factor. Many edge-based systems use this method. Unfortunately, the magnification factor is only correct for vessels which lie in the same plane as the catheter, and for each centimetre which the vessel is "out-of-plane", the error in the radius increases by 1.5% (Wollschlager et al., 1985). When the exact magnification is known, the depth of the object could also be determined using the theorem of intersecting lines.

For a point-based reconstruction, corresponding points in at least two x-ray views from different orientations or locations must be given. If the precise orientation and location of the x-ray system is known for both views, the 3D points can be reconstructed using the epipolar constraint. This is illustrated in Figure 2.9. In most approaches, first the 2D centreline is determined with techniques discussed above and then corresponding points from both projection images are searched for. If the correspondences for all centreline points are given, the complete 3D centreline can be reconstructed. When the 3D position and orientation of the segment are known, the magnification and therewith the absolute vessel dimensions (radii and length) can be determined. This method is most often applied for biplane views. However, it was also applied to triplane views (Blondel et al., 2002), multiple views (Movassaghi et al., 2004; Blondel et al., 2006), stereoscopic views (Fencil et al., 1988) and nearby views (Lee and Poston, 1997).

The problem of finding corresponding points unambiguously is often not trivial. In many systems, corresponding points are identified by the user (Hawkes et al., 1985; Kitamura et al., 1988; Metz and Fencil, 1989; Wahle et al., 1996). When the geometry of the x-ray system is already known, the selection of corresponding points in the second view can be supported by displaying the epipolar line, which indicates all possible positions of the second point. When the centreline in one image is given, the corresponding points in the second image can be searched for on the epipolar line (Guggenheim et al., 1991; Blondel et al., 2002; Movassaghi et al., 2004). But often more than one vessel crosses the epipolar line (Blondel et al., 2002). Kim et al. (1982) tracked the leading edge of a bolus in biplane images to determine corresponding
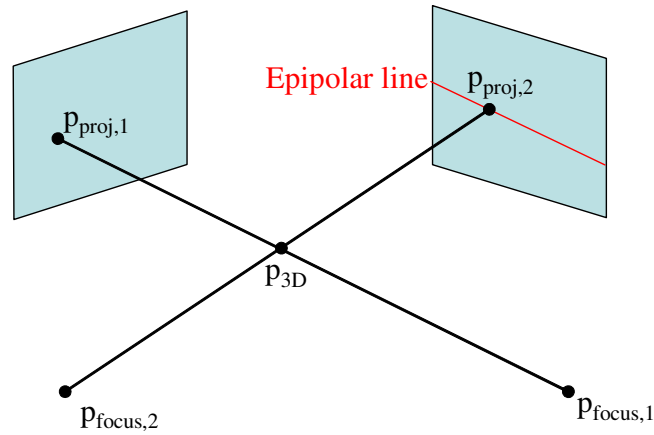
Figure 2.9: Epipolar geometry.

points. If nearby views or stereoscopic views are used, the correspondences can be determined automatically by a cross correlation (Fencil et al., 1988). In this case however, the depth of the vessels is less well defined. In systems with three or more views, it is also easier to determine corresponding points automatically and unambiguously. Blondel et al. (2006) used two views to determine a potential reconstruction and the remaining views to evaluate the quality of the reconstruction. This is repeated for different selections of the two views. In the end, the reconstruction with the best evaluation is chosen. This process is called multi-ocular matching.

The precise orientation and location of the x-ray system can be determined from a geometry calibration. MacKay et al. (1982) proposed to use a calibration cube with 15 steel balls, which are easily detected in the x-ray images. The best geometric parameters are determined so that the distances between the 2D projection points of the known 3D centrepoints of the steel balls and the 2D image coordinates of the steel balls are minimized. If the configuration of the x-ray system only changes in a reproducible way, the calibration can be done beforehand. Some systems only need recalibration after maintenance or after a duration of approximately six months to ensure reproducibility (Movassaghi et al., 2004). However, if the user manually selects the system configuration to obtain the best view of the vessel of interest, the geometry calibration must be repeated for each patient. For this, the patient has to be removed from the field of view and the calibration object is imaged instead. As this disturbs the clinical workflow, methods have been developed to determine the calibration directly from the medical images.

Metz and Fencil (1989) proposed a method to determine the relative geometry of a biplane system by manually identifying eight landmark points (e.g. bifurcation points or stenotic lesions) from the medical images. Wahle et al. (1996) reduced this to five required points. The clinical applicability of this approach is also limited as landmarks cannot be extracted with very high accuracy and reproducibility, and errors in the landmark selection will lead to errors in the 3D reconstruction. Navab et al. (1996) proposed to use a calibration cylinder which could be placed around the head of the patient.

A more recent approach for the 3D reconstruction is able to avoid the correspondence problem. To achieve this, Young et al. (2003) proposed a special version of the fast marching algorithm. The fast marching wavefront is propagated in 3D, but the 3D speed function is based on the 2D image intensities. The geometric parameters have to be known beforehand. To determine the speed value at a 3D point, its projection points are determined for all images and for each projection point a measure of vesselness is determined. The speed value at the 3D point is given by the product of all 2D measures. Young et al. (2003) used the vesselness filter to determine the 2D measure and they applied this method to multiple views. Law et al. (2003) used a local thresholding technique and applied it to biplane views. They successfully reconstructed the right coronary artery. However, it can be argued that biplane views are not sufficient if the image contains more complex vessel trees like in the cerebral vasculature. The main advantages of the fast-marching-based reconstruction is that it works in 3D; if the 3D point is known, the 2D points can be determined unambiguously and the correspondence problem can be avoided. For the geometric calibration, the same considerations as above apply.

Another way to extract 3D information from 2D images is based on the volume reconstruction from rotational angiography. This is mainly used for the examination of cerebral vessel malformations. From a sequence of 2D images acquired on a rotational trajectory, a CT-like volume – the 3DRA dataset – is reconstructed. Special reconstruction algorithms have been developed to take account for the cone beam geometry. Most methods are based on the Feldkamp algorithm (Feldkamp et al., 1984), which assumes that the attenuation of every voxel is constant in time and that the precise orientation and location of the x-ray system are known. Similar calibration methods to those described above are used to determine the geometric parameters. In the 3DRA dataset, the vessel tree can be segmented (Niki et al., 1993; Schmitt et al., 2005). As the 3DRA dataset is not used in the main part of this thesis, methods are not explained in more detail.

For the work of this thesis, the rotational angiographic sequence is used for both blood flow quantification and geometry reconstruction. For the blood flow quantification, it is desirable that the sequence shows how the contrast agent enters the vessel (inflow phase) and how the contrast agent leaves the vessel (outflow phase). This, however, poses a problem for many 3D reconstruction methods. It is impossible to solve the point correspondence problem if the vessel is not filled with contrast agent in one of the two selected images. The selection of the two images is difficult if it is not known beforehand in which images the vessels are enhanced. The CT-like reconstruction assumes that the attenuation of all voxels is constant. However, during the inflow phase and outflow phase, this condition is not met. For this thesis, a method based on the fast marching algorithm was developed.

2.6 Extraction of haemodynamic information from angiographic images

For over 30 years researchers have tried to extract information about blood flow from angiographic images. To achieve this, contrast agent is injected during the acquisition of the x-ray sequence. As the first images of the sequence normally do not show any contrast agent, they can be used for background removal by log-subtracting them from the later images obtained with contrast agent. The resulting digitally subtracted angiographic (DSA) sequence is then used to extract the flow information.

Different types of information about blood flow can be extracted, including relative flow information (increase or decrease with respect to a reference measurement), mean velocity, mean volumetric flow rate, the blood flow waveform (usually averaged over several cardiac cycles), or the instantaneous volumetric flow rate. The latter is the most desirable, but many methods can only determine one of the others.

After the injection, the contrast agent mixes with the blood and is transported by the blood. The contrast agent concentration varies over time and along the vessel. The attenuating material in the contrast agent is iodine. The line integrals of the iodine density along the x-ray beams determine the image intensities in the DSA image. All existing approaches for flow measurements from angiographic images are based on analysing changes in the x-ray image intensity due to changes of the contrast agent concentration.

A convenient way to represent these variations is given by the so-called "flow map", introduced by Colchester et al. (1986) (although they referred to it as a "parametric image"). A flow map is represented as an image in which the intensities depend on the density of iodine, and where the horizontal dimension is time t and the vertical dimension is length l along the vessel. It represents the contrast agent propagation through the vessel. When the flow changes, the flow map changes as well. This is illustrated in Figure 2.10.

Individually, each row of the flow map represents a time intensity curve (TIC), whereas each column represents a distance intensity curve (DIC). The first and last TIC are presented in the second column of Figure 2.10. Different DICs are presented in the third column of Figure 2.10.

The flow map contains two different types of information: kinematic and densitometric information. The densitometric information is captured by the magnitude of the intensities of the flow map, whereas the kinematic information is captured by the gradients of the pattern of the flow map.

Pulsatile blood flow introduces a characteristic pattern in the flow map, and the shape of the pulsatile waveform determines the shape of the pattern. Therefore, information about the waveform can be determined from relative densitometric information.

In general, the flow map contains only relative information about the iodine density because different non-linear effects in the x-ray imaging chain interact making it difficult to determine quantitative information about the iodine density. If this is possible, the concentration of con-
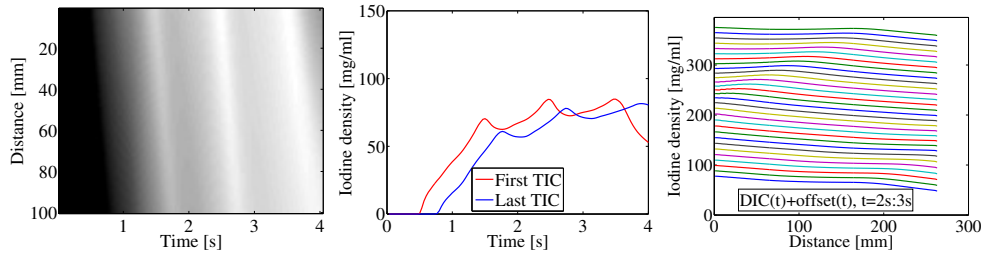
(a) Low flow (from simulation).
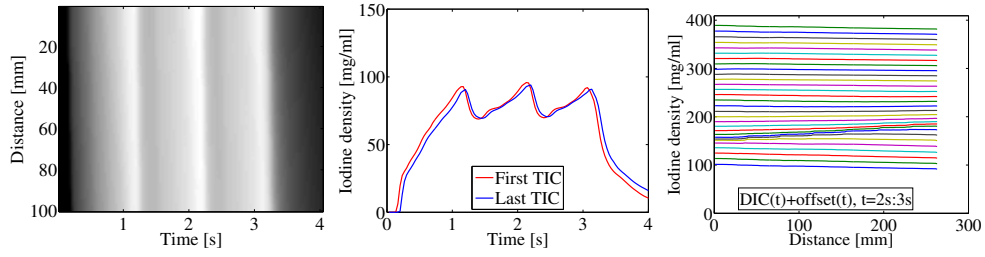
(b) High flow (from simulation).
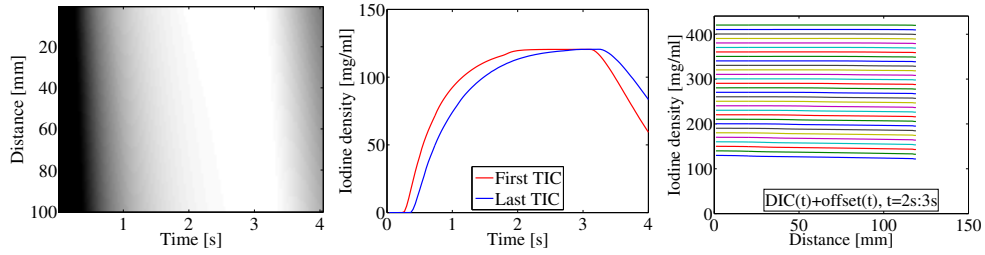
(c) Steady (non-pulsatile) flow (from simulation).
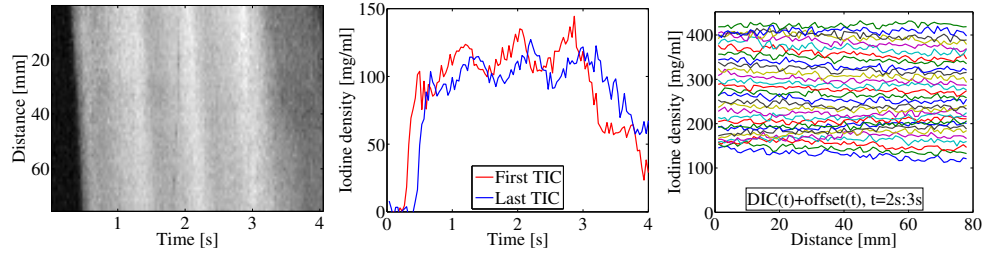
(d) Low pulsatility (from experiments).
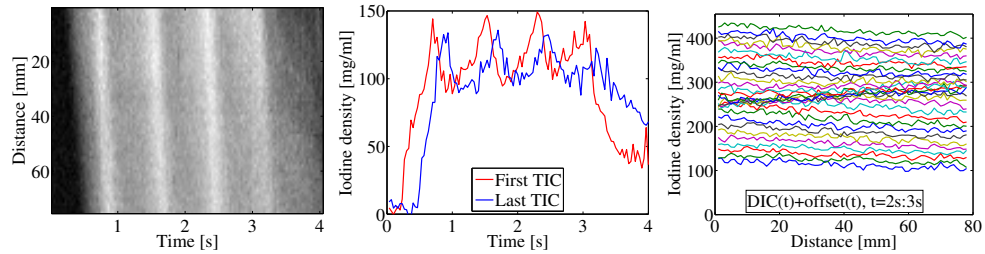
(e) High pulsatility(from experiments).

Figure 2.10: Influence of flow properties on the flow map. Flow maps are shown on the left-hand side. The centre column shows the first and last TIC. The shift between the first and the last TIC depends on the volumetric flow rate. The right-hand side shows different DICs. The contrast of the pattern inside the flow map depends on the pulsatility.

trast agent in a vessel can be determined from the x-ray image. Provided the flow rate of the injection is known, the mean volumetric flow rate of the circulation can be determined from the contrast agent concentration.

The contrast agent transport velocity determines how the pattern changes along the length of the vessel. This is the kinematic information. The velocities vary temporally because of the pulsatile waveform, and they vary spatially because of the flow profile and vessel radius changes. This makes it difficult to interpret this information meaningfully. To reduce the complexity of the kinematic information, many methods make simplifying assumptions. In particular, they either ignore spatial or temporal variations (or both).

If a method ignores the flow profile, the following problem arises: The flow appears to be faster during the inflow phase, whereas it appears to be slower during the outflow phase. The reason for this is the (almost) parabolic flow profile: fast flowing contrast agent in the centre of the vessel appears in the flow map first, and slow flowing contrast agent next to the vessel border leaves the flow map last. From this point onwards, this effect will be referred to as the parabolic flow effect.

Methods presented in the literature use different information from the angiographic sequence, make different assumptions, and determine different information from the angiographic sequence. Most methods can be associated with one of the following categories:

- methods based on TICs at different sites along a vessel (Rutishauser et al., 1967; Yerushalmi and Itzchak, 1976; Silverman and Rosen, 1977; Höhne et al., 1978; Kruger et al., 1983; Fencil et al., 1989; Schmitt et al., 2002, 2005; Bogunovic and Loncaric, 2006);

- methods based on DICs at different points in time (Swanson et al., 1988; Seifalian et al., 1989; Hoffmann et al., 1991; Shpilfoygel et al., 1998; Bladin et al., 1996; Rhode et al., 2005);

- methods based on iso-contours of the flow map (Colchester et al., 1986; Brunt et al., 1992);

- methods based on optical flow (Fitzpatrick, 1985; Efron et al., 1978; Amini et al., 1993; Imbert et al., 1995; Huang et al., 1997a; Rhode et al., 2001);

- methods based on the indicator dilution theory (Korbuly, 1973; Lantz et al., 1980);

- and methods based on the first pass distribution theory (Marinus et al., 1990; Hangiandreou et al., 1991; Molloi et al., 1993, 1998, 2004).

All categories are considered in the following.

2.6.1 Methods based on time intensity curves

Methods based on TICs estimate how long the bolus needs to travel from one vessel site to another. To achieve this, a TIC is determined at least at two sites of the vessel and the bolus

arrival time (BAT) is estimated for each site. The mean velocity is derived from the mean transit time between two sites, given by

$$v = \frac{|\mathbf{p}_2 - \mathbf{p}_1|}{\mathcal{A}(\mathbf{p}_2) - \mathcal{A}(\mathbf{p}_1)}, \tag{2.28}$$

where $|\mathbf{p}_2 - \mathbf{p}_1|$ represents the distance along the vessel centreline between both sites and $\mathcal{A}(\mathbf{p})$ is the BAT at site $\mathbf{p}$. If more than two TICs were determined the process is repeated. Several BAT definitions have been investigated, including:

- the time of the peak of the TIC (Höhne et al., 1978; Forbes et al., 1985; Tenjin et al., 1998; Bogunovic and Loncaric, 2006);

- the time of the leading half peak of the TIC (Silverman and Rosen, 1977; Kwan et al., 1986; Tenjin et al., 1998; Bogunovic and Loncaric, 2006);

- the time of the trailing half peak of the TIC (Tenjin et al., 1998);

- the time of the peak gradient of the TIC (Crepeau and Silverman, 1973);

- the time of the minimum gradient of the TIC (Schmitt et al., 2002);

- the time when a certain threshold is first exceeded (Yerushalmi and Itzchak, 1976);

- and the time corresponding to the centre of gravity of the area under the TIC (Rutishauser et al., 1967).

Relative BATs can be defined using the maximum cross correlation of two TICs (Silverman and Rosen, 1977; Fencil et al., 1989) or by template matching (Schmitt et al., 2005). Definitions which use the complete TIC have been shown to be slightly more successful (Shpilfoygel et al., 2000), and fitting a gamma variate curve (Kruger et al., 1983) or a polynomial (Kwan et al., 1986) to the TIC beforehand improves the stability of the determination of the BAT.

TIC-based methods are fast, easy to implement and they can work on multiple vessel segments. Another advantage is that the centreline of the vessel does not have to be known. However, to get absolute flow estimates, the distance along the centreline and the radii must be known.

Unfortunately, TIC-based methods are also known to give unreliable results in the case of pulsatile flow (Colchester et al., 1986; Hoffmann et al., 1991; Shpilfoygel et al., 2000) and it is not possible to extract a time dependent blood flow waveform, since the method implicitly assumes that the flow is steady. In many publications, steady flow was used during the experimental validation and therefore good results could be reported. However, for pulsatile flow, results of TIC-based methods have been found to vary up to 100% (Hoffmann et al., 1991). Forbes et al. (1985) reported that their method was 40% accurate in 75% of all cases; Fencil et al. (1989) reported an average error of 25%. For most BAT definitions, the resulting velocity estimate depends on the temporal shift of the leading flank of the bolus. Therefore, the method

determines the velocity directly after the start of the injection. If this is systole, the flow will be overestimated; if this is diastole, the flow will be underestimated.

The accuracy of the mean flow measurement could be improved by gating the measurement in a way that the average is computed over exactly one heart cycle or by averaging the measurement over many heart cycles (Shpilfoygel et al., 2000). Another possibility is to use a very short injection during systole and a very short injection during diastole (Kedem et al., 1978).

These methods implicitly assume plug-flow, and because of the parabolic flow effect, the following systematic problem occurs: Using a BAT definition based on the leading flank will result in an overestimation of the flow, whereas using a BAT definition based on the trailing flank will result in an underestimation of the flow. This is probably one reason why definitions which use the complete TIC have been shown to be slightly more successful.

A more recent model-based approach to deal with pulsatility and TICs was proposed by Bredno and Groth (2005). In this approach two TICs are extracted: one at the beginning and one at the end of the vessel segment of interest, called TIC_{in} and TIC_{out}, respectively. A flow model is then used to predict the appearance of the TIC_{out} using the TIC_{in} as an input. The mean volumetric flow rate, the pulsatility, and the flow profile are further inputs. These parameters are adapted to improve the fit of the measured TIC_{out} and the predicted $TIC_{predict}$. The least squared error was chosen as the cost function minimised during the fitting process.

Although this method is based on TICs, it does not have to assume steady flow. However, only the pulsatility factor is estimated during the optimisation and not the shape of the pulsatile waveform. The flow model can assume an arbitrary profile between plug flow and parabolic flow. Therefore, variations of the appearance of the TIC during inflow and during outflow can be explained by the model and do not pose a problem.

All methods based on two TICs ignore most of the information available in the data: In particular, they only use kinematic information and they ignore all the information which is available about the contrast agent concentration between the start and the end point.

2.6.2 Methods based on distance intensity curves

Methods based on DICs, estimate how far the bolus has travelled between two successive frames. The first approaches to determine blood flow from DICs used different features to track the leading edge of the bolus (Spiller et al., 1982; Parker et al., 1987). These methods have the disadvantage that the flow is only determined during the inflow phase and therefore it is systematically overestimated because of the parabolic flow effect. Spiller et al. (1983) determined systolic and diastolic blood flow by tracking the leading edge of injected boluses. They have reported a systematic overestimation of 20%.

What is remarkable about the work of Parker et al. (1987) is that they used explicit information about tapering and branching of the vessel tree. For each branch and each frame, they determined the volume of passage V, defined as the volume of the current branch and all its descendants which has been passed by the leading edge of the bolus. The instantaneous

volumetric flow rate was defined as

$$Q = \frac{\delta V}{\delta t}.$$ (2.29)

They could use observations from several branches and that is why they could make observations during more than one heart cycle although they used only the leading edge of a single contrast agent bolus. They also reported a phasic change in the flow during the cardiac cycle (the pulsatile waveform) and that the flow is 'somewhat high'. Unfortunately this approach has not been developed further; later DIC-based methods assumed a constant radius again.

Swanson et al. (1988) were the first to propose the velocity may be determined from the best shift between two DICs obtained at two consecutive frames. Seifalian et al. (1989) and Hoffmann et al. (1991) proposed similar methods. In their approaches, the best shift s_0 is given by the minimum of the sum of squared differences of the two DICs. The instantaneous velocity $v(t)$ is then given by

$$v(t) = \frac{s_0}{t_{k+1} - t_k}.$$ (2.30)

If the shifts between all DICs from adjacent times steps are estimated, a waveform can be extracted.

In Figure 2.10 it can be seen that the features in the DICs are very weak. Therefore, this approach is very sensitive to noise. Shpilfoygel et al. (1998) suggested to fit a parabola to the difference function. The best shift is given by the minimum of the parabola. For the same reason, Rhode et al. (2002) used polynomial functions to model the DICs prior to determining the optimal shift between successive curves. Furthermore, Rhode et al. proposed a flow waveform shape model based on principal component analysis to constrain the determination of the optimal shifts.

Because of the parabolic flow effect, these methods overestimate the flow during the inflow phase and underestimate the flow during the outflow phase. Brunt et al. (1992) and Hawkes et al. (1994) reported that, in the case of high flows, the results for the first half of the cardiac cycle were poor because of the absence of contrast agent.

Hawkes et al. (1994) stated that there is a trade off between the maximum measurable blood velocity, vessel path length and the acquisition frame rate. If the contrast agent bolus moved completely through the observed vessel area between consecutive frames, the method would fail. Their experiments showed that an overlap of 50% between successive frames was required. At a frame rate of 25 frames/sec and a maximum velocity of 1 m/s, they would require a vessel length of at least 8 cm. The problem is that the vessel is not allowed to taper or to branch on this distance. Rhode et al. (2005) stated that the vessel length could be the limiting factor for a clinical application.

Despite all these problems, many promising results have been reported in literature. The main advantages of DIC-based methods are that they can handle pulsatile flow well and that they use all kinematic information which is available for one segment in the image sequence.

2.6.3   Methods based on iso-contours from the flow map

Colchester and Brunt (1983) were the first to propose the usage of the flow map – they called it "parametric image" – to overcome problems of the TIC-based methods. They proposed to determine the velocity from the slope of iso-concentration contours in the flow map as given by

$$v = \frac{ds}{dt} = \tan\theta, \tag{2.31}$$

where s is distance along the vessel, t is time and θ is the inclination of the iso-contours. The user could manually divide the iso-contours into segments and fit a straight line to each segment. This gives multiple velocity estimates at different times and different positions down the vessel. The main limitations of this approach were that the selection process was subjective and very time consuming (Brunt et al., 1992).

Wicks (1989) and Brunt et al. (1992) presented the method in more detail and also presented an automatic way to determine the slope of the iso-contours by determining the gradient image of the flow map, and determining θ from the direction of the gradients. Brunt et al. (1992) stated that Equation 2.31 is only valid if dispersion is negligible, but because of the parabolic profile and diffusion this is not necessarily true. They also reported that the method is susceptible to noise. The automatic way to determine the iso-contours is equivalent to the 1D optical flow problem. Therefore, it is further discussed in the next section.

2.6.4   Methods based on optical flow

Optical flow was developed in the field of computer vision to determine the motion of rigid objects. For an image sequence $I(x, y, t)$, the basic optical flow equation

$$\frac{dI}{dt} = \frac{\partial I}{\partial x}\frac{\partial x}{\partial t} + \frac{\partial I}{\partial y}\frac{\partial y}{\partial t} + \frac{\partial I}{\partial t} \tag{2.32}$$

relates the temporal object brightness changes dI/dt to the spatial images brightness changes $\partial I/\partial x$ and $\partial I/\partial y$, the temporal images brightness changes $\partial I/\partial t$ and the object velocities dx/dt and dy/dt. Equation 2.32 can be rewritten as

$$\frac{dI}{dt} = I_x \cdot v + I_y \cdot u + I_t. \tag{2.33}$$

In general, it is not possible to solve this equation for u and v without making assumptions about the underlying motion.

Many optical flow methods then assume that the brightness of one point of the object does not change (Efron et al., 1978; Horn and Schunck, 1981; Huang et al., 1997b; Rhode et al., 2001):

$$\frac{dI}{dt} = 0. \tag{2.34}$$

The simplified optical flow equation is then given by

$$\epsilon_1 = I_x \cdot v + I_y \cdot u + I_t = 0. \tag{2.35}$$

This means that the brightness changes in the image must be due to motion of the object. The derivatives can be determined from the image sequence. This results in one equation with two unknowns u and v. To solve the equation a second constraint for the velocity is required.

Horn and Schunck (1981) further assumed that neighbouring points of rigid objects must have similar velocities. This led to the velocity smoothness constraint for the motion of rigid bodies. One way to express the velocity smoothness constraint is to minimize the square of the gradients of the velocity:

$$\epsilon_2 = u_x^2 + u_y^2 + v_x^2 + v_y^2. \tag{2.36}$$

They proposed an iterative method to compute the velocities by minimizing the following function:

$$\int \int (\epsilon_1 + \alpha\epsilon_2)\, dx dy, \tag{2.37}$$

where the integral is evaluated over the whole image and α is a positive weighting parameter.

Cornelius and Kanade (1984) adapted this work and made it more applicable for blood flow measurements. They allowed smooth brightness changes of the object and applied the velocity smoothness constraint only within regions that are separated from the rest of the image by recognizable boundaries (for example, within a blood vessel). They minimized the following function

$$\int_\Omega (\epsilon_3 + \alpha\epsilon_2 + \beta\epsilon_4)\, d\Omega \tag{2.38}$$

with

$$\epsilon_3 = \left(\frac{dI}{dt} - I_x \cdot v - I_y \cdot u - I_t \right)^2$$

$$\epsilon_4 = \left[\frac{\partial}{\partial x}\left(\frac{dI}{dt} \right) \right]^2 + \left[\frac{\partial}{\partial y}\left(\frac{dI}{dt} \right) \right]^2,$$

where the integral is evaluated over a region Ω and β is another weighting parameter. Cornelius and Kanade (1984) applied their method to the motion estimation of the heart from angiographic images. Mongrain et al. (1990) generalised this work and used it to determine the blood velocity profiles in coronary arteries.

Efron et al. (1978) reduced the 2D optical flow problem to the 1D optical flow problem by assuming that the blood flows only parallel to the centreline. The velocity is then given by the 1D optical flow equation

$$v = \frac{I_t}{I_x}. \tag{2.39}$$

In this case, the temporal and spatial derivatives can be determined from the flow map and the velocity can be determined directly. This approach includes the implicit assumption of plug flow. The solution of the 1D optical flow problem is equivalent to the automatic computation of the iso-contours in the flow map.

From my point of view, the main problem of the application of optical flow is that the basic assumption of optical flow – that the object brightness does not change – is not fulfilled for x-ray images of an iodine-based contrast agent injection. Iodine-based contrast agent is a solution and it is not possible to track individual particles. Because of diffusion and the parabolic flow effect the bolus changes its appearance as it travels along the vessel.

Optical flow methods mainly use the kinetic information from the x-ray images. However, for Equation 2.32 to be applicable, the image intensities should depend linearly on the contrast agent concentration. This would require an attenuation calibration. Most of the approaches referenced here do not include an attenuation calibration.

Huang et al. (1997b) reported that the velocity at the leading edge is determined by the central, more rapid flow and thus represents the peak flow. Measurements made after the peak of the bolus should represent average flow, but unfortunately the spatial and temporal derivatives become too small to achieve reliable results. A possible reason for this is that they used steady flow in their experiments. Figure 2.10(c) shows that the spatial derivatives in the flow map with steady flow are zero after the vessel is completely filled with contrast agent.

Rhode et al. (2001) did not use the leading and trailing edges because there the velocity would be overestimated or underestimated due to the parabolic flow effect. Instead, they used the pattern introduced by pulsatility to compute reasonable spatial and temporal derivatives. To overcome the problem of small spatial derivatives, they proposed to weight velocities according to their spatial derivative and then average along the vessel. They later stated that the method is still sensitive to noise when the spatial derivatives were small (Rhode et al., 2005).

Another effect of the dispersion of the bolus is that flow estimates depend on the distance from the injection site. Rhode et al. (2005) reported an almost linear dependence of the flow estimate on the distance. The mean error was zero for a distance of 10 cm. For smaller distances the flow was underestimated and for higher distances it was overestimated.

Imbert et al. (1995) incorporated a parabolic flow profile in the optical flow equation. They assumed that the vessel is parallel to the image plane and that the 2D flow in the projection image has a parabolic flow profile. The 2D flow was modelled as

$$v = v_{\max}\left(1 - \frac{(y - y_0)^2}{R^2}\right) \text{ and } u = 0, \tag{2.40}$$

where R is the radius, y_0 is the centre of the vessel and $v_{\max}$ is the maximum flow in the vessel. The optical flow equation then becomes

$$I_x \cdot v_{\max}\left(1 - \frac{(y - y_0)^2}{R^2}\right) = -I_t. \tag{2.41}$$

The derivatives were determined from the image and R, y_0, and $v_{\max}$, were determined by a least squares fitting. They reported almost perfect results on simulated images. However, their phantom seems to be based on 2D parabolic flow. Therefore, it perfectly fits their assumptions. For the projection of a 3D parabolic flow profile, different velocities would be superimposed and a real vessel is not always parallel to the image. Including a parabolic profile seems to be a good idea, but further improvements are necessary to make it applicable to 3D flow. Imbert et al. also stated that small spatial derivatives pose a problem for the method.

2.6.5 Methods based on the first pass distribution theory

The first pass distribution (FPD) theory is based on Fick's principle:

$$M(T) = \int_0^T Q_a(t) \cdot C_a(t)dt - \int_0^T Q_v(t) \cdot C_v(t), \tag{2.42}$$

which states that the amount M of a marker substance in an organ equals the amount that has been delivered minus the amount that has already left. $Q_a(t)$ and $Q_v(t)$ are the arterial and venous blood flow rate, and $C_a(t)$ and $C_v(t)$ are the arterial and the venous concentration of the marker substance. Non-angiographic methods based on this principle were explained in Section 2.4.1.

The FPD theory is further based on the assumption that there exists a time interval T_F in which the marker substance has not left the organ or the perfusion bed. When $T < T_F$ the venous concentration is zero and the Equation 2.42 reduces to

$$M(T) = \int_0^T Q_a(t) \cdot C_a(t)dt. \tag{2.43}$$

For steady flow, this equation can be solved for Q_a. In the case of pulsatile flow, $Q_a(t)$ is replaced by the average volumetric mean flow $\overline{Q}$ and $C_a(t)$ is replaced by the average input concentration $\overline{C}$ and then the following approximating equation can be obtained

$$\overline{Q} = \frac{M(T)}{\overline{C} \cdot T}. \tag{2.44}$$

Sapirstein (1956) used the assumption of zero venous drainage to determine the distribution of the cardiac output of rats. For this, they used a radioactive isotope of potassium which is well absorbed by the tissue. Before the start of the venous drainage, the rat was sacrified and they determined the distribution of their marker. Mullani and Gould (1983) have presented the model as described above. They used the radioactive rubidium and a PET system to measure myocardial blood flow. Marinus et al. (1990) and Hangiandreou et al. (1991) presented first angiographic versions of the FPD method.

For angiographic FPD-based methods, an iodine-based contrast agent is injected into an artery with a well-defined perfusion bed. Then, a sequence of x-ray images is acquired where the perfusion bed must lie completely in the field of view. From the subtracted images obtained before the start of the venous drainage, the required information about the accumulated amount of iodine M is determined. Two different techniques exist to determine the input concentration $\overline{C}$.

Hangiandreou et al. (1991) and Molloi et al. (1998) just assumed that $\overline{C}$ is known. In Molloi et al. (2004), this is justified with the following explanation: The contrast agent is injected with a rate above the peak expected flow rate so that it replaces blood. Then, the input concentration of iodine $\overline{C}$ is assumed to be constant and equal to the concentration of iodine in the contrast agent. In my opinion, this is problematic because if the blood is replaced by contrast agent, the flow of the contrast agent is measured and not the blood flow.

The second approach was introduced by Marinus et al. (1990), who determined the input concentration from the segment of the vessel which is nearest to the injection site. With this method, they can also determine the time-dependent variations of the input concentration. This inlet segment, however, must not overlap with the perfusion bed.

FPD-based methods use only the densitometric information which is available in the angiographic image, therefore, the image intensity has to be proportional to the amount of iodine on the x-ray path. This can be achieved by calibration, but this limits the clinical applicability of the method. Molloi et al. (1993) proposed to use a dual-energy x-ray system to get quantitative information about the mass of iodine. Later they proposed a calibration procedure to get quantitative information from normal x-ray images.

Kinematic information is ignored by FPD-based methods. So, if the calibration is inaccurate, the flow quantification is also inaccurate and this cannot be detected. The derivation of the FPD model shows that it is only approximately correct for pulsatile flow. Additionally, it can only give accurate results if no contrast agent leaves the field of view. This limits the application to vessels with a small perfusion bed. It is not applicable to fast flow in arteries, where the contrast agent transverses the field of view over a few frames. Another disadvantage of this method and other densitometric methods is that only the flow at the injection site can be determined. An advantage compared to the kinematic methods above is that no assumptions about the velocity distribution across the vessels have to be made.

2.7 Extraction of 3D haemodynamic information from angiographic images

At the beginning of my PhD, all known angiographic flow estimation methods had in common that they extracted information about the blood flow from planar, non-rotating angiographic sequences. As these are projection images, it is not possible to measure absolute blood flow as absolute vessel dimensions cannot be determined and foreshortening cannot be corrected.

Colchester et al. (1986), Brunt et al. (1992), Hawkes et al. (1994), Bladin et al. (1996), and Rhode et al. (2005) all reconstructed the vessel geometry from a biplane system and used this to determine the magnification factor, the angle between vessel and the x-ray beam, and the actual length of the vessel. The magnification factor and the angle are used for correction of the vessel profile, and the real length is needed to determine of the absolute blood flow rate. Parker et al. (1987) presented a similar approach with ECG-gated, single plane images from two different orientations. Huang et al. (1997b) presented an approach with single plane images from three different orientations. Fencil et al. (1989) used a stereoscopic system to correct the magnification error for flow measurements. All approaches enable the determination of absolute flow measurements, but, as explained in the last section, this reconstruction requires a lot of user interaction and, in some cases, it might not be possible to determine the vessel geometry without ambiguities.

Schmitt et al. (2002) used 3DRA for the 3D geometry reconstruction and then mapped the 2D flow information on it. Therefore, they needed two scans, a flow scan and a rotational scan. As there is a time gap between both scans, this attempt requires patient movement compensation.

All methods which were mentioned so far determine the flow information from planar angiographic sequences. More recently, Chen et al. (2006) and Appaji and Noble (2006) independently had the idea of determining flow information from rotational angiography. The main advantage is that the same sequence can be used for the 3D vessel reconstruction and the flow quantification. Both approaches are analysed in detail below.

Chen et al. (2006) proposed to measure blood flow using cone beam CT (using a flat panel detector mounted on a CT-gantry) with an injection of contrast agent. They divided the images into three categories: wash-in, equilibrium and wash-out phase. The wash-in images were used for bolus tracking and the equilibrium images were used for the 3D volume reconstruction. They used the bolus frontier points as feature points for the 3D flow reconstruction similar to a biplane reconstruction; always two 2D feature points were used to reconstruct the 3D point. Their approach has several problems, however:

- It is very difficult to determine the bolus frontier points reliably enough to be used as feature points as the bolus disperses. They did not explain which criterion they used. Especially, because of artefacts due to the rotation of the c-arm system, such as foreshortening and overlapping vessels, a trivial criterion is not sufficient. This will be illustrated in Section 6.2.3.

- The next problem is known from the 2D methods described above: Bolus arrival times are not suitable for reconstructing a quantitative flow measure in the case of pulsatile flow. For both validation setups (computer simulation and phantom experiment) they only used steady flow.

- In the computer simulation, they determined the motion of a sharp, undiluted bolus edge. This simplified the determination of the BAT.

- In the phantom experiment, they did not compare the results to a ground truth measurement.

Appaji and Noble (2006) proposed the following two-step method for reconstructing flow from rotational angiography: first, they estimated a 2D flow field from consecutive frames using an optical flow method and then they corrected for the motion of the rotating c-arm using the reconstructed volume and the calibration information. This method has the following limitations:

- Artefacts, like foreshortening or overlapping vessels, due to the rotation are not adressed. It is difficult to see how the method could handle overlapping vessels or brightness changes

due to foreshortened vessels. The phantom used by Appaji and Noble was designed in such a way that no overlapping occurs.

- Their validation on synthetic data may be regarded as too simplistic: They simulated motion of particles through a straight tube without simulating diffusion, pulsatile flow, and, most importantly, without simulating the rotation of the c-arm. Using an emulsion of contrast agent particles instead of a diluted contrast agent bolus dissolved in blood simplifies the optical flow problem: in the case of an emulsion, motion is visible during the complete sequence; whereas, in the case of a solution, motion is only visible during the inflow and outflow (for steady flow).

- Their validation with the real phantom had limitations as well: They had no ground truth (like an EMF measurement) to compare their results to, and they only compared how well the estimated direction of the flow field fits the direction of the vessel. They concluded that the fit is best if the direction of the vessel is used to constrain the flow direction.

- General limitations of optical flow, like over- and underestimation due to convective dispersion, sensitivity to noise, and the dependence on the distance from the injection site have not been addressed.

In summary, although there is now a reasonably body of work published on flow reconstruction from rotational image sequences, there are still many unsolved problems. In particular, problems like vessel foreshortening and overlapping vessels have not been addressed and no quantitative results have yet been presented in the literature.

2.8   Conclusions

A lot of research has already been done on vessel reconstruction and flow estimation from angiography. However, little research has been done on flow estimation from rotational angiography, and in particular, no quantitative results have yet been presented. Furthermore, the vessel reconstruction from rotational angiography with inflow and possibly outflow of contrast agent has not received much attention.

The main issues of the flow extraction from angiography are:

- under- or overestimation of the flow due to effects of convective dispersion,

- sensitivity to noise,

- the long length required for vessel segments to be considered, and

- how to determine 3D vessel geometry.

For rotational angiography, additional problems are:

- vessel overlapping, and

- changing vessel foreshortening.

All of these issues will be discussed further in this thesis and solutions will be proposed that specifically adress these issues.

3

Flow model

3.1 Introduction

The overall goal of this thesis is the extraction of haemodynamic information from rotational angiography. For flow quantification, a model-based approach is proposed. The underlying model is explained in this chapter.

In Section 2.3.1, computational fluid dynamics (CFD) were introduced. A CFD model can be used to describe blood flow in arteries, including bifurcations, stenoses, and aneurysms. In principle, a CFD model would be appropriate to support the flow quantification. In practice however, the usage of a CFD model is not yet applicable for this task as on a standard PC a pulsatile CFD simulation still takes between hours and days. Real time CFD computations can be achieved by parallelising the computations on very powerful computer clusters (Manos et al., 2008). However, for the flow quantification the model has to be applied iteratively (in the inner loop of an optimisation), so that even massively parallel processing units do not offer the required computational power. Therefore, some assumptions were made to obtain a simpler and less computationally expensive model which can be used in an iterative way to support the flow quantification.

Hawkes et al. (1988) proposed the use of a simple flow simulation to validate their flow quantification method. Huang et al. (1997a) and Rhode et al. (2005) used a similar model for validation. My model is based on their work, but it is not only used for validation but to support the flow quantification.

The proposed model can predict the concentration of iodine after an injection of contrast agent into a pulsatile flow field through a tube or a vessel. This model involves the following components:

- model of the shape of the waveform,

- model of the contrast agent injection,

- model of the mixing of blood and contrast agent at the injection site,

- model of the geometry of the vessel tree,

- model of the contrast agent propagation through the vessel tree.

All parts of the model and the necessary assumptions are explained in this chapter. It is based on concepts explained in Section 2.3.1. In Chapter 4 the model is used to simulate rotational angiography images for validation. In Chapter 7 the use of the model for flow quantification is described.

3.2 Model of the shape of the waveform

The waveform model is used to describe the changes in the volumetric blood flow rate during the cardiac cycle. When modelling the waveform, it is assumed that the waveform can be described by a periodic function. This is reasonable for patients without cardiac arrhythmia over the time scale of a typical rotational angiography acquisition.

The instantaneous volumetric blood flow rate $Q_B(t)$ is given by

$$Q_B(t) = \overline{Q}_B \cdot w(t), \tag{3.1}$$

where $\overline{Q}_B$ is the mean volumetric flow rate and $w(t)$ is a normalised, periodic function given by the waveform model. The shape of the waveform is described by

$$w'(t) = \alpha + cos(2\pi \cdot f(t)), \tag{3.2}$$

where α is a scalar constant which characterises the baseline flow and f is a piecewise linear, monotonic function given by

$$f(t) : [0,1] \to [0,1]$$
$$\text{with } f(0) = 0, \ f(\gamma) = \delta, \ f(\beta) = 0.5, \ f(1) = 1. \tag{3.3}$$

At all other points, f is linearly interpolated. The scalar parameters β, γ, δ specify the shape of the waveform. The function $w'(t)$ must be normalised and made periodic which is achieved by

$$w(t) = \frac{w'(t/T_H)}{\int_0^{T_H} w'(t/T_H)dt}, \tag{3.4}$$

where T_H is the period of the heart cycle. The influence of the different parameters on the waveform model is illustrated in Figure 3.1.

This waveform model is called 4-parameter warped cosine model. In the section about variations of the flow model (Section 3.7), two further waveform models will be described. In the direct comparison experiment (Section 7.3.2), this waveform model gave the best results and it was used for all other experiments.

(a) Variation of α.

(b) Variation of β.

(c) Variation of γ.

(d) Variation of δ.
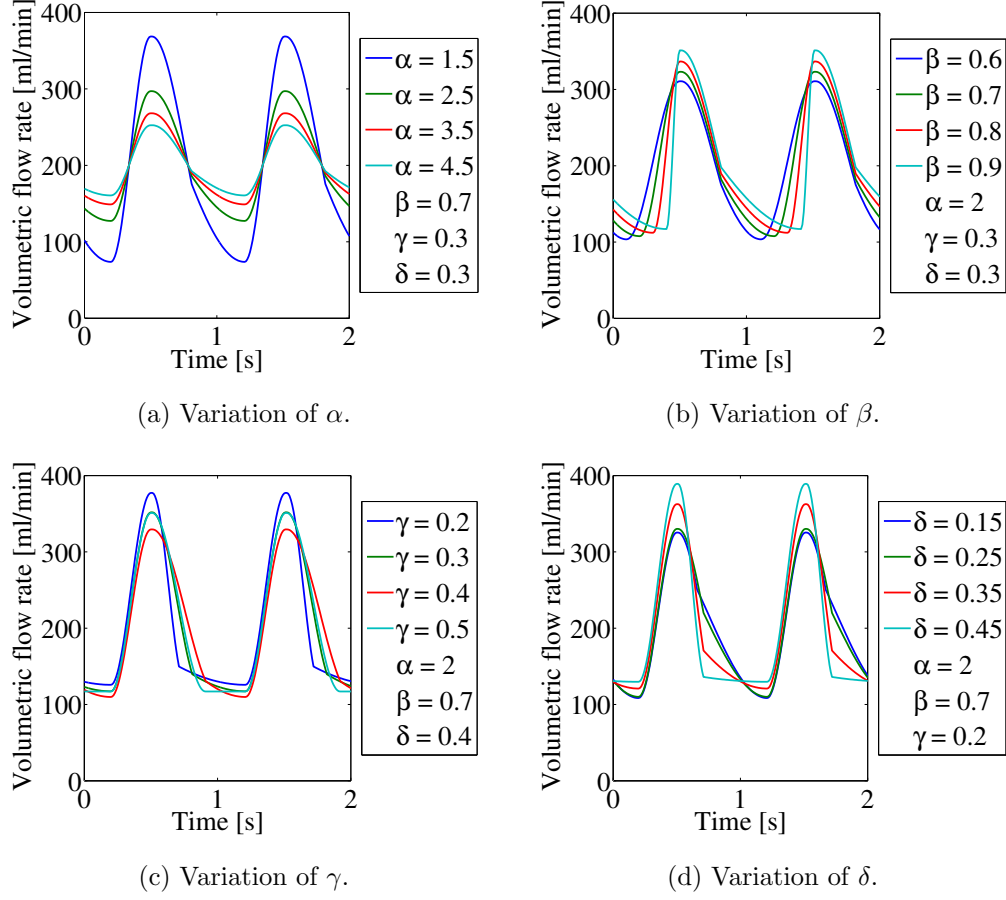
Figure 3.1: Examples of the effect of varying the parameters of the waveform model defined by Equation 3.2 and Equation 3.3.

3.3 Model of the contrast agent injection

For the contrast agent injection, it is assumed that the injection flow at the outlet of the injector can be described by a rectangular function and that the flow circuit behaves in an analogous way to an electrical network. Then, the catheter is equivalent to a resistor plus a capacitor for the contrast agent. Therefore, the injection curve corresponds to the charging curve of a capacitor, and the injection flow rate $Q_I(t)$ can be described by

$$Q_I(t) = \begin{cases} 0, & t < T_S \\ \widetilde{Q}_I \cdot (1 - e^{-(t-T_S)/T_L}), & T_S \leq t \leq T_s + T_D \\ \widetilde{Q}_I \cdot (1 - e^{-T_D/T_L}) \cdot e^{-(t-(T_S+T_D))/T_L}, & t > T_S + T_D, \end{cases} \tag{3.5}$$

where $\widetilde{Q}_I$ is the maximum flow, T_L is the characteristic time of the lag, T_S is the start time of the injection and T_D is the duration of the injection. An example of the injection flow rate as a function of time is given in Figure 3.2(a).

3.4 Model of the mixing of blood and contrast agent

From the blood flow rate $Q_B(t)$ at the time of injection and the injection flow rate $Q_I(t)$, the total flow rate $Q_T(t)$ is given by

$$Q_T(t) = Q_B(t) + Q_I(t). \tag{3.6}$$

It should be noted that the blood flow $Q_B(t)$ might be disturbed by the injection. If one considers the equivalent electrical analogue, the relationship between the physiologic flow and the disturbed flow can be described by

$$Q_{B,phys}(t) = Q_B(t) + m \cdot Q_I(t), \tag{3.7}$$

where $m \in [0,1]$ is a resistance factor, which depends on the relationship between the flow resistances downstream and upstream of the injection site. If the downstream resistances are small, the injection hardly disturbs the blood flow. This is the case in the experimental setup adopted in this study. In the human circulation the downstream resistance is high because of the small radii of the capillary bed. In this case, the injection will disturb the blood flow. The lower the injection flow rate is, the smaller the disturbance will be.

For mixing, it is assumed that the contrast agent mixes uniformly with the blood at the injection site. From x-ray images of the catheter tip, this can be seen to be a reasonable assumption. The contrast agent concentration $C_0(t)$ at the site of injection is then given by

$$C_0(t) = \frac{Q_I(t)}{Q_T(t)}. \tag{3.8}$$

It is important to note that the concentration changes during the cardiac cycle. During systole, when the blood flow is highest, the concentration is low; whereas during diastole, when the blood flow is lowest, the concentration is high. This is particularly important because it explains the characteristic pattern that appears in the flow map. In Figure 3.2(b), an example is given of the concentrations which are determined using the blood flow and injection flow shown in Figure 3.2(a) and Equation 3.8.

3.5 Model of contrast agent propagation

The transport of a soluble substance in a moving medium is determined by convection and diffusion. The convection-diffusion equation and different approaches for solving it were introduced in Section 2.3.2. The approach which is chosen here is based on the method of Bailey and Gogarty (1962) for solving the equation by superimposing convective and diffusive effects alternately. The convection model is based on work from Hawkes et al. (1988) and Rhode et al. (2005), but the formulation has been extended to include a diffusion model.

If a vessel is divided into N laminae (see Figure 3.3), the radius in the middle of lamina $n \in \{1, 2, \ldots, N\}$ is given by

$$r_n = \frac{n - 1/2}{N} R \tag{3.9}$$
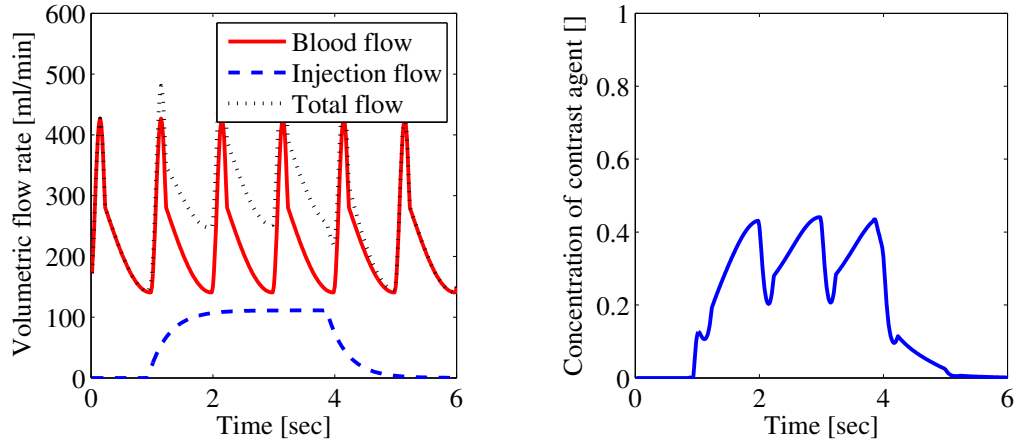
(a) Volumetric flow rates at injection site: The blood flow is given by the waveform model; the injection is given by the injection model.

(b) Resulting contrast agent concentration curve at the injection site.

Figure 3.2: Prediction of contrast agent concentration at the injection site (Waechter et al., 2008b).
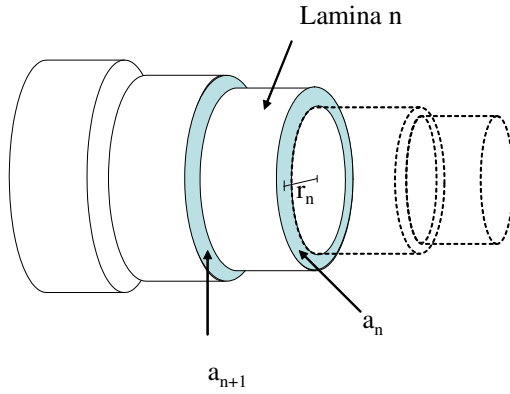
Figure 3.3: Vessel divided into laminae (Waechter et al., 2008b).
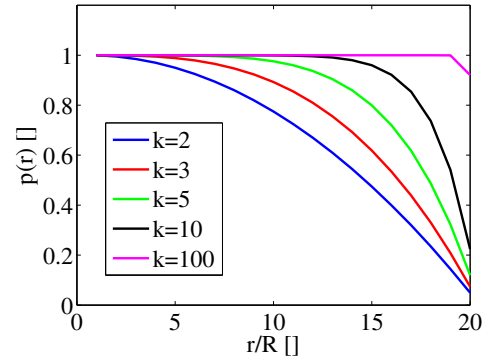
Figure 3.4: Velocity profile.

and the cross sectional area of lamina n is given by

$$a_n = \pi \cdot \left(\frac{n}{N}R\right)^2 - \pi \cdot \left(\frac{n-1}{N}R\right)^2. \tag{3.10}$$

$r \in \{r_1, r_2, \ldots, r_N\}$ indicates the radius of an arbitrary lamina. The velocity distribution over the laminae depends on the flow profile $p(r)$. A profile, given by

$$p(r) = 1 - (r/R)^k, \ 2 \le k < \infty, \tag{3.11}$$

can approximate a profile between plug flow ($k \to \infty$) and parabolic flow ($k = 2$) as illustrated

in Figure 3.4. The velocity in the lamina with radius r is now given by

$$v(r,t) = v_{max}(t) \cdot p(r), \tag{3.12}$$

$$\text{with } v_{max}(t) = \frac{Q_T(t)}{\sum_{n=1}^{N} p(r_n) \cdot a_n}.$$

The transport of contrast agent along a vessel is described by the concentration map $C(r,l,t)$ where r is radial distance, l is longitudinal distance and t is time. It represents the progression of contrast agent concentration along each lamina. At the start of simulation, there is no contrast agent in the vessel, therefore $C(r,l,0)$ is initialised to zero.
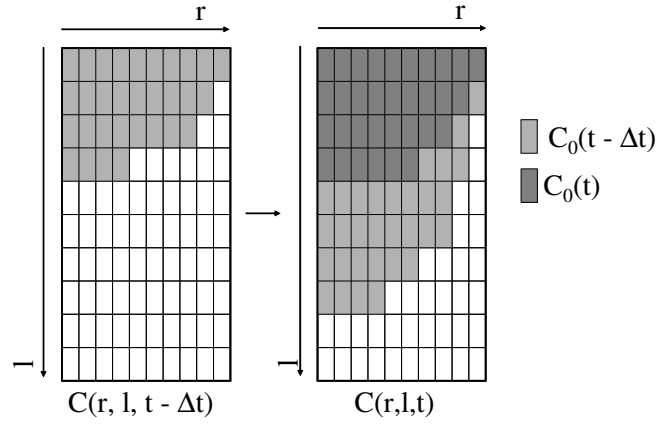
Figure 3.5: Changes in the concentration map due to convection.

The convection of the contrast agent is determined as follows: For each lamina, the concentration values are shifted according to the velocity in the lamina. The shift $s(r,t)$ over a time interval Δt is given by

$$s(r,t) = v(r,t) \cdot \Delta t. \tag{3.13}$$

Changes in the discrete concentration map due to convection at time t during the short interval Δt are simulated by (see Figure 3.5)

$$C'(r,l,t) = \begin{cases} C_{in}(r,t) & l < s(r,t) \\ C(r,l - s(r,t), t - \Delta t) & l \geq s(r,t), \end{cases} \tag{3.14}$$

where $C_{in}(r,t)$ is the contrast agent concentration at the inlet of the segment. $s(r,t)$ is discretised and the residual is taken into account for the next iteration.

The changes in the concentration map due to diffusion of the contrast agent are given by

$$C(r,l,t) = C'(r,l,t) + D \cdot \Delta t \cdot \left(\frac{\partial^2 C'(r,l,t)}{\partial r^2} + \frac{1}{r} \frac{\partial C'(r,l,t)}{\partial r} + \frac{\partial^2 C'(r,l,t)}{\partial l^2} \right), \tag{3.15}$$

where the partial derivatives are computed using central difference quotients. At the radial boundaries, no diffusion should occur, in particular at $r = R$ as this is the border of the

vessel. This is expressed by the boundary condition of the convection-diffusion equation (see Equation 2.12). If a spatial derivative is zero, there is no concentration gradient and therefore no diffusion in the corresponding direction. To respect the boundary condition, C' is padded at the radial boundaries to give a zero derivative. Iterative application of the convection step and the diffusion step gives the progression of the concentration of contrast agent described by the concentration map $C(r, l, t)$.

3.6 Extension to vessel trees

In the description of the contrast agent concentration propagation model above, I assumed for simplicity that the vessel consists only of one segment with a constant radius. In reality, however, the vessels will branch and the radius will vary along the length of the vessel.

The vessel tree consists of branches B_i which are limited by the start point, by a bifurcation point, or by an end point of the vessel tree. Each branch consists of one or more segments S_j depending on the variations of the radius. Each segment is described by a set of centreline points and radii. If l represents the length along the vessel segment and L_j is the total length of the vessel segment, its centreline is given by a set of K_j 3D points $P_j(l)$, $l \in \{l_i \,|\, l_i = i \cdot L_j / K_j, i \in \{1, 2, \ldots, K_j\}\}$ and for each point the corresponding radius is given by $R_j(l)$. Each segment corresponds to one concentration map $C_j(r, l, t)$.

3.6.1 Changes in radius

If the radius varies substantially, for example at a stenosis, a branch can be divided into several segments. However, the radius might still vary slightly within a segment. The laminae then correspond to a relative position in the vessel and their radii are given by

$$r_{n,j}(l) = \frac{n - \frac{1}{2}}{N} R_j(l). \tag{3.16}$$

This concept is illustrated in Figure 3.6(a), which shows the representation of the vessel as it is determined during the vessel reconstruction (centerline radius representation).

If the radius of a vessel segment changes, the velocity changes as it depends on the square of the radius. The flow simulation, however, does not allow changes in velocity along the vessel within one segment. Therefore, an effective radius is determined. If this effective radius is used to determine the velocities, the velocity in lamina n corresponds to the mean of the velocity along a streamline with varying distance $r_n(l)$. Using Equation 3.10 and 3.12 the velocity can be expressed as

$$v_j(n, l, t) = \frac{Q_T(t) \cdot p'(n)}{R_j(l)^2}, \tag{3.17}$$

where $p'(n)$ is based on $p(r)$, but does not depend on the radius $R_j(l)$. The mean velocity in segment S_j along the streamline n is given by

$$\overline{v}_j(n, t) = \frac{1}{K_j} \sum_{l=0}^{L_j} v_j(n, l, t) = \frac{Q_T(t) \cdot p'(n)}{K_j} \cdot \sum_{l=0}^{L_j} \frac{1}{R_j(l)^2}, \tag{3.18}$$

(a) Centreline radius representation.

(b) Effective radius representation.   (c) Inlet and outlet radius representation.
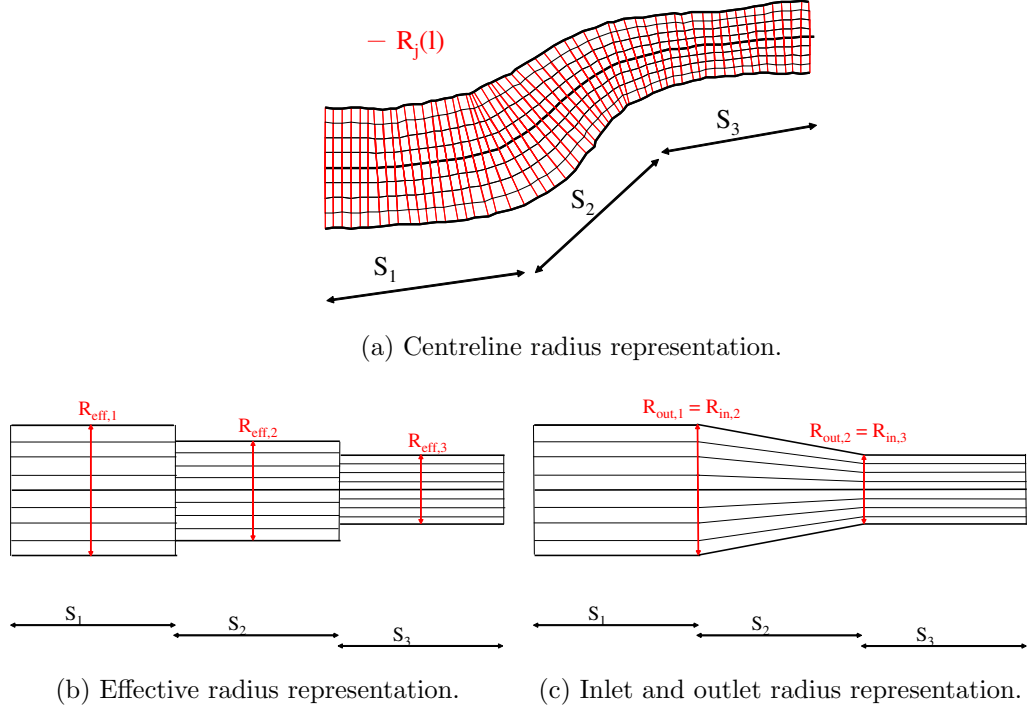
Figure 3.6: Illustration of laminae for different representations of the vessel.

The effective radius $R_{\text{eff},j}$ is then given by

$$R_{\text{eff},j} = \sqrt{\frac{Q_T(t) \cdot p'(n)}{\overline{v}_j(n,t)}} = \sqrt{\frac{1}{\frac{1}{K_j} \sum_{l=0}^{L_j} \frac{1}{R_j(l)^2}}}. \tag{3.19}$$

The effective radius can be used to determine the effective velocity for each lamina n and each segment S_j according to

$$v_{\text{eff},j}(n,t) = \frac{Q_T(t) \cdot p'(n)}{R_{\text{eff},j}^2}. \tag{3.20}$$

The velocities will be discontinuous at the borders of the segment, but the conservation of flow will be respected. The effective radius representation is illustrated in Figure 3.6(b).

For the simulation of angiographic images, each segment is described by its inlet and outlet radius and the radii in between are linearly interpolated. Successive segments must have the same radius at their interfaces. This ensures that the radius is continuous. The effective radius is determined using Equation 3.19. This representation of the vessel is illustrated in Figure 3.6(c).

3.6.2 Bifurcations

A bifurcation is divided into three branches: the mother branch B_i and two daughter branches B_{2i} and B_{2i+1}. Each branch can be divided into multiple segments if the radius varies. If the mother branch is the first branch, the total flow is given by the total flow at the injection site: $Q_{T,i}(t) = Q_T(t)$. Otherwise, it is determined recursively. Assuming that the flow division χ is

independent of time, the flow in the daughter branches is given by

$$Q_{T,2i}(t) = \chi_{2i} \cdot Q_{T,i}(t), \tag{3.21}$$

$$Q_{T,2i+1}(t) = \chi_{2i+1} \cdot Q_{T,i}(t), \tag{3.22}$$

$$\text{with } \chi_{2i} = (1 - \chi_{2i+1}). \tag{3.23}$$

This approach ensures that Bernoulli's flow conservation equation (see Equation 2.7) is obeyed, which means that the flow at the inlet has to equal the sum of the flows at all outlets. Now, the velocities can be determined for each segment according to Equation 3.20 using the effective radius $R_{\text{eff},j}$ of the segment and using the volume flow $Q_{T,i}$ of the branch.

The flow model assumes that the flow profile and the contrast agent concentrations are axially symmetric. After a bifurcation, however, the flow profile is skewed and the contrast agent concentrations are not axially symmetric. After a certain distance the normal flow profile is restored (Nichols and O'Rouke, 2005). Therefore, the observations directly after a bifurcation will not be used for the flow quantification.

3.6.3 Determination of concentrations for a vessel tree consisting of several segments

Each segment S_j corresponds to one concentration map C_j. If the segment is the first segment ($j = 1$), the concentrations at the inlet are given by the concentrations at the injection site: $C_{in,1}(r_{n,1}, t) = C_0(t)$. Otherwise, they are determined from the concentrations at the outlet of the previous segment. If segment S_j is fed by segment S_{j-1}, the concentrations at the inlet of segment S_j are given by

$$
\begin{aligned}
C_{in,j}(r_{n,j}, t) &= C_{out,j-1}(r_{n,j-1}, t) \\
&= \sum_{l=L_{j-1}-s}^{L_{j-1}} \frac{C_{j-1}(r_{n,j-1}, l, t - \Delta t)}{s},
\end{aligned}
\tag{3.24}
$$

where $s = s(r_{n,j-1}, t)$ is the shift in lamina n of segment S_{j-1} given by the convection from Equation 3.13. For this, it is necessary that all segments are divided into the same number (N) of laminae. The concentrations in lamina n of segment S_j is always determined from the concentrations in lamina n of segment S_{j-1}, no matter what the radius is. As the volume flow is conserved between segments, the mass of contrast agent is conserved as well. With this information, the contrast agent propagation can be determined for the complete vessel tree.

3.7 Extensions for the evaluation of the model

The model described in Section 3.1 to 3.6 was used for most parts of the thesis. For the part of the evaluation which is based on computer simulations, I have introduced modifications to the model, which are described below.
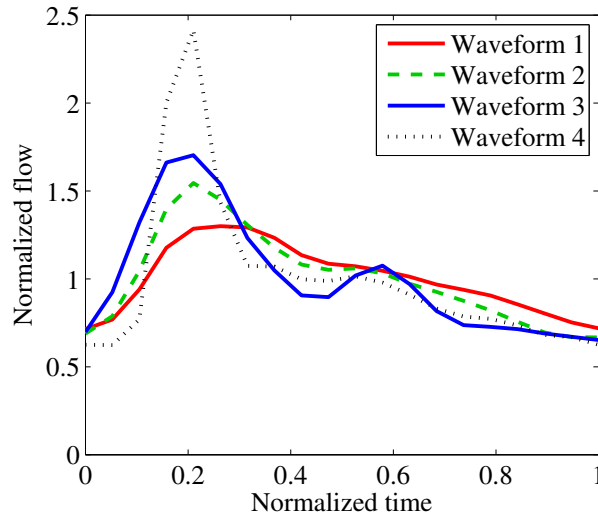
Figure 3.7: Example waveform from database of Marshall et al. (2004).

3.7.1 Blood flow waveform

For the generation of validation datasets, the blood flow waveform was not determined by the waveform model. Instead, four characteristic waveforms were chosen from the waveform database compiled by Marshall et al. (2004). The database consists of blood flow waveforms from the common carotid artery, the internal carotid artery, and the external carotid artery, which were determined from healthy volunteers using MRI. The waveforms were chosen in such a way that the variation in the database is captured: the first one is characterized by a slow decrease after systole; the second one has a small bump after systole; the third one is more pulsatile and has a severe bump after systole; the last one has a sharp peak during systole. The four examples are shown in Figure 3.7.

3.7.2 Other waveform models

As mentioned in Section 3.2, two further waveform models were evaluated besides the 4-parameter warped cosine model. They are referred to as 2-parameter warped cosine model and Laplace model.

The 2-parameter warped cosine model is a simpler version of the 4-parameter warped cosine model, where the parameters γ and δ have been removed.

The Laplace model is a well validated approach for modelling a blood flow waveform. Skidmore and Woodcock (1978) proposed the third order Laplace transform to fit a 3 parameter model in the frequency domain to waveforms determined by ultrasound. This model is supposed to be able to describe 90% of all observed physiological waveforms. It is also possible to fit the inverse Laplace transform

$$w_1'(t) = \frac{\gamma(\alpha^2 + \beta^2)}{(\gamma - \alpha)^2 + \beta^2} \left[e^{-\gamma t} + e^{-\alpha t} \left(\frac{\gamma - \alpha}{\beta} \sin \beta t - \cos \beta t \right) \right] \tag{3.25}$$

in the time domain and this approach was chosen.

3.7.3 Womersley profile

(a) Waveform 1. (b) Waveform 2.

(c) Waveform 3. (d) Waveform 4.
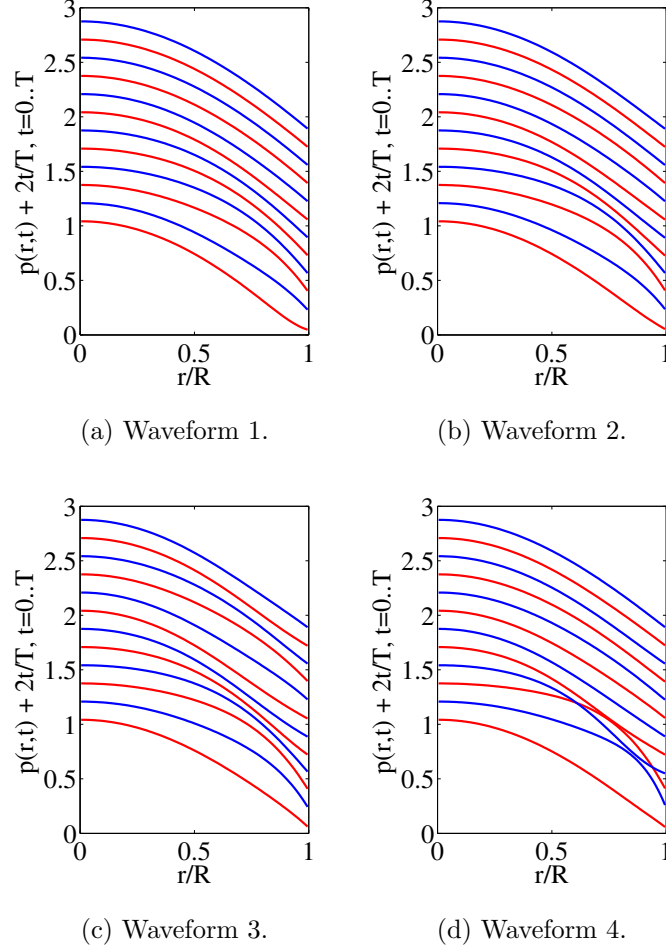
Figure 3.8: Womersley profiles for the waveforms from Figure 3.7.

The ideal solution for the flow profile in the case of pulsatile flow is given by the Womersley solution (Womersley, 1955). For some validation cases, the constant velocity profile was replaced by a Womersley profile. According to Cebral et al. (2005), the Womersley profile can be determined as explained in the following: First, the blood flow $Q_B(t)$ is decomposed into its Fourier modes given by

$$Q_B(t) = \sum_{m=0}^{M} Q_m e^{im\omega t}, \qquad (3.26)$$

where M is the number of modes and ω is the angular frequency obtained from the period of the cardiac cycle. The Womersley profile is then given by

$$p(r,t) = v(r,t)/v_{max}(t) \qquad (3.27)$$

with

$$v(r,t) = \frac{2Q_0}{\pi R^2} \left[1 - \left(\frac{r}{R}\right)^2 \right] + \sum_{m=1}^{M} \frac{Q_m}{\pi R^2} \left[\frac{1 - \frac{J_0(\beta_m r/R)}{J_0(\beta_m)}}{1 - \frac{2J_1(\beta_m)}{\beta_m J_0(\beta_m)}} \right] e^{im\omega t}, \qquad (3.28)$$

and with

$$\beta_n = i^{3/2} Wo\sqrt{m} = i^{3/2} R\sqrt{\frac{m\omega}{\nu}} \tag{3.29}$$

where R is the radius, ν is the kinematic viscosity, J_0 is the zeroth order Bessel function and J_1 is the first order Bessel function. The shape of the profiles is determined by the Womersley number Wo, which can be interpreted as the ratio of the unsteady, pulsatile forces to the viscous forces. A Womersley number of about 5 is characteristic for the carotid arteries. The Womersley profiles for the waveforms from Figure 3.7 are shown in Figure 3.8.

3.7.4 Mixing at the injection site

In the model described above, mixing is assumed to be uniform. However, the distribution of contrast agent at the injection site can vary across the cross section. Here, the variations across the cross section are described by

$$p_I(r) = (1 - r/R)^k, \; 0 \leq k \leq 1. \tag{3.30}$$

For $k = 0$, the distribution is uniform; for $k = 1$, the concentration decreases linearly with the distance from the centre. The contrast agent at the inlet is then given by

$$C_0(r, t) = x \cdot C_0(t) \cdot p_I(r), \tag{3.31}$$

$$\text{with}$$
$$x = \frac{\sum_{n=1}^{N} s(r_n, t) \cdot a_n}{\sum_{n=1}^{N} p_I(r_n) \cdot s(r_n, t) \cdot a_n},$$

where $C_0(t)$ is the mean concentration at the injection site as given by Equation 3.8.

3.8 Discussion

In this chapter, a model for the simulation of contrast agent transport in a vessel tree was described. This model uses many assumptions. In summary, the assumptions of the model without the extensions for validation are:

- The blood flow is periodic and the waveform can be represented by the waveform model.

- The contrast agent injection can be represented as a rectangular function with a lag.

- The mixing at the injection site is uniform.

- The flow circuit behaves in a way that is analogous to an electrical network.

- The vessels can be presented by tubular segments.

- The flow is laminar and axially symmetric.

- The flow profile is constant in time and between parabolic flow and plug flow.

- The contrast agent distribution is axially symmetric.

- The influence of compliance is negligible on the observed distance.

These assumptions hold well for steady flow of a Newtonian fluid in long, straight and rigid tubes, because in this case the flow can be described by Poiseuille's equation as explained in Section 2.3.1 (parabolic flow). Pulsatile flow, limited vessel length, and non-Newtonian viscosity introduce variations in the flow profile. These are approximated by allowing the flow profile to be between plug flow and parabolic flow. Compliance changes the shape of the waveform. Over small distances these changes are negligible, over longer distances they will have to be considered. A possible way to model these changes is given by 1D vascular networks as described by Sherwin et al. (2003).

For a bifurcation, a tortuous vessel, a stenosed vessel or a suddenly widened vessel, these assumptions do not hold. The main problem is that the flow profile and the contrast agent concentration are no longer axially symmetric in this case. However, an approximate model might be sufficient for flow quantification. In the validation section of Chapter 7, I will evaluate the applicability of the model using computer simulations and, more importantly, using images from an experimental flow circuit. There, the model will be analysed and it will be further discussed whether this model is sufficient for blood flow quantification.

The waveform model might be too restrictive for clinical use. If this is the case, it could be replaced by a principal component model as proposed by Rhode et al (2005). For this model, a characteristic set of waveforms is required to determine the mean waveform and the main modes of variation using the principal component analysis, this is called training. The advantage of this model is that it is more flexible than the model chosen for this work. The disadvantage is that the model can only represent the variations which are present in the training database. Therefore, it is not advisable to train a model on waveforms obtained from an experimental setup and later use it for clinical cases. For the model which was selected for this work, the expressive power is chosen by the range of the parameters. In the validation section of Chapter 7, the applicability will be analysed and further discussed.

For the flow quantification, the resistance factor is an important parameter. It will vary within the circulation, the nearer the injection side is to the heart, the nearer to one the resistance factor will be. When known values from literature are used for the upstream and downstream resistances, it can be found that the resistance factor should be very near to one for most parts of the arterial circulation. This means that the blood flow would be decreased in such a way that the total flow remains unchanged. This, however, does not agree with observations from literature as described in Section 2.3.3, which report that the flow is increased in the time interval of the injection.

A possible reason for this discrepancy could be that compliance and inertia were ignored in this simple model. Theoretically, the compliance of peripheral vessels could take up some of the extra volume due to the injection and therefore reduce the disturbance. Additionally, inertia could reduce the backflow directly upstream of the injection site and also reduce the disturbance of the blood flow. To further analyse their effect a lumped parameter simulation

of the circulation was conducted. However, with physiological values for all model parameters, this more complex model also gave unchanged total flow during the time of injection. Further analysis is required to better understand and model the influence of the injection. For the time being, the simple model with a heuristically chosen resistance-factor will be used.

4

Generation of synthetic but realistic image data

4.1 Introduction

A major problem for research which is based on x-ray images is that it is very difficult to obtain patient data. The reason for this is exposure to x-ray radiation, which can be harmful for the patient and the clinician. This is particularly problematic if a non-standard protocol should be used. It is necessary to show that the new method works before an ethics committee will approve a trial. This, however, is difficult if no appropriate image data are available. Therefore, one part of my work was the generation of synthetic but realistic image data. These data were used to develop the methods of this thesis and for validation.

Two different methods were used for image generation: computer simulations and phantom experiments. Both setups give rotational angiographic sequences with inflow and outflow of contrast agent with known flow conditions.

Most of the components required for the experimental setup were provided by Philips Medical Systems (Best, The Netherlands) and similar setups have been described in the literature (Colchester et al., 1986; Rhode et al., 2005). The computer simulation of rotational angiography is based on the software Radonis from Philips Research Europe (Hamburg, Germany). For the simulation of blood flow and contrast agent transport, the model described in Chapter 3 was used.

4.2 Computer simulation of rotational angiographic sequences

4.2.1 Overview

The computer simulation consists of the following steps: First, the contrast agent propagation through a given vessel tree is simulated. The results are mapped to a volume and merged with a CT dataset of the corresponding part of the body. The resulting dataset is used as input for the x-ray simulation of the contrast agent (CA) scan. The original CT dataset is used for the x-ray
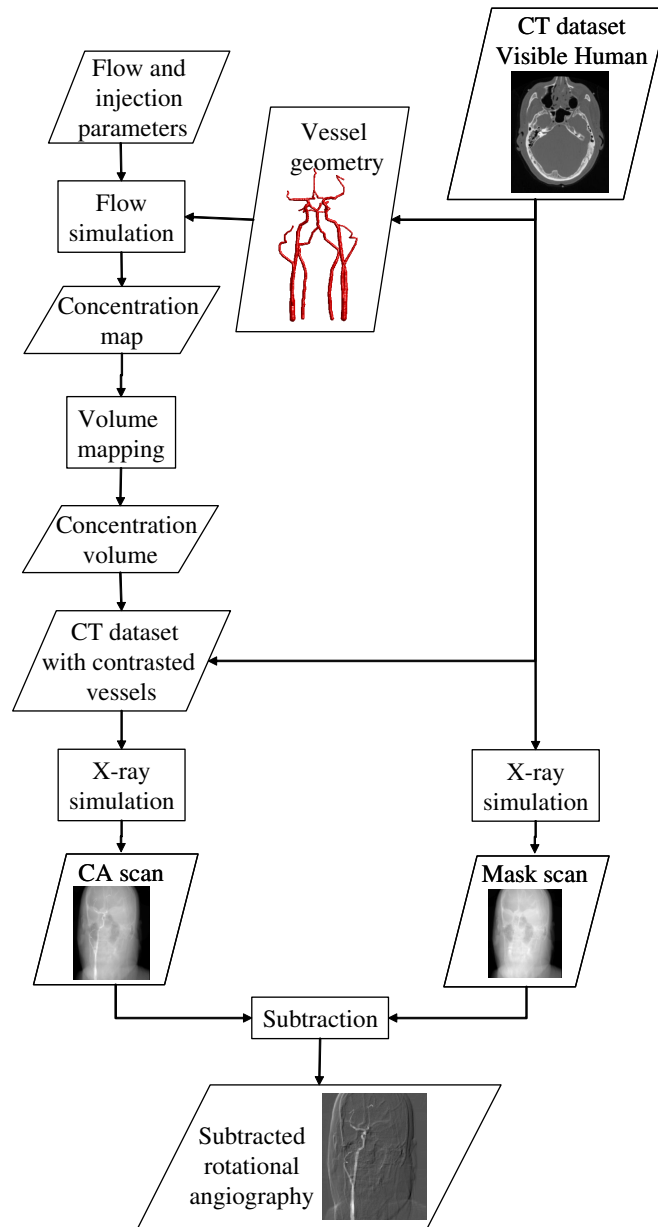
Figure 4.1: Overview of the virtual angiography algorithm.

simulation of the mask scan. Both scans are log-subtracted to obtain the subtracted rotational angiographic sequence. An overview is given in Figure 4.1. All steps are explained in detail below.

4.2.2   Vessel geometry

The vessel geometry was based on the visible human CT dataset (Ackerman et al., 1995). The centrelines of the main vessels of the head and the neck were segmented manually by selecting points in orthogonal views of the CT dataset. The characteristic radii of the vessel segments were determined from the literature (Hillen et al., 1988) (see Table 4.1). A surface model of the resulting vessel tree, including common carotid, internal carotid, external carotid, vertebral and basilar arteries and the Circle of Willis, is shown in Figure 4.2.

Artery	Radius [mm]
Common carotid	4
External carotid (proximal)	2.8
External carotid (distal)	2
Internal carotid (at sinus)	4.4
Internal carotid (proximal)	3
Internal carotid (distal)	2
Middle cerebral	1.75
Posterior communicating	0.5
Posterior cerebral I	1.5
Posterior cerebral II	1.5
Anterior cerebral I	1.25
Anterior cerebral II	1.25
Anterior communicating	0.5
Basilar	2
Vertebral	1.5

Table 4.1: Radii of vessel tree (determined from Hillen et al. (1988) and Kolachalama (2006))
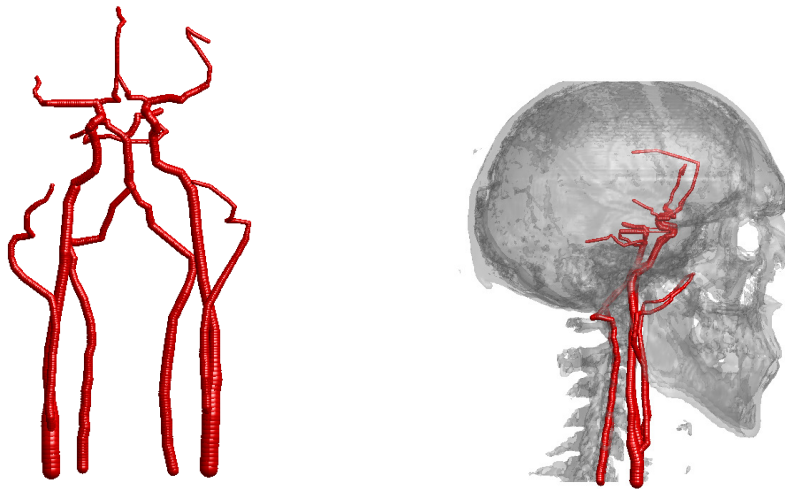
(a) Frontal view of vessel tree.

(b) Vessel tree together with skull from CT dataset.

Figure 4.2: Vessel geometry based on the visible human dataset used for computer simulated rotational angiography (Waechter et al., 2008c).

4.2.3 Simulation of contrast agent propagation

For the simulation of the contrast agent propagation, the model described in Chapter 3 was used.

The velocity profile across the vessel was chosen to be between plug flow and parabolic flow. Characteristic waveforms were determined from the database provided by Rhode et al. (2005) and characteristic volume flows were determined from the literature (Likittanasombut et al., 2006; Oktar et al., 2006). The flow fractions at the bifurcation were set proportional to the cross sectional areas of the daughter branches.

The contrast agent injection was assumed to be intra-arterial and the injection site could be placed at an arbitrary location in the vessel tree. The injection duration was varied and the flow of the injection was either equal to the mean blood flow or half of the mean blood flow.

The simulation as described in Chapter 3 gave the spatial and temporal development of the concentration of contrast agent $C_j(r,l,t)$. From the concentration of contrast agent, the concentration of iodine was determined, assuming that the contrast agent Ultravist-370 (Schering, Berlin, Germany) was used, which has an iodine concentration of 370 mg/ml. From this, the additional attenuation $\mu_j(r,l,t)$ due to the iodine was determined.

4.2.4 Mapping to a volume

From the analytical representation of the vessel tree, three 3D data structures were determined: the object volume $\mathcal{V}_O$, the radius volume $\mathcal{V}_R$, and the length volume $\mathcal{V}_L$. If a voxel $\mathbf{v}$ is part of a vessel segment

- $\mathcal{V}_O(\mathbf{v})$ contains the number of the segment to which the voxel belongs,

- $\mathcal{V}_R(\mathbf{v})$ contains the radial distance of the voxel to the centreline of the corresponding segment,

- $\mathcal{V}_L(\mathbf{v})$ contains the length along the centreline of the corresponding segment.

Each volume is represented by a 3D array. Using these three volumes the attenuation values were mapped to a volumetric representation $\mathcal{V}_\mu$ of the vessel tree at time step t using the following relationship:

$$\mathcal{V}_\mu(\mathbf{v},t) = \mu_j(r,l,t) \tag{4.1}$$

with

$$j = \mathcal{V}_O(\mathbf{v}),\ r = \mathcal{V}_R(\mathbf{v}),\ l = \mathcal{V}_L(\mathbf{v}).$$

4.2.5 X-ray simulation

The x-ray simulation was done with the software package Radonis (Philips Research Europe, Hamburg, Germany). This software models noise and beam hardening (Brooks and Chiro, 1976),

and, as the CT dataset of the visible human was used to provide background attenuation, noise and beam hardening were realistic.

The x-ray input spectrum, the current, the radiation time, the detector size, and the geometric configuration of the c-arm, could all be specified. All values were chosen to represent a rotational angiography protocol on an Allura system (Philips Medical Systems, Eindhoven, The Netherlands).

The simulated x-ray tube consisted of 95% tungsten (W) and 5% rhodium (Rh), and the spectrum was filtered with 0.1 mm copper and 5 mm aluminium. The voltage was 75 kV. This infomation was used to determine the input spectrum using the software X-Sim (Philips Research Europe, Hamburg, Germany). The spectra are shown in Figure 4.3. The current was 125 mA or 250 mA and the radiation time was 5 ms.

During the simulation, the concentration of iodine and of water (or soft tissue) is determined for each voxel. Then, the line integrals of attenuation are determined using the attenuation spectra of water and of iodine. The attenuation spectra, shown in Figure 4.4, were determined from the NIST database (Hubbell and Seltzer, 1996).

(a) Unfiltered Spectrum.

(b) Filtered spectrum (0.1 mm copper, 5 mm aluminum).
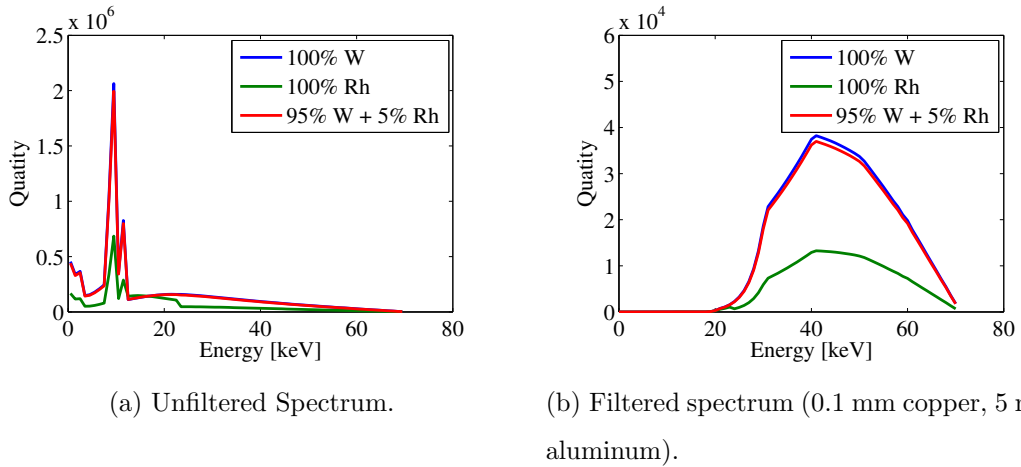
Figure 4.3: Spectra of x-ray tube.

The software package Radonis allows the geometric configuration of the simulated x-ray system to be set. This feature was used to implement a rotational trajectory. The simulated x-ray system rotated 205° in 4 s, during which time 120 images were acquired.

To introduce patient movement artefacts, the CT dataset was slightly rotated or translated for the mask scan. Additionally, the table position could be varied. For every defined acquisition protocol, one scan with contrast agent and one scan without contrast agent were simulated. Both scans were then log-subtracted, meaning

$$I_{\mathrm{DSA}} = e^{\log(I_{\mathrm{CA}}) - \log(I_{\mathrm{Mask}})}, \tag{4.2}$$

to obtain the simulated rotational angiography.

Example output images are shown in Figure 4.5: Figure 4.5(a) shows a subtracted an-
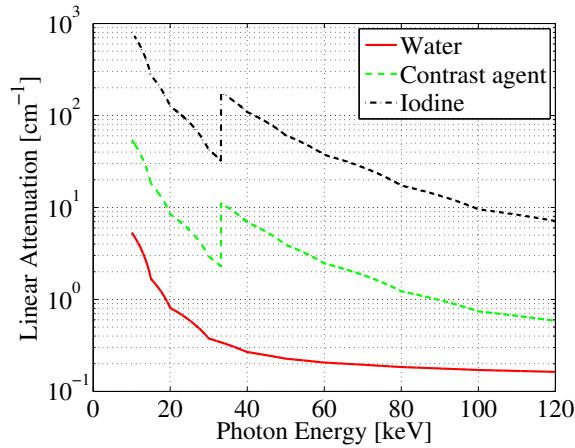
Figure 4.4: Attenuation Spectra (determined from Hubbell and Seltzer (1996)).

giographic image after an injection in the common carotid artery; Figure 4.5(b) shows a subtracted angiographic image after an injection in the vertebral artery; Figure 4.5(c) shows a non-subtracted angiographic image; Figure 4.5(d) shows a subtracted angiographic image with motion artefacts; Figure 4.5(e) shows every 10th image of a rotational angiographic sequence.

An overview of selected parameters is given in Chapter 6, where these images are used for the validation of the vessel reconstruction.

4.3 Experimental setup for rotational angiographic images

4.3.1 Overview

The experimental setup was used to acquire real x-ray images following a contrast agent injection into a phantom. An overview of the setup is given in Figure 4.6. Pictures of all components are shown in Figure 4.7. An overview of all variable parameters for the datasets from the experimental setup is given in the Appendix A.1.

A phantom was connected to a pulsatile flow pump and a fluid was pumped through a circuit. The pulsatile flow pump consisted of a continuous pump (Cole Parmer Instrument Company, Chicago, USA), which generated the required mean flow, and a cylinder (Parker Hannifin, Cleveland, USA), which created a pulsatile waveform. The fluid in the circuit was either saline solution or a blood mimicking fluid. The blood mimicking fluid has a viscosity similar to blood and consists of saline solution (70%) and Glycerine (30%) (Dean, 1992). The ground truth flow was measured with an electromagnetic flow meter (EMF)(Skalar Medical, Delft, The Netherlands).

The rotational x-ray system (Allura Xper with an FD20 detector and a MRC tube, Philips Medical Systems, Eindhoven, The Netherlands), the contrast agent injector (MarkVProVis, Medrad, Indianola, USA), and the contrast agent (Ultravist-370, Schering, Berlin, Germany) were all the same as those found in a typical clinical environment.

(a) Digitally subtracted angiographic image with injection in common carotid.
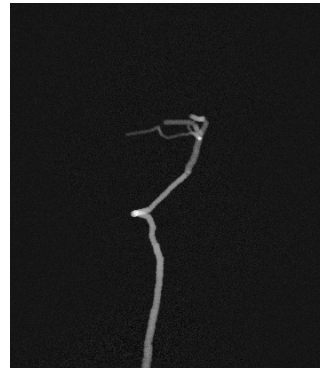
(b) Digitally subtracted angiographic image with injection in vertebral artery.

(c) Angiographic image without digital subtraction.

(d) Digitally subtracted angiographic image with motion artifacts.
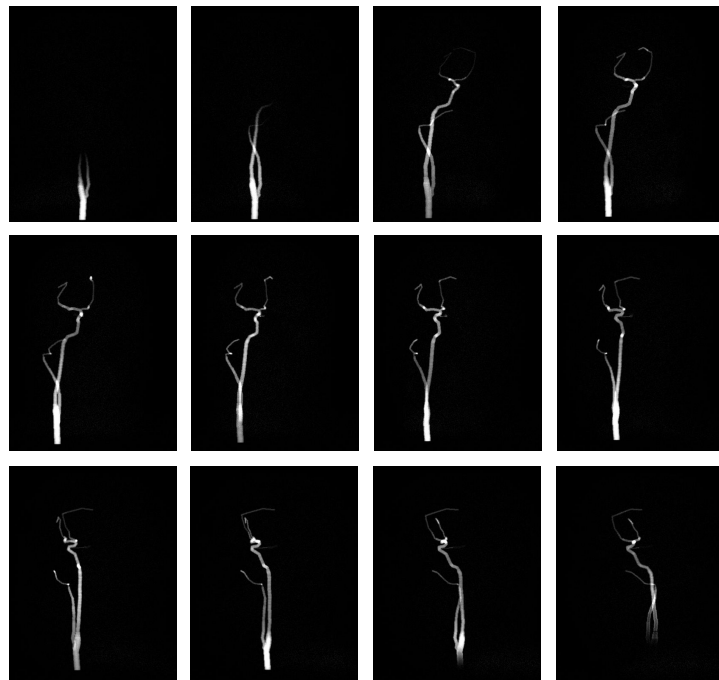
(e) Every 10th frame from of a rotational angiographic sequence.

Figure 4.5: Computer simulated rotational angiography using the visible human dataset (Waechter et al., 2008c).
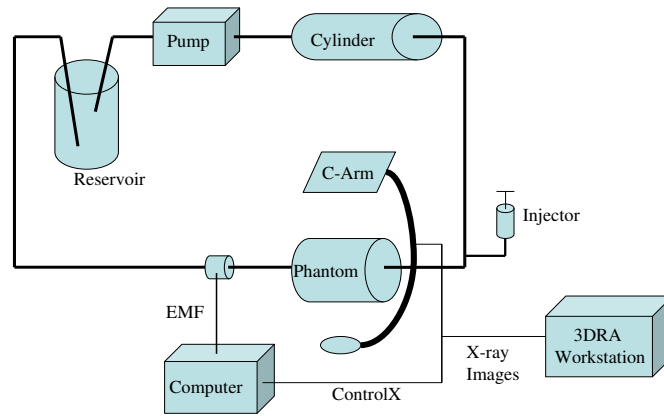
Figure 4.6: Overview of the experimental setup.

4.3.2 Phantom geometries

For the experimental setup, phantom geometries of different complexity were used as follows:

1. a straight rigid tube with a radius of 2 mm,

2. a straight rigid tube with a radius of 3 mm,

3. a glass bifurcation with the dimensions of a normal carotid bifurcation, including the carotid bulb where the base of the internal carotid artery characteristically widens immediately after the bifurcation,

4. a glass bifurcation with the dimensions of a normal carotid bifurcation including a smaller carotid bulb and the tortuous part of the internal carotid artery,

5. a glass bifurcation with the dimensions of a stenosed carotid bifurcation,

6. a compliant bifurcation made from flexible silicone tubing with a radius of 3 and 2 mm,

7. a compliant spiral made from flexible silicone tubing with a radius of 2 mm,

8. an anthropomorphic cerebrovascular vessel phantom consisting of the internal carotid artery and one half of the Circle of Willis made from flexible silicone,

9. an anthropomorphic cerebrovascular vessel phantom consisting of the both internal and external carotid arteries and the complete Circle of Willis embedded in a rigid silicone block.

X-ray images of all phantoms are shown in Figure 4.8. Phantoms 3 to 5 were constructed with the help of the glass workshop of Philips Research Europe (Aachen, Germany). Phantoms 6 and 7 were made by the author. Phantom 8 was contributed by Kawal Rhode (Guys Hospital, London, United Kingdom) and Phantom 9 was rented from Elastrat (Geneva, Switzerland). The fabrication method used to construct the anthropomorphic phantoms is described in Gailloud et al. (1997).

(a) Pump to generate steady flow.
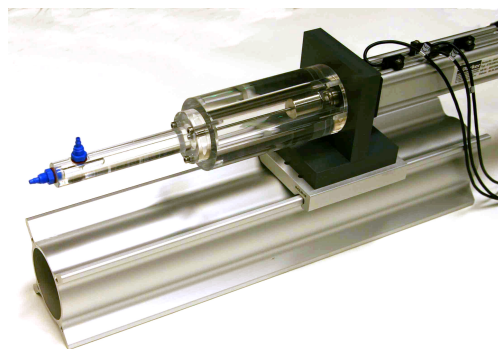
(b) Cylinder to generate pulsatile waveform.

(c) Electromagnetic flow meter.
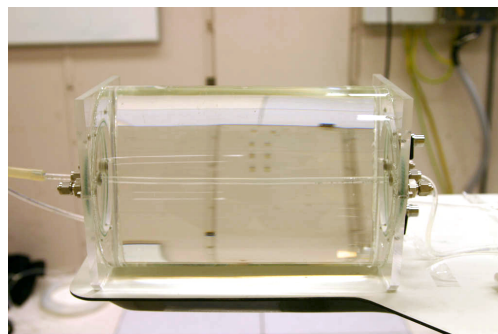
(d) Plexiglass cylinder with straight tube.

(e) X-Ray system with phantom.

(f) Injector.

Figure 4.7: Components of experimental setup for rotational angiography with inflow and outflow of contrast agent.
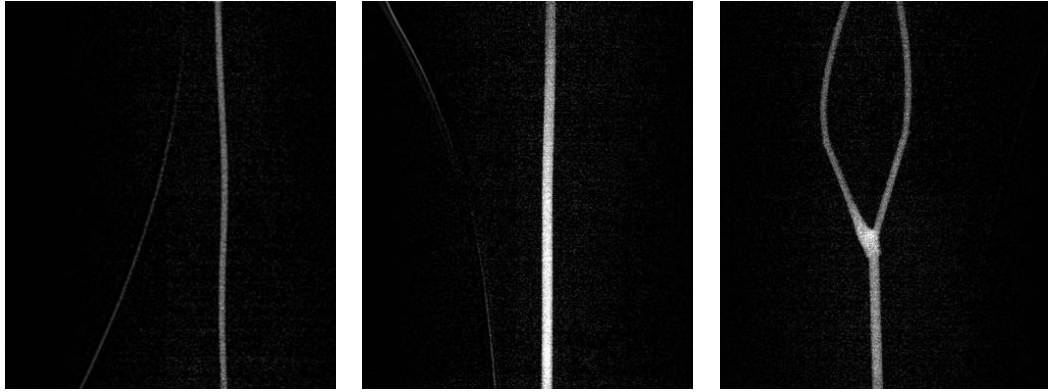
(a) 2 mm radius tube (phantom 1).

(b) 3 mm radius tube (phantom 2).

(c) Carotid - with bulb (phantom 3).
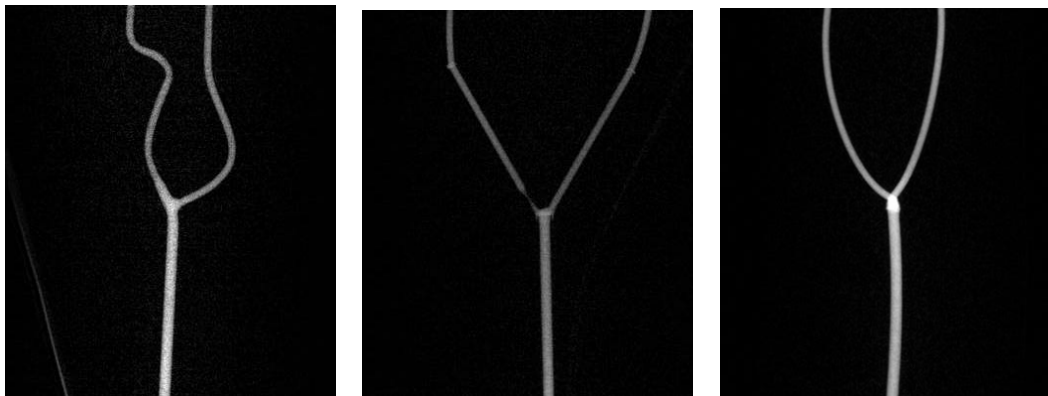
(d) Carotid - with tortuous internal carotid (phantom 4).

(e) Carotid - with stenosis (phantom 5).

(f) Simple bifurcation (phantom 6).
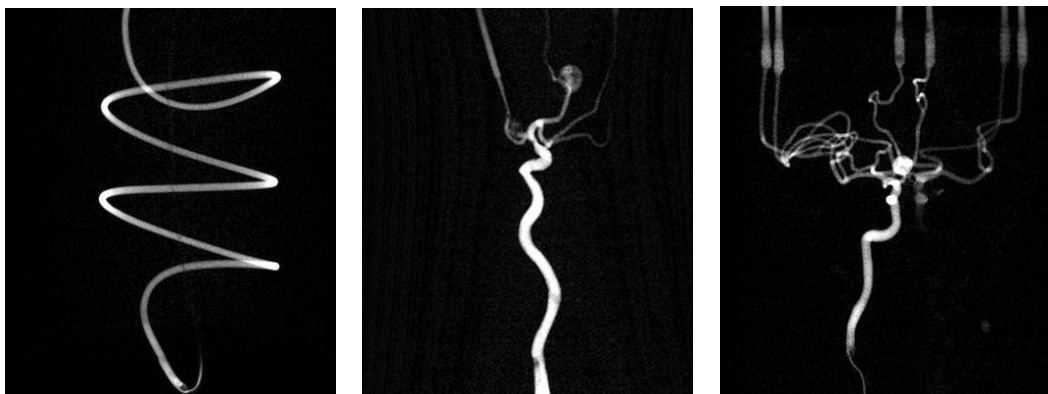
(g) Spiral (phantom 7).

(h) Half of the circle of Willis (phantom 8).

(i) Complete circle of Willis (phantom 9).

Figure 4.8: X-ray images of the phantoms.

Phantoms 1 to 5 and 8 were placed in turn in an elliptical, perspex cylinder filled with water. This cylinder was constructed with the help of the workshop of Philips Research Europe (Aachen, Germany). The inlets and outlets of the cylinder are configurable according to the geometry of the phantom. The cross sectional area corresponds to the shape and size of a human head. The cylinder is shown with phantom 8 mounted inside in Figure 4.9.

The elastic phantoms 6 and 7 were embedded in an agar-based, soft-tissue mimicking material inside a plastic cylinder. The soft tissue mimicking material was created as described by Madsen et al. (2005). Embedding phantom 8 in this soft tissue mimicking material was also attempted, but this failed because one of the vessel segments collapsed and during the attempt to reopen it, one of the aneurysms ruptured.

For all geometries, the material surrounding the phantom generated realistic noise, beam hardening, and scatter during the x-ray acquisitions. For each geometry, a mask scan, obtained without using a contrast agent injection, was acquired first.
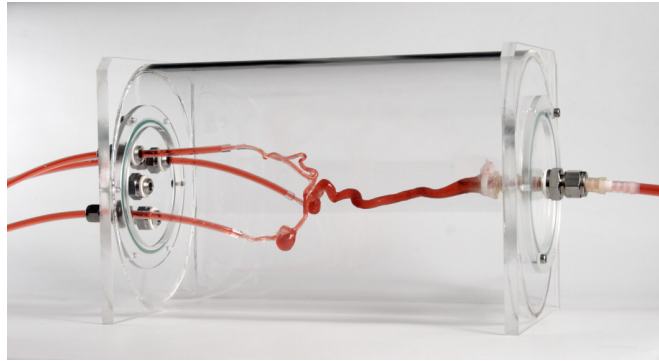
Figure 4.9: Elliptical cylinder with anthropomorphic cerebrovascular phantom fixed inside (Waechter et al., 2008c).

4.3.3 Configuration of the flow system

The mean flow rate in the circuit was varied between 100 ml/min and 300 ml/min depending on the cross sectional area of the main branch of the phantom. Higher flow rates were not possible due to limitations of the pump. Different pulsatile waveforms and a pulsatility factor were selected. The duration of the cardiac cycle was set to 0.8 s.

The injection flow was either set to the mean flow of the circulation or to half of the mean flow of the circulation. The injection duration was 3 s. The injection was started manually immediately after the start of the x-ray acquisition.

4.3.4 Configuration of the x-ray system

An acquisition protocol was configured to give a constant voltage and current (peak 70 kV and 250 mA, respectively). This is a deviation from the standard 3DRA protocol, in which the amperage and voltage can be adjusted during the acquisition according to the thickness of the patient. This, however, is not desirable for a quantitative evaluation of the x-ray images.

(a) EMF and ControlX signal.

(b) Injection flow and circulation flow determined from EMF.
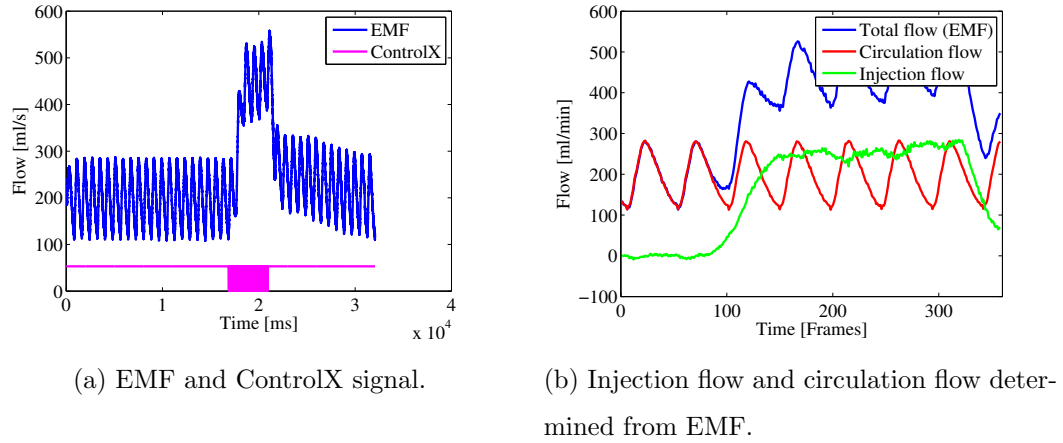
Figure 4.10: Examples of EMF signal.

The x-ray tube consists of 95% tungsten and 5% rhodium. The x-ray system contains a 0.1 mm copper filter and a 1 mm aluminium filter. Additionally, a 1.5 mm aluminium filter was applied. The case of the x-ray tube can be approximated by a 2.5 mm aluminium filter. 120 images were obtained in a pulsed mode with a frame rate of 30 fps and a radiation time of 5 ms per image. The rotation range was 205° and the average rotation speed was 55°/s. The acquisition time was 4 s.

4.3.5 Usage of the EMF

The ground truth instantaneous volumetric flow rate was recorded using an EMF and at the same time the control signal of the x-ray system (ControlX) was recorded (see Figure 4.10(a)). The second is useful for the synchronisation of the rotational image sequence and the electromagnetic flow meter.

From the EMF signal before and after the injection, a mean waveform was determined. This mean waveform was used to separate the EMF signal during the injection into flow due to the pump of the circulation and flow due to the injector (see Figure 4.10(b)).

The EMF was validated in the following way: A steady flow was configured using the EMF signal to choose the mean flow rate and the fluid which passed through the system in a fixed period of time was collected. Then, the fluid was weighed and the ground truth volume flow rate determined. This was done for different flow rates before the main experiments in order to analyse the linearity of the EMF measurements. The results are shown in Figure 4.11(a). Each time after the fluid in the circulation was exchanged, the procedure was repeated using the mean flow of the following set of experiments. The results are shown in Figure 4.11(b). It can be seen that the ratio between the EMF measurements and the ground truth measurements varied throughout the experiments. The mean flow error (see Equation 7.12) of the EMF was 3% ± 3% compared to fluid collection. The variance was higher if the fluid in the circulation was blood mimicking fluid instead of saline solution.
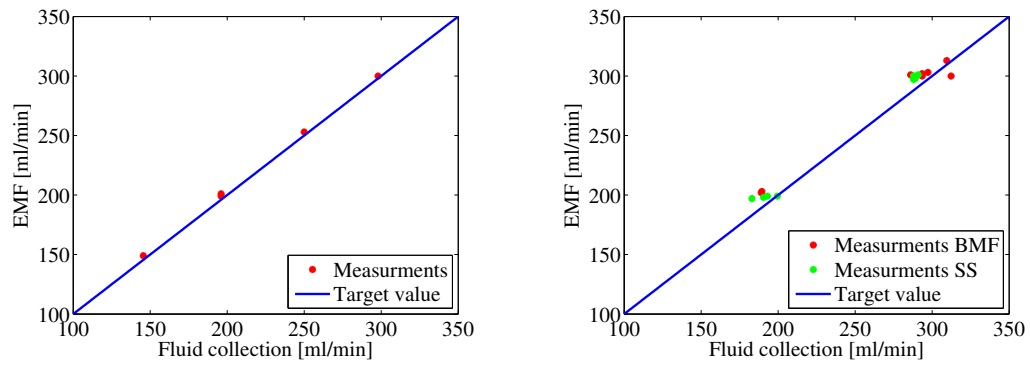
(a) Initial analysis of linearity of EMF measurements.

(b) Verification measurements after exchange of fluid (BMF - blood mimicking fluid, SS - saline solution), the mean flow rate of the following experiment is used.

Figure 4.11: Analysis of EMF signal.

5

Geometry and attenuation calibration

5.1 Introduction

Without any calibration, x-ray images give only relative information. A geometry calibration enables the measurement of absolute length and diameter of the vessel, whereas an attenuation calibration enables the measurement of absolute iodine concentrations.

If a 3D point is given, it must be possible to determine its 2D projection points in the rotational sequence, which are required for the geometry reconstruction and for the flow reconstruction. The relation is given by the projection function. As the detector does not have a perfect circular orbit, the parameters of the projection function have to be determined by performing a geometry calibration. This is the subject of the first part of this chapter.

Additionally, for flow reconstruction, it is beneficial to obtain quantitative information about the concentration of iodine in a vessel. The amount of iodine on the x-ray beam path determines the x-ray image intensity, but the relationship is complex. An attenuation calibration can turn x-ray image intensities into line integrals of iodine density. This is the subject of the second part of this chapter.

5.2 Geometry calibration

5.2.1 Coordinate systems

To determine the projection of a voxel onto an image plane, four coordinate systems should be considered: the image coordinate system i, the detector coordinate system d, the focus coordinate system f, and the global coordinate system g. All coordinate systems are shown in Figure 5.1 and indicated by a superscript.

The voxel volume is given in global coordinates. The origin of the global coordinate system is the isocentre of rotation $\mathbf{o}^g = \mathbf{p}_{\mathrm{iso}}$ and its orientation is given by the set of unit vectors $\{\mathbf{n}_x^g, \mathbf{n}_y^g, \mathbf{n}_z^g\}$. The detector coordinate system rotates with the detector. Its origin is the centre of the detector $\mathbf{o}^d = \mathbf{p}_{\mathrm{det}}$ and its orientation is given by the set of unit vectors $\{\mathbf{n}_x^d, \mathbf{n}_y^d, \mathbf{n}_z^d\}$,
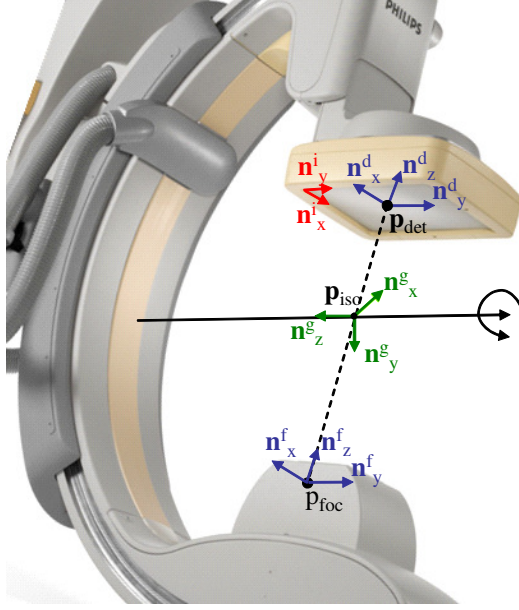
Figure 5.1: Coordinate systems of c-arm.

where $\mathbf{n}_z^d$ points away from the focus and $\mathbf{n}_x^d$ and $\mathbf{n}_y^d$ describe the plane of the detector. The focus coordinate system rotates with the focus. Its origin is given by the focus point $\mathbf{o}^f = \mathbf{p}_{\text{foc}}$, but its orientation is given by the orientation of the detector. The image coordinate system is a 2D system. Its origin is at the upper left corner of the detector. Its orientation is determined by the orientation of the detector: $\mathbf{n}_y^d$ and $\mathbf{n}_y^i$ have the same orientation, whereas $\mathbf{n}_x^d$ and $\mathbf{n}_x^i$ have opposite orientation.

5.2.2 Transformation between coordinate systems

In the following description, homogeneous coordinates are used. The transformation from Cartesian to homogeneous coordinates is given by

$$\begin{pmatrix} x \\ y \\ z \end{pmatrix} \mapsto \begin{pmatrix} x \\ y \\ z \\ 1 \end{pmatrix}. \tag{5.1}$$

In homogeneous coordinates the transformation from coordinate system a to b can be expressed as a multiplication by a 4×4 matrix

$$\mathbf{p}^b = \mathbf{T}^{b \leftarrow a} \cdot \mathbf{p}^a \tag{5.2}$$

with

$$\mathbf{T}^{b \leftarrow a} = \begin{pmatrix} \mathbf{R} & \mathbf{t} \\ \mathbf{0} & 1 \end{pmatrix}, \tag{5.3}$$

where $\mathbf{R}$ is a 3×3 rotation matrix and $\mathbf{t}$ is the translation vector that together define a rigid body transformation from coordinate system a to coordinate system b.

For every orientation of the rotating system, the calibration data gives the position of isocentre $\mathbf{p}_{\text{iso}}^d(t)$ and focus $\mathbf{p}_{\text{foc}}^d(t)$ in detector coordinates and 3 rotation angles $\alpha_x(t)$, $\alpha_y(t)$ and $\alpha_z(t)$ around the three axes, respectively. The set of all time-dependent geometric parameters will be indicated by $G(t)$. Additionally, the size of the detector s_x and s_y and the number of pixels n_x and n_y must be known.

The translation from the origin of the detector coordinate system at time t to the origin of the global coordinate system is given by

$$\mathbf{t}_t^{g\leftarrow d} = \mathbf{p}_{\text{iso}}^d(t) - \mathbf{p}_{\text{det}}^d. \tag{5.4}$$

The rotation $\mathbf{R}$ is composed of 3 rotations, first around the Y-axis, then around the (rotated) X-axis and last around the (twice rotated) Z-axis. Each rotation can be described by a rotation matrix

$$
\begin{aligned}
\mathbf{R}_t^{g\leftarrow d} &= \mathbf{R}_z(\alpha_z(t)) \cdot \mathbf{R}_x(\alpha_x(t)) \cdot \mathbf{R}_y(\alpha_y(t)) \\
&= \begin{pmatrix} c(\alpha_z) & s(\alpha_z) & 0 \\ -s(\alpha_z) & c(\alpha_z) & 0 \\ 0 & 0 & 1 \end{pmatrix} \cdot \begin{pmatrix} 1 & 0 & 0 \\ 0 & c(\alpha_x) & s(\alpha_x) \\ 0 & -s(\alpha_x) & c(\alpha_x) \end{pmatrix} \cdot \begin{pmatrix} c(\alpha_y) & 0 & s(\alpha_y) \\ 0 & 1 & 0 \\ -s(\alpha_y) & 0 & c(\alpha_y) \end{pmatrix},
\end{aligned}
\tag{5.5}
$$

where c denotes cosine and s denotes sine. The transformation from detector to global coordinates is then given by

$$\mathbf{T}_t^{g\leftarrow d} = \begin{pmatrix} \mathbf{R}_t^{g\leftarrow d} & \mathbf{t}_t^{g\leftarrow d} \\ \mathbf{0} & 1 \end{pmatrix}. \tag{5.6}$$

The next required transformation is the transformation from detector coordinates to focus coordinates. As mentioned above, the orientation is the same. Therefore, the rotation matrix is the identity matrix $\mathbf{I}$. The translation from the origin of the detector coordinate system at time t to the origin of the focus coordinate system at time t is given by

$$\mathbf{t}_t^{f\leftarrow d} = \mathbf{p}_{\text{foc}}^d(t) - \mathbf{p}_{\text{det}}^d. \tag{5.7}$$

The transformation from detector to focus coordinates is then given by

$$\mathbf{T}_t^{f\leftarrow d} = \begin{pmatrix} \mathbf{I} & \mathbf{t}_t^{f\leftarrow d} \\ \mathbf{0} & 1 \end{pmatrix}. \tag{5.8}$$

For both transformations described above the inverse transformations are given by the inverse of the transformation matrices, i.e.

$$\mathbf{T}_t^{d\leftarrow g} = \left(\mathbf{T}_t^{g\leftarrow d} \right)^{-1}, \tag{5.9}$$

$$\mathbf{T}_t^{d\leftarrow f} = \left(\mathbf{T}_t^{f\leftarrow d} \right)^{-1}. \tag{5.10}$$

The last required transformation is the transformation between detector coordinates and image coordinates. The transformation from detector to image coordinates consists of the reflection,
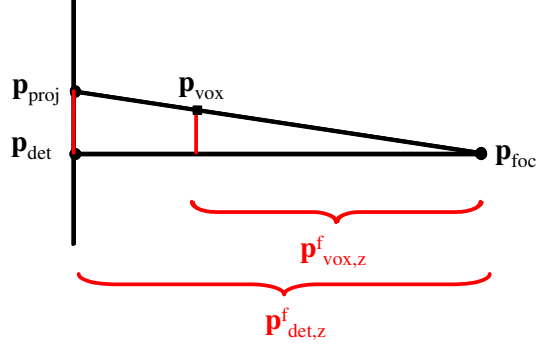
Figure 5.2: Projection of voxel to detector plane.

the scaling, the translation of the origin, and the limitation to x and y components:

$$\mathbf{T}^{i \leftarrow d} = \begin{pmatrix} -n_x/s_x & 0 & 0 & n_x/2 \\ 0 & n_y/s_y & 0 & n_y/2 \\ 0 & 0 & 0 & 1 \end{pmatrix}. \tag{5.11}$$

It is important to note that this transformation assumes that the point lies on the detector. The transformation from image to detector coordinates is given by

$$\mathbf{T}^{d \leftarrow i} = \begin{pmatrix} -s_x/n_x & 0 & s_x/2 \\ 0 & s_y/n_y & -s_y/2 \\ 0 & 0 & 0 \\ 0 & 0 & 1 \end{pmatrix}. \tag{5.12}$$

Both these transformations are time independent.

5.2.3 Projection

To determine the projection of a voxel $\mathbf{v}$ with the global coordinates $\mathbf{p}^g_{\mathrm{vox}}$ at time t, the following steps have to be performed: First, the global coordinates are transformed to focus coordinates as follows:

$$\mathbf{p}^f_{\mathrm{vox}}(t) = \mathbf{T}^{f \leftarrow d}_t \cdot \mathbf{T}^{d \leftarrow g}_t \cdot \mathbf{p}^g_{\mathrm{vox}}. \tag{5.13}$$

In focus coordinates, the projection point can be found by a scaling with the magnification factor λ as illustrated in Figure 5.2:

$$\mathbf{p}^f_{\mathrm{proj}}(t) = \begin{pmatrix} \lambda \cdot \mathbf{I} & \mathbf{0} \\ \mathbf{0} & 1 \end{pmatrix} \cdot \mathbf{p}^f_{\mathrm{vox}}(t), \tag{5.14}$$

with

$$\lambda = \frac{\mathbf{p}^f_{\mathrm{det},z}(t)}{\mathbf{p}^f_{\mathrm{vox},z}(t)}, \tag{5.15}$$

where $\mathbf{p}^f_{\mathrm{det},z}(t)$ and $\mathbf{p}^f_{\mathrm{vox},z}(t)$ are the z-coordinates of the respective points. The projection point $\mathbf{p}^f_{\mathrm{proj}}(t)$ is now given in focus coordinates. In the following, the projection point is required to be in image coordinates as given by

$$\mathbf{p}^i_{\mathrm{proj}}(t) = \mathbf{T}^{i \leftarrow d} \cdot \mathbf{T}^{d \leftarrow f}_t \cdot \mathbf{p}^f_{\mathrm{proj}}(t). \tag{5.16}$$
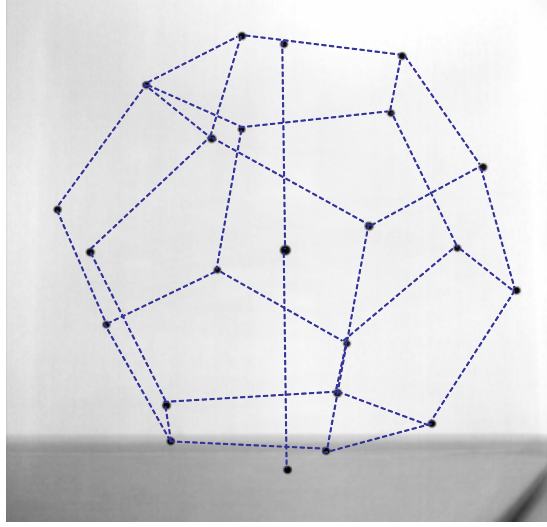
Figure 5.3:   X-ray image of geometry calibration phantom, the dodecahedron and the central axis are displayed as an overlay.

The projection function Π, which is used in the following chapters, is defined for a voxel $\mathbf{v}$ with global coordinates $\mathbf{p}^g_{\mathrm{vox}}$ as

$$\Pi(\mathbf{v}, G(t)) := \begin{pmatrix} \mathbf{p}^i_{\mathrm{proj,x}}(t) \\ \mathbf{p}^i_{\mathrm{proj,y}}(t) \end{pmatrix}, \tag{5.17}$$

where $\mathbf{p}^i_{\mathrm{proj}}$ is determined as described above and $G(t)$ describes the geometric parameters of the c-arm at time t. The detector used for the experiments was a flat detector, so it was not necessary to consider distortion.

5.2.4   Calibration

To determine the projection of the voxel $\mathbf{v}$, the geometric parameters $G(t)$ of the c-arm have to be known. Every configuration of the rotating system is described by the following parameters: the position of isocentre $\mathbf{p}^d_{\mathrm{iso}}$ and focus $\mathbf{p}^d_{\mathrm{foc}}$ in detector coordinates and 3 rotation angles α_x, α_y and α_z around the three axes, respectively. These parameters vary as the c-arm rotates. Due to gravitational and inertial forces, the c-arm and its supporting stand are deformed during the rotation. Therefore, the rotation is not perfectly circular and the position of the focus in relationship to the detector varies. As the variations are reproducible, however, a geometric calibration can be used to determine the calibration parameters (Wiegert, 2006; Movassaghi et al., 2004).

For the geometry calibration, images of a dodecahedron-shaped calibration phantom are acquired (Philips Medical Systems, Best, The Netherlands). A dodecahedron has 20 corners, in each a bronze calibration ball is placed. All calibration balls have the same distance from the centre, which is 85 mm. Three additional calibration balls are placed on the central axis. All calibration balls have a radius of 1.5 mm, except the one in the centre, which has a radius of 2 mm. An example x-ray image of the calibration phantom is shown in Figure 5.3.
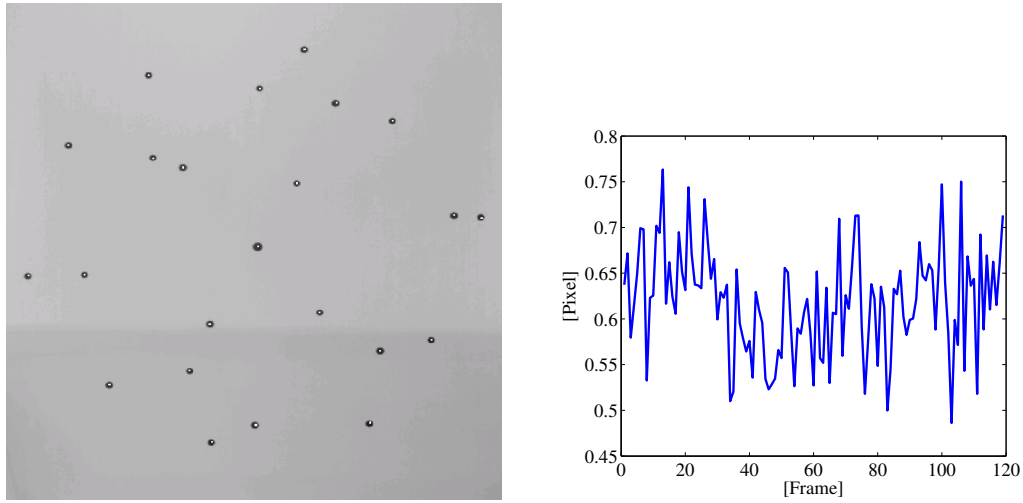
(a) Projection of centre points of calibration balls (Projection points are marked with white dots).

(b) Distance between projected centre points and detected calibration balls (mean distance per frame).

Figure 5.4: Results from geometry calibration using my projection function (Equation 5.17).

The software CaliburXP (Philips Medical Systems, Best, The Netherlands) was used to determine the calibration parameters for every configuration. An overview of the calibration method used by CaliburXP was given by Koppe et al. (1995). Besides the exact geometry of the calibration phantom, CaliburXP requires the exact pixel size and initial values of the calibration parameters. The software uses the initial values of the calibration parameters to project the centre point of the calibration balls onto the detector plane. In the neighbourhood of the projection points in the image, the calibration balls are detected. At least 15 of the 23 calibration balls should be detected for a successful calibration. The calibration parameters are optimised to minimise the distance between the projection points and the centre points of the detected calibration balls.

5.2.5 Evaluation setup and results

The following setup was used to evaluate the geometry calibration and my implementation of the projection function: The 3D coordinates of the centre points of the calibration balls can be obtained from CaliburXP. These are projected to all frames using the calibration parameters from CaliburXP and my projection function. At the projection points, the calibration balls are detected and the distance of the projection points to the centre points of the detected calibration balls is determined. Figure 5.4(a) shows the projection points using the parameters from CaliburXP and my projection function. Figure 5.4(b) shows the resulting deviations.

5.2.6 Discussion

The remaining errors after the calibration are quite small: the mean distance between projected centre points and detected calibration balls is slightly higher than half a pixel. That should be accurate enough for my applications. These errors can be partly due to differences between my

detection of the calibration balls and the internal detection from Calibur.

5.3 Attenuation calibration

5.3.1 Introduction

In Section 2.6, it was explained how absolute densitometric information can be used for flow quantification. An attenuation calibration enables the determination of the absolute density of iodine using a contrast agent image and a mask image. This section gives more information about the attenuation calibration.

For a monochromatic x-ray spectrum the theoretical relationship between an x-ray image and the attenuating material is given by Lambert-Beer's Law:

$$I_1 = I_0 e^{-\int \mu(x)dx},$$

(5.18)

where I_0 is the x-ray intensity emitted by the tube and I_1 is the intensity after the attenuating material characterised by $\mu(x)$. Theoretically, the line integral of attenuation is given by

$$\Lambda_\mu = \int \mu(x)dx = -\ln\left(\frac{I_1}{I_0}\right).$$

(5.19)

However, for many reasons, the measured line integral deviates from the ideal line integral. The main reason is beam hardening, which is the phenomenon that polychromatic X-rays become more penetrating (harder), as they propagate through matter. Another reason is scattered radiation. The influence of beam hardening can be reduced by introducing a copper or aluminium filter, whereas the influence of scatter can be reduced with an anti-scatter grid. However, in both cases, the reduction is not sufficient. I have tried an analytical preprocessing which used a model of beam hardening and scatter, but I did not get satisfactory results. Therefore, a preprocessing step based on an attenuation calibration is described here.

5.3.2 Attenuation calibration samples

For the attenuation calibration, samples with different concentrations of contrast agent are required. As a container, small tubes which have the size of a medium-sized artery were chosen as shown in Figure 5.5. These were made from glass with an internal radius of 2 mm and a wall thickness of 1 mm. Altogether, nine calibration tubes were made: The first was filled with pure water and the others with increasing concentrations of contrast agent mixed with water. The chosen concentrations were: 12.5%, 25%, 37.5%, 50%, 62.5%, 75%, 87.5%, and 100%.

Before making the samples, it was observed that the contrast agent separated after the bottle was opened. It was assumed that the contrast agent reacts with oxygen. Therefore, the mixing and filling were done in the protective atmosphere of a glove box.

For the mixing, fixed units of water and contrast agent were collected in a small container. To ensure that all units had the same volume, an automatic pipette was used. Before the mixture was filled into the tube, it was well shaken in the container.

Figure 5.5: Tubes with different concentrations of contrast agent.

Figure 5.6: Setup with one tube and the elliptical cylinder. The cylinder produces scatter and increases beam hardening.

During the flow experiments, it was observed that contrast agent was settling on the bottom of the tubes. To remove gradients in the concentration after storage of the samples, small steel balls were put into each tube to ensure good mixing when the tubes are shaken.

5.3.3 Phantom setup

To ensure realistic scatter and beam hardening, a simple head phantom was placed in the field of view. This phantom consisted of a water-filled perspex cylinder, which had an elliptical cross section with the dimensions of the human head. The axis of the cylinder was aligned with the rotation axis. Because of this shape, beam hardening and scatter varied during the rotation, as it is the case during clinical scans.

For the first scan (the mask scan), the calibration tube filled with pure water was placed next to the cylinder as shown in Figure 5.6. Then, for the contrast agent (CA) scans, one calibration tube filled with a different concentration of contrast agent was always placed next to the cylinder (see Figure 5.7(a). To obtain the DSA scan, the mask scan was subtracted from the CA scan (see Figure 5.7(b)).

5.3.4 Measuring line integrals of attenuation

The x-ray system used for these experiments was an Allura Xper with a FD20 detector and a MRC tube configured as described in the previous chapter. For this system, images are already offset-, gain-, and defect-corrected by the system. Additionally, white compression is applied to allow for more efficient processing of the images. For later quantitative processing, images were uncompressed by applying the inverse white compression denoted by W^{-1}. In Figure 5.8, examples of different inverse white compression functions are shown.

After inverse white compression, images are normalized by dividing by I_0. As the current and voltage are constant throughout the acquisition, the maximum of the measured image intensities can be used as an estimation of I_0. If all images contain direct radiation, each image is divided by its maximum to correct for small variations in the tube amperage. Finally, the
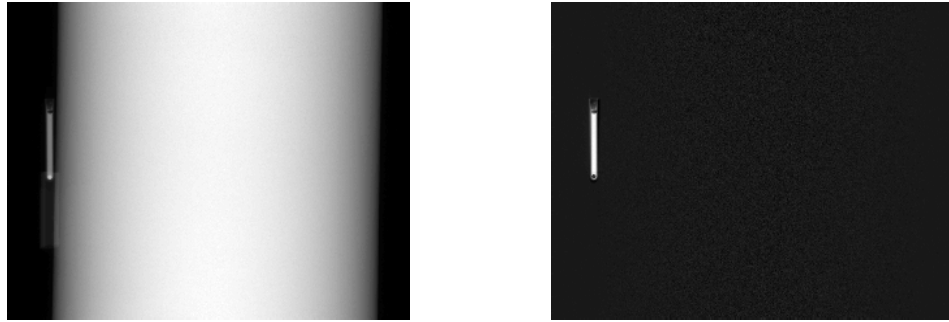
(a) Image from CA scan. (b) Image from DSA scan.

Figure 5.7: X-ray images from tube and cylinder.
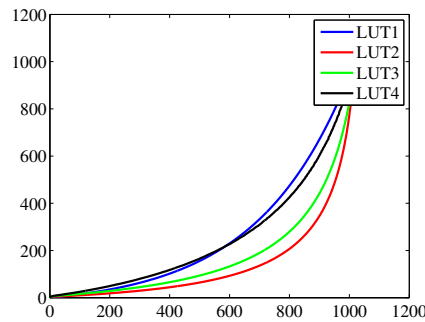
Figure 5.8: Different examples of inverse white compression functions.

measured line integral of attenuation is given by

$$\Lambda_\mu = P(I_m) = -\ln\left(\frac{W^{-1}(I_m)}{I_0}\right),$$ (5.20)

where I_m is a measured intensity of the x-ray image, as it is output from the x-ray system.

5.3.5 Attenuation map

For each DSA scan, the attenuation map of the calibration tube was determined. The attenuation map was determined in the same way as the flow map for a vessel segment (see Section 2.6 and Section 7.2.1). In the case of the flow map, the intensities mainly changed because the concentrations of contrast agent changed. In the calibration tubes, however, concentrations were constant. Therefore, the intensities should be constant in the attenuation map.

However, Figure 5.10 indicates that they were not constant. The measurements were constant along the centreline but they varied with the angle of rotation, which is why from now on, all measurements are presented after averaging along the centreline.

Figure 5.11(a) shows variations in the attenuation in the DSA scan during the rotation for different concentrations of contrast agent. During the rotation, the intersection length of the x-ray beam and the cylinder varies as shown in Figure 5.11(b). Therefore, the attenuation in the mask scan varies as shown in Figure 5.11(c). This results in variations in beam hardening
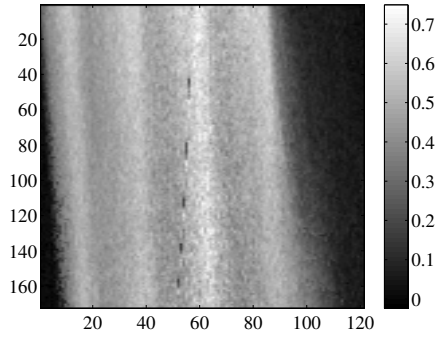
Figure 5.9: Flow map.
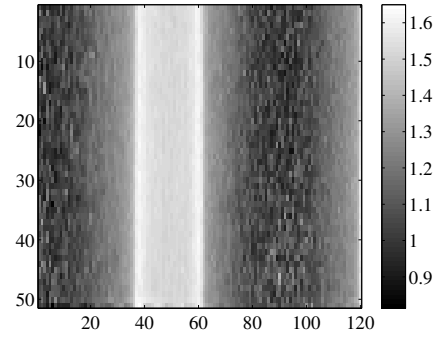
Figure 5.10: Attenuation map.
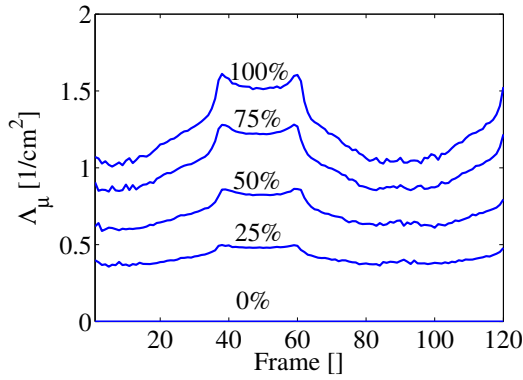
(a) Variations of attenuation during rotation for tubes with different concentrations of contrast agent(from DSA scan).
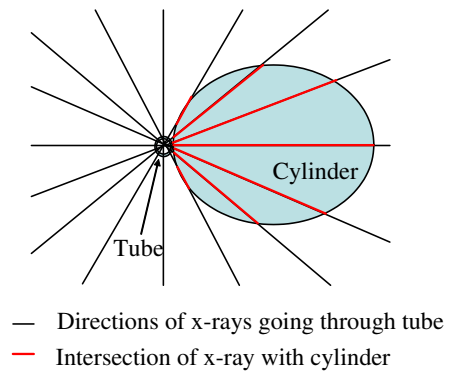
(b) Variations of the intersection length of the x-ray beam with the cylinder.
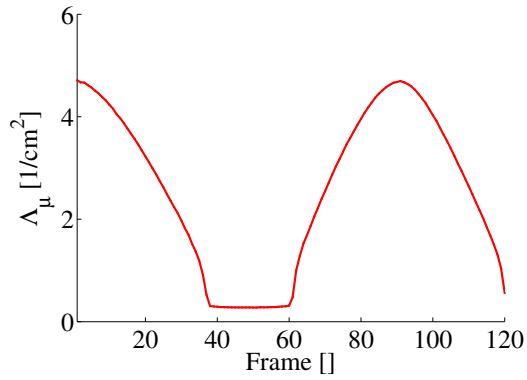
(c) Variations of attenuation during rotation for cylinder and water-filled tube (from mask scan).

Figure 5.11: Variation of measured attenuation during rotation.
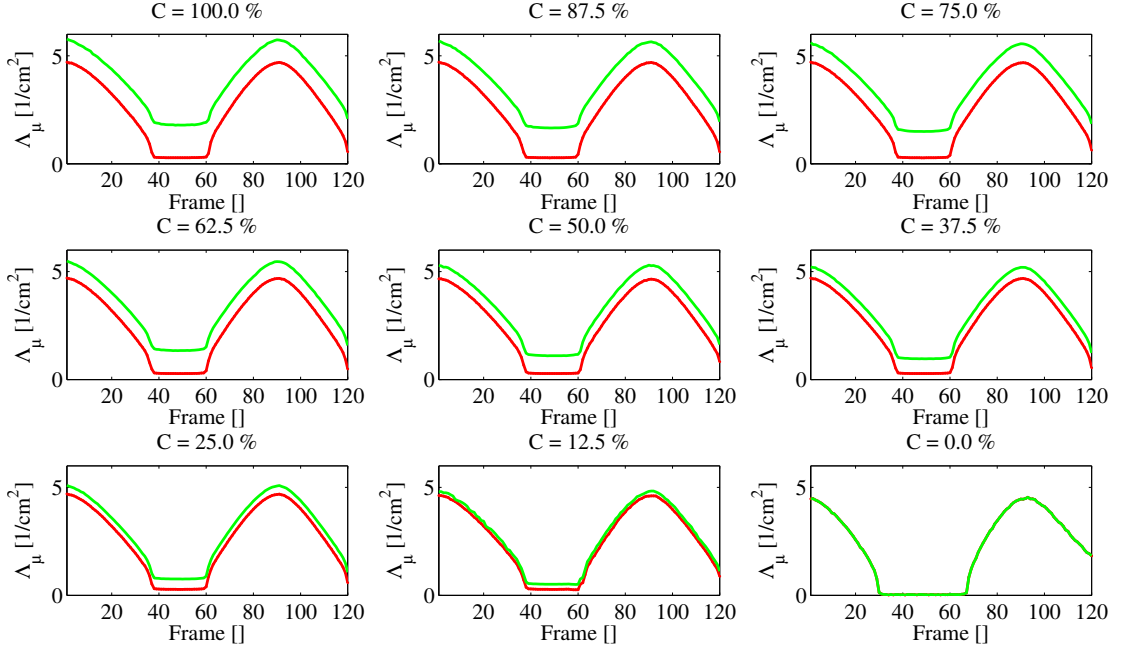
Figure 5.12: Variation in the line integral of attenuation from the mask scan (red) and from CA scans (green) for different concentrations of CA during the rotational scan.

and scatter, which are responsible for the unwanted variations in the DSA scan. These figures show the need for an attenuation calibration to obtain quantitative angiography.

5.3.6 Generation of LUTs for attenuation calibration

The look-up table (LUT) for the attenuation calibration maps a measured line integral of attenuation of the mask scan $\Lambda_{\mu,\text{Mask}}$ and a measured line integral of attenuation of the CA scan $\Lambda_{\mu,\text{CA}}$ to the ideal line integral of iodine density Λ_ρ.

For all CA scans and the mask scan, the attenuation map was determined which gives the variation of the line integral of attenuation during the rotation (see Figure 5.12). The line integral of iodine density Λ_ρ was determined for each tube by

$$\Lambda_\rho = C \cdot \rho_I \cdot r, \tag{5.21}$$

where C is the concentration of contrast agent in the tube, ρ_I is the density of iodine in the contrast agent (in this case 370 mg/ml), and r is the radius of the tube. From all scans, samples of the format $(\Lambda_{\mu,\text{Mask}}, \Lambda_{\mu,\text{CA}}, \Lambda_\rho)$ are determined (see Figure 5.13). Then, the thin plate spline (Meinguet, 1979) which approximates all data points best was determined (see Figure 5.14). This thin plate spline defines the LUT.

If $I_{\text{Mask}}(x, y, t)$ is the measured mask sequence and $I_{\text{CA}}(x, y, t)$ is the measured CA sequence, the calibrated, rotational, angiographic sequence is given by

$$I_\rho(x, y, t) = \text{LUT}(P(I_{\text{Mask}}(x, y, t)), P(I_{\text{CA}}(x, y, t))). \tag{5.22}$$
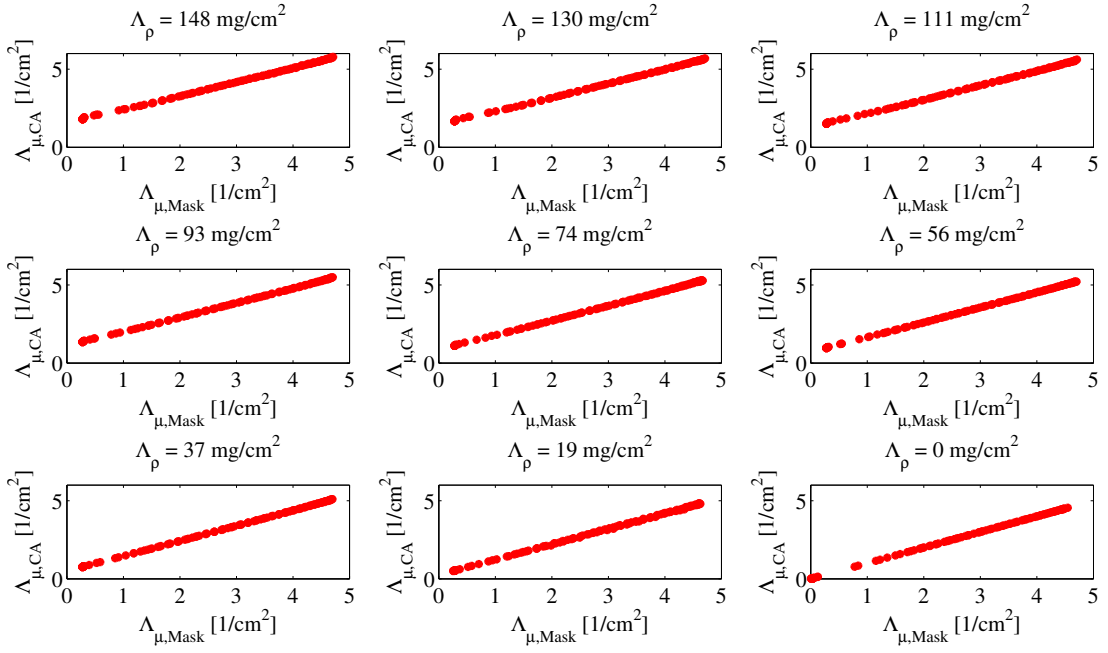
Figure 5.13: Relation of line integral of attenuation from mask scan and from CA scan for different line integrals of iodine density.
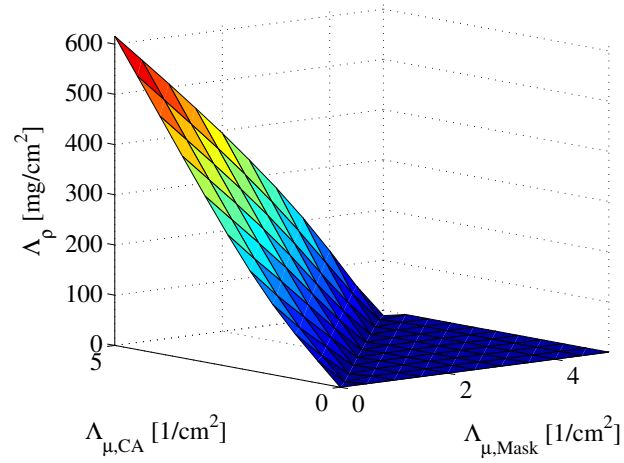
Figure 5.14: LUT for the line integral of iodine density of CA.

5.3.7 Evaluation setup and results

To validate the calibration procedure and to analyse how many calibration samples are required, LUTs were determined for different subsets of calibration tubes:

- (100%, 87.5%, 75%, 62.5%, 50%, 37.5%, 25%, 12.5%, 0%),

- (100%, 75%, 50%, 25%, 0%),

- (100%, 75%, 25%, 0%),

- (100%, 50%, 0%).

All LUTs were then used to determine the line integral of iodine density from all rotational sequences of the different tubes and the cylinder. The mean and the standard deviation were determined for each LUT and for each calibration tube.

In the first case above, exactly the same datasets were used for the determination of the LUT and for the validation, which is why a "leave-one-out" study was conducted, whereby always one calibration tube was left out during the determination of the LUT. This LUT was then used to determine the line integral of iodine density for this calibration tube.

The results for the LUT which made use of all calibration tubes are shown in detail in Figure 5.15(a). It presents the results for frames in which the background attenuation is greater than one. The frames in which the calibration tubes were not occluded by the cylinder were removed because this would not happen in a flow scan as the phantom is inside the cylinder. Figure 5.15(b) shows the mean of the measurements of the line integral of iodine density. The densities vary slightly during the rotational scan. However, the mean is very near to the ground truth concentration.

The results for different subsets are shown in Figure 5.15(c) to 5.15(e). The characteristic variations during the rotational scan can be corrected even with a low number of samples in the calibration subset. The deviation in the results increased by only a small amount. The mean error, however, was increasing as the number of samples in the subset was decreased. The results for the leave-one-out study are given in Figure 5.15(f).

A summary of all results is given in Table 5.1. For each sample and each LUT, the relative mean error is given and for each LUT the relative root mean square error (RMS) was determined.

5.3.8 Discussion

If the attenuation calibration is used for a densitometric method for flow quantification, it is important that the attenuation calibration is not biased. The bias is measured by the relative mean error.

The relative mean error should be as small as possible for each individual sample. The relative mean errors were between 0.1% and 19.1%. To evelute each LUT, the RMS error was determined for each LUT. This showed that only the LUT which was created with the smallest subset was substantially less accurate. Therefore, at least 4 samples should be used
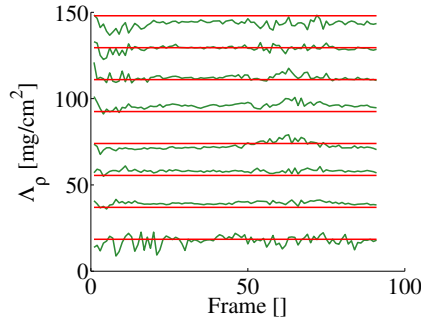
(a) Results from LUT based on all subset of samples for different frames with varying background attenuation.
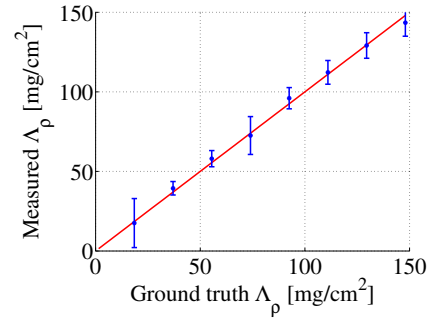
(b) Results from LUT based on all subset of samples.
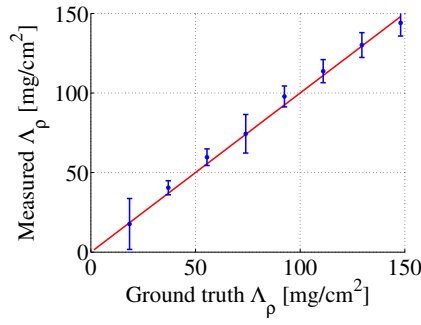
(c) Results from LUT based on first subset of samples.
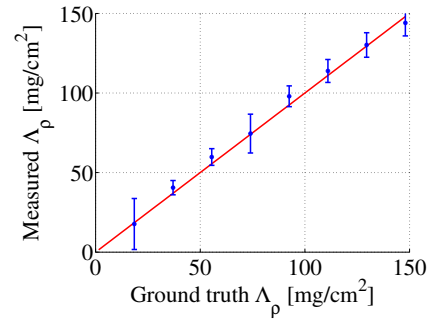
(d) Results from LUT based on second subset of samples.
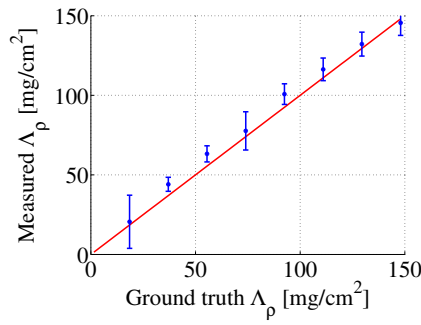
(e) Results from LUT based on third subset of samples.
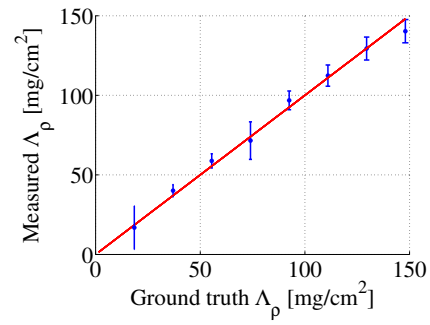
(f) Results from leave-one-out study.

Figure 5.15: Results from calibration with different LUTs; Mean and standard deviation of measured values (blue) in relation to the ground truth (red) for different concentrations of contrast agent.

Line integral of iodine density [mg/cm^2]	All [%]	Subset 1 [%]	Subset 2 [%]	Subset 3 [%]	Leave-one-out [%]
148	-2.6	-2.7	-2.7	-1.7	-5.2
130	-0.1	0.5	0.5	2.1	-0.1
111	1	2.5	2.6	4.8	1.3
93	3.5	5.8	5.9	8.9	4.7
74	-2.3	0.5	0.7	4.9	-3.3
56	4.2	7.5	7.7	13.9	5.9
37	5.7	9.3	9.5	19.1	8.3
19	-4.8	-4.4	-4.5	11	-8.9
RMS	3.5	5.1	5.2	10.0	5.5

Table 5.1: Summary of results, the relative mean error is given for all experiments.

for attenuation calibration. The leave-one-out study showed that interpolation gave satisfactory results. Extrapolation, however, did not give accurate results.

It is important to note that it is also possible that the concentrations of the samples slightly deviate from the assumed concentrations and that these errors became apparent as the number of samples was decreased.

During the attenuation calibration, the thickness of the background material (mainly the water-filled cylinder) was varied between 0.6 cm (water-filled tube) and 20 cm (water-filled tube and long axis of elliptical cylinder). This was achieved by changing the intersection length of the x-ray beam and the cylinder during the rotation. The resulting LUT will be applicable for background objects which consist mainly of water and are of smaller or equal size to the cylinder, but not for objects of larger size.

6

Using flow information to support vessel reconstruction

6.1 Introduction

The overall goal of this work is to extract blood flow information from rotational angiography. To be able to get absolute flow estimates, the 3D geometry of the vessel system must be known. It can, for example, be obtained from the 3DRA reconstruction.

Most information about the blood flow is contained in the image sequence if the inflow of contrast agent is visible in the rotational angiographic sequence. Images with this property, however, are not well suited to standard 3DRA reconstruction algorithms. These algorithms assume constant attenuation for every voxel and, as the concentration of contrast agent varies, especially during inflow and outflow, this condition is not met.

This can give rise to the following artefacts: Smaller vessel segments can disappear and vessels can appear to have an elliptical cross section although they actually have a circular cross section. These artefacts are described in more detail in Waechter et al. (2008c).

The following section describes my algorithm for reconstructing vessels from a rotational angiographic sequence, which explicitly uses information about blood flow and contrast agent propagation to make the reconstruction feasible for cases with inflow and possibly outflow of contrast agent during the acquisition.

6.2 Method

This method is based on the fast marching algorithm, which was introduced in Section 2.5. In summary, the fast marching algorithm is a wavefront propagation method where the speed of the wavefront depends on a positive speed function.

The fast marching algorithm is used to determine the order in which voxels are analysed. For each voxel $\mathbf{v}$, that is visited by the algorithm, a speed value $\mathcal{S}(\mathbf{v})$ is determined. Ideally,

only voxels inside a vessel or next to a vessel are visited. To achieve this, the speed function should only be high for voxels inside a vessel.

The propagation starts from a seed point and is terminated when all end points are reached. These points are manually selected in two orthogonal projection views. To aid the user, the epipolar line is displayed in the second view. Then, from each set of 2D points, a 3D point is reconstructed using the epipolar constraint. The manual selection and the reconstruction take a few seconds for each 3D point. The total time depends on the number of end points but is usually less than 1 min.

The core part of this method is the definition of the speed function. It is based on the rotational time intensity curve (R-TIC) and the bolus arrival time (BAT) and is a product of three terms: The first is a measure for how likely it is that the current voxel is inside a vessel; the second imposes a constraint which enforces continuity of the BATs; and the third is a measure of the distance to the centre of the vessel. The mathematical formulation of the method is explained in the following subsections resulting in the definition of the speed function. Figure 6.1 shows an overview of the algorithm.

When the propagation of the fast marching algorithm has reached all end points, the result can be used to determine a 3D path which connects the seed and any given end point. As the wavefront propagates, its arrival times are determined for each traversed voxel (N.B. these arrival times should not be confused with the bolus arrival times). As the speed function is strictly positive, the wavefront arrival times decrease monotonically from any end point of the vessel tree towards the seed point, where the arrival time is, by definition, zero. For this reason, a simple greedy search (Cormen et al., 1990) can be used to determine the minimum cost path from the end point to the seed point where the cost is defined inverse to the speed. This path describes the 3D vessel centreline.

6.2.1 Rotational time intensity curve

The input data for this method consist of a subtracted, rotational, angiographic sequence of M projection images $I(x, y, t)$, acquired at the time steps $t \in \{t_i \,|\, t_i = i \cdot T_A/M,\, i \in \{1, 2, \ldots, M\}\}$ at different geometric configurations $G(t)$ of the rotating c-arm, where T_A is the duration of the image acquisition. A geometric calibration, as described in Section 5.2, is used beforehand to determine $G(t)$.

The R-TIC at a voxel with position $\mathbf{v}$, is given by

$$\mathcal{R}(\mathbf{v}, t) = I(\Pi(\mathbf{v}, G(t)), t), \tag{6.1}$$

where $\Pi(\mathbf{v}, G(t))$ is the projection function as defined in Section 5.2.3. The determination of the R-TIC is illustrated in Figure 6.2.

The contrast agent concentration within a voxel determines its attenuation, and the attenuation along the x-ray beam determines the intensity within an x-ray image. Therefore, the values of the R-TIC put an upper limit on the concentration within the corresponding voxel
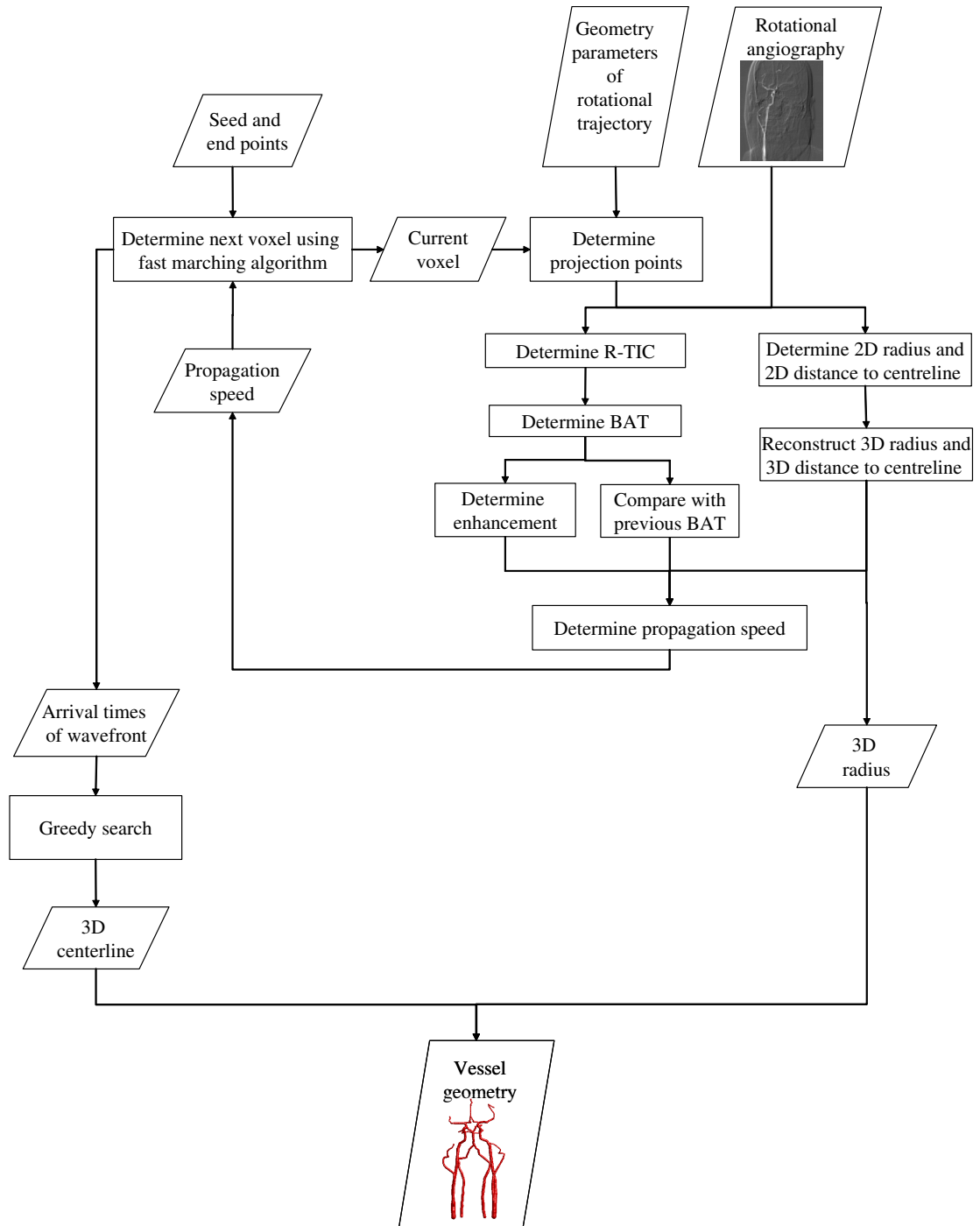
Figure 6.1: Overview of the reconstruction and segmentation algorithm.
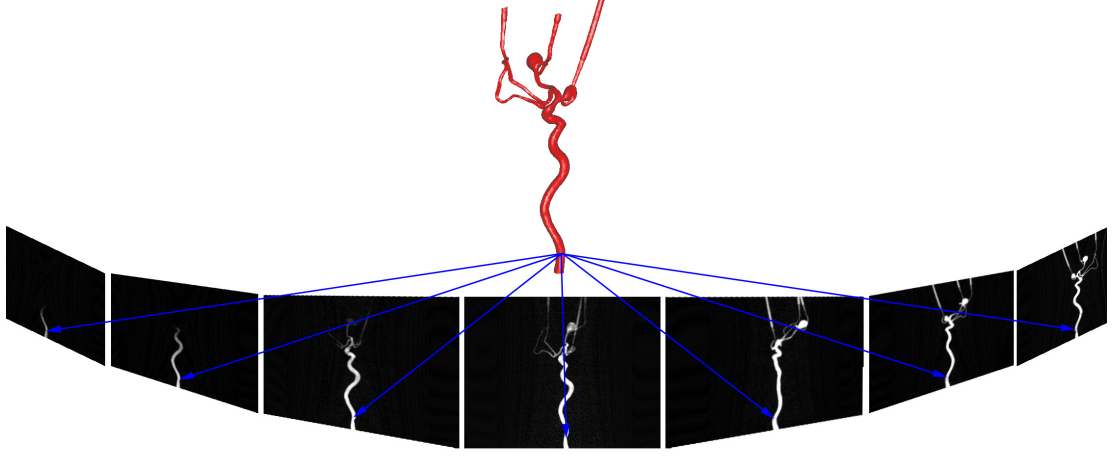
Figure 6.2: Determination of an R-TIC: The current voxel is projected onto all projection planes, each corresponding to a different orientation of the x-ray system; the image intensities at the projection points form the R-TIC (Waechter et al., 2008c).

at each time step. In contrast to the TIC, the R-TIC has a changing perspective due to the rotation of the x-ray system. This results in two different errors in the R-TIC, namely errors due to foreshortening and errors due to overlapping vessels.

In the literature, the term foreshortening is generally used to describe the effect where a vessel appears shortened in the projection image when the local direction of the vessel is not perpendicular to the direction of the x-ray beam (Chen et al., 2002; Wink et al., 2003). When foreshortening of an enhanced vessel occurs, an intensity change occurs in the projection image. The vessel appears to be denser because the x-ray beam traverses a longer path through the vessel. Foreshortening is a general problem, which introduces broad additional peaks into the R-TIC (see Figure 6.3).

Overlapping vessels are multiple vessels which lie on the x-ray beam path from the source through the current voxel to the detector. They only arise for some configurations of the rotating c-arm, where they lead to sharp additional peaks in the R-TIC (see Figure 6.3).

6.2.2 Vessel enhancement

The enhancement measure $\mathcal{E}(\mathbf{v}, t, \Delta t)$ of a voxel $\mathbf{v}$ quantifies how well the voxel $\mathbf{v}$ can be enhanced due to the contrast agent in the interval starting at time t with duration Δt. It is based on the R-TIC and is defined in a way to emphasize the duration rather than the magnitude of enhancement. The reason for this is that a voxel which is near to a large vessel might seem enhanced for a short duration because this large vessel is between the voxel and the x-ray beam (see Figure 6.3(c)). However, it is likely to be inside a vessel, if the voxel is enhanced for the complete duration of the contrast agent injection.

(a) Undisturbed R-TIC

(b) R-TIC with foreshortening (frames 20-30 and 90-100) and overlapping vessels(frames 55-60 and frames 70-75).

(c) R-TIC for a voxel outside a vessel.
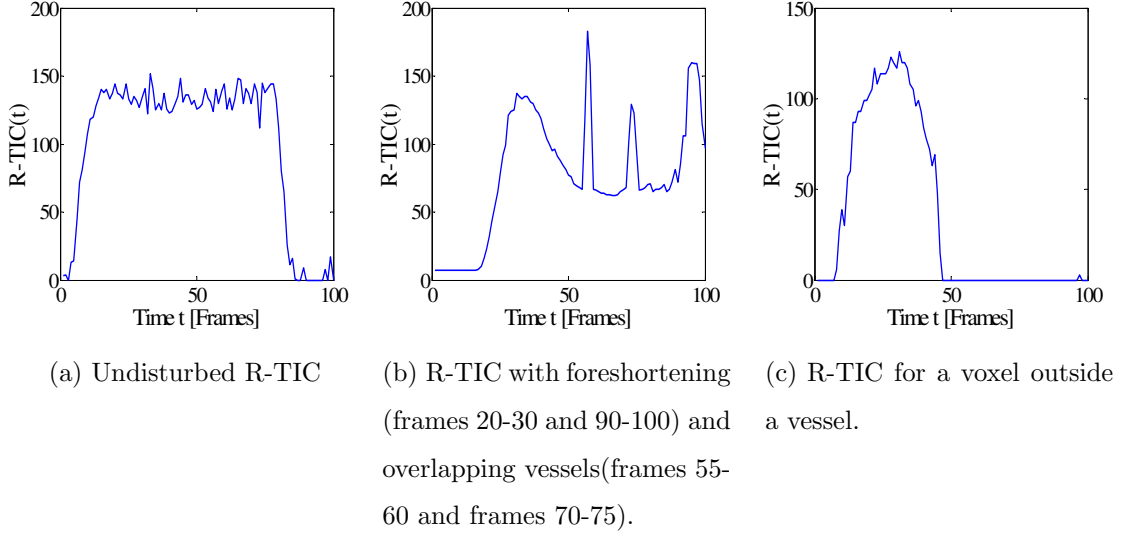
Figure 6.3: Examples of rotational time intensity curves (Waechter et al., 2008c).

(a) R-TIC inside a vessel.

(b) R-TIC outside a vessel.
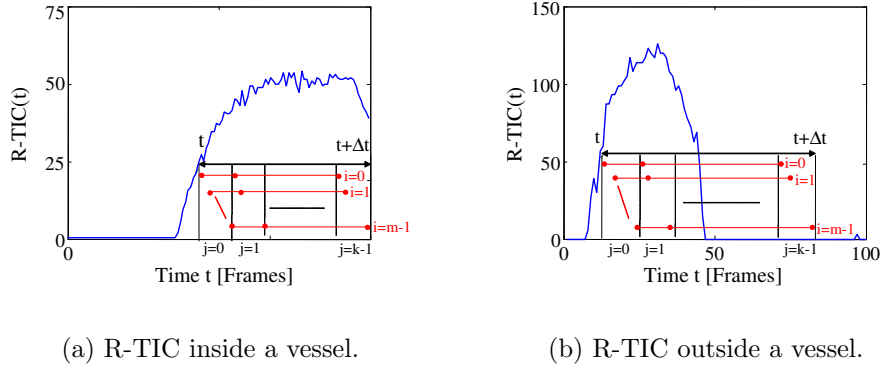
Figure 6.4: Determination of the enhancement. The interval Δt is divided in k subintervals of size m (Waechter et al., 2008c).

To achieve the emphasis on the duration, the interval $[t, t+\Delta t]$ is divided into k subintervals of size m (see Figure 6.4). Only if the R-TIC is high in each subinterval, should the enhancement be high. The enhancement over the interval $\Delta t = m \cdot k$ is then defined as:

$$\mathcal{E}_1(\mathbf{v}, t, \Delta t) = \sqrt[m]{\prod_{i=0}^{m-1} \min_{j=0}^{k-1}\{\mathcal{R}(\mathbf{v}, t+i+j \cdot m)\}}. \tag{6.2}$$

If the values of the R-TIC are low in one subinterval, all the minima are low and the overall enhancement, given by the geometric mean, will be low as well. The required duration Δt is limited by the duration of the contrast agent injection Δt_{Inj}, or by the end T of the sequence, as follows (Δt is omitted to improve readability later on):

$$\mathcal{E}_2(\mathbf{v}, t) = \begin{cases} \mathcal{E}_1(\mathbf{v}, t, \Delta t_{Inj}), & \text{if } t + \Delta t_{Inj} < T \\ \\ \mathcal{E}_1(\mathbf{v}, t, T - t), & \text{if } t + \Delta t_{Inj} \geq T. \end{cases} \tag{6.3}$$
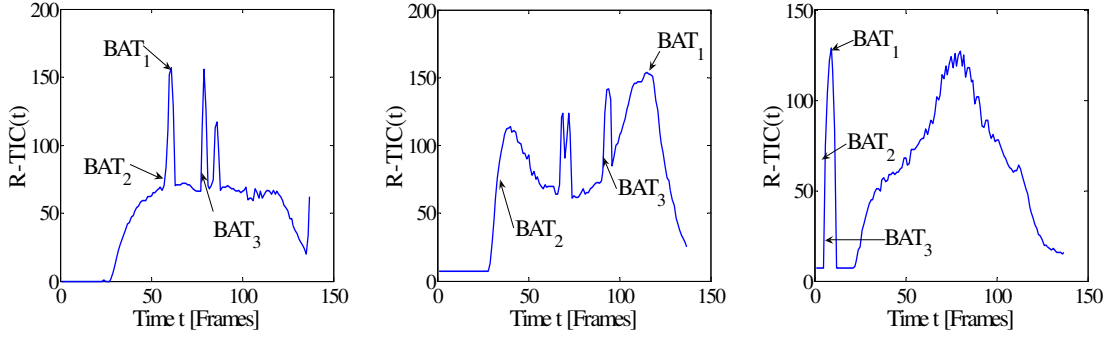
(a) R-TIC with overlapping vessels.

(b) R-TIC with foreshortening and overlapping vessels.

(c) R-TIC with an overlapping vessel before the BAT.

Figure 6.5: Examples where conventional definitions of the bolus arrival time (BAT) fail due to errors caused by the rotation of the c-arm: BAT_1: Time of peak opacification, BAT_2: Time of leading half peak opacification, BAT_3: Time of peak gradient (Waechter et al., 2008c).

If the voxel lies inside a vessel, the values of the R-TIC stay high after the arrival of the contrast agent bolus for at least the duration of the contrast agent injection. Therefore,

$$\mathcal{S}_1(\mathbf{v}) = \mathcal{E}_2(\mathbf{v}, \mathcal{A}(\mathbf{v})) \tag{6.4}$$

is a measure for the 'vesselness', where $\mathcal{A}(\mathbf{v})$ is the BAT as defined in the next section. $\mathcal{S}_1$ provides the first term of the speed function.

6.2.3 Bolus arrival time

For planar angiography, there are several definitions of BAT as explained in Section 2.6.1 of the literature review. However, because of the errors introduced into the R-TIC due to c-arm rotation, none of these definitions were found to be robust for rotational data. The problem becomes apparent when considering the examples shown in Figure 6.5 where overlapping vessels and foreshortening lead to errors in the BAT estimation using three example definitions.

The BAT criterion proposed in this thesis is a combination of three criteria and is based on the following assumptions:

1. before the BAT, the contrast agent concentration is zero;

2. around the BAT, there is a large increase of contrast agent concentration;

3. after the BAT, the contrast agent concentration stays high for a period given by the duration of the injection.

This results in the following three criteria:

1. before the BAT, the value of the R-TIC should be below a threshold s_0;

2. the first derivative of the R-TIC, denoted by $\frac{\partial \mathcal{R}}{\partial t}$, at the BAT should be large and positive;
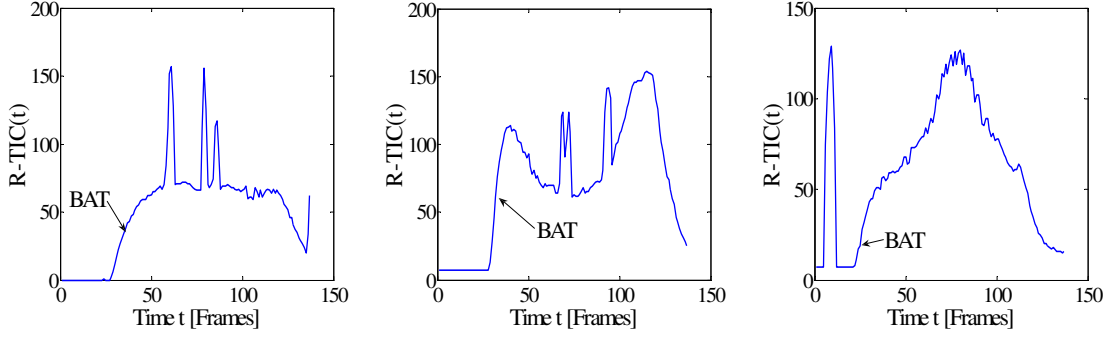
(a) R-TIC with overlapping vessels.

(b) R-TIC with foreshortening and overlapping vessels.

(c) R-TIC with an overlapping vessel before the BAT.

Figure 6.6: Bolus arrival times estimated with criterion proposed in this thesis (Waechter et al., 2008c).

3. the enhancement $\mathcal{E}_2(\mathbf{v}, t)$, as defined in Equation 6.3, after the BAT should be as large as possible.

Combining these criteria, a measure $\mathcal{V}(\mathbf{v}, t)$ of how likely it is that for voxel $\mathbf{v}$ the BAT occurs at time t can be defined as

$$\mathcal{V}(\mathbf{v}, t) = \begin{cases} \frac{\partial \mathcal{R}(\mathbf{v}, t)}{\partial t} \cdot \mathcal{E}_2(\mathbf{v}, t), \text{ if } \mathcal{R}(\mathbf{v}, t - h) < s_0 \\ \\ 0, \text{ if } \mathcal{R}(\mathbf{v}, t - h) \geq s_0, \end{cases} \tag{6.5}$$

where the threshold s_0 is determined by the noise level and h is a small time step to indicate a time before the BAT. Then, the BAT, denoted by $\mathcal{A}(\mathbf{v})$, is assumed to be the time when the value of $\mathcal{V}(\mathbf{v}, t)$ has a maximum, given by

$$\mathcal{A}(\mathbf{v}) = \arg \max_{t \in \{1:T\}} (\mathcal{V}(\mathbf{v}, t)). \tag{6.6}$$

Figure 6.6 shows the estimated BAT for the examples of Figure 6.5 in which conventional criteria from the literature fail.

The method described above makes the assumption that neighbouring voxels which belong to the same vessel must have similar BATs. As the fast marching algorithm considers voxels on a propagating wavefront, every voxel besides the seed voxel has a preceding voxel. If the current voxel, $\mathbf{v}$, belongs to the same vessel as the preceding voxel, $P(\mathbf{v})$, the absolute difference between their BATs, given by

$$\mathcal{D}(\mathbf{v}) = |\mathcal{A}(\mathbf{v}) - \mathcal{A}(P(\mathbf{v}))|, \tag{6.7}$$

should be small. The corresponding term for the speed function is given by

$$\mathcal{S}_2 = e^{-\alpha \cdot \mathcal{D}(\mathbf{v})}. \tag{6.8}$$

where α is a constant which determines how fast the speed function decreases as the difference in BAT increases.

Centerline

Minimum cost path using
simple speed function
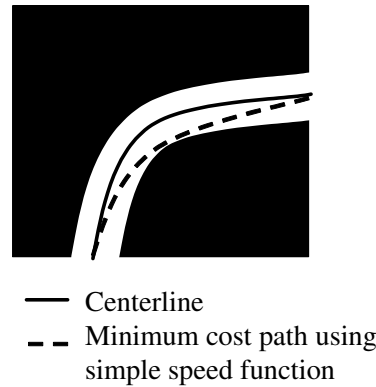
Figure 6.7: Illustration of the problem of minimum cost path extraction using a speed function which is constant inside the vessel: in this example, it can be seen that the centreline and the minimum cost path do not coincide (Waechter et al., 2008c).

This condition prevents a voxel near to a vessel with an early BAT to be assigned as a voxel inside the same vessel with a late BAT. Additionally, it allows for the so-called 'kissing vessel' problem to be addressed, since consideration of the difference in the BAT provides a means of distinguishing kissing vessels with different BATs (Tomandl et al., 1999). $\mathcal{S}_2$ provides the second term of the speed function.

6.2.4 Centring strategy and radius extraction

The terms of the speed function defined so far are more or less constant within a vessel. In areas where the speed function is constant, the minimum cost path is the path of minimum Euclidean length. For curved vessel segments, the minimum Euclidean length path does not pass through the centre of the vessel. This problem, described in detail by Deschamps (2001), is illustrated in Figure 6.7. To overcome this problem, the definition of the speed function should contain a term which penalises larger distances from the centreline.

For the method described here, a precise definition for a 3D centreline is required. As the 3D centreline is determined from the projection images, the 3D centreline definition is derived from a 2D centreline definition. The 2D centreline of a vessel in an angiographic projection image is defined such that, at any point on the centreline, the distances to both vessel edges in the direction normal to the centreline are equal (Brown et al., 1977). Based on this, the 3D centreline is defined as the path between the seed point and the end point, which results in the smallest error when projected back to the image planes and compared with the original 2D centrelines.

As all information about the vessel is contained in the projection images, for every voxel $\mathbf{v}$, the neighbourhood of the projection points $\Pi(\mathbf{v}, G(t))$ in the rotational angiography images is analysed for every i-th frame during the interval when the segment is enhanced. For every selected frame, the edge elements near to the projection point are determined and two parallel lines are fitted to the edge elements to get the 2D borders of the vessel. From this, the local
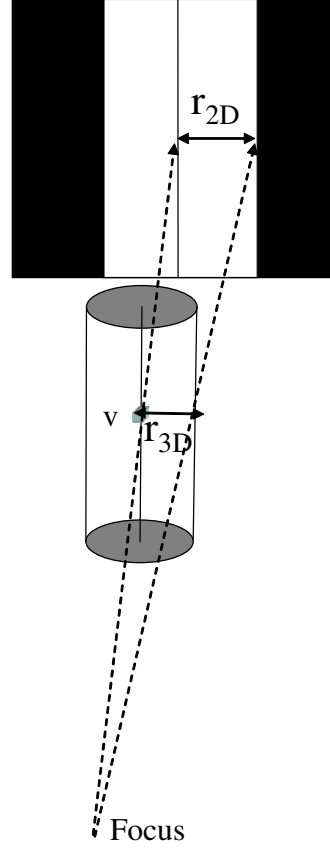
Figure 6.8: Estimation of the 3D radius from a single estimate of a 2D radius obtained from a projection image (Waechter et al., 2008c).

vessel direction, the 2D radius $R_{2D}(\mathbf{v}, t)$ and the 2D distance $D_{2D}(\mathbf{v}, t)$ of the current projection point to the centre of the vessel are determined.

From every 2D radius estimate, an estimate of the 3D radius can be calculated using information about the geometry of the c-arm system, the co-ordinates of the corresponding 3D point, and the assumption that, locally, the vessel has the shape of a cylinder. The position of the 3D point determines the magnification of the 2D radius as illustrated in Figure 6.8. The same relationship is used to estimate the 3D distance to the centreline from every 2D distance estimate. The final estimates of the 3D radius $R_{3D}(\mathbf{v})$ and the 3D distance $D_{3D}(\mathbf{v})$ are then given by the median of all estimates. The median was chosen to decrease the influence of outliers due to overlapping vessels, which might otherwise result in an overestimation of the radius in some frames.

The estimates of the 3D radius are later used to determine the local radius of the vessel for each centreline point. The 3D distance is used to define a measure of vessel centricity:

$$\mathcal{S}_3(\mathbf{v}) = e^{-\beta D_{3D}(\mathbf{v})}, \tag{6.9}$$

where β is a constant which determines how fast S_3 decreases as the 3D distance from the centre increases. S_3 provides the third term of the speed function.

6.2.5 Definition of the speed function

The speed function for the fast marching algorithm can now be defined as

$$\mathcal{S}(\mathbf{v}) = \mathcal{S}_1(\mathbf{v}) \cdot \mathcal{S}_2(\mathbf{v}) \cdot \mathcal{S}_3(\mathbf{v}), \tag{6.10}$$

where $\mathcal{S}_1$, $\mathcal{S}_2$, and $\mathcal{S}_3$ are defined in Equations 6.4, 6.8, and 6.9, respectively. Inspection of this speed function reveals that $\mathcal{S}(\mathbf{v})$ has a high value when the enhancement measure is high, its BAT is similar to the BAT of the preceding voxel, and it is near to the centre of the vessel. The results of the fast marching algorithm can then be used to determine the 3D vessel centreline as explained at the beginning of Section 6.2.

6.3 Evaluation setups and results

For the evaluation of the centreline and radius extraction method, rotational angiographic images generated by the setups described in Chapter 4 were used.

The computer simulation was used to simulate 60 volume datasets corresponding to various physiological flow conditions and injection protocols. For each, rotational angiography image acquisitions were simulated using a range of different acquisition protocols, table positions, and patient movement conditions. Up to eight rotational angiography sequences were obtained for each dataset. Overall, 420 rotational angiographic sequences were obtained. These datasets were used to analyse the influence of x-ray acquisition, blood flow, and contrast agent injection parameters. An overview of all parameters is given in Table. 6.1. In the case of the computer simulation, the ground truth centreline and radii were given by the description of the geometry.

For the experimental setup, the first anthropomorphic phantom (phantom 8, see Figure 4.8(h)) was used. First, a mask sequence (without contrast agent injection) was acquired, followed by two flow sequences with short contrast agent injections (4 s) and one sequence with a long injection (6 s). The mask sequence was used for background removal so that from each flow sequence a DSA sequence is obtained. The DSA sequences were used for the testing of the proposed algorithm and the last sequence was used to determine the ground truth centreline. As this sequence did not show inflow or outflow of contrast agent, the standard 3DRA reconstruction produced by the Allura system could be used. The ground truth was determined manually by selecting points firstly from two orthogonal projections (see Figure 6.9) of the rotational angiography sequence and secondly from the standard 3DRA reconstruction (see Figure 6.10). For each sequence and method, two manual segmentations were performed.

For each dataset from both setups, the start and end points of the vessel tree were manually selected from orthogonal views and the duration of the contrast agent injection was determined. Then, the proposed method was used to reconstruct the 3D centreline and the 3D radius at each point along the centreline. For each set of start and end points, the connecting ground truth centreline was selected. Then, for every point of each determined centreline, the absolute distance to the next point of the corresponding ground truth centreline and the absolute difference

Table 6.1: Parameters for the computer simulated rotational angiography.

Parameter	Unit	Value
Blood flow:		
Average Blood Flow	[ml/min]	100, 200, 400
Pulsatility	[]	none, medium, high
Heart Frequency	[beats/min]	60
Injection:		
Injection duration	[180/55 s]	0.5, 0.75, 1
Injection flow	[ml/s]	50,100,200
Iodine concentration	[mg/ml]	370
Acquisition:		
Tube voltage	[kV]	70
Tube current	[mA]	125, 250
Radiation time	[ms]	2.61
Max rotation (primary)	[°]	210, 305
Max Rotation (secondary)	[°]	110
Start angle	[°]	0, 90
Frame rate	[frames/s]	30
Rotation speed	[°/s]	55
Detector Size (portrait)	[mm]	300x387
Detector Size (zoom)	[mm]	160x160
Patient Movement:		
Rotation (medial axis)	[°]	0, 1
Translation	[mm]	(0,0,0), (1,1,1)
Table Position:		
Rotation	[°]	20
Translation	[mm]	(0,0,0), (0,40,0)

between the measured radius and the ground truth radius was determined. Finally, errors were averaged along the centreline.

For the datasets from the computer simulation, the overall mean absolute error of the reconstructed 3D centreline was 0.44 mm with a standard deviation of 0.11 mm. The overall mean absolute error of the reconstructed 3D radius was 0.25 mm with a standard deviation of 0.06 mm. For an example dataset, the reconstructed and ground truth radius are shown in Figure 6.11(a) and the reconstructed and ground truth centreline are shown in 6.11(b).

An overview of the influence of the flow and injection parameters is given in Figure 6.12(a) and an overview of the influence of the acquisition parameters is given in Figure 6.12(b).

It was observed that the pulsatility of blood flow had no negative influence on the results;
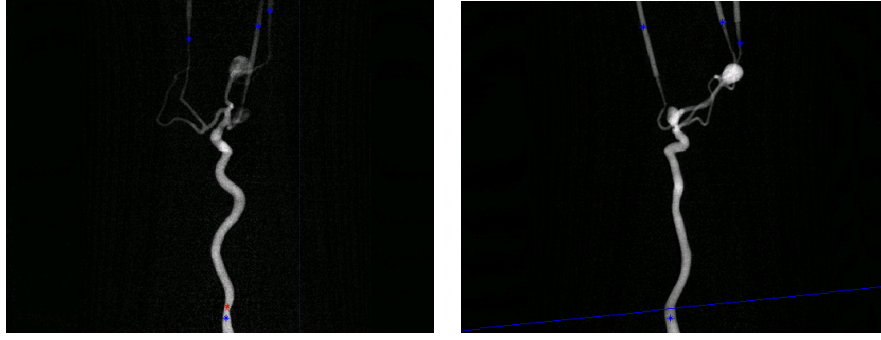
(a) Manual selection of centreline points with help of an epipolar line and given start and end points.
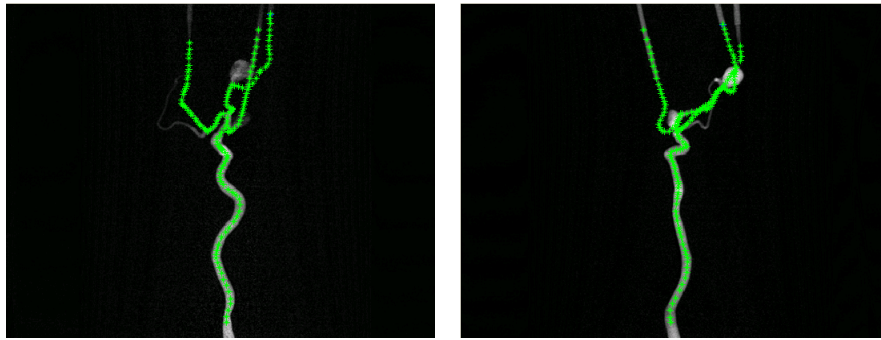
(b) Results of manual selection of centreline points.

Figure 6.9: Manual centreline selection from orthogonal projection views.
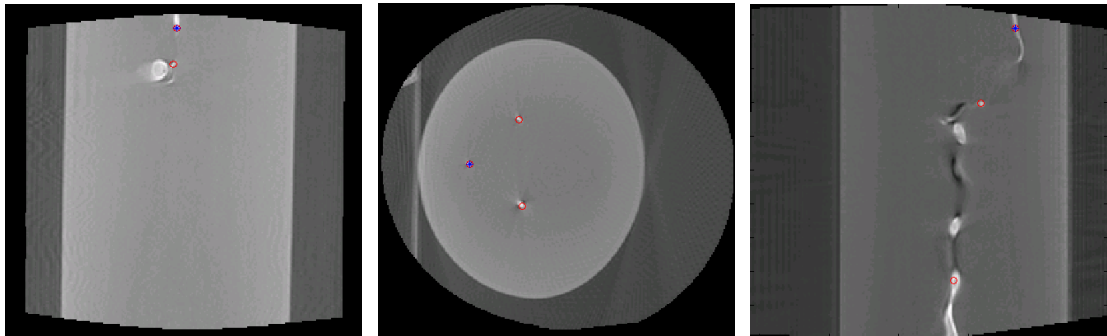
Figure 6.10: Selection of points from orthogonal slices of 3DRA volume.

on the contrary, the average error for datasets with high pulsatility was slightly lower than for datasets with steady flow.

The angular difference of the rotating system during the period in which a vessel segment contained contrast agent imposed the main influence on the quality of the reconstruction result. This period depended on the duration of the contrast agent injection and the rotation speed of the x-ray system. It was possible to perform a reconstruction if every segment was enhanced over the duration that corresponds to a rotation of $90°$, but this case had the highest error and visual inspection showed that one vessel segment was missed in some cases. Reliable results were obtained if every vessel segment was enhanced over the duration that corresponds to a rotation

of 135°. It is important to note that it was not necessary for all segments to be enhanced at the same time.

The blood flow had a similar influence as the injection duration. If the flow was higher, the complete vessel tree was enhanced earlier. This improved the results.

The signal to noise ratio decreased as the radiation time, the amperage, or the amount of contrast agent decreased. Figure 6.12 shows that the error in the radius increased slightly in these cases, but the quality of the centreline was not affected.

Subtraction artefacts due to patient motion between scans increased both errors slightly, but visual inspection showed that the segmentation was still successful. A translation of the head had a bigger influence on the result than rotation of the head. The latter artefact should happen more often in reality.

A longer rotation did not improve the results significantly as long as the injection duration was not increased as well. However, results were improved if the rotation started at 90° instead of 0°. The starting angle was most important for short injections. In the case of a injection duration that corresponds to a 90° rotation and a rotation range from 0° to 205°, the carotids overlapped each other for most of the time while they were enhanced. This was not the case for a rotation range from 90° to 295°, and the results were much better.

In most cases, the reconstruction of common carotid, internal carotid, external carotid, middle cerebral and pericallosal arteries took 60 s and the reconstruction of vertebral, basilar and anterior cerebral arteries took 40 s on a 3 GHz Xeon processor. In some cases, if the fast marching algorithm leaked, the number of analysed voxels increased and the reconstruction time went up to 120 s. This had no negative influence on the reconstruction result.

For the datasets from the experimental setup, the overall mean error of the 3D centreline localisation estimation was 0.45 mm. Figure 6.13 shows an example of the reconstructed centreline projected onto the x-ray image. The phantom contains two aneurysms. The first one did not hinder the segmentation, although it overlapped or kissed the feeding vessel in most images. The second aneurysm led to an error in the segmentation, but the manual segmentation of the vessels around this aneurysm was only possible with knowledge of the geometry as well. If the part with the second aneurysm is excluded, the mean absolute error is 0.35 mm. The mean absolute difference between a manual segmentation from orthogonal views and from the 3DRA volume was 0.33 mm after registration. The mean reconstruction time for the method was 80 s. A manual segmentation from orthogonal views took 60 min and from 3DRA volume it took 40 min.

6.4 Discussion

In this chapter, I have shown how it is possible to extract flow information and 3D vessel geometry from rotational angiography sequences that exhibit both inflow and outflow of contrast agent. The reconstruction accuracy is promising. This shows that flow information in the form of the BAT is suitable to support the vessel reconstruction algorithm. As BAT definitions from
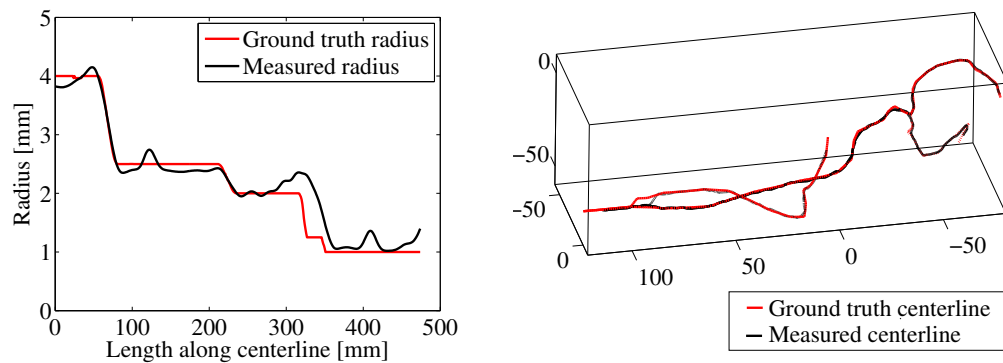
(a) Radius estimation along the centreline.

(b) 3D model of the reconstructed centreline together with the ground truth centreline.

Figure 6.11: Example results from computer simulations (Waechter et al., 2008c).

[a] Injection duration corresponds to the rotation of 180°
[b] Injection duration corresponds to the rotation of 135°
[c] Injection duration corresponds to the rotation of 90°
[d] 400 ml/min
[e] 200 ml/min
[f] Injection flow equals blood flow
[g] Injection flow is half of blood flow

[a] Standard protocol:
   voltage: 70 keV,
   amperage: 250mA,
   acquisition time: 2.61 mm,
   rotation: 0°-205°,
   no patient movement between scans
[b] As standard protocol but amperage: 125 mA
[c] As standard protocol but rotation: 90°-295°
[d] As standard protocol but patient translation between scans
[e] As standard protocol but patient rotation between scans
[f] As standard protocol but rotation: 0°-305°

(a) Influences of different flow and injection parameters on the centreline and radius error (averaged over all acquisition parameters).

(b) Influences of different acquisition protocols on the centreline and radius error (averaged over all flow and injection parameters).

Figure 6.12: Overview of influence of different parameters (Waechter et al., 2008c).
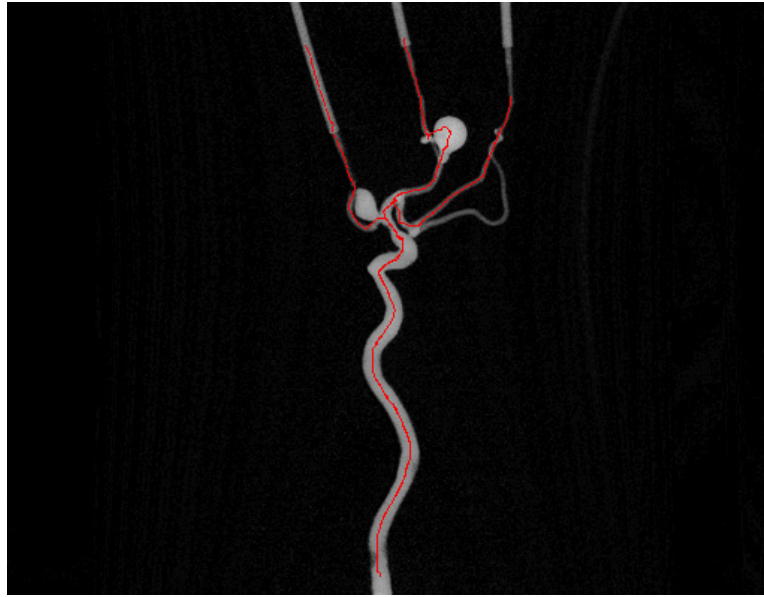
Figure 6.13: Reconstructed centreline back-projected onto the x-ray image. This image shows two examples of how the centreline could be extracted in the case of a kissing vessel. The centreline in the aneurysm is not well defined (Waechter et al., 2008c).

the literature fail in the case of rotational data because of errors due to overlapping vessels and vessel foreshortening, I have proposed a new BAT criterion, which is robust to errors introduced by the rotation of the c-arm.

The validation included all cases which could lead to problems with real patient images, i. e. stenoses; aneurysms; kissing vessels; vessels which appear overlapping in many x-ray projections; vessels pairs that are orthogonal to each other and to the rotation axis; tortuous vessels; and small vessels with a diameter down to 1.5 mm. The images obtained in this study were of similar quality as patient images, and were subject to noise, scatter and beam hardening.

One advantage of this method is that it can determine the radius of the vessel from projection images, where the edges of the vessel are better defined than in a standard 3DRA reconstruction. The existing error of the radius estimation is partly due to the fact that the radius is ill-defined at the bifurcation in the model of the computer simulation. Directly after the bifurcation, the two branches overlap (in 3D) and appear as one vessel with a larger radius. Therefore, the estimated radius increases at the bifurcation, but the ground truth radius does not increase. Figure 6.11(a) illustrates this problem. A mean error of 0.25 mm is sufficiently small as, for example, in the selection of an arterial stent, the required maximal error is about 0.5 mm. An advantage over the extraction from orthogonal views is that errors in the radius estimation when vessels overlap can be compensated for, because views from many directions are available. A further advantage is that the method needs very little user interaction compared with biplane reconstructions.

In the literature, it is stated that BAT methods are not suitable for determining volumetric

blood flow rates under pulsatile flow conditions (Shpilfoygel et al., 2000; Rhode et al., 2005). Here however, I use the flow information to support vessel reconstruction and have shown that the pulsatility does not decrease the accuracy of it.

Currently, the inflow or outflow of contrast agent present a problem for accurate vessel reconstruction from rotational angiography. In this approach, the presence of contrast agent inflow and outflow is used as a feature to aid the reconstruction. This has the following benefits: Firstly, it is not necessary that the complete vessel tree is enhanced during the complete acquisition, so the amount of required contrast agent can be reduced. This results in a lower risk due to contrast-agent toxicity for the patient. Secondly, contrast agent inflow gives extra information, which can be used to solve the kissing vessel problem. This is described in more detail in Waechter et al. (2008c). Finally, it enables the flow quantification which will be described in the next chapter.

A satisfactory reconstruction and segmentation accuracy (mean error centreline 0.5 mm, mean error radius 0.29 mm) was achieved when every vessel segment was filled with contrast agent over $135°$. As a standard c-arm can rotate $205°$, typically about one third of the acquisition can show inflow or outflow of contrast agent. This makes quantitative flow estimation feasible, since most flow information is present if inflow and possibly outflow of contrast agent is visible during the sequence.

7

Model-based flow quantification

7.1 Introduction

The quantification of blood flow from planar angiography already is a challenging task and different approaches were presented in the literature review in Section 2.6. The task becomes even more difficult for rotational angiography because of artefacts due to the rotation of the c-arm.

In this section, a method for blood flow quantification is proposed and validated which uses a model of blood flow and contrast agent transport, and employs a method to overcome problems due to rotational artefacts.

This chapter is the core part of this thesis. The proposed method uses the flow model described in Chapter 3. Images from the experimental setup described in Chapter 4 are used for the validation. The approach assumes that an attenuation calibration and a geometry calibration as described in Chapter 5 were done beforehand. Finally, it assumes that the vessel centreline and radii were determined as described in Chapter 6.

7.2 Method

Before the flow quantification, the vessel tree is divided into segments and for each segment the centreline and radii are determined. Then, for each segment, the so-called reliability map and flow map are extracted. The flow map and its characteristics were described in Section 2.6. Since the observed flow maps were extracted from an image sequence, they will be referred to as extracted flow maps.

For flow quantification, a simulated flow map is fitted to the extracted flow map. Therefore, this process is referred to as flow map fitting. The simulated flow map is generated using a model based on the physics of blood flow and contrast agent transport. During the fitting process, the optimal parameters of the model, including the blood flow waveform, and for the contrast agent injection are determined. An overview of the algorithm is given in Figure 7.1. All components are described in detail in the following sections.
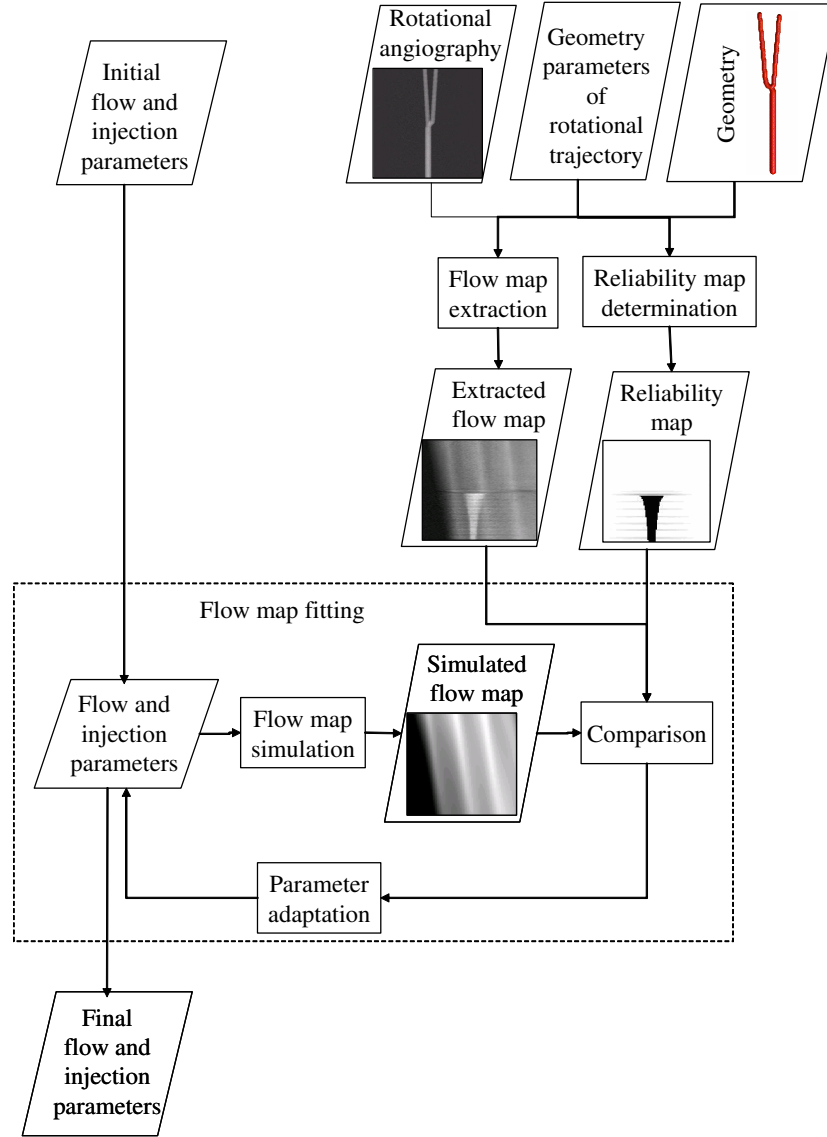
Figure 7.1: Overview of the flow map fitting algorithm.

7.2.1 Extraction of flow maps and reliability maps

The inputs for the flow quantification algorithm are rotational angiographic images which are preprocessed to give quantitative information about the density of iodine on the x-ray path. This is done by digital subtraction of a mask sequence and an attenuation calibration. A sequence consists of M preprocessed images $I(x, y, t)$, each acquired at the time steps $t \in \{t_i \mid t_i = i \cdot T_A / M, \, i \in \{1, 2, \ldots, M\}\}$ at different geometric configurations $G(t)$ of the rotating c-arm, where T_A is the duration of the image acquisition and M is the total number of images. A geometric calibration, as described in Section 5.2, is used beforehand to determine $G(t)$.

The 3D vessel centreline and radii are determined from the rotational angiographic sequence as described in Chapter 6. To initialise the geometry reconstruction, the user has to indicate the start and end point of each segment considered in the flow quantification. In the following, the segment number is indicated by the subscript j. If l represents the length along the vessel
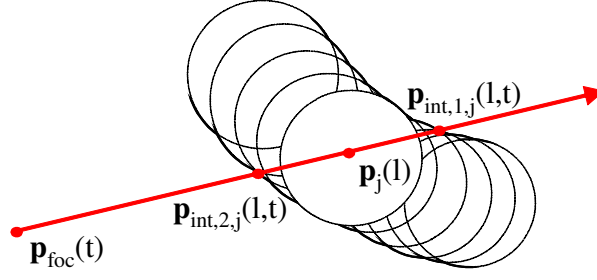
Figure 7.2: Determination of the distance map.

segment and L_j is the total length of the vessel segment, its centreline is given by a set of K_j 3D points $\mathbf{p}_j(l)$, $l \in \{l_i \,|\, l_i = i \cdot L_j/K_j, i \in \{1, 2, \ldots, K_j\}\}$ and for each point the corresponding radius is given by $R_j(l)$.

In the next step, the so-called distance map $D_j(l,t)$ is determined, which is later used for the distance-correction of the flow map. $D_j(l,t)$ gives the distance which the x-ray beam transverses through the vessel. To determine the distance map, the vessel tree is modelled by the bounding surface of a set of spheres. The centre and radii of the spheres are given by $\mathbf{p}_j(l)$ and $R_j(l)$, respectively. For each centreline point $\mathbf{p}_j(l)$ and each geometric configuration $G(t)$, the path of the x-ray beam from the focus $\mathbf{p}_{foc}(t)$ through $\mathbf{p}_j(l)$ is determined. Then, the nearest intersection points $\mathbf{p}_{int,1,j}(l,t)$ and $\mathbf{p}_{int,2,j}(l,t)$ of the x-ray beam and the vessel tree represented by the set of spheres are determined. This is illustrated in Figure 7.2. As $\mathbf{p}_j(l)$ lies in the centre of one of the spheres, two intersection points must exist. The distance map is then given by

$$D_j(l,t) = \|\mathbf{p}_{int,1,j}(l,t) - \mathbf{p}_{int,2,j}(l,t)\|. \tag{7.1}$$

To avoid discretisation errors the sampling of the centreline points is increased for the determination of the distance map.

Now, the flow map can be determined. The uncorrected flow map (F_U) of the segment j is given by the image intensities at the projection points of all centreline points as expressed by

$$F_{U,j}(l,t) = I(\Pi(\mathbf{p}_j(l), G(t)), t), \tag{7.2}$$

where $\Pi(\mathbf{v}, G(t))$ is the projection function as defined in Section 5.2.3. The extracted flow map (F_E) of the segment j is given after distance-correction by

$$F_{E,j}(l,t) = \frac{I(\Pi(\mathbf{p}_j(l), G(t)), t)}{D_j(l,t)}. \tag{7.3}$$

If an attenuation calibration has been done beforehand, the image intensities give the line integral of the iodine density. After division by the respective entries of the distance map, the flow map contains quantitative information about the spatial and temporal progression of the mean density of iodine in the vessel. The mean is determined across a line through the centre of the vessel. Without an attenuation calibration, the flow map contains information about the mean attenuation of the vessel.
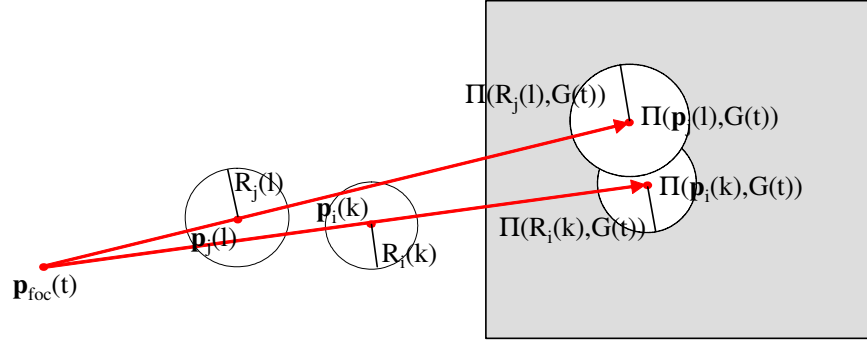
Figure 7.3: Determination of the reliability map, example for $R_{F,j}(l,t) = 0$.

The last prerequisite step of the flow quantification is the determination of a reliability map. The reliability map gives the reliability of each entry of the flow map. Due to the rotation of the c-arm, two artefacts can occur in the flow map: artefacts due to foreshortening and artefacts due to overlapping vessels (Chen et al., 2002). In addition to that, subtraction artefacts due to motion between the CA scan and the mask scan can occur. The first two can be detected automatically. The reliability map is defined as follows:

$$R_{F,j}(l,t) = \begin{cases} 0 & \text{, if overlap or foreshortening is detected} \\ 0 & \text{, if indicated by the user} \\ 1 & \text{, otherwise,} \end{cases} \tag{7.4}$$

where the condition for overlap or foreshortening is satisfied if and only if the following is true

$$\begin{aligned} \exists i,k : \qquad\qquad |\mathbf{p}_j(l) - \mathbf{p}_i(k)| &> a \cdot (R_j(l) + R_i(k)) \quad \wedge \\ |\Pi(\mathbf{p}_j(l), G(t)) - \Pi(\mathbf{p}_i(k), G(t))| &< b \cdot (\Pi(R_j(l), G(t)) + \Pi(R_i(k), G(t))), \end{aligned} \tag{7.5}$$

where $\Pi(R(l), G(t))$ gives the projected length of the radius, and a and b are scalar parameters. When $a = b = 1$, overlap or foreshortening is detected for the centreline point $\mathbf{p}_i(l)$, if another centreline point $\mathbf{p}_i(k)$ exists which is further away than the sum of the radii (first condition of Equation 7.5) but its projection point is nearer than the sum of the projected radii (second condition of Equation 7.5). An illustration of this is shown in Figure 7.3. For $a = b = 1$, most entries in the flow map would be unreliable as both conditions would be true for most neighbouring centreline points. The lower the value of b and the higher the value of a is, the more entries are marked as reliable. Reasonable choices for a and b were found empirically to be $a \in [1.1, 1.5]$ and $b \in [0.6, 0.9]$.

7.2.2 Simulation of flow maps

The blood flow and contrast agent propagation model from Chapter 3 gives the spatial and temporal distribution of the contrast agent concentration $C_j(r, l, t)$. The required geometric description of the vessel tree can be determined from the centreline and radius representation of the vessel tree. The other input parameters are either determined from the protocol (for example, the frame rate or the maximum injection flow), from the literature (such as the diffu-

sion coefficient), or they are estimated during the fitting process (for example, the blood flow parameters).

The simulated flow map $F_{S,j}(l,t)$ for segment j can be determined from its concentration map $C_j(r,l,t)$ by

$$F_{S,j}(l,t) = \rho_I \cdot \sum_{n=1}^{N} C_j(r_n,l,t), \tag{7.6}$$

where ρ_I is the density of iodine in the contrast agent. All flow maps of one vessel tree are denoted by F_S. The simulated flow maps can then be used for the flow map fitting.

7.2.3 Flow map fitting

For the flow map fitting, the simulated flow maps F_S are fitted to the extracted flow maps F_E. The appearance of the simulated flow maps is determined by the different flow parameters. The flow parameters which give the best fit are assumed to approximate the flow in the blood vessel.

The vector of all variable flow parameters is denoted by $\mathbf{q}$ and the flow maps which are simulated using these parameters are denoted by $F_S(\mathbf{q})$. The flow map fitting can then be posed as an optimisation problem:

$$\min_{\mathbf{q} \in \mathbb{R}^n} E(F_S(\mathbf{q})), \ \mathbf{q}_l \leq \mathbf{q} \leq \mathbf{q}_u \tag{7.7}$$

where $E(F_S(\mathbf{q}))$ is the error measure and the vectors $\mathbf{q}_l$ and $\mathbf{q}_u$ contain the lower and upper bounds of the variables within $\mathbf{q}$. The error measure is a dissimilarity measure between the flow maps that were simulated with the parameters $\mathbf{q}$ and the extracted flow maps, and is given by

$$E(F_S(\mathbf{q})) = \sum_{j=1}^{J} \sum_{l=l_1}^{L_j} \sum_{t=t_1}^{T_A} [a \cdot E1_j(l,t) + b \cdot E2_j(l,t)] \cdot R_{F,j}(l,t), \tag{7.8}$$

with

$$E1_j(l,t) = [f \cdot F_{S,j}(l,t) - F_{E,j}(l,t)]^2, \tag{7.9}$$

$$E2_j(l,t) = \left[\frac{\partial}{\partial t}(f \cdot F_{S,j}(l,t)) - \frac{\partial}{\partial t}(F_{E,j}(l,t)) \right]^2, \tag{7.10}$$

where a and b are weighting factors, which are normally set to one, and f is the attenuation calibration factor. The reliability map R serves the purpose of excluding potentially corrupted values from the error computation.

The attenuation calibration factor relates the intensities in the simulated flow maps to the intensities in the extracted flow maps. It can be determined at every step of the fitting process by

$$f = \frac{P_{90}(F_E)}{P_{90}(F_S)}, \tag{7.11}$$

where P_{90} is the 90th percentile of all values within the flow map. The mean or the median cannot be used for the following reason: During the first iterations of the flow map fitting, the start and duration of the injection might not be correct. This would lead to a substantial difference in the number of entries in the flow map where the concentration is zero. This introduces a difference in the mean and therefore an error in the determination of the attenuation calibration factor,

which can prevent convergence of the flow map fitting. Without noise the maximum of both flow maps could be used to determine the attenuation calibration factor. The 90th percentile was used as a compromise in the effort to reduce the influence of noise and to reduce the influence of a different quantity of zero-elements. If an attenuation calibration was done beforehand, f can be set to one.

Different configurations for the error function were evaluated at the beginning of this work. It was found that using the differences of the temporal gradients in addition to the differences of both flow maps, improved the convergence of the flow map fitting. Using the spatial gradients of both flow maps did not improve the flow map fitting. The reason for this probably is that the spatial gradients are much smaller than the temporal gradient. This is apparent in Figure 2.10.

This optimisation problem has the following properties: The error measure is a multi-variable, non-linear, and reasonably smooth function and the variables are subject to bounds. As it is reasonably smooth, a derivative-based approach is possible. Normally, the error measure would consist of two equations per entry of the flow map (see Equation 7.9 and 7.10). This would lead to a heavily overdetermined optimisation. With the formulation in Equation 7.8, the best fit in the least squares sense is searched for.

For this work, the Matlab optimisation toolbox (Matlab R2007a, The Mathworks Ltd, Cambridge, UK) was available. Of the optimisation algorithms provided by this toolbox, only one algorithm is applicable for a problem with the properties described above. The used algorithm is the subspace trust region method which is based on the interior-reflective Newton method described by Coleman and Li (1994, 1996).

Besides the fact that an implementation of this optimisation algorithm was readily available, further advantages are the following (Coleman and Li, 1994): the number of iterations grows very slowly when the number of variables is increased, a special line search technique is used to accelerate convergence, and all iterates are strictly within the bounds. The first two are important as each evaluation is computationally expensive. The last is important as for some variables the simulation of the flow map is not possible when these have values outside the bounds.

The result of the flow map fitting are the different flow parameters $\mathbf{q}$ and in particular, the waveform parameters α, β, γ, and δ and the mean volumetric flow rate $\overline{Q_b}$.

7.3 Evaluation setups and results

The proposed method was evaluated using flow maps from rotational angiographic images obtained from phantom experiments and using simulated flow maps. The experimental setup was described in Chapter 4. For each dataset, the flow map and reliability map were determined as explained above. The simulated flow maps were determined as explained in Section 7.2.2, but with small variations in the model as explained in Section 3.7. The values of the reliability map are set equal to one for all entries in this case.

7.3.1 Evaluation setups

In the basic configuration of the flow map fitting, the mean volumetric flow rate $\overline{Q}_B$, the baseline flow parameter α, the waveform shape parameters β, γ, δ, the flow profile parameter k, the start of the injection T_S, the duration of the injection T_D, and the lag time of the injection T_L are estimated.

The following parameters were assumed to be known: the start time of the cardiac cycle, the duration T_H of the cardiac cycle, the maximum flow of injection $\widetilde{Q}_I$, the diffusion constant D, the resistance factor m, the density of iodine in contrast agent ρ_I, the duration of acquisition T_A, the total number of images M and the distance between the injection site and the first observation point.

For all of the unknown parameters, an initial value and lower and upper limits were set. Table 7.3.1 shows for all relevant parameters either their initial values and their limits or in the case of known values their fixed values. The mean flow was initialised at half of its ground truth value and the waveform parameters were initialised with the parameters of a non-warped cosine-function (more precisely $2 + \cos$). In the case of the flow map from the experimental setup, the duration and maximum flow of the injection were determined from the display of the injector. In the case of the simulated flow maps, this information is given by the input of the simulation.

To support the flow map fitting, additional information can be used. Two possible ways will be evaluated here: The first one is to set the attenuation calibration factor to a fixed value and the second one is to set some parameters from the flow model to a fixed value and to exclude them from the optimisation. Three different configurations were used as follows:

- The basic configuration as described above. This will be referred to as 'no constraints'.

- The start time of the injection was fixed. The time was determined from the EMF signal. This will be referred to as 'fixed injection'.

- The attenuation calibration factor was set to 1. This configuration is only possible if an attenuation calibration has been done beforehand and the images were preprocessed accordingly. This will be referred to as 'fixed calibration'.

The setup with fixed injection and fixed attenuation calibration gave the same results as the setup that used only a fixed calibration (Waechter et al., 2008b). Therefore, the results for this setup are not shown here.

All flow maps were used to determine the mean volumetric flow rate and the flow waveform using the flow map fitting method. The resulting flow estimates of the method were compared to the ground truth flow. In cases where flow maps were determined from images from the experimental setup, the ground truth was given by the EMF. In the cases of simulated flow maps, the ground truth was given by the input of the simulation. The relative error of the mean

	Symbol	Value	Initial value	Lower limit	Upper limit	Unit
Acquisition						
Number of images	M	120				[]
Duration	T_A	4				[s]
Injection						
Max flow	$\widetilde{Q}_I$	a.t.s.				[ml/min]
Start	T_S		-0.5	-1	1	[s]
Duration	T_D		a.t.s.	1	4	[s]
Lag time	T_L		0.2	0.1	0.7	[s]
Density iodine	ρ_I	a.t.s.				[mg/ml]
Diffusion	D	10^{-6}				[m^2/s]
Resistance factor	m	1				[]
Blood flow						
Mean flow	$\widehat{Q}_B$		a.t.s.	50	400	[ml/min]
Baseline flow	α		2	1.2	5	[]
Shape parameter	β		0.5	0.5	0.9	[]
Shape parameter	γ		0.25	0.01	0.49	[]
Shape parameter	δ		0.25	0.01	0.49	[]
Duration cardiac cycle	T_H	0.8				[s]
Flow profile	k		5	2	10	[]
Algorithm						
Number of laminae	N	10				[]
Weighting parameter	a	1				[]
Weighting parameter	b	1				[]

Table 7.1: Parameters used in the flow model for flow map fitting. Depending on the way the flow map fitting uses the parameter, the actual value or the initial value and its limits are given. a.t.s. means 'according to setup'. All parameters were explained in Chapter 3.

volumetric flow rate is given by

$$E_M(Q_{B,Est}) = \frac{\overline{Q}_{B,Est} - \overline{Q}_{B,GT}}{\overline{Q}_{B,GT}}, \qquad (7.12)$$

and the relative error of the instantaneous volumetric flow rate is given by

$$E_W(Q_{B,Est}) = \sqrt{\frac{1}{M} \sum_{m=1}^{M} \left(\frac{Q_{B,Est}(t_m) - Q_{B,GT}(t_m)}{\overline{Q}_{B,GT}} \right)^2} \qquad (7.13)$$

where $Q_{B,Est}$ is the estimated volumetric flow rate and $Q_{B,GT}$ is the ground truth volumetric flow rate. Hereafter, $E_M(Q_{B,Est})$, and $E_W(Q_{B,Est})$ are referred to as mean flow error and waveform error, respectively.

In the evaluation below, different properties are analysed and all error measurements from one category (one noise level, one length, one configuration of the flow map fitting) are averaged over all datasets and expressed as a percentage. As the mean flow error is signed, averaging only gives information about an estimation bias. The variability of the estimation is expressed by the standard deviation. The waveform error gives information about how well the shape of the waveform is approximated.

7.3.2 Evaluation using computer simulation

The evaluations with flow maps from the computer simulation were carried out before the evaluation of the data from the phantom experiments to ensure under known conditions that the flow map fitting can give appropriate results. Although more issues were evaluated (see Waechter et al. (2008a)), mainly the ones which were difficult or impossible to repeat with phantom experiments are discussed below.

In the following, the default setup is given by the following baseline experiment: Flow maps were generated using all four example waveforms shown in Figure 3.7, a constant flow profile and the example parameters shown in Table 7.2. The acquisition parameters were chosen to reflect those that might be chosen for a clinical protocol and the flow parameters represent typical patient values. A moderate level of noise was added to the flow maps (PSNR levels 21.0 dB or 18.0 dB). These flow maps were used as extracted flow maps during the validation.

	Symbol	Value	Unit
Acquisition			
Number of images	M	120	[]
Duration	T_A	4	[s]
Injection			
Max flow	$\widetilde{Q}_I$	[50, 100, 150]	[ml/min]
Start	T_S	0	[s]
Duration	T_D	3	[s]
Lag time	T_L	0.1	[s]
Density of iodine in contrast agent	ρ_I	300	[mg/ml]
Diffusion	D	10^{-6}	[m^2/s]
Resistance factor	m	1	[]
Flow			
Mean flow	$\overline{Q}_B$	100, 200, 300	[ml/min]
Duration of heart cycle	T_H	0.8	[s]
Flow profile	k	2, 5, 10	[]
Algorithm			
Number of laminae	N	10	[]

Table 7.2: Parameters used in the flow model for simulation of flow maps for validation. All parameters were explained in Chapter 3.

Analysis of error function

In the first part of the evaluation of
the flow map fitting method, the er-
ror function was analysed. One of the
simulated flow maps was used as the
extracted flow map. This flow map
was simulated with a mean flow of
$\overline{Q}_B = 200$ ml/min and with a flow
profile of $k = 5$. The error function
was evaluated for different values of the
mean flow and the flow profile. First,
the attenuation calibration factor was
fixed then it was flexible. All other
parameters were hold at the optimal
value.

The shape of the error function de-
pends on the configuration of the flow
map fitting. If the attenuation calibra-
tion factor is fixed, the error function
is much steeper compared to the case
when it is flexible. Examples for both
cases are shown in Figure 7.4. Fixing
the injection does not change the error
function; it only reduces the number of
variables which are optimised. In case
of the flexible calibration, the value of
the mean flow which gives the best fit
depends on the value of the flow pro-
file. The reason for this is that the flow
appears to be faster if the flow profile
is more parabolic.
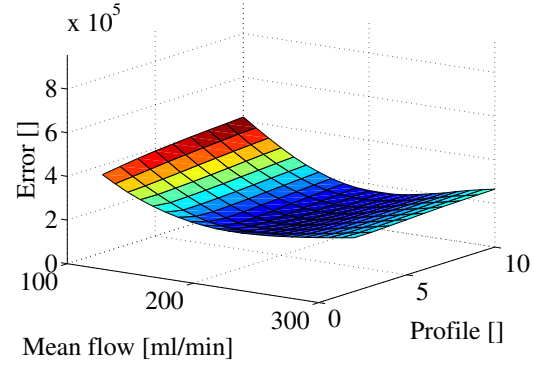
(a) Flexible Calibration.
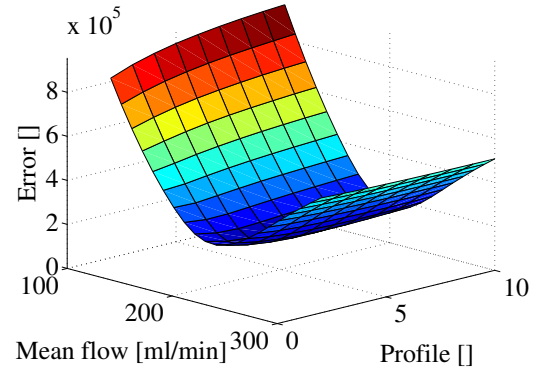
(b) Fixed Calibration.

Figure 7.4: Plots of error function.

Waveform model

In Section 3.2 and 3.7, three different waveform models were described: the 2-parameter warped cosine model, the 4-parameter warped cosine model, and the Laplace model. The goal of this experiment was to find the waveform model which is best suited to be used during the flow fitting. A model with fewer parameters, will reduce the degrees of freedom during the optimisation, while a more complex model might be able to represent the waveform more accurately.

Flow maps were generated using the default configuration with all four waveforms. Then, the flow map fitting with fixed calibration was applied using all three waveform models. In addition, all three waveform models were fitted directly to the waveforms for comparison. For all cases, the waveform error was determined.

An overview of the results is given in Figure 7.5. In general, the errors of the direct fit were only slightly lower than the errors of the flow map fitting. In both cases, the errors strongly depended on the waveform and the waveform model. The 2-parameter warped cosine model only gave good results for the simple (1st) waveform. Overall, the 4-parameter warped cosine model gave lowest errors. In the following, only this waveform model is used.
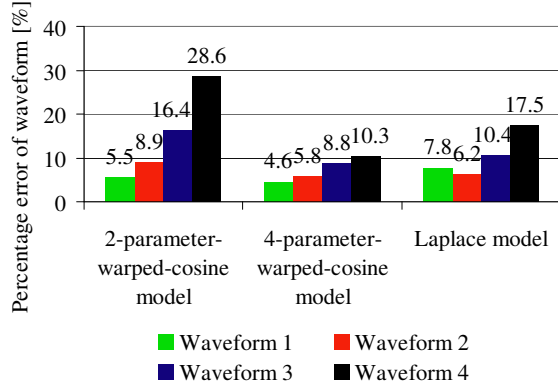
(a) Flow map fitting.
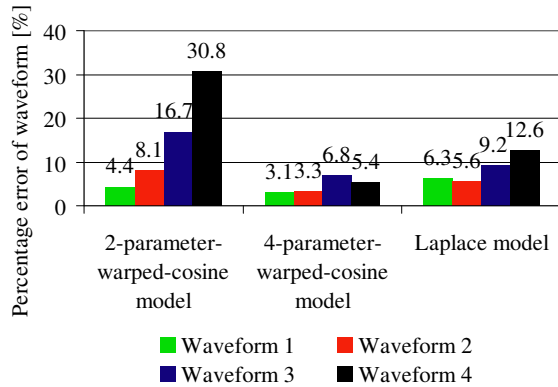
(b) Direct fit.

Figure 7.5: Influences of the waveform model.

Womersley profile

For pulsatile flow, the flow profile is
also varying with time. My flow model
ignores these variations. The goal of
this experiment was to evaluate the in-
fluence of this simplification.

Flow maps were generated with a
time dependent flow profile according
to the Womersley solution (see Sec-
tion 3.7.3). The Womersley number
was varied using the values 0.5, 1, 2, 4,
and 8. Then, the flow map fitting with
fixed calibration was applied. The av-
erage error of the waveform was deter-
mined for each example waveform and
for each value of the Womersley num-
ber.

All results are presented in Fig-
ure 7.6. In Figure 7.6(a) the results
are compared to the results which were
obtained using a steady profile. For
the first two waveform examples (which
were less pulsatile), the introduction
of the Womersley profile had almost
no influence on the results. For the
third and the fourth, the errors were in-
creased. In these cases, the changes of
the Womersley profile with time were
more apparent. In Figure 7.6(b) the re-
sults are shown for the different Wom-
ersley numbers. Surprisingly, the er-
rors did not increase as the Womersley
number increased.
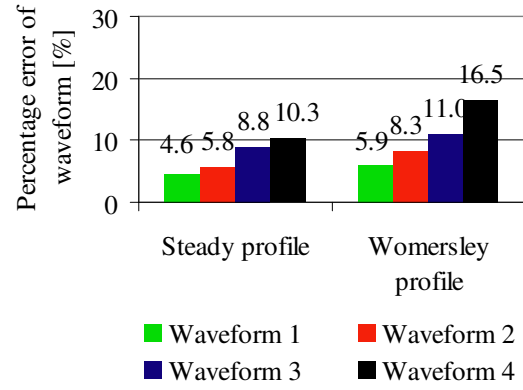
(a) Influence of waveform shape.
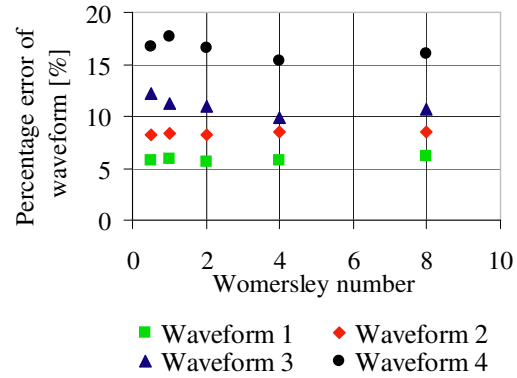
(b) Influence of Womersley number.

Figure 7.6: Influences of the Womersley profile.

Contrast agent distribution at injection site

It is not known how the contrast agent is distributed over the vessel cross section at the injection site. My flow model assumes that the contrast agent is initially distributed uniformly over the vessel cross section. The goal of this experiment is to determine the impact of this assumption if the mixing is not uniform at the injection site.

 Flow maps were generated with a varying distributions of contrast agent at the injection site. The injection profile constant k was set to 0, 0.25, 0.5, 0.75, and 1.0 (see Section 3.7.4). Also the molecular diffusion coefficient was varied ($D = 10^{-6}$, $D = 10^{-7}$). Then, the different configurations of the flow map fitting were applied. The mean flow error was averaged for each injection profile constant and each diffusion coefficient.

 In the 'Fixed injection' case, the non-uniform concentration introduced a positive bias. For a higher value of the injection profile constant, the concentration in the central laminae, where the velocities are higher, increases. Therefore, the flow appears to be higher. In the 'Fixed calibration' case, the non-uniform concentration at the injection site introduced a negative bias. This could be explained by the following: The values of the flow map are averaged along the centreline and each lamina is weighted equally. The laminae have the same thickness but not the same volume. That is why the concentrations in the flow map increase, when the injection profile constant is increased. In the fixed calibration mode, higher concentrations correspond to a lower flow.
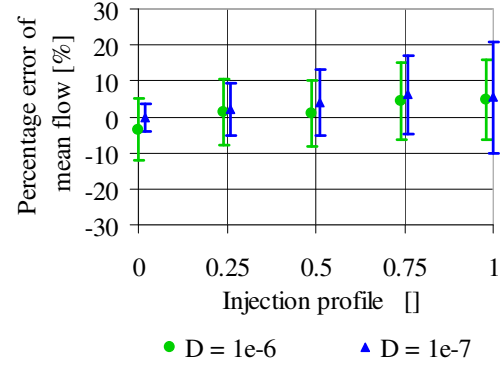
(a) No constraints.
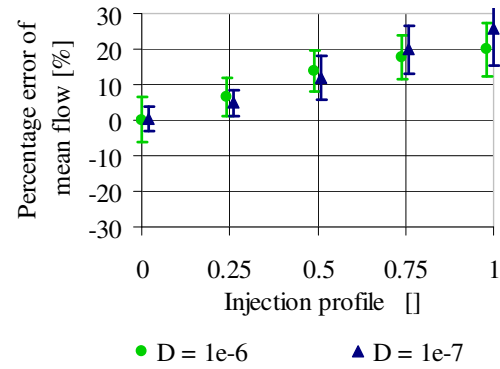
(b) Fixed injection.
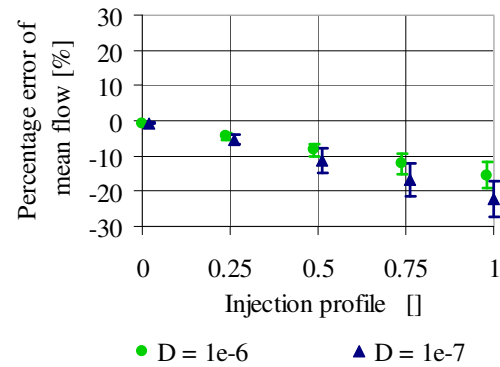
(c) Fixed calibration.

Figure 7.7: Influences of contrast agent distribution at injection site.

Frame rate

The blood is moving very fast. There-
fore, a high frame rate is required
for most flow quantification methods.
The higher the frame rate, the smaller
is the contrast agent's shift between
consecutive frames and the better the
kinematic information can be extracted
from the sequence. This experiment
analyses the impact of the frame rate
on the flow map fitting method.

Flow maps were generated with
varying frame rates using 15 fps, 30 fps,
45 fps, 60 fps. Then, all three config-
urations of the flow map fitting were
applied. For each frame rate and
each configuration the results were av-
eraged.

In case of flow map fitting with-
out constraints, the frame rate of the
acquisition had an important influence
on the results. The higher the frame
rate, the more accurate was the flow
map fitting: The bias and the variabil-
ity of the mean flow and the waveform
error decreased. For the flow map fit-
ting with fixed injection, increasing the
frame rate also improved the accuracy.
In case of fixed calibration, the frame
rate had almost no influence. All re-
sults are shown in Figure 7.8.
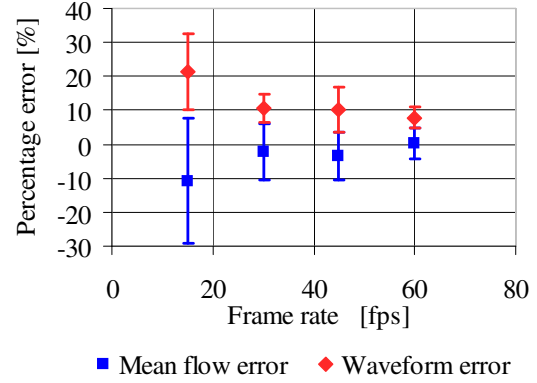
(a) No constraints.
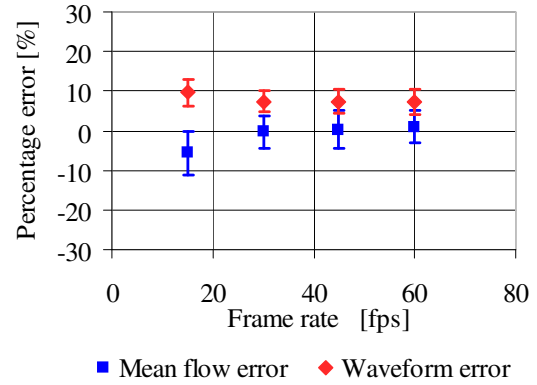
(b) Fixed injection.
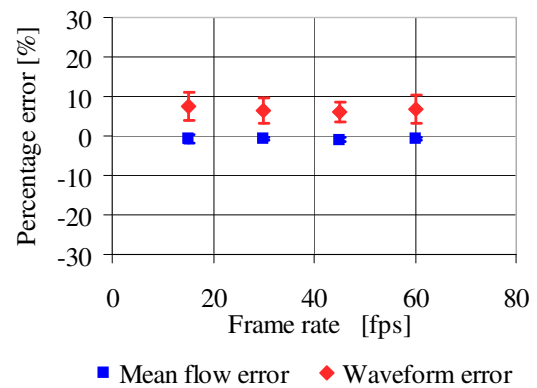
(c) Fixed calibration.

Figure 7.8: Influence of frame rate.

Sensitivity to noise

A problem with previously proposed methods, in particular optical flow methods, is that they are sensitive to noise. The following experiment was conducted to evaluate the influence of noise on the flow map fitting method.

Flow maps were generated as described above and different levels of Gaussian noise were added. The noise level is quantified using the peak signal to noise ratio (PSNR) given by

$$\text{PSNR} = 10 \cdot \log \left(\frac{\text{MAX}^2}{\text{MSE}} \right), \quad (7.14)$$

where MAX is the maximum intensity of the simulated flow map and MSE is the mean squared error of the flow map with additional noise compared to the original flow map. PSNR levels were determined to be ∞, 27 dB, 21 dB, 17 dB, and 14 dB. The noise level in a real flow map should be in the covered range. It depends on the ratio of the injection flow to the flow in the circulation, on the amperage of the x-ray tube, on the diameter of the vessel and on the thickness of the surrounding material.

The results are presented in Figure 7.9. For the flow map fitting without constraints, the variability of the mean flow estimates and the waveform error increase substantially as the PSNR is decreased. This is also observed for the flow map fitting with fixed injection, but to a lesser extent. For the flow map fitting with fixed calibration, the noise had almost no influence on the accuracy.
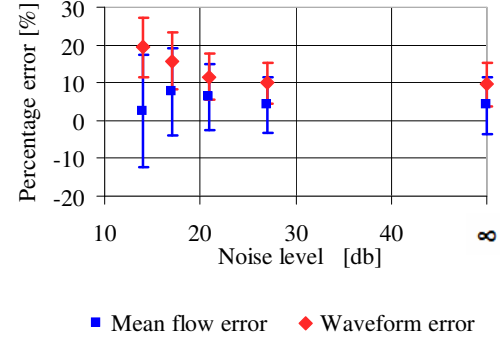
(a) No constraints.
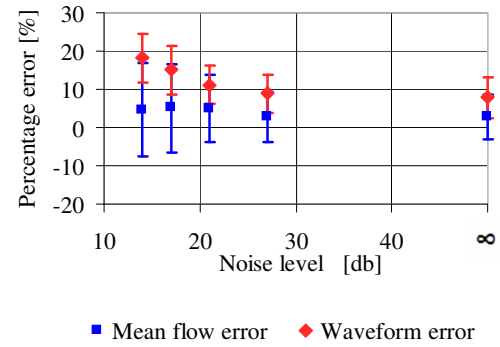
(b) Fixed injection.
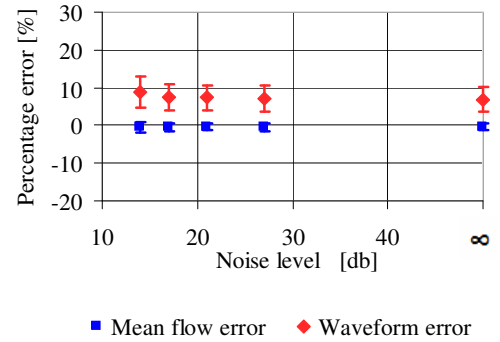
(c) Fixed calibration.

Figure 7.9: Influence of different noise levels.

7.3.3 Evaluation with straight, tubular parts of phantoms

For the experiments in this section, data from the straight tube phantom and data from the straight part of the bifurcation phantoms were used. This resulted in 28 datasets in total. The experiments were conducted for the following reasons:

- to estimate the overall accuracy of the flow map fitting;

- to evaluate the differences between the three configurations of the flow map fitting;

- to analyse the influence of the length of the flow map;

- and to find out whether the inflow phase has to be visible in the sequence.

For the first experiment, all 28 datasets were used. All three configurations of the flow map fitting were applied and for each configuration the averaged errors were determined.

Figure 7.10 gives an overview of the results. Detailed results are presented in Appendix A.2. The configurations of the algorithm with constraints gave better results than the configuration without constraints. The flow map fitting with fixed injection gave the smallest bias, but the overall accuracy was similar for both configurations with constraints. Examples of typical results and the corresponding errors are shown in Figure 7.11.
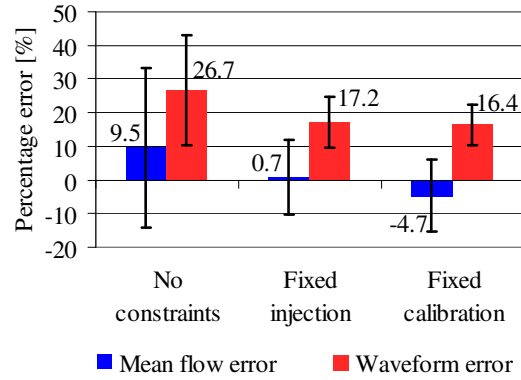
Figure 7.10: Overview of results.

(a) Mean flow error 4%, waveform error 5%.

(b) Mean flow error 9%, waveform error 9%.

(c) Mean flow error 2%, waveform error 15%.
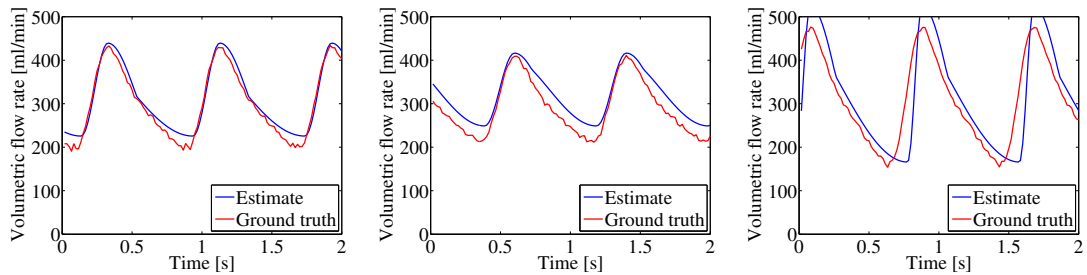
Figure 7.11: Examples of results (Waechter et al., 2008b).

Length of flow map

A further problem with previously pro-
posed methods is that they require long
vessel segments. This may especially
be a limitation in the clinical setup
where the patient's vessel tree bifur-
cates rapidly in many regions. The
following experiment was conducted to
evaluate the influence of the length of
the flow map on the flow map fitting
method.

For these experiments only a lim-
ited length of the flow maps were used.
The shortest of the flow maps was 8 cm
long. Therefore, segments of the fol-
lowing lengths were used: 1 cm, 2 cm,
4 cm, 6 cm, and 8 cm. For many ves-
sels of a patient, the length would lie
within this range. Results were aver-
aged for each segment length and for
each configuration of the flow map fit-
ting algorithm.

The results are presented in Fig-
ure 7.12. For the flow map fitting with-
out additional constraints, a negative
bias was introduced as the length of the
flow map decreased. For the flow map
fitting with fixed injection, the variabil-
ity of the mean flow estimate increased
only moderately as the length was de-
creased. For the flow map fitting with
fixed calibration, the errors were not
influenced.
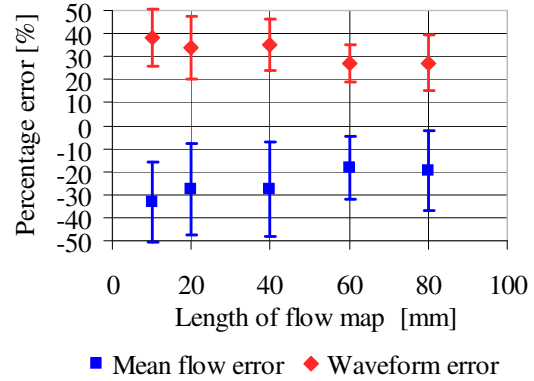
(a) No constraints.
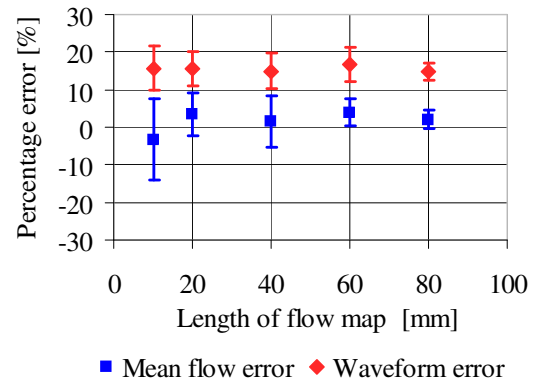
(b) Fixed injection.
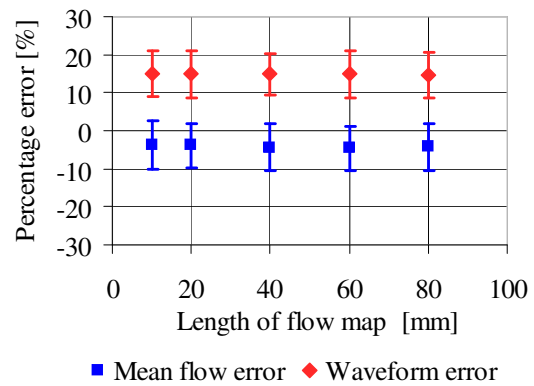
(c) Fixed calibration.

Figure 7.12: Influence of flow map length.

Visibility of the inflow phase

The part of the flow information which is directly visible to the human observer is contained in the inflow phase. One can see how fast the contrast agent fills the vessel. However, if the rotational angiographic sequence should also be used for volume reconstruction, it is beneficial if the injection is timed in a way that no inflow is visible in the sequence. In this experiment, I analyse how the results of the different versions of the flow map fitting method change if the inflow phase is not visible or only part of the inflow phase is visible in the sequence.

For this experiment, the first 0 frames, 10 frames, 20 frames, or 30 frames were removed from the flow maps. When 30 frames were removed, the inflow phase was removed from all datasets. Results are averaged for each start time and for each configuration of the flow map fitting.

The results are presented in Figure 7.13. For the flow map fitting without additional constraints, the errors changed only slightly and no trend is recognizable. For the flow map fitting with fixed injection, the waveform errors and the variability of the mean flow rose to the same level as in the flow map fitting without additional constraints when the inflow phase is not visible. For the flow map fitting with fixed calibration, the errors were not influenced.
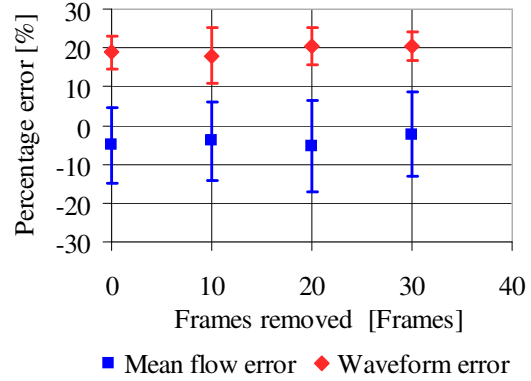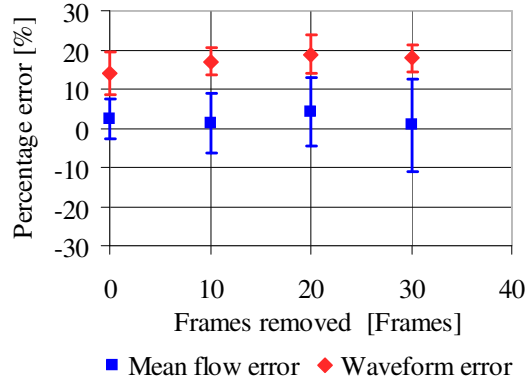
(a) No constraints.

(b) Fixed injection.
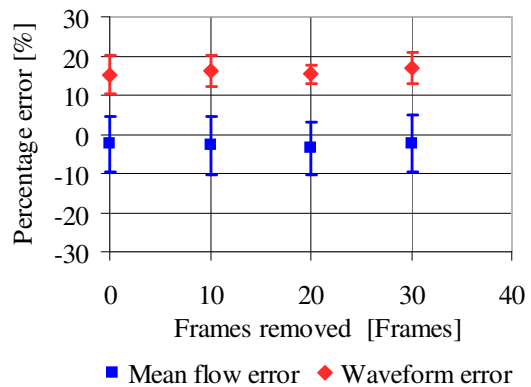
(c) Fixed calibration.

Figure 7.13: Influence of the visibility of the inflow phase.

Accuracy of constraints

The experiments above have shown that it is possible to improve results by introducing additional constraints. In this experiment, I analyse how the results from the flow map fitting change if inaccurate information is used to constrain the flow map fitting.

The flow map fitting with fixed injection time was used with varying injection start time. An offset of -2 frames, -1 frames, 0 frames, 1 frames, or 2 frames was added to the injection start time. The flow map fitting with fixed calibration factor was used with varying calibration factor. The calibration factor was set to 0.8, 0.9, 1.0, 1.1, or 1.2. Finally, the flow map fitting with fixed injection and fixed calibration was used with both variations.

The results are presented in Figure 7.14. An inaccurate injection start time was found to introduce a bias to the mean flow estimation. An inaccurate calibration factor was also found to introduce a bias to the mean flow estimation. An almost linear relationship can be observed. The percentage error of the mean flow is about twice the percentage error of the calibration. If the injection time is inaccurate but the calibration factor is accurate, the bias is removed. The converse is not true, however: if the calibration factor is inaccurate but the injection time is accurate, the bias remains.
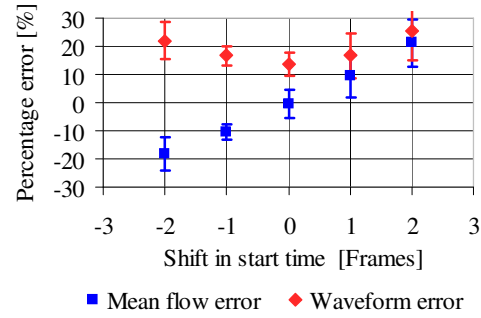
(a) Inaccurate injection start time (fixed injection).
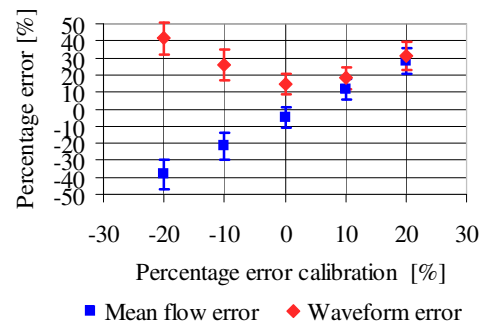
(b) Inaccurate attenuation calibration (fixed calibration).
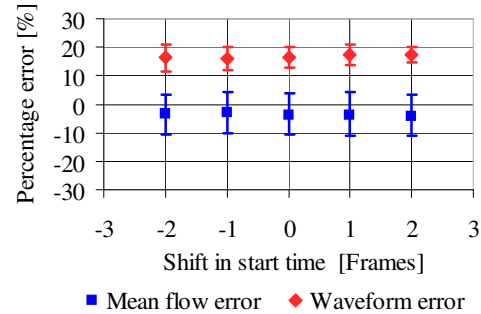
(c) Inaccurate injection start time, but accurate attenuation calibration (both fixed).
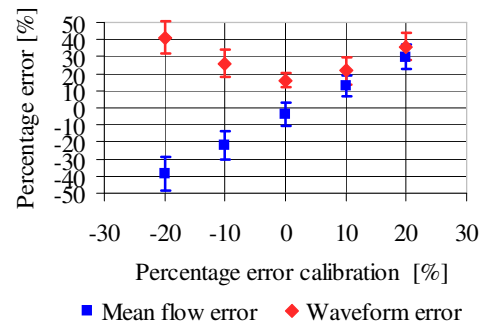
(d) Inaccurate attenuation calibration, but correct injection start time (both fixed).

Figure 7.14: Influence of inaccurate constraints.

7.3.4   Evaluation with a spiral phantom

The spiral phantom consists of a long tube which was formed to a spiral with a radius of about 5 cm. The spiral phantom was used for the following reasons:

- to test whether the flow model is applicable over long distances;

- to test whether the flow model is applicable for bending vessels;

- to demonstrate the effect of the reliability map;

- and to test the flow map fitting at different distances from the injection site.

An example of the spiral flow map is shown in Figure 7.15. The flow map contains both overlapping parts and foreshortening. These artefacts make it difficult to observe the normal flow pattern in the flow map. If the unreliable parts of the flow map are masked, the normal flow pattern becomes apparent again.

(a) Uncorrected flow map.

(b) Extracted flow map after distance-correction.

(c) Reliability map.

(d) Reliable elements of flow map.
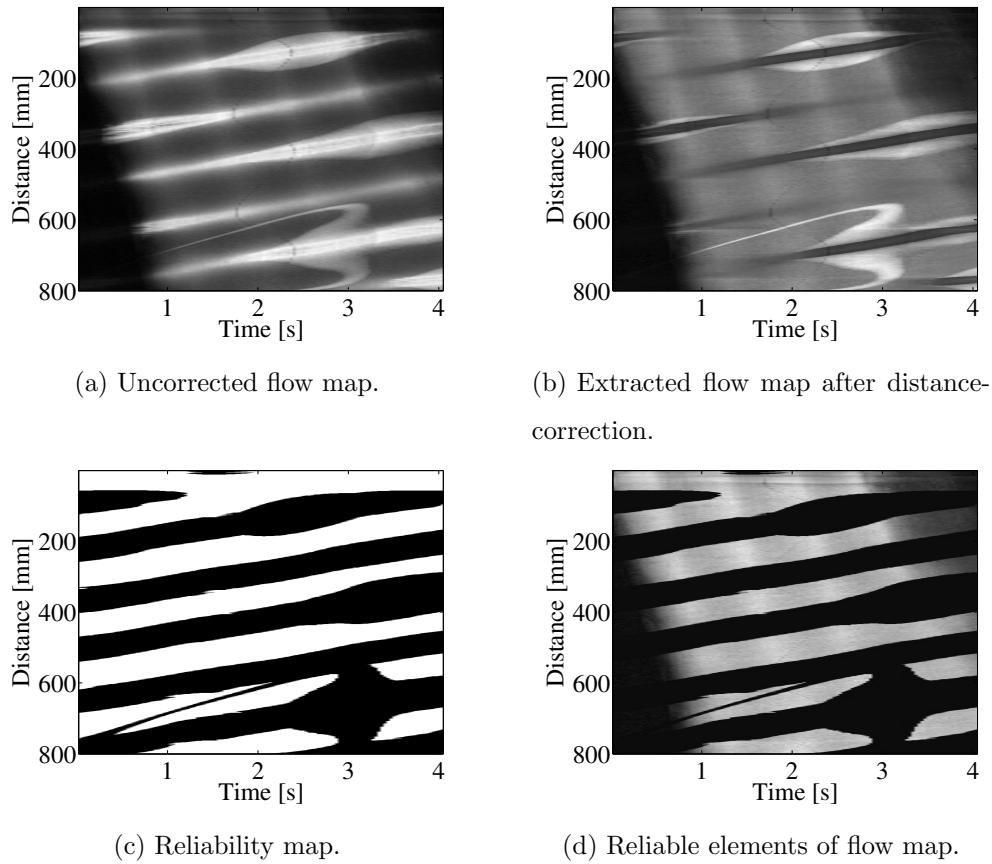
Figure 7.15: Flow map from the spiral phantom: Illustration of the effect of the reliability map Waechter et al. (2008b).

Applicability of the model

Bends in the spiral phantom cause a change of the flow profile. The flow profile gets skewed and the flow is no longer axially symmetric. Therefore, one of the assumptions of the model is no longer valid. One goal of this experiment was to find out whether this has an impact on the flow quantification. The second goal was to analyse whether the flow model is applicable over long distances and whether the choice of the diffusion coefficient has an impact on the flow quantification. At points which are far away from the injection site, diffusion has a greater impact on the appearance of the flow map. The diffusion coefficient is not known and values in the literature vary substantially (10^{-5} m^2/s to 10^{-9} m^2/s).

For this experiment, the complete spiral flow map was used. Overall, 12 datasets were used and all three configurations of the flow map fitting were applied.

An overview of the results is presented in Figure 7.16. Detailed results are presented in Appendix A.2. Accurate results were obtained with all three configurations of the algorithms. In particular, the flow map fitting without constraints gave more accurate results compared to the experiments with the straight tube. This configuration particularly benefits from the long length of the spiral. The choice of the diffusion coefficient was observed not to influence the results.
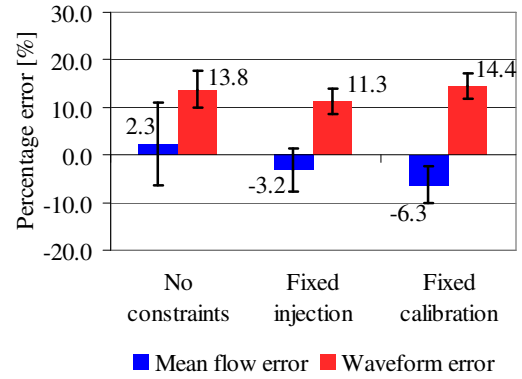
Figure 7.16: Results from flow map fitting using the acquisitions of the spiral phantom.

Reliability map

Overlapping vessels and foreshortening cause artefacts in the flow map. The reliability map is used to reduce the influence of these artefacts on the flow estimation. The goal of this experiment was to analyse how the method performs if no reliability map is used.

For this experiment, a 15 cm segment of all spiral flow maps was selected. Then, all three configurations of the flow map fitting were applied, once with the reliability map and once without the reliability map.

The results for both cases are presented in Figure 7.17. The waveform error increases for all configurations of the flow map fitting when the reliability map is removed. For the flow map fitting with fixed calibration the the bias of the mean flow error also increases.
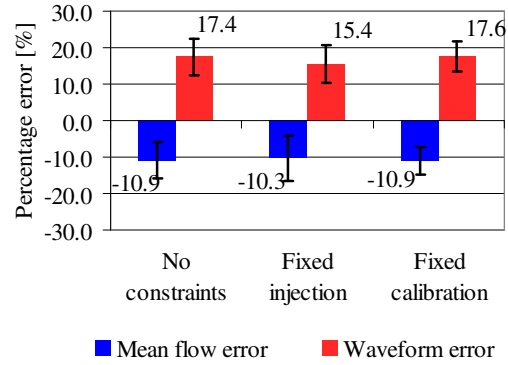
(a) With reliability map.
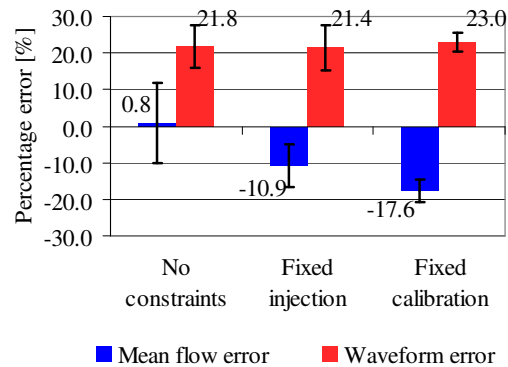
(b) Without reliability map.

Figure 7.17: Influence of reliabilty map.

Distance from the injection site

For optical flow methods and DIC methods, it was shown that flow estimates depend strongly on the distance between the observation and the injection site. The goal of this experiment is to analyse the influence of the distance between the beginning of the flow map and the injection site on the three versions of the flow map fitting.

15 cm long pieces were cut at different distances from all flow maps from the spiral phantom. The distance was varied from 2 cm, 5 cm, 10 cm, to 15 cm. Then, all three versions of the flow map fitting were applied. Results were averaged for each distance and for each version of the flow map fitting.

The results are presented in Figure 7.18. The errors of the flow map fitting without constraints and of the flow map fitting with fixed injection decrease as the distance from the injection site increases. The accuracy of the flow map fitting with fixed calibration does not depend on the distance from the injection site.
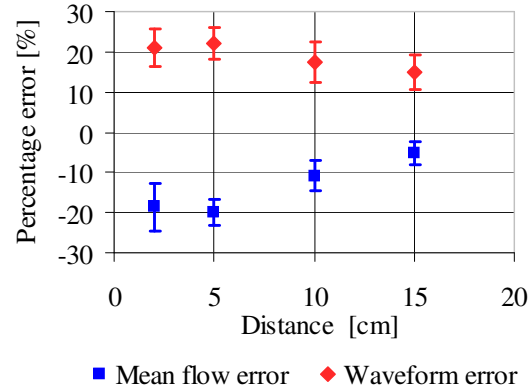
(a) No constraints.
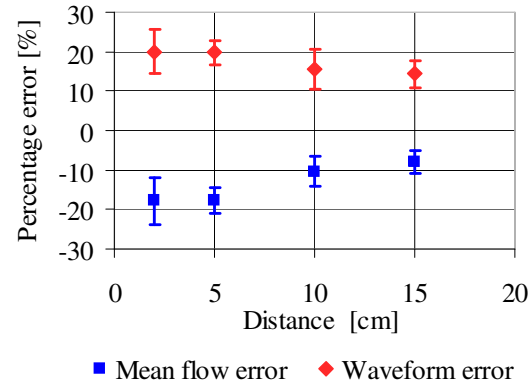
(b) Fixed injection.
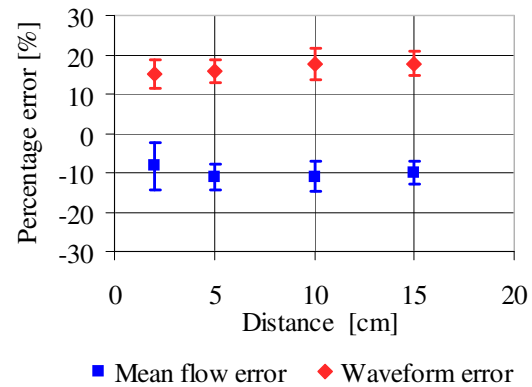
(c) Fixed calibration.

Figure 7.18: Influence of distance of flow map from injection site.

7.3.5 Evaluation with bifurcation phantoms

The goals of the experiments using the bifurcation phantoms were:

- to test the flow model with more complex geometries;

- to analyse how accurately the flow division at the bifurcation can be estimated;

- and to analyse the influence of the stenosis and the widening which is characteristic for the carotid artery bulb.

Three different bifurcation phantoms were used: the carotid bifurcation with the enlarged carotid bulb, the carotid bifurcation with stenosis and the simple compliant bifurcation.

(a) Vessel tree.　　　　(b) Centreline 1.　　　　(c) Centreline 2.

(d) Reliable parts of flow map 1.　　　(e) Reliable parts of flow map 2.
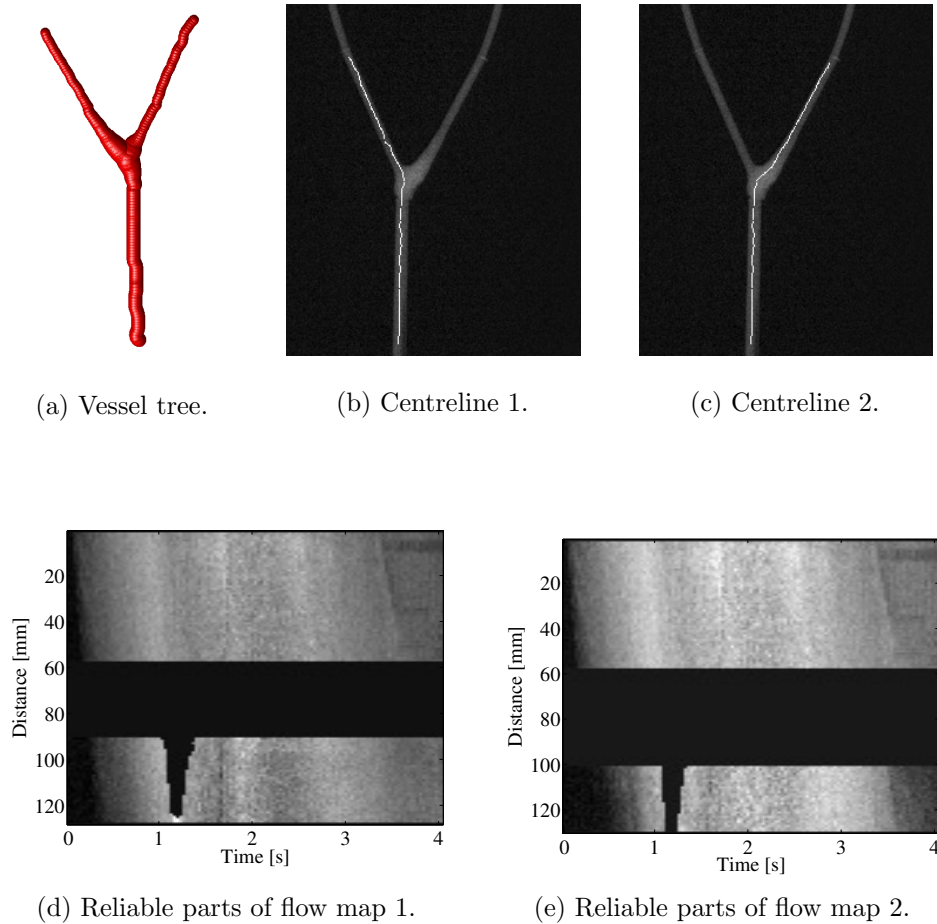
Figure 7.19: Extraction of flow map and reliability map (Carotid - with bulb).

(a) Vessel tree.   (b) Centreline 1.   (c) Centreline 2.

(d) Reliable parts of flow map 1.   (e) Reliable parts of flow map 2.
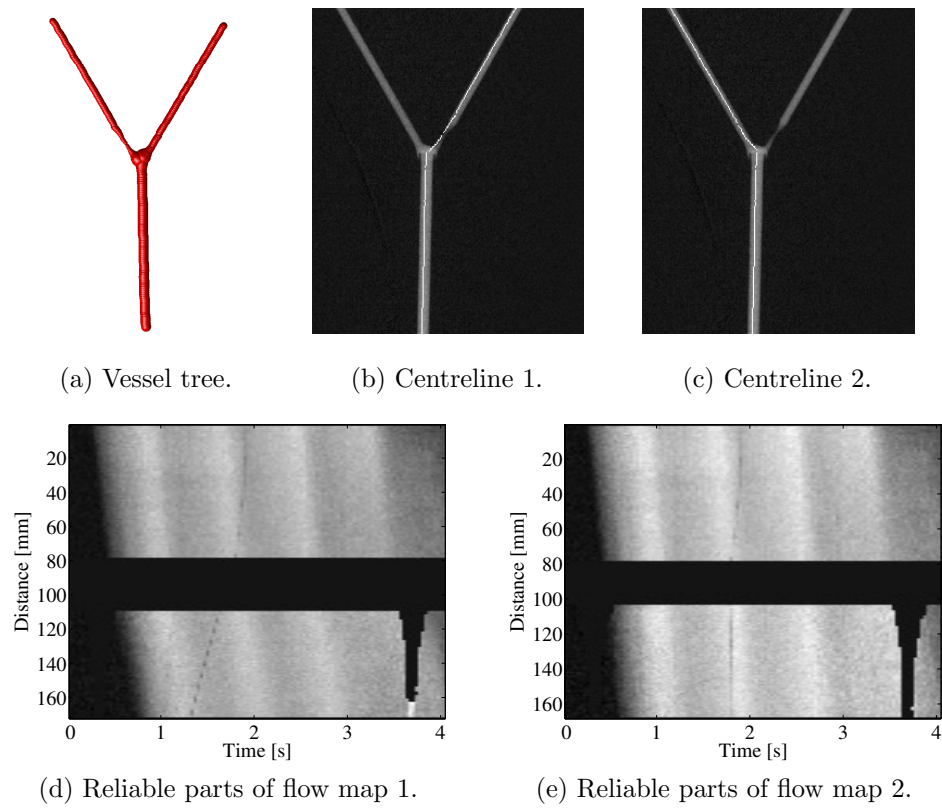
Figure 7.20: Extraction of flow map and reliability map (Carotid - with stenosis).

(a) Vessel tree.   (b) Centreline 1.   (c) Centreline 2.

(d) Reliable parts of flow map 1.   (e) Reliable parts of flow map 2.
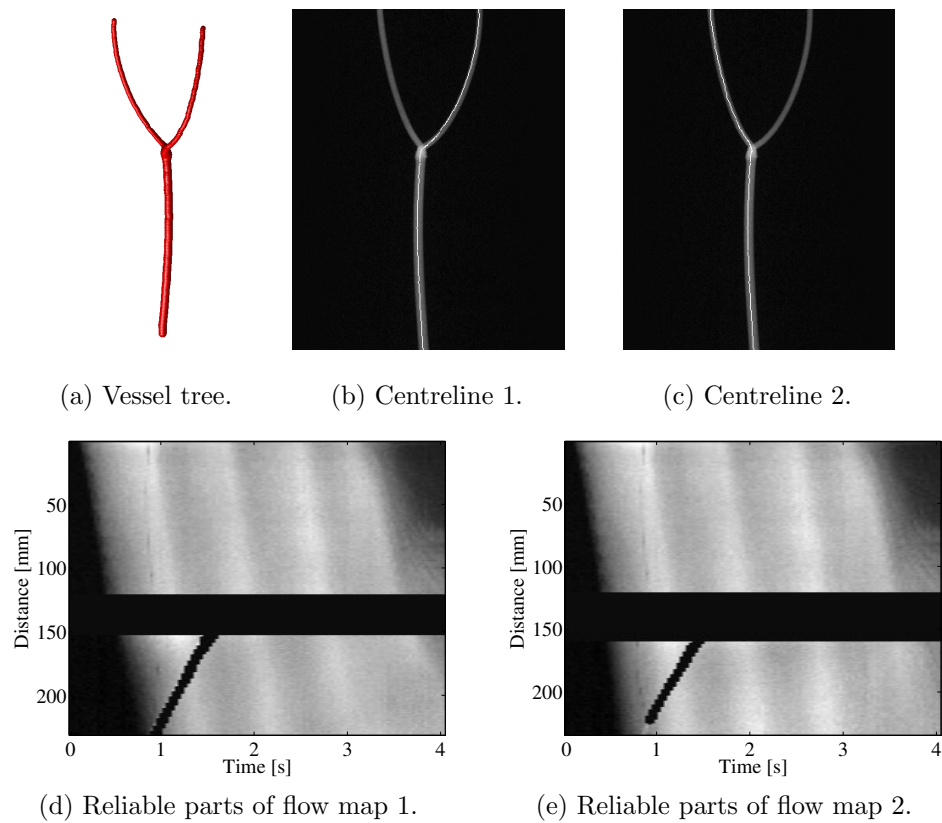
Figure 7.21: Extraction of flow map and reliability map (simple bifurcation).
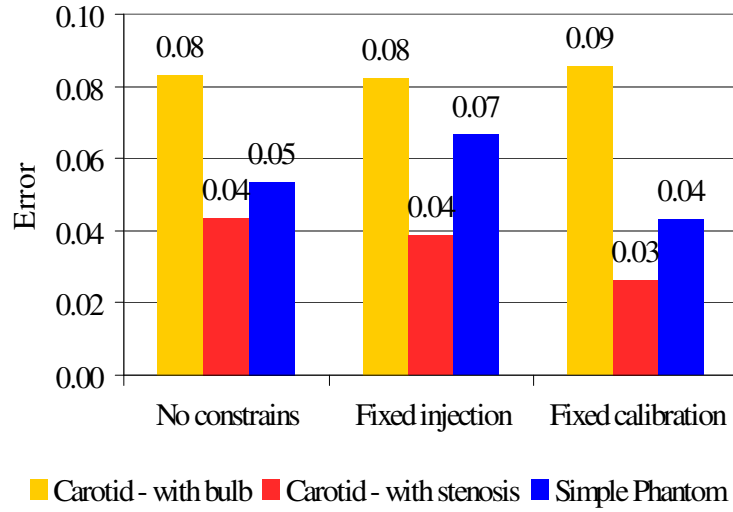
Figure 7.22: Results from the flow division estimation for three different bifurcation phantoms.

The centreline and radii were determined and this information was used to determine the flow map and reliability map for all datasets. Examples of the reconstructed vessel tree, the centrelines and the reliable parts of the corresponding flow maps of all three bifurcation phantoms are shown in Figures 7.19 - 7.21. Then, the three configurations of the flow map fitting were applied. In addition to the mean flow and the flow waveform, the flow division was estimated. As the former quantities were already assessed in the previous experiments, I concentrate on the results of the flow division estimation here. For the error estimation of the flow division, the absolute difference between the ground truth value and estimate is determined. Results were averaged for each phantom and for each configuration of the flow map fitting.

An overview of the results is presented in Figure 7.22. Detailed results are presented in Appendix A.2. The choice of the configuration of the flow map fitting had only a small influence on the accuracy of the results. However, results varied for the different phantoms. Results were most accurate for the carotid bifurcation with stenosis and least accurate for the carotid bifurcation with the carotid bulb.

7.3.6   Evaluation with Circle of Willis phantom

The goal of the experiments with the Circle of Willis phantom was to analyse the general feasibility of the flow map fitting algorithms for complex vessel geometries. The main question was whether suitable flow maps can be extracted and whether enough parts are reliable to quantify the blood flow in realistic cerebral vessels. A quantitative analysis was not possible, as the phantom has six outlets and only one EMF was available.

For most datasets, the right and the left side of the cerebral vasculature were filled with contrast agent. This generally does not happen in the clinical case: normally only one side is enhanced. The enhancement of both sides results in a lot of vessel overlap and therefore many unreliable parts in the flow map.

In the following, a case is analysed where only one side was enhanced. Figure 7.23 shows the extracted vessel tree. Figure 7.24 shows three different paths of vessel centrelines and the corresponding flow maps. In Figure 7.25 the different intermediate results of the flow map extraction are shown in detail for another path. The horizontal black lines indicate the borders of the different segments. The uncorrected flow map shows many artefacts. The influence of artefacts due to foreshortening and variations of the radii is reduced after the distance-correction. Masking with the reliability map removes most corrupt parts of the flow map. Even after distance-correction and masking, the flow pattern in the small vessel segments is difficult to distinguish.

The flow map fitting was applied and besides the flow rate at the inlet all flow division factors were determined. Using all flow division factors, the volumetric flow rate can be determined for all segments. As explained in Section 3.6.2, the flow conservation is enforced, which means that the flow at the inlet has to equal the sum of the flows at all outlets. The resulting flow rates for different vessel segments are shown in Figure 7.26. For some segments only small parts of the flow map were reliable. In this case the result is unlikely to be reliable.

(a) Frontal view.   (b) Lateral view.
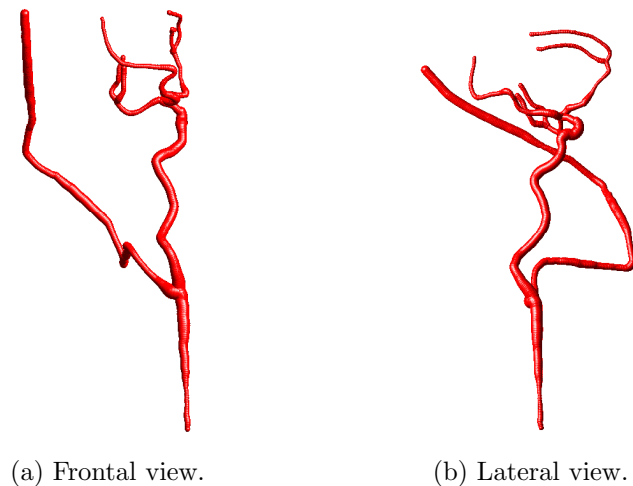
Figure 7.23: Reconstructed vessel tree of Circle of Willis phantom.
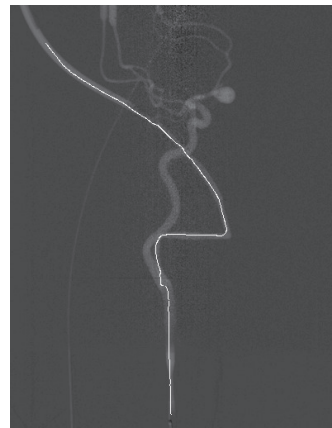
(a) Centreline 1.
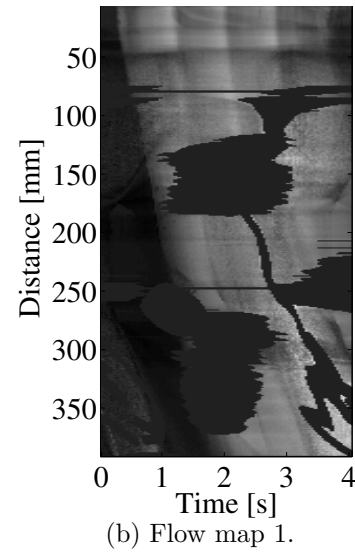
(b) Flow map 1.

(c) Centreline 2.
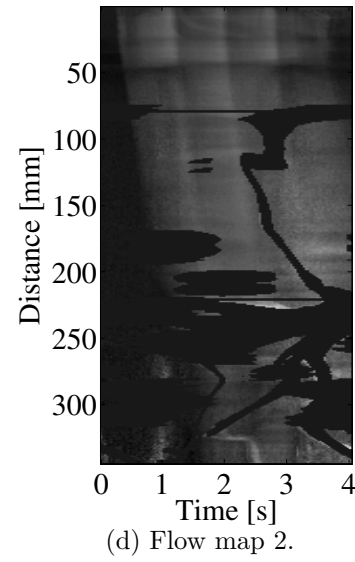
(d) Flow map 2.

(e) Centreline 3.
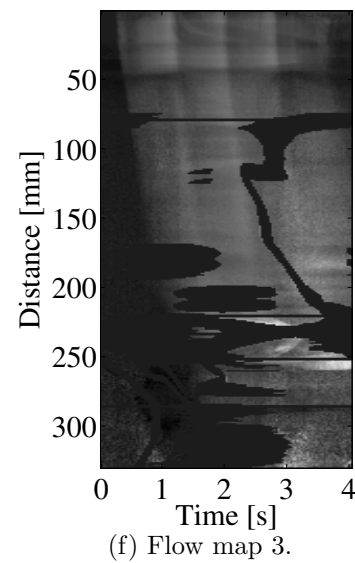
(f) Flow map 3.

Figure 7.24: Flow maps of Circle of Willis phantom.

(a) Centreline.

(b) Uncorrected flow map.

(c) Distance map

(d) Distance-corrected flow map.

(e) Reliability map.

(f) Reliable parts of flow map.
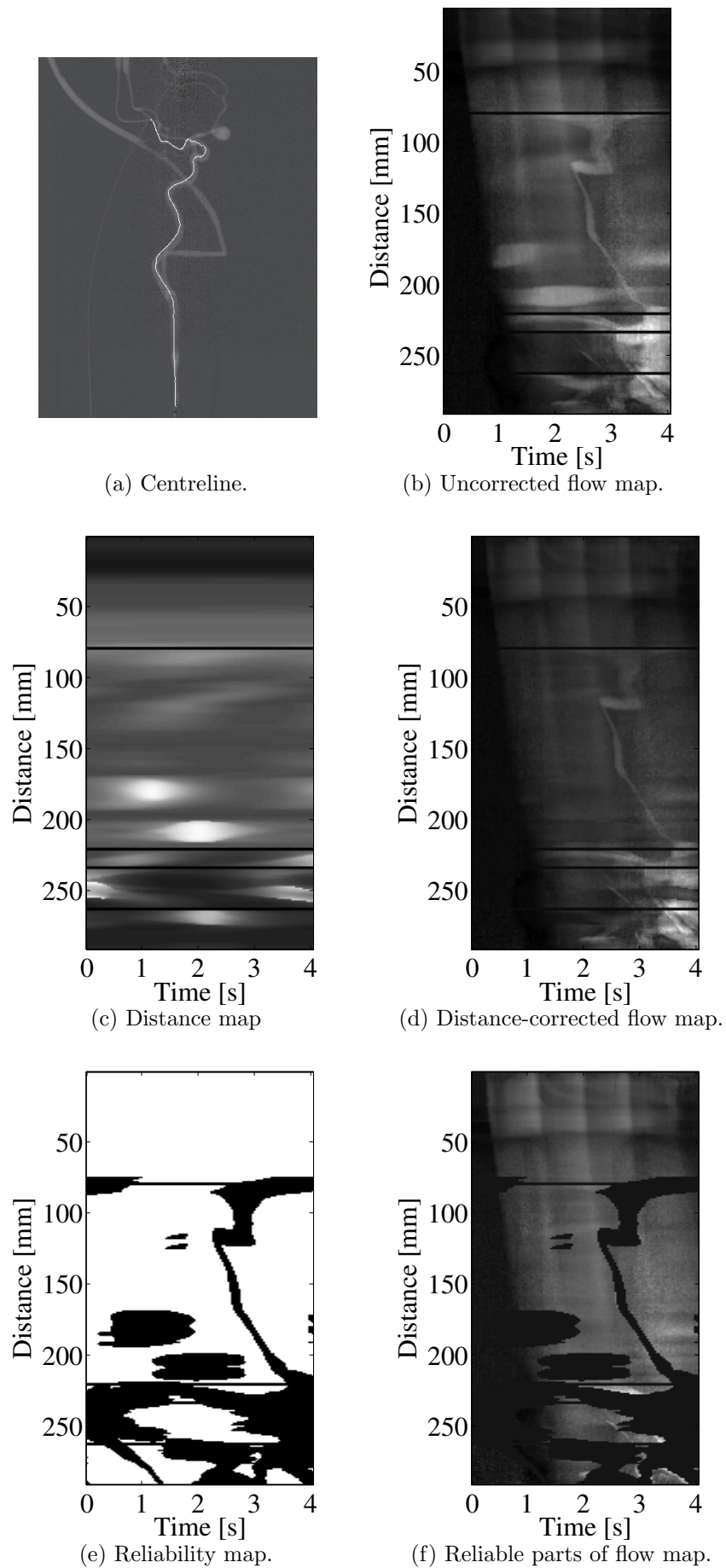
Figure 7.25: Intermediate results of flow map extraction for one path through the Circle of Willis phantom.
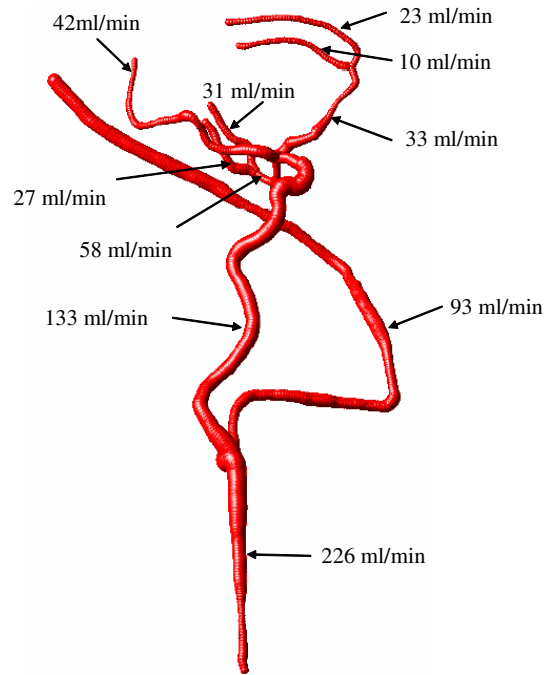
Figure 7.26:   Results from the flow quantification in the Circle of Willis phantom.

7.3.7   User interaction and required time for computations

The required time for user interaction and computation of flow parameters depends on the complexity of the vessel tree.

If the flow is to be determined just in one segment, the user only has to indicate the start and the end point of that segment. The precision of the point selection is not important provided the point lies within the corrected vessel segment. This should take only a few seconds. For such a case, the flow map fitting took between 4 and 8 minutes on a PC with an Intel Xeon, 3 GHz processor.

If the flow before and after a bifurcation is to be determined, the user must select at least 3 points. More than 3 points are required if the user wants to divide the branches into segments which is necessary for the analysis of a stenosed vessel, for example. In such a case, a sufficient number of points can be defined within a minute. The division into segments could also be done automatically. For bifurcations, the flow map fitting took between 15 and 20 minutes on a PC with the specification given above.

If the flow is to be determined in a complex vessel tree like the Circle of Willis phantom, the required user interaction is considerable. All bifurcation points and end points have to be selected and the connectivity has to be defined. For this case the flow map fitting took about 30 minutes on a PC with the specification given above.

In this work, the flow map fitting algorithm was implemented in Matlab and was not optimised for speed. However, a considerable speed-up should be possible using a more efficient implementation.

7.4 Discussion

In this chapter, I have presented a method for estimating a blood flow waveform and the mean volumetric blood flow rate from rotational angiography. Any method for estimating blood flow from rotational angiography needs to be more robust than for planar angiography because of artefacts due to changing foreshortening and overlapping vessels introduced by the rotation of the c-arm. To achieve this, I proposed a novel approach which utilises a flow model in conjunction with a reliability map.

To the best of my knowledge, this is the first study to present quantitative results for flow estimation from rotational angiographic images. Therefore, I am unable to directly compare my results to those obtained by other methods. However, I have investigated and addressed known limitations of optical flow and DIC-based methods which work on planar angiographic images.

A major advantage of my method is that it uses an explicit model for the flow and contrast agent propagation. In this case, a simple convective dispersion model with laminar flow was used. The framework adopted for the flow map fitting algorithm is such that the model can be readily replaced with an alternative, more sophisticated model if required.

The convective dispersion model used in my study can account for changes in the appearance of the flow map at different distances from the injection site and at different times after the start of the injection. Therefore, information from the inflow or outflow phase can be used without introducing a bias, which is known to exist for methods based on optical flow and DICs (Huang et al., 1997a; Rhode et al., 2005).

A further advantage is that the model allows the use of additional information, for example information about the injection or information from the attenuation calibration. On the other hand, if this information is not available, the method can still give quantitative flow estimates. Unknown injection and calibration parameters can be estimated during the fitting process.

Depending on the amount of prior information available, the characteristics of the flow map fitting algorithm change. The main reason for this is that the method can use two different kinds of information from the flow map: kinematic and densitometric information. The kinematic information is contained in the gradients of the pattern of the flow map. The densitometric information is contained in the absolute or relative magnitude of the intensities of the flow map. To the best of my knowledge, this is the first method which used both pieces of information concurrently.

The basic version of the flow map fitting uses kinematic information for the determination of the mean flow and kinematic and relative densitometric information to determine the waveform. During systole, the resulting iodine density is relatively low. During diastole, the resulting iodine density is relatively high. The pulsatility determines the difference in density. Therefore, the information about the shape of the waveform is encoded in the pulsatile pattern.

If the start time of the injection is fixed, the same kind of information is still used. It is more reliable for the following reason: A longer flow map often results in a better flow estimate.

If the start time of the injection is fixed, the point of the injection site can be seen as virtual first line of the flow map and the virtual flow map length can be extended from the position of the injection site to the start of the flow map.

If the attenuation calibration factor is fixed, additional densitometric information for the mean flow estimate is available. The attenuation gives the absolute magnitude of the density of iodine, which is proportional to the concentration of contrast agent; the mean concentration of contrast agent gives the mean volumetric flow rate of the circulation (provided the flow rate of the injection is known).

In theory, the model based approach, in particular the mixing model, together with the attenuation calibration makes it feasible that the volumetric flow rate can be determined from one row of the flow map (TIC): the mean flow rate is given by the mean of the TIC, whereas the shape of the waveform is given by the shape of the pulsatile pattern. In reality, one TIC is not sufficient because of noise and artefacts. The influence of these is reduced, the longer the flow map is. Additionally, the kinematic information can only be used if the flow map has a certain length. If kinematic and densitometric information is used concurrently, a redundancy is established which can help to avoid inaccuracies.

If the calibration factor was set to an accurate value, the flow map fitting with fixed calibration was superior. Inspection of the error function shows that the minimum of the error function is well defined in this case. Therefore, convergence should be good. This is confirmed by small standard deviations in most experiments with fixed calibration. In this case, the flow map fitting was also found to be very robust against noise, the frame rate, the length of the flow map and the distance from the injection site to the beginning of the flow map did not influence the accuracy, and it was not necessary that inflow phase of contrast agent was visible in the image sequence.

Fixing the calibration factor to an inaccurate value, however, introduced a bias. A bias in the radius estimation, increased background attenuation at the end of the sequence due to perfusion, or an error in the attenuation calibration correspond to an inaccurate calibration factor. Additionally, for clinical applications, the attenuation calibration could require changes to the clinical workflow, which might not be desirable.

The flow map fitting with fixed injection was almost as robust as the flow map fitting with fixed calibration: only for the highest level of noise and the shortest length of the flow map did the accuracy decrease. A drawback of this version is that the inflow phase must be visible in the image sequence. This can be a limitation as this can hamper the volume reconstruction from rotational angiography. If the injection site is in the field of view, it is easy to determine the start of the injection, otherwise a synchronisation signal of x-ray acquisition and injection must be recorded.

The flow map fitting without constraints was not as robust as the other versions. The results showed that the accuracy depended on the signal to noise ratio, length of the flow map and the

frame rate. However, results were still acceptable. In many experiments without constraints, a negative bias can be observed. To understand this, it is important to remember that the mean flow was initialised with a value half as great as the expected mean flow. Therefore, a negative bias indicates that the optimisation did not converge.

For the case of the spiral phantom, it was shown that the reliability map improved the results. Without the reliability map, it is more difficult to determine the shape of the waveform because the pattern due to pulsatility in the flow map is obscured by artefacts of overlapping and foreshortening. Because of the overlapping vessels, the mean intensity of the flow map is higher and therefore the estimate of the mean volumetric flow rate has a negative bias in case of the flow map fitting with fixed calibration. However, quantitative flow estimates were still possible without the reliability map, which shows the robustness of the method. This is an advantage because in a clinical setup it might not be possible to mark all areas which are unreliable without user interaction.

This effect can also be seen in the evaluation with the Circle of Willis phantom: Not all corrupted areas were marked as unreliable. Possible reasons for remaining artefacts are missing segments in the reconstruction (segments after the selected end points) and small errors in the vessel reconstruction. The evaluation with the Circle of Willis phantom showed that it is possible to determine flow maps for a complex vessel tree and that it is possible to estimate the flow in the vessel tree. However, many parts of the flow map in the distal vessels are not reliable and the flow pattern is quite weak. Therefore, the accuracy of the flow estimates is questionable.

The chosen flow model is very simple compared to state-of-the-art computational fluid dynamics (CFD) models. I have chosen this simple model because it is computationally efficient while being still able to approximate blood flow in the large arteries. The former is important because it has to be applied iteratively in the fitting process. The phantom experiments showed that the flow model was able to explain the real transport of contrast agent in a flowing medium. In a bend, at a bifurcation, or at a stenosis, the assumption of the model that the flow is laminar and axially symmetric does not hold. Nevertheless, I was able to use the model to compute quantitative flow estimates. The largest errors were observed at the carotid bulb. I believe that these errors are due to secondary flow in the carotid bulb. Further investigations are necessary to determine how the flow map fitting method performs for more complex vessel geometries, such as that found in the distal carotid arteries or around an aneurysm, where more complicated haemodynamics might be present.

Three different waveform models were compared using different patient waveforms: the 2-parameter warped cosine model, the 4-parameter warped cosine model, and the Laplace model. The 2-parameter warped cosine model was not powerful enough to explain the observed variations. The Laplace model, which should be able to explain 90% of all patient waveforms (Skidmore and Woodcock, 1978), also exhibited problems. Best results were obtained with the 4-parameter warped cosine model. Therefore, this waveform model was used for all other ex-

periments. Although this model is more restrictive than a principal component model (Rhode et al., 2005), I conclude that it is not necessary to invest in the training of such a model at this stage of the work.

The flow model cannot be used to describe flow in aneurysms. Nevertheless, the flow map fitting method might be usefully applied in the assessment of aneurysms by providing patient specific boundary conditions for CFD simulations, such as those described by Steinman et al. (2003) and Castro et al. (2006). In these studies, rotational angiography was used to determine a patient specific mesh of the vessel lumen, but flow boundary conditions were determined from sex and age matched volunteers. Therefore, it would be beneficial if rotational angiography could also be used to determine patient specific flow boundary conditions.

In most cases, relative errors between 5% and 10% for the volumetric mean flow rate and between 10% and 15% for the blood flow waveform could be obtained. The manual interactions took at most 1 min and the computational time for the flow map fitting was between 4 and 20 minutes on a PC.

To apply the method to clinical images, some changes should be applied to standard rotational angiography protocols. From the experience with images from the experimental setup, I consider the following issues to be important:

- Ideally, only one injection of contrast agent should be used for flow quantification and vessel reconstruction. For a standard rotational angiography protocol, the injection duration is chosen to be longer than the x-ray acquisition to ensure that the vessel tree is completely filled during the x-ray acquisition. For the flow map fitting, it is beneficial that the inflow phase of the contrast agent is visible in the rotational angiographic sequence.

- In standard rotational angiography protocols, the volumetric flow rate of the injection is sometimes so high that the contrast agent replaces the blood. In order to measure blood flow and not contrast agent flow, the injection flow rate has to be reduced.

- The flow map fitting method requires either the catheter to be in the field of view or that the ECG of the patient is recorded. When the catheter is in the field of view, the first TIC can be extracted and utilised to determine the start of the injection and start and duration of the heart cycle.

- A mask scan is required for the background subtraction. This is part of some rotational angiography protocols.

- An attenuation calibration and a geometry calibration should be done beforehand.

8

Clinical application

In this chapter, first tests of the flow map fitting on clinical images are presented. The clinical images were acquired at the University Hospital of Geneva by members of the group of Prof. Ruefenacht. The acquisitions were similar to those done for the Aneurist project (Frangi et al., 2007) and therefore they could be covered by an addendum to the ethics approval of the Aneurist project. It is important to note that for the application of the flow quantification method, special requirements have to be fulfilled. Recommendations for the acquisition protocol and injection protocol were given in the previous chapter. Additionally, information about the acquisition (e.g. the frame rate), the injection (e.g. the volumetric flow rate) and the patient (e.g. the heart rate) must be provided. Therefore, it is not possible to evaluate the flow map fitting method using arbitrary existing angiographic sequences.

8.1 Rotational angiography

8.1.1 Clinical protocol

In the last chapter, I have given recommendations for a clinical protocol. Unfortunately, it was not possible to change the x-ray protocol or the injection protocol in this clinical study because this would require a dedicated ethics approval. Therefore, some recommendations, as detailed below, could not be implemented.

For each patient, two rotational angiographic sequences were acquired with the standard x-ray protocol: one with contrast agent (CA sequence) and one without contrast agent (mask sequence). 120 images were acquired in 4 seconds during which the c-arm rotated 205°. The peak voltage was 75 kV and the amperage was adapted during the first frames by the x-ray system according to the patient thickness. The injection flow rate was 3 ml/s, the duration was 6 s and it was started 2 s before the acquisition. The catheter was in the field of view.

Before the patient acquisitions, a geometry calibration and an attenuation calibration were performed. The geometry calibration was successful, meaning that error during the calibration was less than half a pixel. However, during the evaluation of the images from the attenuation

calibration, it was discovered that the clinical protocol uses a dose level at which the detector is overexposed in areas of direct radiation. This fact, together with the fact that the amperage was not fixed, made it impossible to perform an attenuation calibration beforehand.

As the catheter was in the field of view, an ECG signal was not required. However, it was not possible to change the injection timing to see the contrast agent inflow phase in the acquisition or to decrease the injection flow, as this might introduce artefacts in the 3DRA reconstruction. The clinical indication for obtaining these images was the reconstruction of the 3D vasculature using the 3DRA, therefore it was not acceptable to decrease the quality of the 3DRA intentionally.

The main difference from the standard 3DRA protocol was that an additional mask sequence was acquired. This is required for the flow quantification and also for the vessel reconstruction method described in this thesis.

8.1.2 Results

Two patient datasets were acquired. Unfortunately, the first patient moved considerably between the CA sequence and the mask sequence. This led to severe subtraction artefacts as shown in Figure 8.1. Compensation for the motion was tried using a rigid 2D registration using mutual information as a similarity measure and a brute force search. This worked reasonably well for images from the lateral view as the motion in these images could be described by a rigid transformation (see Figure 8.2(a)). For images from the anterior-posterior view, however, it did not give satisfactory results (see Figure 8.2(b)) as in this case the 3D motion could not be described by a 2D transformation. For the second patient, a better subtracted sequence could be obtained with only minor subtraction artefacts as shown in Figure 8.3.

For both datasets, the flow map and reliability map were determined as described in Chapter 7. As it was not possible to change the injection timing, neither flow maps show the inflow phase of the contrast agent. In the flow map from Patient 1, no flow pattern can be recognised (see Figure 8.4). The variations in the image intensities caused by artefacts in the subtraction are higher than the expected variations due to the pulsatile pattern. In the flow map from Patient 2, a weak flow pattern can be recognised (see Figure 8.5). In Figure 8.5(c) the troughs of the pulsatile pattern in the flow map are indicated.

8.1.3 Discussion

It was not possible to obtain flow maps from rotational angiographic sequences which were suitable for flow quantification with the flow map fitting method. The main reason for this is the weak flow pattern in the flow map. The most likely cause of which is that the flow rate of the contrast agent injection was too high. In this case, the following can happen: During diastole a considerable amount of the contrast agent moves upstream, whereas during systole, when the concentration should be low, it is transported downstream again and increases the concentration. The second reason are subtraction artefacts due to the motion of the patient between the CA sequence and the mask sequence.
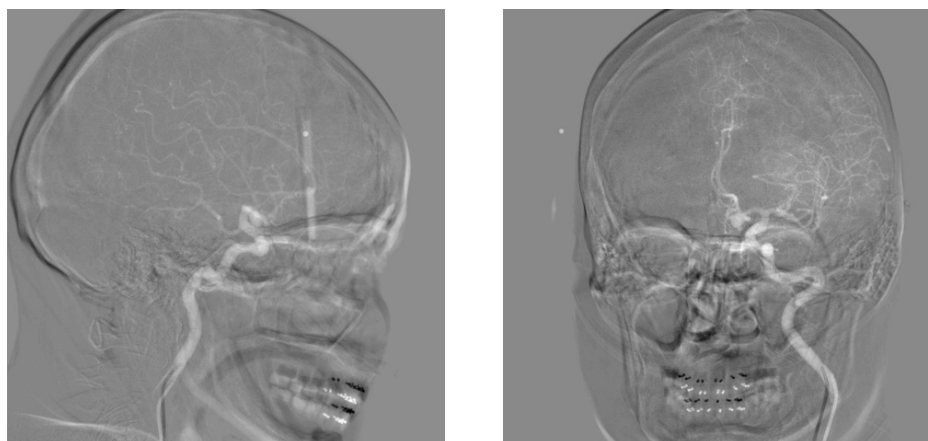
(a) Lateral view. (b) Anterior-posterior view.

Figure 8.1: Patient 1 - subtraction image before registration.
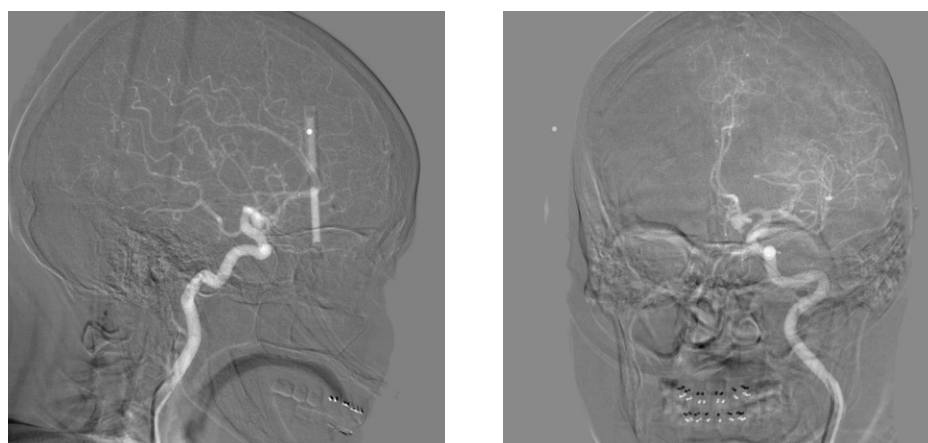
(a) Lateral view. (b) Anterior-posterior view.

Figure 8.2: Patient 1 - subtraction image after registration.
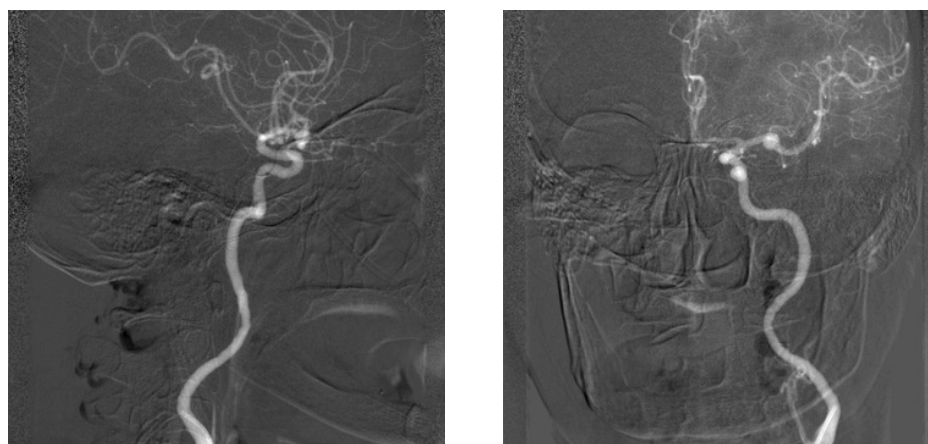
(a) Lateral view. (b) Anterior-posterior view.

Figure 8.3: Patient 2 - subtraction image without registration.

(a) Uncorrected flow map. (b) Corrected flow map. (c) Corrected flow map with unreliable parts masked out.
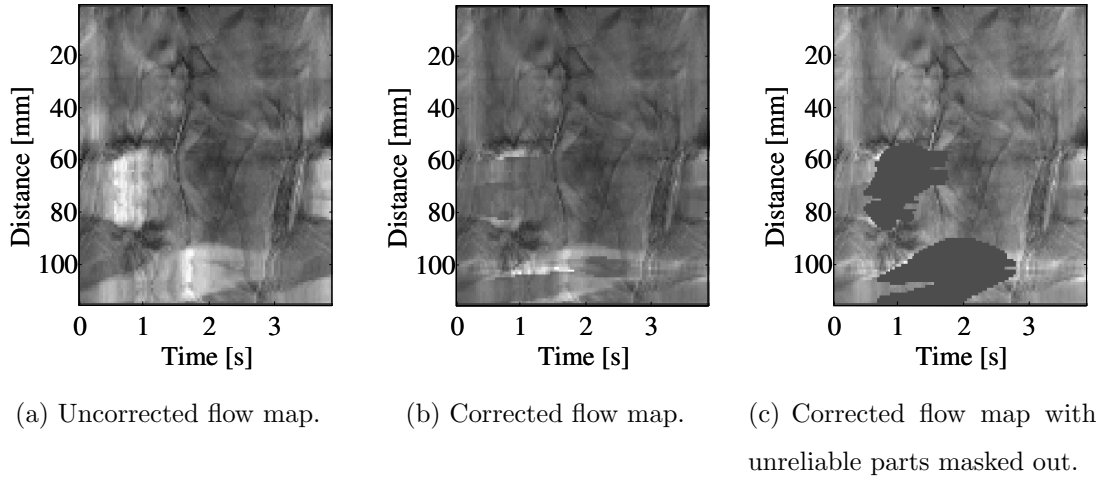
Figure 8.4: Flow map of patient 1.

(a) Uncorrected flow map. (b) Corrected flow map. (c) Corrected flow map with unreliable parts masked out and marked flow pattern.
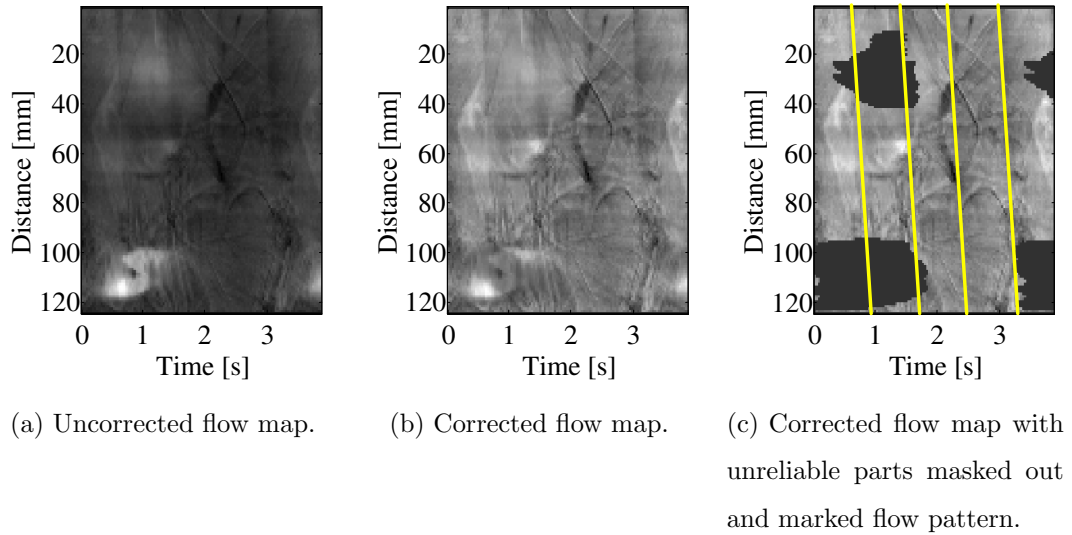
Figure 8.5: Flow map of patient 2.

This section only showed results of an initial trial of the flow map fitting method applied to clinical rotational angiography. Although it was not possible to use the obtained flow maps for flow quantification, I am still convinced that this would be possible with small changes in the clinical protocol. In particular, the flow rate and duration of the contrast agent injection should be decreased. Additionally, the x-ray protocol should be changed to give a constant voltage and amperage and no overexposure. These changes however, would require a dedicated ethics approval and therefore further trials were beyond the scope of this thesis.

8.2 Planar angiography

As it was not possible to obtain suitable clinical rotational angiographic images, the applicability of the flow model and the flow map fitting for real blood flow was analysed on a combination of rotational and planar angiographic sequences.

8.2.1 Clinical protocol

For each patient, a rotational angiography was acquired using the standard protocol, as explained above. However, this time no mask sequence was acquired. The CA sequence was used to reconstruct the 3DRA volume. Care was taken that the catheter appeared in the field of view.

Then, for each patient, between one and three planar acquisitions were made (flow sequence). This time, amperage and voltage were kept constant. The ECG signal was recorded for each frame of the flow sequence. The injection flow was 2 ml/s. The duration of the acquisitions was 6 s, the duration of the injection was 3 s, and the injection was started about 1 s after the acquisition. Therefore, the first images can be used as mask images to obtain the DSA sequence. If possible, the catheter tip was placed in the field of view. In this case, this was more difficult as the field of view was smaller. If multiple acquisitions were made, the orientation of the c-arm was changed for some patients. Before or after the intervention, the volumetric blood flow in the main internal carotid artery was estimated with transcranial colour Doppler (TCCD, see Section 2.4.4).

Overall, this protocol agrees much better with the recommendations given in the previous chapter compared with the protocol for rotational angiography. The injection flow is lower and the duration of the acquisition and injection allowed imaging of the inflow and outflow phase. Also, the x-ray protocol was tailored to flow quantification.

However, as this is a complex protocol, it could not be followed strictly for all patients. For some patients for example, the ECG signal was not recorded due to technical difficulties. For some patients, it was not possible to place the catheter in the field of view, because it would have been too near to an aneurysm, which might rupture due to the pressure of the injection. For some patients, TCCD measurements were not possible because the sonographer was not available or because it was a surgical case. During surgery, TCCD cannot be applied because of sterility issues and after surgery, it is difficult because the inflammation of soft tissue could disturb the signal.

8.2.2 Processing

The 3DRA datasets were utilised to determine the 3D centrelines and radii. The vessels were divided into segments according to their radius. Then, an interactive 2D-3D registration was used to determine the geometric parameters of the c-arm during the acquisition of the flow sequence with respect to the 3DRA dataset. They were required to project the 3D centreline onto the flow sequence. With all this information, the flow- and reliability maps could be determined in the same way as described in Chapter 7.

For this setup, no attenuation calibration was available. Therefore, the flow map fitting could not be applied in the 'Fixed Calibration' mode (see Section 7.3.1). If the catheter was in the field of view of the flow sequence, the start and duration of the injection were determined from the first TIC. Otherwise, they were determined manually. Then, the flow map fitting could be applied in the 'Fixed Injection' mode (see Section 7.3.1).

Several parameters also had to be set beforehand: If the catheter was in the field of view, the time of systole and the heart rate were also determined from the first TIC. Otherwise, they were determined from the ECG signal. The diffusion coefficient was set to $10^{-6}\mathrm{m}^2/\mathrm{s}$ and the resistance factor was set to 0.5. The distance to the injection site was measured from the 3DRA.

For each flow sequence, the flow map fitting was repeated with 24 different combinations of initial values: The initial values for the mean flow, for the shape of the waveform, and for the flow profile were varied. Then, the best fit (the result with the lowest value of the optimization function) was determined for each flow sequence.

8.2.3 Results

Data from 10 different patients was available for this evaluation and, overall, 17 flow sequences were available. Table 8.1 gives a summary of the data which was available for each patient. During the evaluation, the flow in the main vessel was determined: In most cases, this was the internal carotid artery, but for Patients 9 and 10, this was the vertebral artery. All 17 flow sequences were analysed. Detailed intermediate results, however, are only shown for one acquisition per patient. The resulting flow estimates are later shown for all acquisitions.

In Figures 8.6(a) - 8.15(a), the projected centrelines are indicated in maximum intensity images for all patients. In Figures 8.6(b) - 8.15(b), the reconstructed geometric models of the vessels are shown for all patients. The different segments are indicated by different colors. In Figures 8.6(c) - 8.15(c), the extracted flow maps are shown. The parts of the flow map which are unreliable are masked out. In many cases, the first part of the flow map is missing, because the corresponding part of the vessel was not in the field of view.

In Figures 8.6(d) - 8.15(d), the simulated flow maps which gave the best fit are shown. In Figures 8.6(e,f) - 8.15(e,f), extracted and fitted TICs are displayed together to show the quality of the fit. They were averaged over one segment. As the length of the segment varied, the noise level in the extracted TICs varied.

It was possible to apply the flow map fitting, for nine out of ten patients. Only for Patient 10 it was not possible to apply the fow map fitting, as no pulsatile pattern was visible in the flow map. For the others, the quality of the best fit was judged through visual inspection. The criterion is the agreement of the extracted and fitted TICs. A very good fit was achieved for Patient 3 and 5. Good fits were achieved for Patient 1, 7, 8, and 9. Problems could be observed for Patients 4, 6, and 10, these will be discussed later.

The resulting flow estimates are given by the flow parameters of the best fit of the flow map fitting method. They are shown in Figure 8.16. If more than one flow sequence was availiable, one estimate is shown for each flow sequence. Although only data from ten patients was available for this evaluation, these patients cover quite a wide range of different blood flow patterns. The mean flow varied between 75 ml/min and 230 ml/min (mean 167 ml/min). The pulsatility index ($[\max(Q_B(t)) - \min(Q_B(t))]/\overline{Q}_B$) varied between 0.51 and 1.45 (mean 0.78). The shape of the waveform also varied substantially between the patients. These variations are reflected by the

Patient 1

Case:	Anterior communicating
	artery aneurysm
Type of procedure:	Follow up
Treatment:	Already clipped
Number acquisitions:	3
First TIC available:	Yes
TCCD available:	Yes
ECG available:	Yes

Patient 2

Case:	Middle cerebral artery aneurysm
Type of procedure:	Diagnostic
Treatment:	Clipping
Number acquisitions:	1
First TIC available:	Yes
TCCD available:	No
ECG available:	No

Patient 3

Case:	Cavernous internal carotid
	artery aneurysm
Type of procedure:	Interventional
Treatment:	Coiling
Number acquisitions:	1
First TIC available:	No
TCCD available:	No
ECG available:	No

Patient 4

Case:	Haemoraged, sub-giant,
	middle cerebral artery aneurysm
Type of procedure:	Diagnostic
Treatment:	Clipping
Number acquisitions:	1
First TIC available:	Yes
TCCD available:	Yes
ECG available:	No

Patient 5

Case:	Carotidophtalmic aneurysm
Type of procedure:	Follow up
Treatment:	None
Number acquisitions:	1
First TIC available:	No
TCCD available:	Yes
ECG available:	No

Patient 6

Case:	Middle cerebral artery aneurysm
Type of procedure:	Diagnostic
Treatment:	Clipping
Number acquisitions:	2
First TIC available:	Yes
TCCD available:	No
ECG available:	No

Patient 7

Case:	Internal carotid artery aneurysm
Type of procedure:	Interventional
Treatment:	Stenting
Number acquisitions:	2
First TIC available:	No
TCCD available:	Yes
ECG available:	Yes

Patient 8

Case:	Middle cerebral artery aneurysm
Type of procedure:	Diagnostic
Treatment:	Clipping
Number acquisitions:	2
First TIC available:	No
TCCD available:	No
ECG available:	Yes

Patient 9

Case:	Basilar tip aneurysm
Type of procedure:	Diagnostic + interventional
Treatment:	Coiling
Number acquisitions:	2
First TIC available:	No
TCCD available:	No
ECG available:	Yes

Patient 10

Case:	Vertebro-basilar fusiform aneurysm
Type of procedure:	Diagnostic
Treatment:	Stenting
Number acquisitions:	2
First TIC available:	No
TCCD available:	Yes
ECG available:	No

Table 8.1: Summary of information which is available for different patients.

(a) Centreline in DSA image.
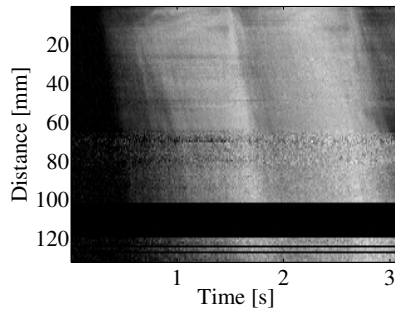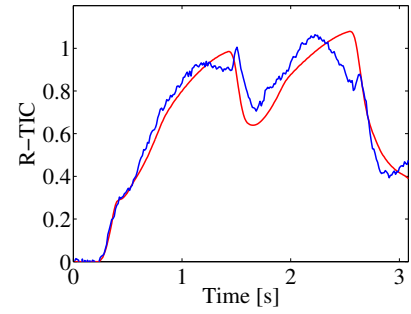
(c) Reliable parts of extracted flow map.

(e) Extracted (blue) and fitted (red) TIC, proximal segment.

(b) Reconstructed geometric model.
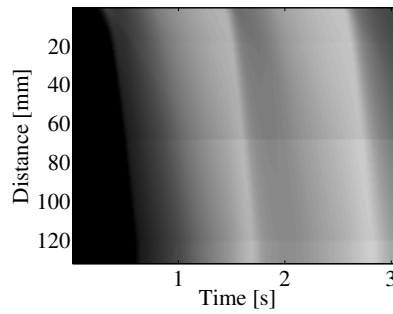
(d) Simulated flow map (best fit from flow map fitting).
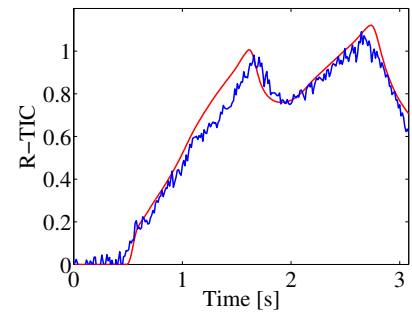
(f) Extracted (blue) and fitted (red) TIC, distal segment.

Figure 8.6: Overview patient 1.

(a) Centreline in DSA image.
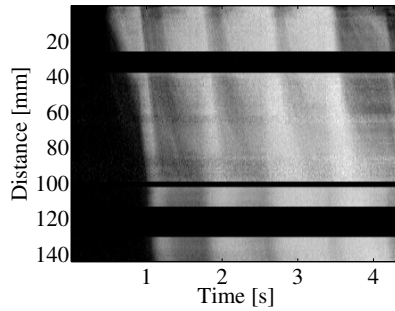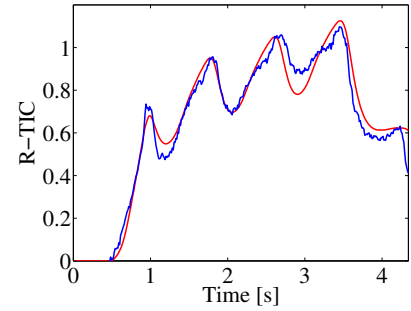
(c) Reliable parts of extracted flow map.

(e) Extracted (blue) and fitted (red) TIC, proximal segment.

(b) Reconstructed geometric model.
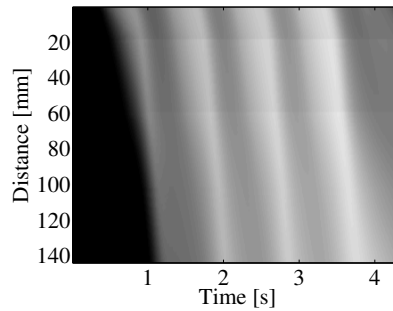
(d) Simulated flow map (best fit from flow map fitting).
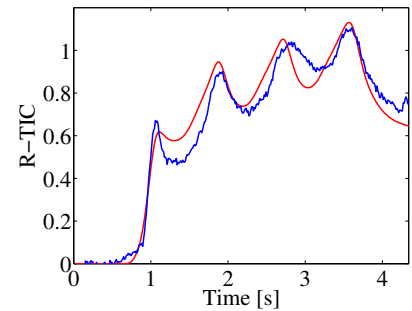
(f) Extracted (blue) and fitted (red) TIC, distal segment.

Figure 8.7: Overview patient 2.
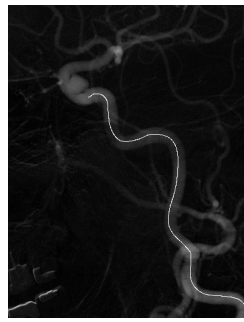
(a) Centreline in DSA image.
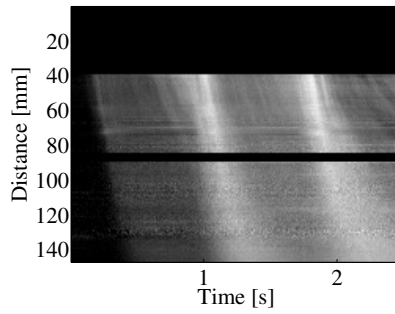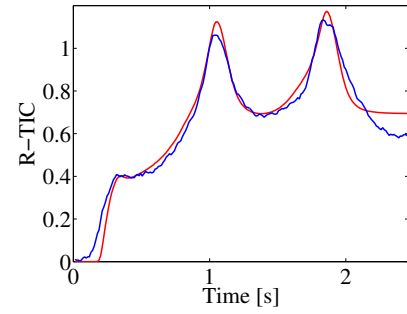
(b) Reconstructed geometric model.

(c) Reliable parts of extracted flow map.

(d) Simulated flow map (best fit from flow map fitting).
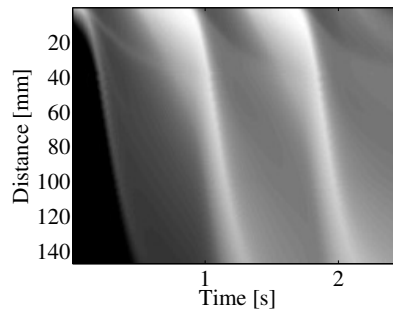
(e) Extracted (blue) and fitted (red) TIC, proximal segment.
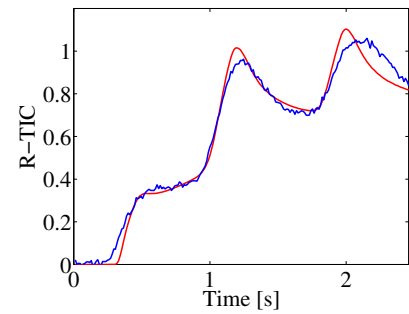
(f) Extracted (blue) and fitted (red) TIC, distal segment.

Figure 8.8: Overview patient 3.
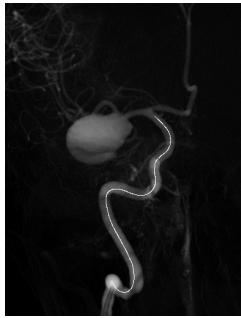
(a) Centreline in DSA image.
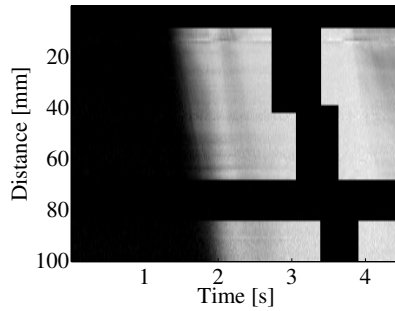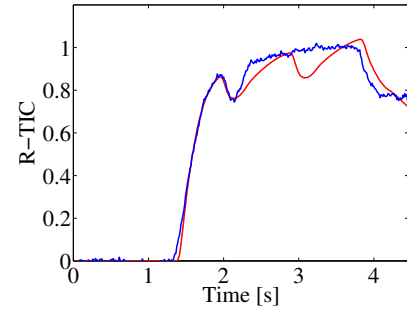
(b) Reconstructed geometric model.

(c) Reliable parts of extracted flow map.
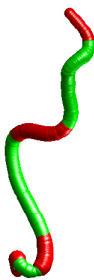
(d) Simulated flow map (best fit from flow map fitting).
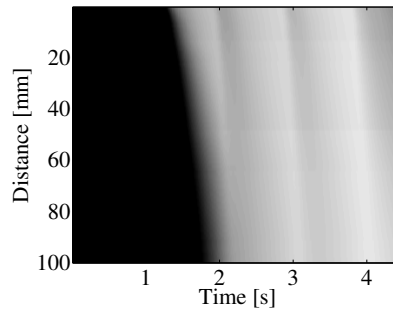
(e) Extracted (blue) and fitted (red) TIC, proximal segment.
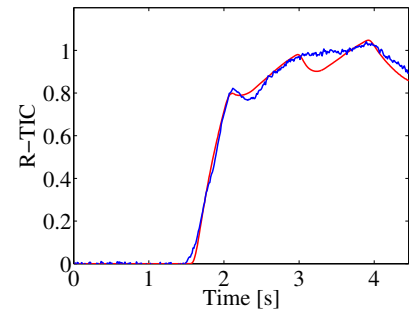
(f) Extracted (blue) and fitted (red) TIC, distal segment.

Figure 8.9: Overview patient 4.

(a) Centreline in DSA image.
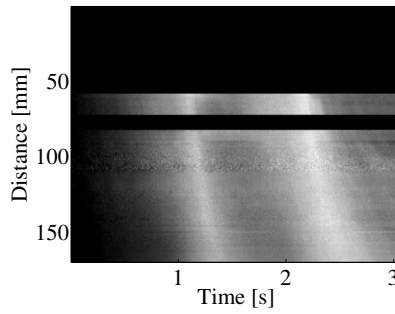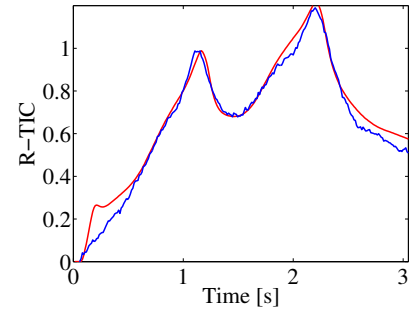
(c) Reliable parts of extracted flow map.

(e) Extracted (blue) and fitted (red) TIC, proximal segment.

(b) Reconstructed geometric model.
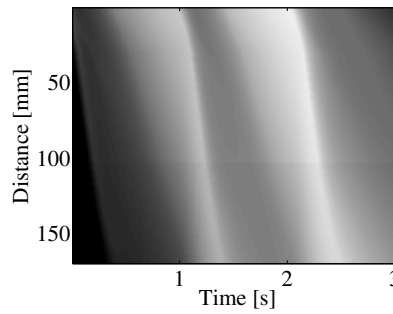
(d) Simulated flow map (best fit from flow map fitting).
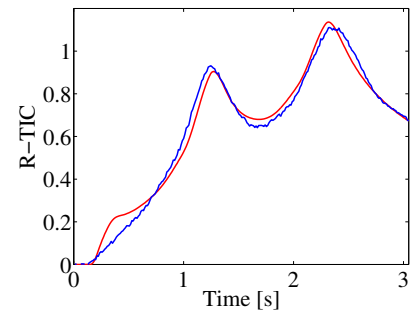
(f) Extracted (blue) and fitted (red) TIC, distal segment.

Figure 8.10: Overview patient 5.
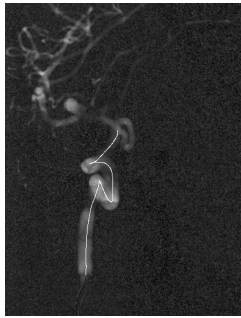
(a) Centreline in DSA image.
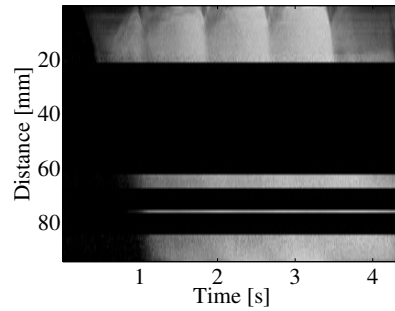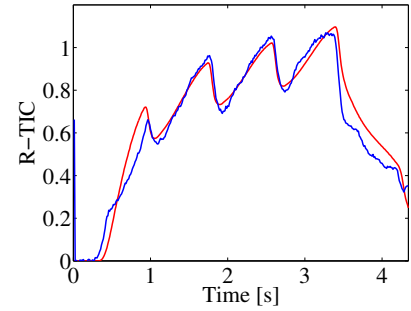
(c) Reliable parts of extracted flow map.

(e) Extracted (blue) and fitted (red) TIC, proximal segment.
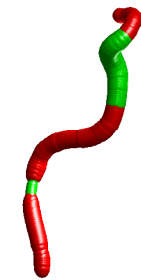
(b) Reconstructed geometric model.
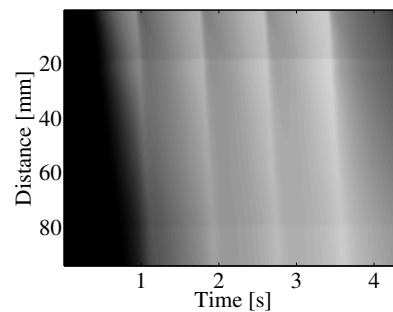
(d) Simulated flow map (best fit from flow map fitting).
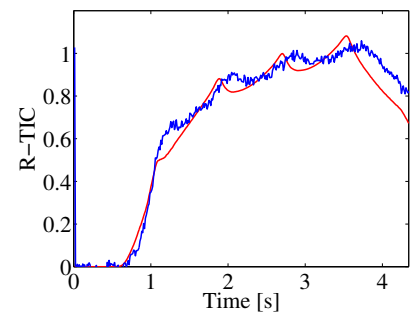
(f) Extracted (blue) and fitted (red) TIC, distal segment.

Figure 8.11: Overview patient 6.

(a) Centreline in DSA image.

(b) Reconstructed geometric model.

(c) Reliable parts of extracted flow map.

(d) Simulated flow map (best fit from flow map fitting).

(e) Extracted (blue) and fitted (red) TIC, proximal segment.

(f) Extracted (blue) and fitted (red) TIC, distal segment.
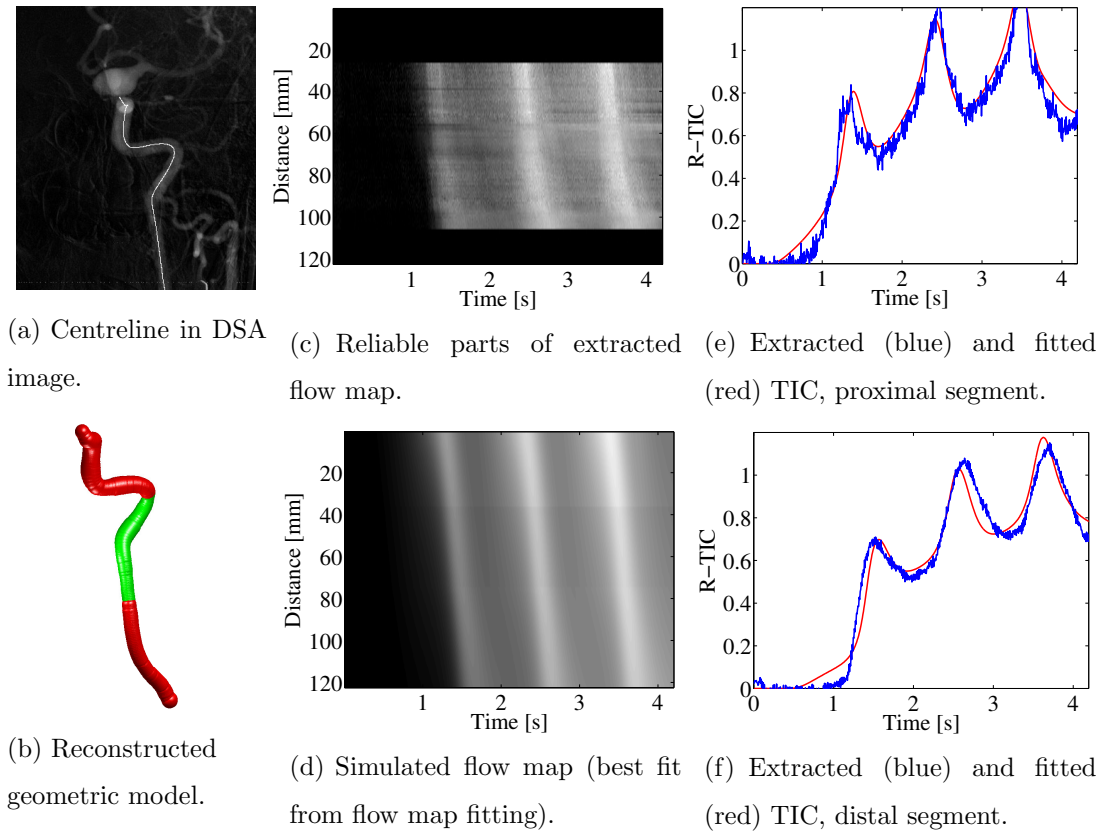
Figure 8.12: Overview patient 7.

(a) Centreline in DSA image.

(b) Reconstructed geometric model.

(c) Reliable parts of extracted flow map.

(d) Simulated flow map (best fit from flow map fitting).

(e) Extracted (blue) and fitted (red) TIC, proximal segment.

(f) Extracted (blue) and fitted (red) TIC, distal segment.
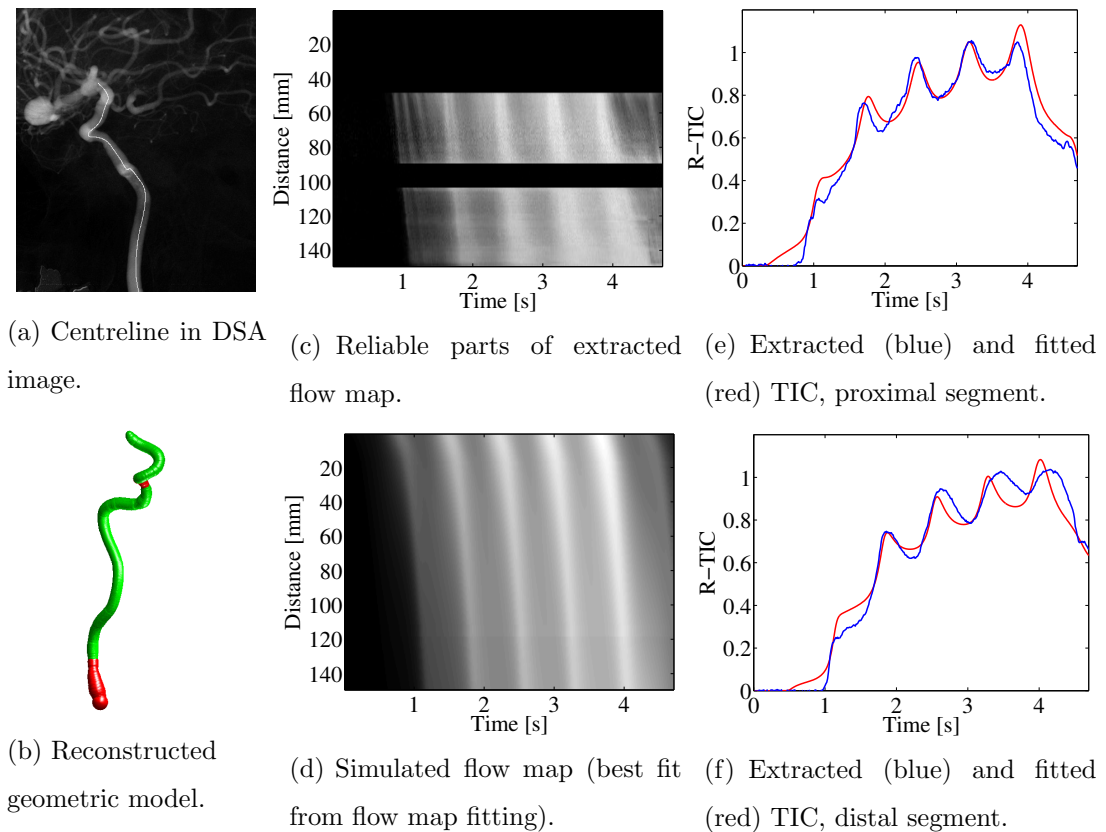
Figure 8.13: Overview patient 8.

(a) Centreline in DSA image.

(b) Reconstructed geometric model.

(c) Reliable parts of extracted flow map.

(d) Simulated flow map (best fit from flow map fitting).

(e) Extracted (blue) and fitted (red) TIC, proximal segment.

(f) Extracted (blue) and fitted (red) TIC, distal segment.
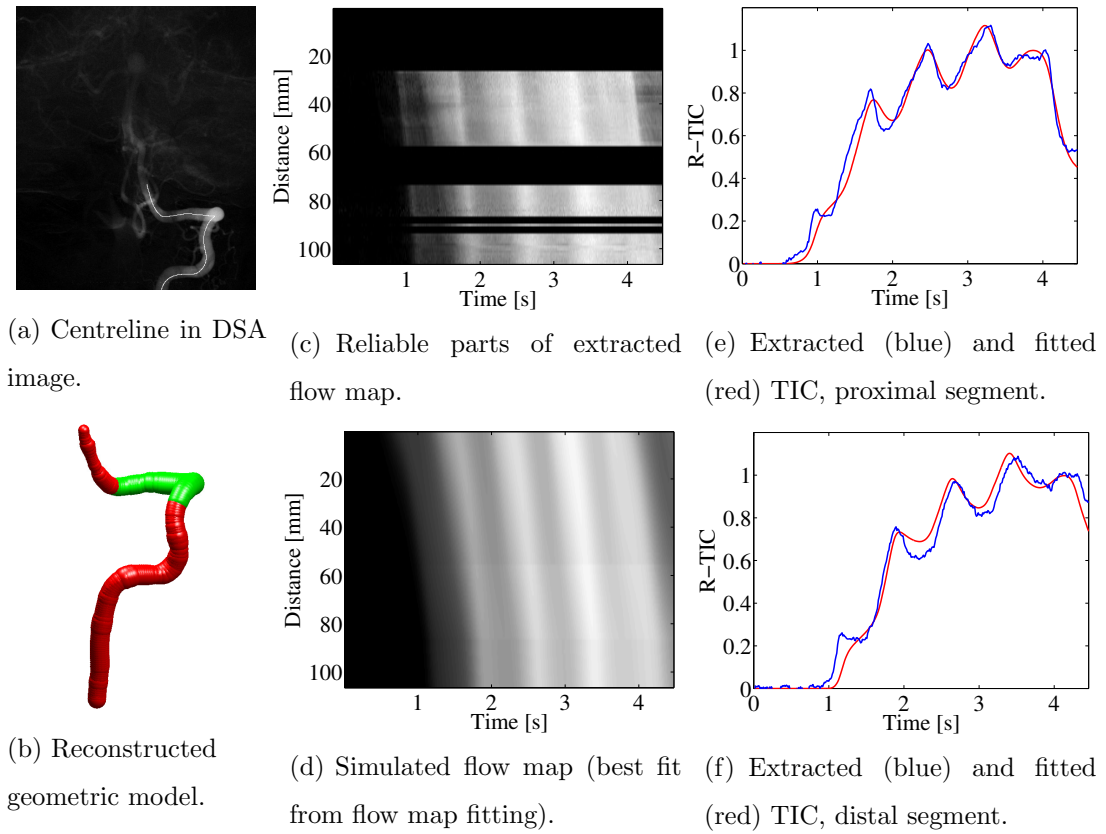
Figure 8.14: Overview patient 9.

(a) Centreline in DSA image.

(b) Reconstructed geometric model.

(c) Reliable parts of extracted flow map.

(d) No simulated flow map available.

(e) Extracted TIC, proximal segment.

(f) Extracted TIC, distal segment.
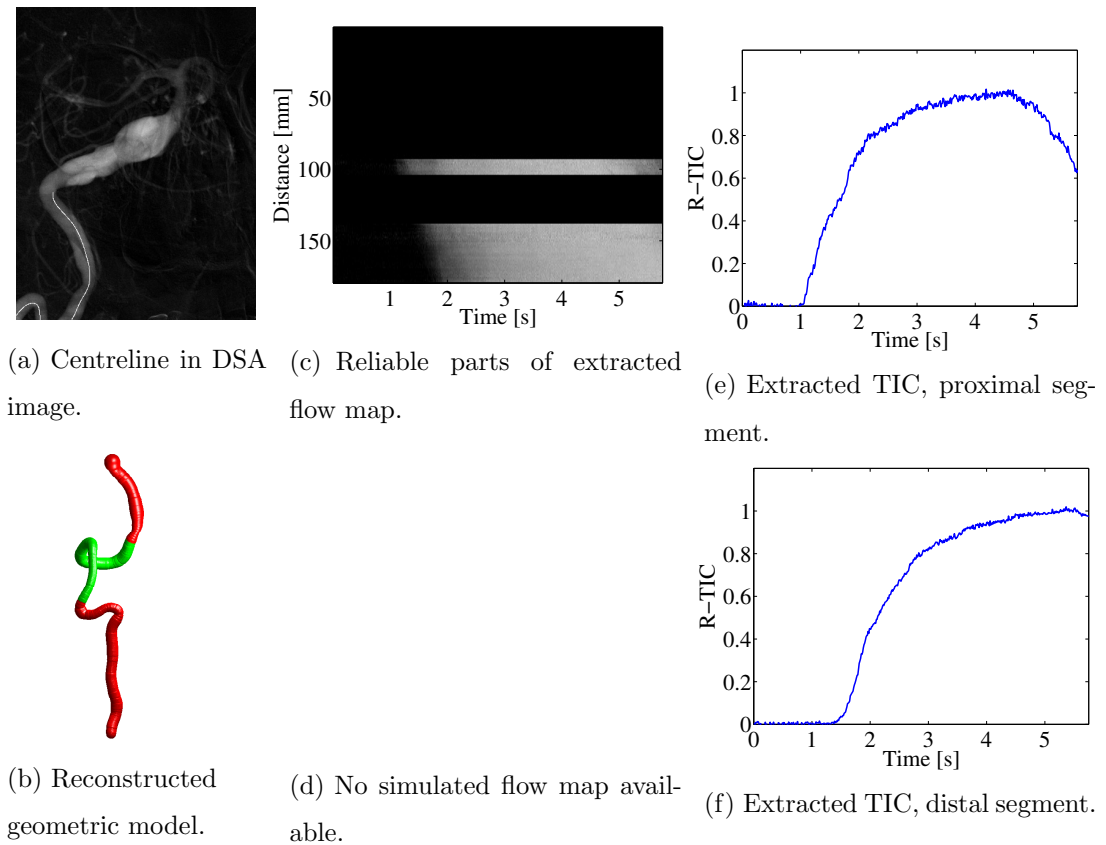
Figure 8.15: Overview patient 10.
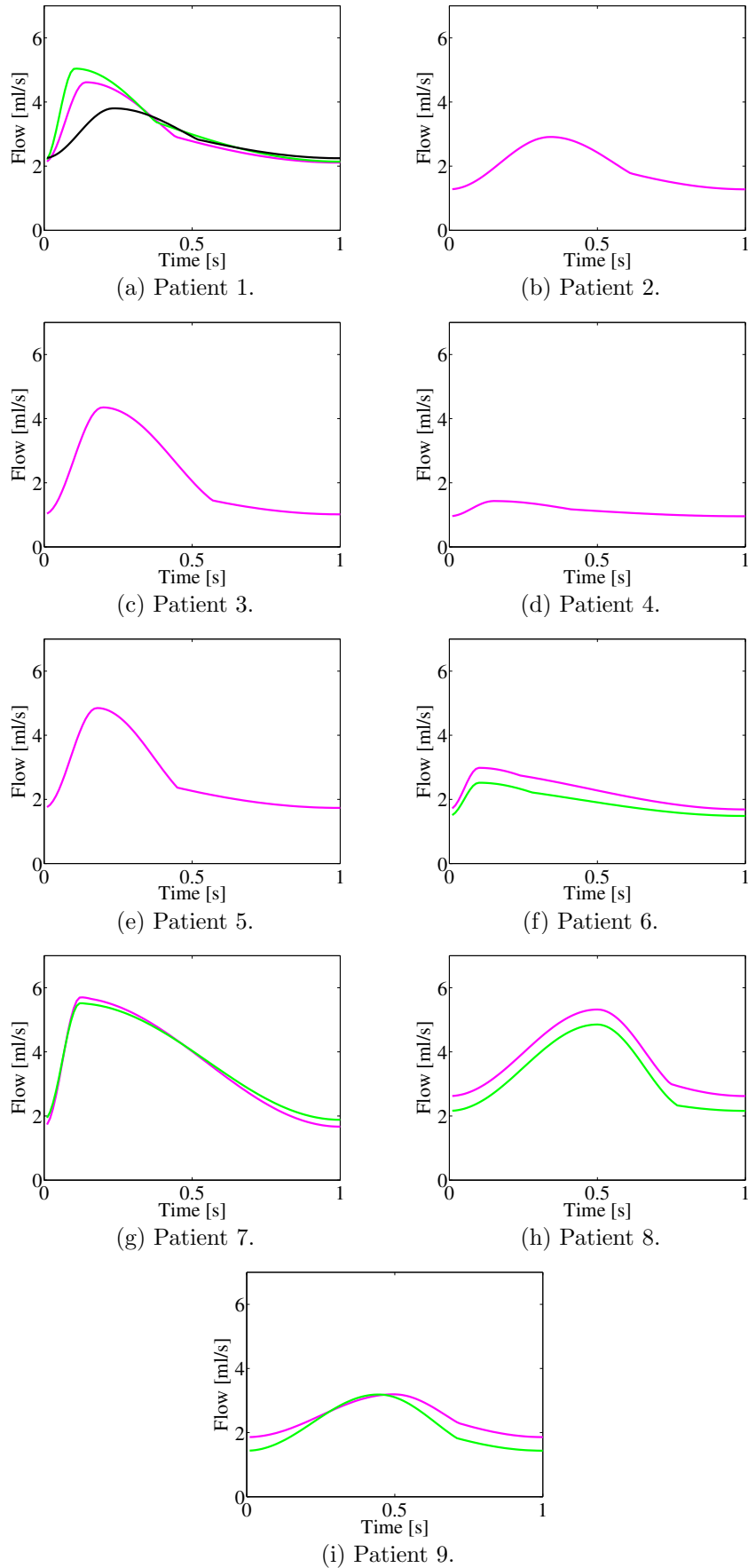
Figure 8.16: Results of flow quantification using the flow map fitting method. Estimates from different angiographic runs are shown in different colours.

Patient number	Mean flow error [%]	Waveform error [%]
1b	-5.4	8.6
1c	4.0	14.3
6	12.8	13.3
7	-1	3.4
8	11.6	11.6
9	9.3	11.6

Table 8.2: Reproducibility study: comparison between estimates from flow map fitting from repeated acquisitions.

(a) Patient 1.

(b) Patient 5.
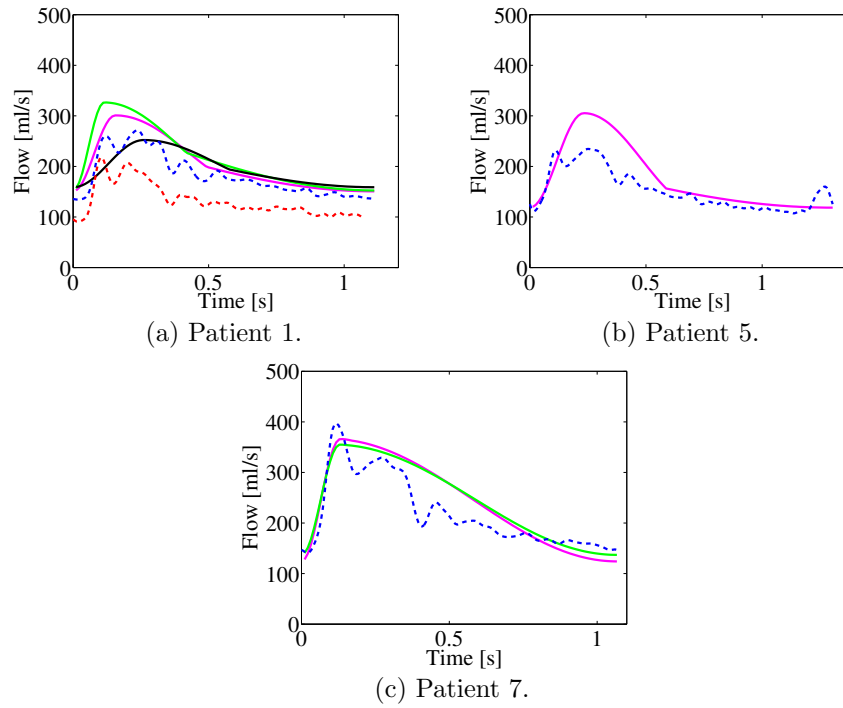
(c) Patient 7.

Figure 8.17: Comparison of results from flow map fitting with TCCD measurements, for patients with a good fit. Estimates from the flow map fitting are presented as solid lines, measurements from TCCD are presented as dashed lines, repeated measurements are shown in different colors.

variations of the patterns in the flow map.

For the patients, where multiple flow sequences were available the reproducability can be analysed. For this analysis the flow estimate of the first sequence is considered as ground truth. Then, the mean flow error and the waveform error error were determined using Equations 7.12 and 7.13, respectively. Table 8.2 shows the results.

For some patients, TCCD flow measurements were obtained beforehand. If TCCD measurements were available, they were used for comparison. The resulting flow estimates of the best fit of the flow map fitting are shown together with the TCCD flow measurements in Fig-

(a) Patient 2.   (b) Patient 4.
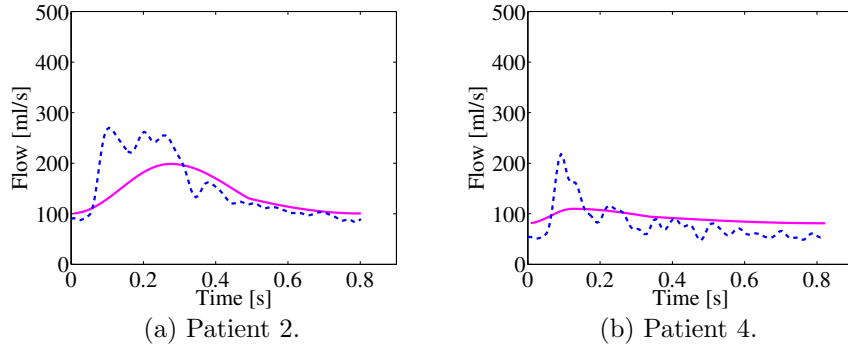
Figure 8.18: Comparison of results from flow map fitting with TCCD measurements, for patients where problems were apparent during the fitting. Estimates from the flow map fitting are presented as solid lines, measurements from TCCD are presented as dashed lines.

Patient number	Mean flow error [%]	Waveform error [%]
1a	-12.3	15.5
1b	-18.4	23.3
1c	-7.7	13.8
5	-16.0	26.0
7a	-9.8	19.3
7b	-11	18.6

Table 8.3: Comparison between estimates from flow map fitting and TCCD measurements for patients where no problems were apparent during the fitting.

ure 8.17 and Figure 8.18. The former contains the results for the patients where no problems were apparent during the fitting, the later contains the results for the remaining patients.

For the patients, where TCCD was available the mean flow error and the waveform error were determined using Equations 7.12 and 7.13, respectively, with the TCCD as the ground truth. Table 8.3 shows the results for the patients where no problems were apparent during the fitting. Table 8.4 shows the results for the remaining patients.

8.2.4 Discussion

In this section, the flow map fitting method was applied to clinical, planar DSA images. The main questions were whether the extracted flow maps are suitable for the flow map fitting, whether the flow model is capable of explaining blood flow and contrast agent transport in

Patient number	Mean flow error [%]	Waveform error [%]
2	7.0	29.0
4	-13.9	38.2

Table 8.4: Comparison between estimates from flow map fitting and TCCD measurements for patients where problems were apparent during the fitting.

patients, how reproducible the flow estimates are, and how the flow estimates compare with the TCCD measurements.

Before the interpretation of the results, it is important to note that the TCCD measurements do not necessarily present an accurate ground truth. Firstly, they were acquired about 30 min before or after the intervention and, secondly, they might be inaccurate as volumetric flow measurements with ultrasound are less reliable than velocity measurements. The sonographer performing the TCCD scans stated that the radius can have an error up to 20%, which would give an error up to 40% for the mean volumetric flow rate, assuming that the velocity can be measured accurately. For Patient 1, two TCCD measurements are available and the mean flow differs by 30% between these measuements.

For nine out of ten patients, flow maps which were suitable for the flow map fitting could be extracted. A flow map is suitable for the flow map fitting if the flow pattern is visible. For Patient 1 to 9 the flow pattern was clearly visible. Only for Patient 10, the flow map was not suitable as no pattern was visible. A possible reason for this is the large distance between the observed region and the injection site. The flow map from Patient 4 exhibits an irregular flow pattern: where a second trough due to high flow during systole is expected, the intensities in the flow map stay high. A possible explanation for this is an asystole. To make the flow map fitting possible, this part of the flow map was regarded as unreliable.

To analyse whether the flow model can explain blood flow and contrast agent transport in a patient, the quality of the fit was analysed. For all 9 patients it was possible to fit a simulated flow map to the extracted flow map. Very good fits were obtained for two patients, good fits were obtained for four patients. For Patient 2 and Patient 6 a good fit could be obtained in the proximal part of the flow map but some problems with the fit were apparent in the distal part of the flow map. Therefore, I conclude that the model is applicable for most patients. Further analysis is required to find the reasons for the two case where problems were apparent.

For five patients, multiple angiographic acquisitions were available. For all five patients the mean flow (mean flow error $5.2\% \pm 7.3\%$) and the shape of the waveform (waveform error $10.5\% \pm 4\%$) were very similar for consecutive sequences, even when these were acquired using different orientations of the c-arm. Therefore, I conclude that the flow estimates of the flow map fitting method are reproducible.

For five patients, TCCD measurements were available. Overall the agreement was better for the dataset where no problems were apparent during the flow map fitting. In this case, the mean flow error was $12.5\% \pm 4.0\%$ and the waveform error was $19.4\% \pm 4.6\%$. For Patient 1, two TCCD measurements were acquired. The mean flow rate of both measurements, however, differed by about 30%. The estimates from the flow map fitting agree resonably well with the measurement with the higher mean flow rate. For Patients 5 and 7, the estimates from the flow map fitting also agree reasonably well with the TCCD measurements. For the problematic datasets, the shape of the TCCD waveforms and the estimated waveform differ more (waveform

error $33.6\% \pm 6.5\%$) . For Patient 4, this can be explained with the problems during the fitting. For Patient 2, this can be explained by the irregular flow pattern. The mean flow estimates, however, agree well with the TCCD measurements (mean flow error $-3.1\% \pm 14.3\%$).

The blood flow estimates of the flow map fitting depend on the resistance factor, which describes how the physiological flow is disturbed by the injection. During the flow map fitting, only the disturbed flow can be determined. The physiological flow is then determined according to Equation 3.7. The resistance factor is zero if the injection does not disturb the blood flow and it is one when the injection replaces the blood so that the total flow remains unchanged. Its value depends on the ratio of the upstream and downstream resistances. Theoretically, the value should be near to one as for an arterial injection the downstream resistance is much higher than the upstream resistance. However it was reported in the literature that the total flow is affected by the injection, which indicates that the resistance factor must be lower.

The sonographer, who conducted the TCCD measurements for this study, tried to measure the flow before and during the injection to determine the resistance factor. However, in our setup it was not possible to measure the flow during the injection with TCCD. During image acquisition, only the disturbed flow can be observed. Therefore, the resistance factor cannot be determined during the flow map fitting. Introducing the resistance factor as an optimisation variable would create an underdetermined system and arbitrary flow results.

For this evaluation, the resistance factor was set to 0.5. The resulting estimate for the physiological flow would be lower if the resistance factor had been lower. For patient 1, the influence of the resistance factor on the blood flow estimate is shown in Figure 8.19(a). If the flow rate of the injection can be reduced, the disturbance will be reduced as well. The theoretical influence on the blood flow estimate of a reduced injection is shown in Figure 8.19(b).

In retrospect, the best overall agreement with TCCD would have been achieved with a resistance factor of 0.29. When this resistance factor was used, the mean flow error could be reduced to -0.25% ± 4.5% and the waveform error can be reduced to $15.3\% \pm 4.2\%$. This value is in good agreement with a value that can be determined from the work of Jacobson et al. (1981). The material presented in this work allows computation of the resistance factor for the canine superior mesenteric artery. For an injection of half the blood flow rate, the resistance factor was 0.36. For an injection with equal flow rate as the blood flow, the resistance factor was 0.29. For an injection of twice the blood flow rate, the resistance factor was 0.2. Although these values are in good agreement, further research is required to determine the *in-vivo* resistance factor and its dependence on the injection flow rate, on the artery where the catheter is placed, and possibly on other factors.

For some patients, small changes in the model had to be made. For earlier patients, the catheter was filled with contrast agent at the beginning of the acquisition and then the concentration gradually increased. To model this, the rectangle function in the mixing model had to be replaced by a ramp function. For some patients, small parts of the contrast agent moved
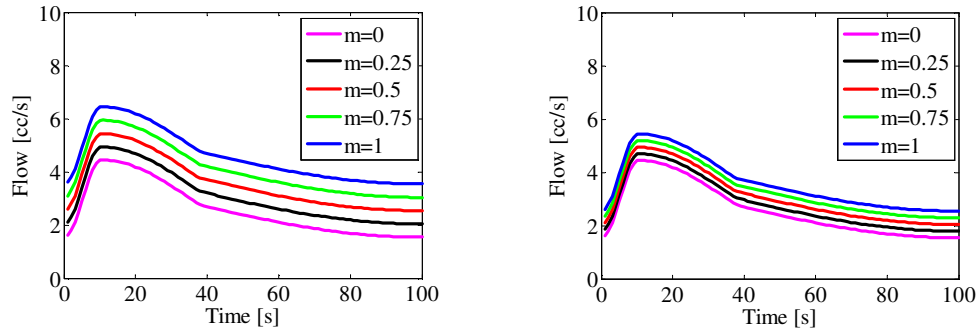
(a) Influence of resistance factor on blood flow estimate for an injection of 2 ml/s.

(b) Influence of resistance factor on blood flow estimate for a theoretical injection of 1 ml/s.

Figure 8.19: Influence of resistance factor on blood flow estimate.

upstream and increased the concentration in the later frames, this was also incorporated in the mixing model.

Although the flow map fitting was designed for flow quantification from rotational angiography, it could successfully be applied to a combination of 3DRA and planar angiography. Many concepts, which were developed to make the method robust enough for rotational angiography, are also beneficial for planar angiography. One example is the reliability map: For no patient, a complete flow map with neither foreshortening nor overlapping vessel could be extracted. Therefore, some other methods would not be applicable. The reliability map together with the model-based approach made it possible to use only observations which were not corrupted.

9

Conclusions and future work

In this thesis, I have presented a system for the quantification of blood flow from rotational angiography: First, the centreline and radii are determined from the rotational sequence. Using this information and plus additional information from the geometry and attenuation calibration, the flow map can be determined. During the flow map fitting, the volumetric mean flow rate and the blood flow waveform are estimated. To achieve this, a simulated flow map, which was generated using a model of blood flow and contrast agent transport, is fitted to the flow map which was extracted from the angiographic images. The model parameters of the best fit give the flow estimate.

For the flow quantification from rotational angiography, it is beneficial if the rotational sequence shows inflow and outflow of contrast agent. This, however, hampers the standard 3D reconstruction. I have proposed a method for 3D vessel reconstruction, which uses flow information to overcome this problem. A satisfactory reconstruction and segmentation accuracy (centreline error 0.50 mm $\pm$ 0.12 mm, radius error 0.29 mm $\pm$ 0.05 mm) was achieved when every vessel segment was filled with contrast agent over 135°. As a standard c-arm can rotate 205°, typically about one third of the acquisition can show inflow or outflow of contrast agent. This makes it feasible that the vessel geometry and blood flow are determined from the same angiographic sequence.

Compared with alternative state-of-the-art methods, the flow map fitting approach has the following fundamental advantages: Firstly, it uses an explicit, physically-based model for the contrast agent propagation to support the flow quantification. Secondly, it is capable of using both kinematic and densitometric information from angiographic images concurrently; the convection model enables the use of kinematic information, whereas the model of the mixing at the injection site enables the use of densitometric information. Relative densitometric information, given by the pulsatile pattern of the flow map, is used to determine the shape of the waveform. Absolute densitometric information can be used to determine the mean volumetric flow rate.

Because of these properties, several important improvements on state-of-the-art methods can be achieved:

- The method is very robust to noise and artefacts because the whole flow map is used at once.

- The method can be adapted to different scenarios. For example, if information from an attenuation calibration or information about the timing of the injection is available, this can be used to support the flow quantification. Missing information can be estimated.

- If additional information is available, the method can compute flow estimates from flow maps that are very short (in the spatial dimension). This increases the clinical applicability as the vessel length in patients is limited.

- As a convective dispersion model is used, the flow estimate does not depend on the distance from the injection site, and overestimation during the inflow phase and underestimation during the outflow phase, reported elsewhere, can be prevented.

- Because of the choice of representation of the vessel geometry, changes in vessel lumen radius (for instance, at a stenosis) and bifurcations can be handled. Therefore, observations from several vessel segments can be combined.

The flow map fitting algorithm was designed specifically for flow quantification from rotational angiography, although the method is also applicable to planar angiography. On the one hand, this has the advantage that the 3D geometry can be determined from the same sequence, but, on the other hand, there is the disadvantage that the rotation introduces artefacts in the flow map because of overlapping vessels and foreshortened vessels. Therefore, a method for flow quantification from rotational angiography must be more robust against artefacts in the flow maps than a method for planar angiography. This was apparent from the rotational flow maps from the more complex phantoms used in the experimental work described in the thesis, and in the rotational flow maps from the patient images. For this reason, a reliability map was introduced to reduce the influence of artefacts. To the best of my knowledge, I have presented the first quantitative results for flow estimation from rotational angiography. For most datasets from the computer simulation and the experimental setup, the relative error was between 5% and 10% for the volumetric mean flow rate, and between 10% and 15% for the blood flow waveform. From these results, I conclude that the flow map fitting has the potential to determine flow from rotational angiography with an accuracy that is clinically useful. Importantly, the analysis of the data from the computer simulation and the experimental setup have also led to recommendations for a clinical protocol.

Unfortunately, the clinical injection and acquisition protocol of rotational angiography could not be adapted without dedicated ethical approval, which could not be obtained within the time-frame and resources available for this thesis. Therefore, some of the proposed protocol

recommendations could not be met. As a result of this, the rotational flow maps from the patient sequences were not suitable for the flow map fitting method. However, I believe that application of the flow map fitting is possible if small changes in the rotational angiography protocol are implemented (as detailed below).

The flow map fitting was also applied to flow maps from planar angiographic sequences of patients. For nine out of ten patients, flow maps which are suitable for the flow map fitting could be obtained from the angiographic sequences. A good agreement of the extracted and the simulated flow map could be obtained for six out of nine patients, although some problems were apparent for the remaining three patients. From this, I conclude that the flow model is applicable to the majority of patients. Further improvements of the model might improve the fit for the remaining patients.

For the patients where a good fit could be obtained, the resulting flow estimates agreed reasonably well with the measurements from TCCD. For a resistance factor (which describes the disturbance of the blood flow due to the injection) of 0.5, the mean flow error was $12.5\% \pm 4.0\%$ and the waveform error was $19.4\% \pm 4.6\%$. Best agreement with TCCD was obtained with a resistance factor of 0.29 (mean flow error $-0.2\% \pm 4.5\%$ and waveform error $15.3\% \pm 4.2\%$). For some patients, no TCCD measurements were available, but flow map fitting on repeated angiographic sequences showed that the results were reproducible (mean flow error $5.2\% \pm 7.3$, waveform error $10.5\% \pm 4\%$). I, therefore, conclude that the quantification of blood flow using the flow map fitting method is clinically feasible.

In this thesis, many ideas and solutions for the flow quantification from rotational angiography were presented. However, to become clinically useful, some more problems have to be solved. In particular, future work could address the following aspects:

- **Design of a suitable clinical protocol for flow quantification from rotational angiography**: As explained in the previous section, a suitable clinical protocol should contain a contrast agent injection with a lower flow rate, so that a pulsatile pattern can develop, and a shorter duration, so that the inflow phase is visible in the sequence. The x-ray protocol should allow for an attenuation calibration.

- **Extension to more complex vessel trees and pathologies**: When the flow map fitting is applied to more complex vessel trees, it might be necessary to incorporate an elastic model which describes the changes of the flow waveform in segments further away from the injection site. Additionally, the flow map fitting should be evaluated on smaller vessels. An important issue is the presence of aneurysms, since the flow model cannot describe complex haemodynamics in aneurysms. However, it should be possible to describe the flow before and after an aneurysm by modelling the aneurysm as a reservoir which takes up contrast agent and releases it later. For the flow quantification at the Circle of Willis, the flow model should be adapted to incorporate junctions.

- **Extension to flow quantification in the coronary arteries**: The flow quantification

in the coronary arteries is of particular interest, but it is also particular challenging. To extract the flow map, motion-compensated DSA and vessel tracking are required. The contraction of the heart changes the blood flow, and, therefore, it might be necessary to adapt the flow model.

- **Analysis of disturbance of the blood flow due to the injection**: The contrast agent injection disturbs the blood flow. To accurately determine the physiological blood flow, this has to be taken into account. The issue requires further in-vivo examinations and probably an adaptation of the flow model.

- **Validation with CFD simulations**: For the validations which were based on simulated flow maps, a very similar model was used as during the flow map fitting. This could be replaced with a CFD simulation. The model which is used for the flow map fitting could be replaced in the future when the required computational power is available.

- **Utilisation of this work's results to determine boundary conditions for CFD simulations**: Many CFD simulations determine the patient specific vascular geometry from the 3DRA reconstruction but the flow boundaries are typically determined from sex- and age-matched volunteers. It would be of interest to determine the flow boundary conditions from the rotational angiographic sequence.

A

Appendix

A.1   Overview of parameters for datasets from experimental setup

Phantom number	Mean flow circulation [ml/min]	Pulsatility []	Concentration of Glycerine []	Maximum flow injection [ml/s]	Duration injection [s]	Flow division at bifurcation []
1	100	0.7	0.3	2	3	-
1	150	0.7	0.3	3	3	-
1	250	0.7	0.3	5	3	-
1	200	0.7	0	4	3	-
1	200	0.7	0	2	3	-
1	200	0.7	0	3	3	-
1	200	0.7	0	4	3	-
1	200	0.5	0	4	3	-
3	300	0.6	0.3	3	3	0.5
3	300	0.7	0.3	3	3	0.5
3	300	0.8	0.3	3	3	0.5
3	300	0.6	0.3	3	3	0.5
3	300	0.8	0.3	3	3	0.5

Phantom number	Mean flow circulation [ml/min]	Pulsatility []	Concentration of Glycerine []	Maximum flow injection [ml/s]	Duration injection [s]	Flow division at bifurcation []
3	300	0.6	0	3	3	0.5
3	300	0.7	0	3	3	0.5
3	300	0.8	0	3	3	0.5
3	300	0.6	0	3	3	0.66
4	300	0.8	0.3	3	3	0.4
4	300	0.8	0.3	3	3	0.5
4	300	0.8	0.3	3	3	0.5
4	300	0.8	0.3	3	3	0.6
4	300	0.8	0.3	6	3	0.34
4	300	0.8	0.3	6	3	0.45
4	300	0.8	0.3	6	3	0.55
4	300	0.8	0.3	6	3	0.65
4	300	0.8	0.3	6	3	0.35
4	300	0.8	0.3	6	3	0.45
4	350	0.8	0.3	6	3	0.6
4	350	0.8	0.3	6	3	0.6
4	350	0.8	0.3	6	3	0.5
4	350	0.8	0.3	6	3	0.4
5	300	0.7	0	6	3	0.66
5	300	0.7	0	3	3	0.66
5	300	0.5	0	3	3	0.66
5	300	0.6	0	3	3	0.66
5	300	0.8	0	3	3	0.66
5	300	0.7	0	3	2	0.66
5	300	0.7	0	3	3	0.83
5	300	0.8	0	3	3	0.83
6	300	0.7	0	6	3	0.5
6	300	0.7	0	6	3	0.66
6	300	0.7	0	6	3	0.83
7	200	0.7	0.3	2	3	-

Continued on Next Page...

Phantom number	Mean flow circulation [ml/min]	Pulsatility []	Concentration of Glycerine []	Maximum flow injection [ml/s]	Duration injection [s]	Flow division at bifurcation []
7	200	0.7	0.3	3	3	-
7	200	0.7	0.3	4	3	-
7	200	0.5	0.3	4	3	-
7	200	0.9	0.3	4	3	-
7	200	0.7	0	2	3	-
7	200	0.7	0	3	3	-
7	200	0.7	0	4	3	-
7	150	0.7	0	3	3	-
7	250	0.7	0	5	3	-
7	200	0.5	0	4	3	-
8	100	0	0	2	3	-
8	100	0	0	2	3	-
8	150	0	0	3	4	-
8	150	0	0	4	6	-
9	200	0.8	0	4	3	-
9	200	0.8	0	4	3	-
9	150	0.8	0	3	3	-
9	250	0.8	0	5	3	-

Table A.1: Overview of variable parameters of experimental setup.

For the description of the setup, see Section 4.3.

A.2 Tabulation of results of flow map fitting

Phantom number	EMF mean flow [ml/min]	Estimated mean flow [ml/min]	Waveform error [%]	Mean flow error [%]
1	193.3	213.0	19.7	10.2
1	92.5	106.6	15.3	15.3
1	147.3	167.5	13.7	13.7
1	239.4	230.2	11.1	-3.8
1	191.1	205.3	13.9	7.4
1	189.2	199.4	11.6	5.4
1	192.4	201.5	11.0	4.7
1	195.7	233.3	22.6	19.2
1	197.8	230.2	16.4	16.4
3	278.6	247.4	11.5	-11.2
3	276.1	247.1	10.6	-10.5
3	282.3	258.0	10.3	-8.6
3	294.9	303.9	11.8	3.1
3	290.7	297.8	18.1	2.5
3	294.9	248.4	16.0	-15.8
3	297.1	249.0	17.8	-16.2
3	288.1	243.1	16.6	-15.6
5	303.3	333.8	13.1	10.1
5	303.7	311.2	5.3	2.5
5	295.2	315.9	7.7	7.0
5	300.7	307.3	7.3	2.2
5	304.7	300.8	7.8	-1.3
5	299.5	280.6	10.2	-6.3
5	295.4	277.5	8.5	-6.1
5	288.6	258.4	15.4	-10.5
6	281.4	300.0	22.9	6.6
6	297.5	290.8	14.3	-2.3
6	291.7	270.2	13.9	-7.4
7	192.3	167.4	13.0	-13.0
7	197.6	185.4	7.3	-6.2
7	191.6	193.1	10.7	0.8
7	247.8	245.4	6.6	-1.0
7	193.3	198.9	5.7	2.9

Continued on Next Page. . .

Phantom number	EMF mean flow [ml/min]	Estimated mean flow [ml/min]	Waveform error [%]	Mean flow error [%]
7	196.8	188.2	11.7	-4.4
7	191.3	176.5	7.9	-7.8
7	191.2	177.7	9.1	-7.1
7	191.6	189.3	9.3	-1.2
7	146.1	147.0	12.7	0.6
7	247.4	244.4	10.0	-1.2
7	198.0	195.5	8.0	-1.3

Table A.2: Results of flow map fitting with fixed calibration in main branch of phantoms. For description of setup, see Section 7.3.3 and 7.3.4.

Phantom number	EMF mean flow [ml/min]	Estimated mean flow [ml/min]	Waveform error [%]	Mean flow error [%]
1	193.3	175.5	11.3	-9.2
1	92.5	122.9	33.0	33.0
1	147.3	192.4	31.2	30.6
1	239.4	209.3	12.6	-12.6
1	191.1	209.6	17.2	9.7
1	189.2	200.0	13.3	5.7
1	192.4	199.5	15.8	3.7
1	195.7	174.1	14.0	-11.1
1	197.8	209.8	13.2	6.1
3	278.6	250.7	10.8	-10.0
3	276.1	261.6	7.4	-5.3
3	282.3	262.5	9.8	-7.0
3	294.9	251.9	16.4	-14.6
3	290.7	235.8	18.9	-18.9
3	294.9	284.2	11.9	-3.6
3	297.1	257.9	13.8	-13.2
3	288.1	211.9	27.2	-26.4
5	303.7	270.2	11.0	-11.0
5	295.2	311.9	6.9	5.7

Phantom number	EMF mean flow [ml/min]	Estimated mean flow [ml/min]	Waveform error [%]	Mean flow error [%]
5	300.7	283.0	7.3	-5.9
5	304.7	325.0	11.9	6.7
5	299.5	253.6	15.3	-15.3
5	295.4	279.6	7.5	-5.4
5	288.6	294.4	6.2	2.0
6	281.4	286.9	19.1	2.0
6	297.5	294.9	11.8	-0.9
6	291.7	293.6	11.5	0.7
7	192.3	169.2	12.0	-12.0
7	197.6	196.6	8.8	-0.5
7	191.6	182.7	9.5	-4.7
7	247.8	226.1	12.2	-8.8
7	193.3	179.7	9.3	-7.0
7	196.8	178.6	15.2	-9.2
7	191.3	184.7	11.7	-3.5
7	191.2	186.2	10.2	-2.6
7	191.6	185.9	15.1	-3.0
7	146.1	141.9	13.7	-2.8
7	247.4	215.6	12.8	-12.8
7	198.0	182.0	9.6	-8.1

Table A.3: Results of flow map fitting with fixed injection in main branch of phantoms. For description of setup, see Section 7.3.3 and 7.3.4.

Phantom number	EMF mean flow [ml/min]	Estimated mean flow [ml/min]	Waveform error [%]	Mean flow error [%]
1	193.3	273.2	42.6	41.3
1	92.5	138.5	49.8	49.8
1	147.3	211.8	44.6	43.8
1	239.4	260.8	14.3	8.9
1	191.1	224.6	22.3	17.5
1	189.2	240.3	30.9	27.0

Phantom number	EMF mean flow [ml/min]	Estimated mean flow [ml/min]	Waveform error [%]	Mean flow error [%]
1	278.6	328.8	18.0	18.0
1	276.1	341.2	23.6	23.6
1	282.3	378.5	34.1	34.1
3	294.9	315.4	10.2	6.9
3	290.7	302.1	10.0	3.9
3	294.9	292.0	7.4	-1.0
3	297.1	295.6	13.8	-0.5
3	288.1	271.1	13.5	-5.9
3	303.3	274.4	9.6	-9.5
3	303.7	251.6	17.2	-17.2
3	295.2	275.2	9.9	-6.8
5	300.7	260.2	14.6	-13.5
5	304.7	251.6	19.7	-17.4
5	299.5	364.1	21.6	21.6
5	299.5	216.3	27.8	-27.8
5	295.4	372.7	26.2	26.2
4	295.4	374.6	26.8	26.8
5	288.6	334.8	16.2	16.0
5	288.6	296.0	6.7	2.6
6	281.4	309.4	21.0	10.0
6	297.5	264.5	11.9	-11.1
6	291.7	275.8	10.4	-5.4
7	192.3	180.5	7.0	-6.1
7	197.6	219.4	11.9	11.1
7	191.6	192.6	9.9	0.5
7	247.8	266.9	10.8	7.7
7	193.3	215.4	12.4	11.5
7	196.8	222.1	18.2	12.9
7	191.3	187.8	6.8	-1.8
7	191.2	161.6	15.5	-15.5
7	191.6	208.2	15.1	8.7
7	146.1	148.6	14.3	1.7
7	247.4	229.8	8.5	-7.1
7	198.0	205.7	9.2	3.9

Table A.4: Results of flow map fitting without constraints in main branch of phantoms. For description of setup, see Section 7.3.3 and 7.3.4.

Phantom number	EMF flow division []	Estimated flow division []	EMF flow branch 1 [ml/min]	Estimated flow branch 1 [ml/min]	EMF flow branch 2 [ml/min]	Estimated flow branch 2 [ml/min]
3	0.50	0.58	139.3	145.9	139.3	105.6
3	0.50	0.58	138.1	140.7	138.1	101.9
3	0.50	0.60	141.2	146.7	141.2	97.8
3	0.50	0.46	147.5	130.2	147.5	152.9
3	0.50	0.43	145.3	117.8	145.3	156.2
3	0.50	0.56	147.4	145.4	147.4	114.2
3	0.50	0.58	148.6	146.0	148.6	105.7
3	0.50	0.57	144.0	145.2	144.0	109.6
5	0.34	0.37	103.1	117.2	200.2	199.5
5	0.34	0.27	103.3	83.4	200.5	225.5
5	0.34	0.36	100.4	106.2	194.8	188.7
5	0.34	0.30	102.2	87.7	198.4	204.7
5	0.34	0.35	103.6	103.3	201.1	191.8
5	0.34	0.34	101.8	99.0	197.7	192.2
5	0.17	0.15	50.2	40.2	245.2	227.6
5	0.17	0.15	49.1	39.9	239.5	226.0
6	0.50	0.44	140.7	127.3	140.7	162.1
6	0.34	0.30	101.1	87.5	196.3	204.1
6	0.17	0.20	49.6	56.2	242.1	224.7

Table A.5: Results of flow map fitting with fixed calibration at bifurcations of phantoms. For description of setup, see Section 7.3.5.

Phantom number	EMF flow division []	Estimated flow division []	EMF flow branch 1 [ml/min]	Estimated flow branch 1 [ml/min]	EMF flow branch 2 [ml/min]	Estimated flow branch 2 [ml/min]
3	0.50	0.58	139.3	150.5	139.3	109.0
3	0.50	0.60	138.1	156.2	138.1	104.1
3	0.50	0.58	141.2	146.1	141.2	105.8
3	0.50	0.47	147.5	118.1	147.5	133.2
3	0.50	0.43	145.3	122.0	145.3	161.8
3	0.50	0.58	147.4	138.8	147.4	100.5
3	0.50	0.54	148.6	174.6	148.6	148.7
3	0.50	0.58	144.0	154.7	144.0	112.0
5	0.34	0.28	103.1	96.7	200.2	248.5
5	0.34	0.30	103.3	90.6	200.5	211.5
5	0.34	0.29	100.4	87.9	194.8	215.1
5	0.34	0.28	102.2	75.6	198.4	194.4
5	0.34	0.34	103.6	109.2	201.1	212.0
5	0.34	0.30	101.8	103.5	197.7	241.4
5	0.17	0.13	50.2	36.7	245.2	245.5
5	0.17	0.15	49.1	42.3	239.5	239.9
6	0.50	0.38	140.7	135.1	140.7	220.4
6	0.34	0.26	101.1	85.7	196.3	243.8
6	0.17	0.17	49.6	55.0	242.1	268.6

Table A.6: Results of flow map fitting with fixed injection at bifurcations of phantoms. For description of setup, see Section 7.3.5.

Phantom number []	EMF flow division []	Estimated flow division []	EMF flow branch 1 [ml/min]	Estimated flow branch 1 [ml/min]	EMF flow branch 2 [ml/min]	Estimated flow branch 2 [ml/min]
3	0.50	0.57	139.3	140.6	139.3	106.1
3	0.50	0.60	138.1	143.1	138.1	95.4
3	0.50	0.57	141.2	135.7	141.2	102.4
3	0.50	0.46	147.5	128.3	147.5	150.6
3	0.50	0.45	145.3	124.4	145.3	152.1
3	0.50	0.59	147.4	148.7	147.4	103.3
3	0.50	0.54	148.6	134.7	148.6	114.8
3	0.50	0.58	144.0	143.0	144.0	103.6
5	0.34	0.35	103.1	117.9	200.2	218.9
5	0.34	0.28	103.3	83.9	200.5	215.7
5	0.34	0.29	100.4	89.1	194.8	218.3
5	0.34	0.25	102.2	79.2	198.4	237.7
5	0.34	0.31	103.6	103.4	201.1	230.0
5	0.34	0.29	101.8	105.7	197.7	258.7
5	0.17	0.15	50.2	40.5	245.2	229.6
5	0.17	0.13	49.1	38.6	239.5	258.5
6	0.50	0.43	140.7	144.6	140.7	191.7
6	0.34	0.26	101.1	87.4	196.3	248.9
6	0.17	0.18	49.6	62.3	242.1	284.0

Table A.7: Results of flow map fitting without constraints at bi-
furcations of phantoms. For description of setup, see Section 7.3.5.

Publications and patents

Journal papers

Waechter, I., Bredno, J., Hermans, R., Weese, J., Barratt, D. C. and Hawkes, D. J. (2008d), Model-based blood flow quantification from rotational angiography, *Medical Image Analysis* **12**(5), 586–602.

Waechter, I., Bredno, J., Weese, J., Barratt, D. C. and Hawkes, D. J. (2008c), Using Flow Information to Support 3D Vessel Reconstruction From Rotational Angiography, *Medical Physics* **35**(7), 3302–3316.

Papers in conference proceedings

Waechter, I., Bredno, J., Hermans, R., Barratt, D. C., Weese, J., and Hawkes, D. J. (2008b), Quantifying blood flow division at bifurcations from rotational angiography, *in 5th IEEE International Symposium on Biomedical Imaging: From Nano to Macro*, 632–635.

Durant, J., Waechter, I., Hermans, R., Weese, J., and Aach, T. (2008), Toward quantitative virtual angiography: Evaluation with in vitro studies, *in 5th IEEE International Symposium on Biomedical Imaging: From Nano to Macro*, 632–635.

Waechter, I., Bredno, J., Hermans, R., Weese, J., Barratt, D. C. and Hawkes, D. J. (2008a), Evaluation of model based blood flow quantification from rotational angiography, *in SPIE Medical Imaging*, **6916**.

Waechter, I., Bredno, J., Weese, J., Barratt, D. C. and Hawkes, D. J. (2007), Quantification of Blood Flow from Rotational Angiography, *in Medical Image Computing and Computer-Assisted Intervention (MICCAI)*, **4791**, 634–641.

Waechter, I., Bredno, J., Weese, J., and Hawkes, D. J. (2006), Using Flow Information to Support 3D Vessel Reconstruction From Rotational Angiography (Abstract only), *Medical Physics* **33**(6), 1983.

Patents

Waechter, I., Bredno, J., Weese, J., Rhode, K. and Hawkes, D. J. (2007), Extracting flow from incomplete flow maps.

Bibliography

Aaslid, R., Markwalder, T. M. and Nornes, H. (1982), Noninvasive transcranial Doppler ultrasound recording of flow velocity in basal cerebral arteries, *Journal of Neurosurgery* **57**(6), 769–774.

Ackerman, M. J., Spitzer, V. M., Scherzinger, A. L. and Whitlock, D. G. (1995), The Visible Human data set: an image resource for anatomical visualization, *Medinfo* **8**(2), 1195–1198.

Almén, T. (1987), Effects of iodixanol, iopentol, iohexol and metrizoate on femoral blood flow after injection into the femoral artery of the dog., *Acta Radiology Supplement* **370**, 69–72.

Alperin, N., Hoffmann, K. and Doi, K. (1991), Automated extraction of vascular information from angiographic images using a vessel-tracking algorithm, *Proceedings of the SPIE* **1396**, 27–31.

Alperin, N., Hoffmann, K. R., Doi, K. and Chua, K. G. (1989), Automated analysis of coronary lesions from cineangiograms using vessel tracking and iterative deconvolution techniques, *Computers in Cardiology* pp.153–156.

Amini, A., Egglin, T. and Pollak, J. (1993), Physical models for measurement of blood velocity and flow from diagnostic images, *Computers in Cardiology* pp.783–786.

Appaji, A. and Noble, J. (2006), Estimating cerebral blood flow from a rotational angiographic system, *in Biomedical Imaging: Macro to Nano*, pp.161–164.

Argosy Publishing (2008), The visible body, http://www.visiblebody.com/.

Aris, R. (1960), On the dispersion of a solute in pulsating flow through a tube, *Proceedings Royal Society of London A* **259**, 370–376.

Bailey, H. R. and Gogarty, W. B. (1962), Numerical and experimental results on the dispersion of a solute in a fluid in laminar flow through a tube, *Proceedings of the Royal Society of London. Series A, Mathematical and Physical Sciences* **269**(1338), 352–367.

Bass, A. (2004), The cerebral hyperperfusion syndrome: what every family doctor should know, *The Israel Medical Association Journal* **6**(1), 52–53.

Baumgartner, R. W., Mathis, J., Sturzenegger, M. and Mattle, H. P. (1994), A validation study on the intraobserver reproducibility of transcranial color-coded duplex sonography velocity measurements, *Ultrasound in Medicine & Biology* **20**(3), 233–237.

Büchi, M., Hess, O. M., Kirkeeide, R. L., Suter, T., Muser, M., Osenberg, H. P., Niederer, P., Anliker, M., Gould, K. L. and Krayenbühl, H. P. (1990), Validation of a new automatic system for biplane quantitative coronary arteriography, *International Journal of Cardiac Imaging* **5**(2-3), 93–103.

Beier, J., Oswald, H. and Fleck, E. (1992), Edge detection for coronary angiograms: Error correction and impact of derivatives, *Computers in Cardiology* pp.513–516.

Bladin, C. F., Colchester, A. C., Hawkes, D. J., Seifalian, A. M., Iqbal, N. and Hardingham, C. R. (1996), Morphological and hemodynamic assessments of carotid stenosis using quantitative digital subtraction angiography, *Stroke* **27**(9), 1672–1678.

Blondel, C., Malandain, G., Vaillant, R. and Ayache, N. (2006), Reconstruction of coronary arteries from a single rotational X-ray projection sequence, *IEEE Transactions on Medical Imaging* **25**(5), 653–663.

Blondel, C., Vaillant, R., Devernay, F., Malandain, G. and Ayache, N. (2002), Automatic trinocular 3D reconstruction of coronary artery centerlines, *in Proceedings Computer Assisted Radiology and Surgery*, pp.1073–1078.

Bogunovic, H. and Loncaric, S. (2006), Blood flow and velocity estimation based on vessel transit time by combining 2D and 3D X-ray angiography, *Proceedings of Medical Image Computing and Computer-Assisted Intervention* **4191**, 117–124.

Bredno, J. and Groth, A. (2005), Model based flow analysis and visualization, Patent Application Serial No.: 60/748,808.

Bresler, Y. and Macovski, A. (1984), Estimation of 3-D shape of blood vessels from X-ray image, *in Proceedings IEEE Symposium on Medical Images and Icons*.

Brooks, R. A. and Chiro, G. D. (1976), Beam hardening in x-ray reconstructive tomography., *Phys Med Biol* **21**(3), 390–398.

Brown, B. G., Bolson, E., Frimer, M. and Dodge, H. T. (1977), Quantitative coronary arteriography: estimation of dimensions, hemodynamic resistance, and atheroma mass of coronary artery lesions using the arteriogram and digital computation, *Circulation* **55**(2), 329–337.

Brunt, J. N., Wicks, D. A., Hawkes, D. J., Seifalian, A. M., du Boulay, G. H., Colchester, A. F. and Wallis, A. (1992), The measurement of blood flow waveforms from X-ray angiography. Part 1: Principles of the method and preliminary validation, *Proceedings of the Institution of Mechanical Engineers* **206**(2), 73–85.

Caplan, L. R. (1998), Should intracranial aneurysms be treated before they rupture?, *The New England journal of medicine* **339**(24), 1774–1775.

Carroll, B. A. (1991), Carotid sonography., *Radiology* **178**(2), 303–313.

Castro, M., Putman, C. and Cebral, J. (2006), Patient-specific computational fluid dynamics modeling of anterior communicating artery aneurysms: a study of the sensitivity of intra-aneurysmal flow patterns to flow conditions in the carotid arteries, *American Journal of Neuroradiology* **27**(10), 2061–2068.

Cebral, J., Castro, M., Appanaboyina, S., Putman, C., Millan, D. and Frangi, A. (2005), Efficient pipeline for image-based patient-specific analysis of cerebral aneurysm hemodynamics: technique and sensitivity, *IEEE Transactions on Medical Imaging* **24**(4), 457–467.

Cebral, J. R., Castro, M. A., Soto, O., Löhner, R. and Alperin, N. (2003), Blood-flow models of the circle of Willis from magnetic resonance data, *Journal of Engineering Mathematics* **47**(3), 369–386.

Cebral, J., Yim, P., Löhner, R., Soto, O., and Choyke, P. L. (2002), Blood flow modeling in carotid arteries with computational fluid dynamics and MR imaging, *Acta Radiologica* **9**(11), 1286–1299.

Center for Endovascular and Exovascular Therapy (2008), AVM Embolization, http://www.neurosurgery.pitt.edu/endovascular/treatments/avm.html.

Chen, S. Y. J., Carroll, J. D. and Messenger, J. C. (2002), Quantitative analysis of reconstructed 3-D coronary arterial tree and intracoronary devices, *IEEE Transactions on Image Processing* **21**(7), 724–740.

Chen, Z., Ning, R., Conover, D. and Lu, X. (2006), Blood Flow Measurement by Cone-Beam CT Bolus Imaging, *in Proceedings SPIE Medical Imaging*.

Colchester, A. and Brunt, J. (1983), Measurement of vessel calibre and volume blood flow by dynamic quantitative digital angiography, *Journal of Cerebral Blood Flow & Metabolism* **3**, 640–641.

Colchester, A., Hawkes, D., Brunt, J., du Boulay, G. and Wallis, A. (1986), Pulsatile flow measurements with the aid of 3D-reconstruction from dynamic angiographic recordings, *Information Processing in Medical Imaging* pp.247–265.

Coleman, T. and Li, Y. (1994), On the Convergence of Reflective Newton Methods for Large-Scale Nonlinear Minimization Subject to Bounds, *Mathematical Programming* **67**(2), 189–224.

Coleman, T. and Li, Y. (1996), An Interior, Trust Region Approach for Nonlinear Minimization Subject to Bounds, *SIAM Journal on Optimization* **6**, 418–445.

Cormen, T. H., Leiserson, C. E. and Rivest, R. L. (1990), *Introduction to Algorithms*, MIT Press.

Cornelius, N. and Kanade, T. (1984), Adapting optical-flow to measure object motion in reflectance and x-ray image sequences (abstract only), *SIGGRAPH Computer Graphics* **18**(1), 24–25.

Crawford, D. W., Brooks, S. H., Barndt, R. and Blankenhorn, D. H. (1977), Measurement of atherosclerotic luminal irregularity and obstruction by radiographic densitometry., *Investigative Radiology* **12**(4), 307–313.

Crepeau, R. L. and Silverman, N. R. (1973), Video-densitometric vascular flowrate measurement–some error considerations, *Medical & Biological Engineering & Computing* **11**(3), 319–325.

Dean, John, A. (1992), *Lange's Handbook of Chemistry*, McGraw-Hill.

Delfino, A., Stergiopulos, N., Moore, J. E. and Meister, J. J. (1997), Residual strain effects on the stress field in a thick wall finite element model of the human carotid bifurcation., *Journal of Biomechanics* **30**(8), 777–786.

Department of Health Western Australia (2007), Diagnositic Imaging Pathways, http://www.imagingpathways.health.wa.gov.au/.

DeRouen, T. A., Murray, J. A. and Owen, W. (1977), Variability in the analysis of coronary arteriograms, *Circulation* **55**(2), 324–328.

Deschamps, T. (2001), Extraction de courbes et surfaces par methodes de chemins minimaux et ensembles de niveaux. applications en imagerie medicale 3D, PhD thesis, L'Universite de Paris-Dauphine.

Deschamps, T. and Cohen, L. (2002), Fast extraction of tubular and tree 3D surfaces with front propagation methods, *Proceedings 16th International Conference on Pattern Recognition* **1**, 731–734.

Doriot, P. A., Suilen, C., Guggenheim, N., Dorsaz, P. A., Chappuis, F. and Rutishauser, W. (1992), Morphometry versus densitometry–a comparison by use of casts of human coronary arteries, **8**(2), 121–130.

Doriot, P., Dorsaz, P., L., D. and Rutishauser, W. (1997), Is the indicator dilution theory really the adequate base of many blood flow measurement techniques?, *Medical Physics* **24**(12), 1889–1898.

Dorsaz, P.-A., Dorsaz, L., Doriot, P.-A., Chatelain, P. and Rutishauser, W. (1995), Three-dimensional densitometric assessment of coronary artery stenosis, *Computers in Cardiology* pp.161–164.

Edvinsson, L., MacKenzie, E. T. and McCulloch, J. (1993), *Cerebral Blood Flow and Metabolism*, Raven Press.

Efron, U., Price, R. R., Smith, C. W. and Brill, A. B. (1978), Method to determine the instantaneous blood-flow using cine- or video-densitometric data, *Proceedings of the SPIE* **143**, 154–161.

Eichel, P. H., Delp, E. J., Koral, K. and Buda, A. J. (1988), A method for a fully automatic definition of coronary arterial edges from cineangiograms, *IEEE Transactions on Medical Imaging* **7**(4), 313–320.

Ekambara, K. and Joshi, J. B. (2004), Axial mixing in laminar pipe flows, *Chemical Engineering Science* **59**(18), 3929–3944.

Fabre, P. (1932), Utilisation des forces electromotrices d'induction pour l'enregistrement des variations de vitesse des liquides conducteurs: un nouvel hemodromograph sans palette dans le sang, *Comptes rendus de l'Académie des sciences Paris* **194**, 1097–1098.

Faraday, M. (1832), The Bakerian Lecture: Experimental Researches in Electricity, *Philosophical Transactions of the Royal Society of London* **122**, 163–184.

Feldkamp, L. A., Davis, L. C. and Kress, J. W. (1984), Practical cone-beam algorithm, *Journal of the Optical Society of America A* **1**(6), 612.

Fencil, L., Doi, K., Chua, K. and Hoffman, K. (1989), Measurement of absolute flow rate in vessels using a stereoscopic DSA system, *Computers in Medicine and Biology* **34**(6), 659–671.

Fencil, L. E., Doi, K. and Hoffman, K. R. (1988), Accurate analysis of blood vessel sizes and stenotic lesions using stereoscopic DSA system, *Investigative Radiology* **23**(1), 33–41.

Fick, A. (1870), Ueber die Messung des Blutquantums in den Herzenventrikeln, *Sitzung der Physikalisch Medizinischen Gesellschaft zu Würzburg* p.36.

Fitzpatrick, J. (1985), A Method for calculating velocity in time dependent images based on the continuity equation, *in Proceeedings IEEE Computer Vision and Pattern Recognition.*

Fleagle, S. R., Johnson, M. R., Wilbricht, C. J., Skorton, D. J., Wilson, R. F., White, C. W., Marcus, M. L. and Collins, S. M. (1989), Automated analysis of coronary arterial morphology in cineangiograms: geometric and physiologic validation in humans, *IEEE Transactions on Medical Imaging* **8**(4), 387–400.

Forbes, G., Gray, J. E. and Felmlee, J. P. (1985), Phantom testing of peripheral artery. Absolute blood flow measurement with digital arteriography, *Investigative Radiology* **20**(2), 186–192.

Ford, M., Stuhne, G., Nikolov, H., Habets, D., Lownie, S., Holdsworth, D. and Steinman, D. (2005), Virtual angiography for visualization and validation of computational models of aneurysm hemodynamics, *IEEE Transactions on Medical Imaging* **24**(12), 1586–1592.

Fox, A. (1993), How to measure carotid stenosis, *Radiology* **186**, 316–318.

Frangi, A. F., Hose, R. H. and Ruefenacht, D. A. (2007), The @neurIST Project: Towards understanding cerebral aneurysms, *SPIE Newsroom* .

Frangi, A., Niessen, W., Vincken, K. and Viergever, M. (1998), Muliscale vessel enhancement filtering, *in Proceedings of Medical Image Computing and Computer-Assisted Intervention*, pp.130–137.

Fritts, H. W. and Cournand, A. (1958), The Application of the Fick Principle to the Measurement of Pulmonary Blood Flow, *Proceedings of the National Academy of Sciences* **44**(10), 1079–1087.

Frydrychowicz, A., Markl, M., Harloff, A., Stalder, A. F., Bock, J., Bley, T. A., Berger, A., Russe, M. F., Schlensak, C., Hennig, J. and Langer, M. (2007), Flow-sensitive in-vivo 4D MR imaging at 3T for the analysis of aortic hemodynamics and derived vessel wall parameters, *Rofo* **179**(5), 463–472.

Fujita, H., Doi, K., Fencil, L. E. and Chua, K. G. (1987), Image feature analysis and computer-aided diagnosis in digital radiography, *Medical Physics* **14**(4), 549–556.

Gailloud, P., Pray, J. R., Muster, M., Piotin, M., Fasel, J. H. and Rüfenacht, D. A. (1997), An in vitro anatomic model of the human cerebral arteries with saccular arterial aneurysms, *Surgical and radiologic anatomy* **19**(2), 119–121.

Glor, F., Ariff, B., Hughes, A., Crowe, L., Verdonck, P., Barratt, D., Thom, S., Firmin, D. and Xu, X. (2004), Image-based carotid flow reconstruction: a comparison between MRI and ultrasound, *Physiological Measurement* **25**(6), 1495–1509.

Grant, E. G., Benson, C. B., Moneta, G. L., Alexandrov, A. V., Baker, J. D., Bluth, E. I., Carroll, B. A., Eliasziw, M., Gocke, J., Hertzberg, B. S., Katanick, S., Needleman, L., Pellerito,

J., Polak, J. F., Rholl, K. S., Wooster, D. L. and Zierler, R. E. (2003), Carotid artery stenosis: gray-scale and Doppler US diagnosis–Society of Radiologists in Ultrasound Consensus Conference., *Radiology* **229**(2), 340–346.

Grass, M., Suurmond, R., Schmitt, H., Heiland, S., Haehnel, S. and Sartor, K. (2002), Improved flow reconstruction in 3D rotational angiography (3DRA), *IEEE Nuclear Science Symposium Conference Record* **3**, 1474–1476.

Graves, V. B., Strother, C. M., Partington, C. R. and Rappe, A. (1992), Flow dynamics of lateral carotid artery aneurysms and their effects on coils and balloons: an experimental study in dogs, *American Journal of Neuroradiology* **13**(1), 189–196.

Groden, C., Laudan, J., Gatchell, S. and Zeumer, H. (2001), Three-dimensional pulsatile flow simulation before and after endovascular coil embolization of a terminal cerebral aneurysm., *J Cereb Blood Flow Metab* **21**(12), 1464–1471.

Guggenheim, N., Doriot, P. A., Dorsaz, P. A., Descouts, P. and Rutishauser, W. (1991), Spatial reconstruction of coronary arteries from angiographic images, *Physics in Medicine and Biology* **36**(1), 99–110.

Guo, D. and Richardson, P. (1998), Automatic vessel extraction from angiogram images, *Computers in Cardiology* pp.441–444.

Hamilton, W. F., Moore, J., Kinsman, J. and Spurling, R. G. (1928), Simultaneous determination of the pulmonary and systemic circulation times in man and of a figure related to the cardiac output, *American Journal of Physiology* **84**(2), 338–344.

Hangiandreou, N. J., Folts, J. D., Peppler, W. W. and Mistretta, C. A. (1991), Coronary blood flow measurement using an angiographic first pass distribution technique: a feasibility study, *Medical Physics* **18**(5), 947–954.

Haris, K., Efstratiadis, S., Maglaveras, N., Pappas, C., Gourassas, J. and Louridas, G. (1999), Model-based morphological segmentation and labeling of coronary angiograms, *IEEE Transactions on Medical Imaging* **18**(10), 1003–1015.

Harpen, M. D. and Lecklitner, M. L. (1984), Derivation of gamma variate indicator dilution function from simple convective dispersion model of blood flow, *Medical Physics* **11**(5), 690–692.

Harrison, D. G., White, C. W., Hiratzka, L. F., Doty, D. B., Barnes, D. H., Eastham, C. L. and Marcus, M. L. (1984), The value of lesion cross-sectional area determined by quantitative coronary angiography in assessing the physiologic significance of proximal left anterior descending coronary arterial stenoses, *Circulation* **69**(6), 1111–1119.

Hartmann, A., Mast, H., Choi, J. H., Stapf, C. and Mohr, J. P. (2007), Treatment of arteriovenous malformations of the brain, *Current Neurology and Neuroscience Reports* **7**(1), 28–34.

Hassan, T., Timofeev, E., Ezura, M., Saito, T., Takahashi, A., Takayama, K. and Yoshimoto, T. (2003), Hemodynamic analysis of an adult vein of Galen aneurysm malformation by use of 3D image-based computational fluid dynamics, *American Journal of Neuroradiology* **24**(6), 1075–1082.

Hawkes, D., Colchester, A., Brunt, J., Wicks, D., du Bolay, G. and Wallis, A. (1988), Development of a model to predict the potential accuracy of vessel blood flow measurements from dynamic angiographic recordings, *Mathematics and Computer Science in Medical Imaging* pp.469–478.

Hawkes, D., Colchester, A., de Belder, M., Norbury, R., Camm, A. and Davies, M. (1992), The measurement of absolute lumen cross sectional area and lumen geometry in quantitative angiography, *in Medical Images: Formation, Handling and Evaluation. Heidelberg, Germany: Springer; NATO ASI Series*, pp.609–626.

Hawkes, D. J., Mol, C. B. and Colchester, A. C. F. (1985), The accurate 3D reconstruction of the geometric configuration of vascular trees from X-ray recordings, *in Physics and Engineering of Medical Imaging*, pp.250–258.

Hawkes, D. J., Seifalian, A. M., Colchester, A. C., Iqbal, N., Hardingham, C. R., Bladin, C. F. and Hobbs, K. E. (1994), Validation of volume blood flow measurements using three-dimensional distance-concentration functions derived from digital x-ray angiograms, *Investigative Radiology* **29**(4), 434–442.

Hedrick, W. R., Hykes, D. L. and D.E.Starchan (2004), *Ultrasound physics and instrumentation*, Elsevier Mosby.

Hermiller, J. B., Cusma, J. T., Spero, L. A., Fortin, D. F., Harding, M. B. and Bashore, T. M. (1992), Quantitative and qualitative coronary angiographic analysis: review of methods, utility, and limitations, *Catheterization and Cardiovascular Diagnosis* **25**(2), 110–131.

Höhne, K. H., Böhm, M., Erbe, W., Nicolae, G. C., Pfeiffer, G. and Sonne, B. (1978), Computer angiography: a new tool for x-ray functional diagnostics, *Medical Progress Through Technology* **6**(1), 23–28.

Hilal, S. K. (1966), Hemodynamic changes associated with the intra-arterial injection of contrast media. New toxicity tests and a new experimental contrast medium., *Radiology* **86**(4), 615–633.

Hillen, B., Drinkenburg, B. A., Hoogstraten, H. W. and Post, L. (1988), Analysis of flow and vascular resistance in a model of the circle of Willis, *Journal of Biomechanics* **21**(10), 807–814.

Hoffmann, K. R., Chan, H. P., Fencil, L., Fujita, H. and Muraki, A. (1986), Automated tracking of the vascular tree in DSA images using a double-squarebox region-of-search algorithm, *in Proceedings of the SPIE*, Vol. 626, pp.326–333.

Hoffmann, K. R., Doi, K. and Fencil, L. E. (1991), Determination of instantaneous and average blood flow rates from digital angiograms of vessel phantoms using distance-density curves, *Investigative Radiology* **26**(3), 207–212.

Hoffmann, K. R., Nazareth, D. P., Miskolczi, L., Gopal, A., Wang, Z., Rudin, S. and Bednarek, D. R. (2002), Vessel size measurements in angiograms: a comparison of techniques, *Medical Physics* **29**(7), 1622–1633.

Horn, B. and Schunck, B. (1981), Determining optical flow, *Artificial Intelligence* **17**, 185–203.

Huang, S. P., Chapman, B. E., Muhlestein, J. B., Blatter, D. D. and Parker, D. L. (1997a), Computer simulation of convection and diffusion effects on velocity estimations from X-ray contrast density time curves, *Information Processing in Medical Imaging* **1230**, 453–458.

Huang, S. P., Decker, R. J., Goodrich, K. C., Parker, D. J., Muhlestein, J. B., Blatter, D. D. and Parker, D. L. (1997b), Velocity measurement based on bolus tracking with the aid of three-dimensional reconstruction from digital subtraction angiography, *Medical Physics* **24**(5), 677–686.

Hubbell, J. H. and Seltzer, S. M. (1996), Tables of X-Ray Mass Attenuation Coefficients and Mass Energy-Absorption Coefficients, Technical Report, National Institute of Standards and Technology.

Huber, P. and Handa, J. (1967), Effect of contrast material, hypercapnia, hyperventilation, hypertonic glucose and papaverine on the diameter of the cerebral arteries. Angiographic determination in man., *Investigative Radiology* **2**(1), 17–32.

Hughes, W. F. (1979), *An Introduction to Viscous Flow*, Hemisphere publishing corporation.

Imbert, B., Meunier, J., Mongrain, R., Hudon, G. and Bertrand, M. (1995), Blood flow assessment from optical flow in cineangiography, *in Computers in Cardiology*, pp.537–540.

Jacobson, E. D., Eldon, C. and Fondacaro, J. D. (1981), Hemodynamic effects of rapid injection into the canine superior mesenteric artery., *Dig Dis Sci* **26**(10), 905–910.

Johnston, S. C., Gress, D. R. and Kahn, J. G. (1999), Which unruptured cerebral aneurysms should be treated? A cost-utility analysis, *Neurology* **52**(9), 1806–1815.

Kagstrom, E., Lindgren, P. and Tornell, G. (1958), Changes in cerebral circulation during carotid angiography with sod acetrizoate (triurol) and sodium diatrizoate (hypaque): an experimental study., *Acta radiology* **50**(1-2), 151–159.

Kallehauge, H. E. and Praestholm, J. (1982), Iopamidol, a new nonionic contrast medium in peripheral angiography., *Cardiovascular and Interventional Radiology* **5**(6), 325–328.

Kedem, D., Kedem, D., Smith, C. W., Dean, R. H. and Brill, A. B. (1978), Velocity distribution and blood flow measurements using videodensitometric methods, *Investigative Radiology* **13**(1), 46–56.

Kety, S. and Schmidt, C. (1945), The determination of cerebral blood flow in man by the use of nitrous oxide in low concentrations, *American Journal of Physiology* **143**, 53–66.

Kim, H. C., Min, B. G., Lee, T. S., Lee, S. J., Lee, C. W., Park, J. H. and Han, M. C. (1982), Three-dimensional digital subtraction angiography, *IEEE Transactions on Medical Imaging* **1**(2), 152–158.

Kipshidze, N., Fareed, J., Serruys, P. W. and Moses, J. (eds.) (2007), *Textbook of Interventional Cardiovascular Pharmacology*, Informa HealthCare.

Kirbas, C. and Quek, F. (2004), A review of vessel extraction techniques and algorithms, *ACM Computing Surveys* **36**(2), 81 – 121.

Kitamura, K., Tobis, J. and Sklansky, J. (1988), Estimating the 3D skeletons and transverse areas of coronary arteries from biplane angiograms, *IEEE Transactions on Medical Imaging* **7**(3), 173–187.

Kolachalama, V. B. (2006), Predictive haemodynamics of the human carotid artery, PhD thesis, University of Southampton.

Kolin, A. (1936), An electromagnetic flowmeter, principle of the method and its application to blood flow measurement, *Proceedings of the Society for Experimental Biology and Medicine* **35**, 53–56.

Kolin, A., Assali, N., Herrold, G. and Jensen, R. (1957), Electromagnetic determination of regional blood flow in unanesthetized animals., *Proceedings of the National Academy of Sciences of the United States of America* **43**(6), 527–540.

Kooijman, C., Reiber, J., Gerbrands, J., Schuurbiers, J., Slager, C., den Boer, A. and Serruys, P. (1982), Computer-aided quantitation of the severity of coronary obstructions from single view cineangiograms, *Proceedings IEEE Computer Society International Symposium on Medical Imaging and Image Interpretation* pp.59 – 64.

Koppe, R., Klotz, E., de Beek, J. O. and Aerts, H. (1995), 3D vessel reconstruction based on Rotational angiography, *in Proceedings of Computer Assisted Radiology*, pp.101–107.

Korbuly, D. E. (1973), Determination of the pulsatile blood flow by a radiographic method, *Investigative Radiology* **8**, 255–258.

Krejza, J., Mariak, Z. and Babikian, V. L. (2001), Importance of angle correction in the measurement of blood flow velocity with transcranial Doppler sonography, *American Journal of Neuroradiology* **22**(9), 1743–1747.

Kruger, R. A. (1981), Estimation of the diameter of and iodine concentration within blood vessels using digital radiography devices, *Medical Physics* **8**(5), 652–658.

Kruger, R. A., Bateman, W., Liu, P. Y. and Nelson, J. A. (1983), Blood flow determination using recursive processing: a digital radiographic method, *Radiology* **149**(1), 293–298.

Ku, D. N. (1997), Blood flow in arteries, *Annual Review of Fluid Mechanics* **29**, 399–434.

Kwan, E. S., Hall, A. and Enzmann, D. R. (1986), Quantitative analysis of intracranial circulation using rapid-sequence DSA, *American Journal of Neuroradiology* **146**(6), 1239–1245.

Lantz, B. M., Foerster, J. M., Link, D. P. and Holcroft, J. W. (1980), Determination of relative blood flow in single arteries: new video dilution technique, *American Journal of Neuroradiology* **134**(6), 1161–1168.

Law, A., Zhu, H. and Chan, F. (2003), 3D reconstruction of coronary artery using biplane angiography, *Proceedings of the 25th Annual International Conference of the IEEE Engineering in Medicine and Biology Society* **1**, 533–536.

Lee, W. S. and Poston, T. (1997), Rapid 3D tube reconstruction from nearby views, *Fifth International Conference in Central Europe on Computer Graphics and Visualization* **2**, 262–271.

Leeds, N. E. and Kieffer, S. A. (2000), Evolution of Diagnostic Neuroradiology from 1904 to 1999, *Radiology* **217**(2), 309–318.

LeFree, M., Simon, S., Lewis, R., Bates, E. and R.A., V. (1985), Digital radiographic coronary artery quantification, *Computers in Cardiology* pp.99–102.

Levin, D. C., Phillips, D. A., Lee-Son, S. and Maroko, P. R. (1977), Hemodynamic changes distal to selective arterial injections., *Investigative Radiology* **12**(2), 116–120.

Likittanasombut, P., Reynolds, P., Meads, D. and Tegeler, C. (2006), Volume flow rate of common carotid artery measured by Doppler method and Color Velocity Imaging Quantification (CVI-Q), *Journal of Neuroimaging* **16**(1), 34–38.

Lou, Z. and Yang, W. J. (1991), A computer simulation of the blood flow at the aortic bifurcation, *Biomedical Materials and Engineering* **1**(3), 173–193.

MacKay, S. A., Potel, M. J. and Rubin, J. M. (1982), Graphics methods for tracking three-dimensional heart wall motion, *Computers and Biomedical Research* **15**(5), 455–473.

Madsen, E. L., Hobson, M. A., Shi, H., Varghese, T. and Frank, G. R. (2005), Tissue-mimicking agar/gelatin materials for use in heterogeneous elastography phantoms, *Physics in Medicine and Biology* **50**(23), 5597–5618.

Malladi, R. and Sethian, J. A. (1995), Image processing via level set curvature flow., *Proc Natl Acad Sci U S A* **92**(15), 7046–7050.

Mancini, G. B., Simon, S. B., McGillem, M. J., LeFree, M. T., Friedman, H. Z. and Vogel, R. A. (1987), Automated quantitative coronary arteriography: morphologic and physiologic validation in vivo of a rapid digital angiographic method, *Circulation* **75**(2), 452–460.

Manos, S., Zasada, S., Mazzeo, M. D., Haines, R., Doctors, G., Brew, S., Pinning, R., Brooke, J. and Coveney, P. V. (2008), Patient specific whole cerebral blood flow simulation: A future role in surgical treatment for neurovascular pathologies, *in TeraGrid*.

Marinus, H., Buis, B. and van Benthem, A. (1990), Pulsatile coronary flow determination by digital angiography, *International Journal of Cardiac Imaging* **5**(2-3), 173–182.

Marshall, I., Zhao, S., Papathanasopoulou, P., Hoskins, P. and Xu, Y. (2004), MRI and CFD studies of pulsatile flow in healthy and stenosed carotid bifurcation models., *Journal of biomechanics* **37**(5), 679–687.

Meier, P. and Zierler, K. (1954), On the theory of the indicator-dilution method for measurement of blood flow and volume, *Journal of Applied Physiology* **6**(12), 731–744.

Meinguet, J. (1979), Multivariate Interpolation at Arbitrary Points Made Simple, *Zeitschrift für Angewandte Mathematik und Physik (ZAMP)* **30**(2), 292–304.

Metz, C. E. and Fencil, L. E. (1989), Determination of three-dimensional structure in biplane radiography without prior knowledge of the relationship between the two views: theory, *Medical Physics* **16**(1), 45–51.

Molloi, S., Bednarz, G., Tang, J., Zhou, Y. and Mathur, T. (1998), Absolute volumetric coronary blood flow measurement with digital subtraction angiography, *International Journal of Cardiac Imaging* **14**(3), 137–145.

Molloi, S., Qian, Y. J. and Ersahin, A. (1993), Absolute volumetric blood flow measurements using dual-energy digital subtraction angiography, *Medical Physics* **20**(1), 85–91.

Molloi, S., Zhou, Y. and Kassab, G. S. (2004), Regional volumetric coronary blood flow measurement by digital angiography: in vivo validation, *Academic Radiology* **11**(7), 757–766.

Mongrain, R., Bertrand, M., Mailloux, G., Meunier, J. and Bourassa, M. (1990), Obtaining blood velocity profile from coronary arteriograms via optimally controlled optical flow, *in Computers in Cardiology*, pp.13–16.

Moore, S., Moorhead, K., Chase, J., David, T. and Fink, J. (2005), One-dimensional and three-dimensional models of cerebrovascular flow, *Journal of Biomechanical Engineering-Transactions of the Asme* **127**(3), 440–449.

Morris, T. W., Kern, M. A. and Katzberg, R. W. (1982), The effects of media viscosity on hemodynamics in selective arteriography., *Investigative Radiology* **17**(1), 70–76.

Mostbeck, G. H., Caputo, G. R. and Higgins, C. B. (1992), MR measurement of blood flow in the cardiovascular system., *American Jounal of Roentgenology* **159**(3), 453–461.

Movassaghi, B., Rasche, V., Grass, M., Viergever, M. A. and Niessen, W. J. (2004), A quantitative analysis of 3-D coronary modeling from two or more projection images, *IEEE Transactions on Medical Imaging* **23**(12), 1517–1531.

Mullani, N. A. and Gould, K. L. (1983), First-pass measurements of regional blood flow with external detectors, *Journal of Nuclear Medicine* **24**(7), 577–581.

NASCET (1991), Beneficial effect of carotid endarterectomy in symptomatic patients with high-grade carotid stenosis. North American Symptomatic Carotid Endarterectomy Trial Collaborators, *The New England journal of medicine* **325**(7), 445–453.

Nauert, C., Langer, M. and Mützel, W. (1989), Hemorrheologic effects of iotrolan after intra-arterial injection in rabbits: comparison with other types of contrast media., *RöFo : Fortschritte auf dem Gebiete der Röntgenstrahlen und der Nuklearmedizin Ergänzungsband* **128**, 40–45.

Navab, N., Bani-Hashemi, A. R., Mitschke, M. M., Holdsworth, D. W., Fahrig, R., Fox, A. J. and Graumann, R. (1996), Dynamic geometrical calibration for 3D cerebral angiography, *Proceedings SPIE Medical Imaging* **2708**(1), 361–370.

Nguyen, T. V. and Sklansky, J. (1986), Computing the skeleton of coronary arteries in cineangiograms, *Computers and Biomedical Research* **19**(5), 428–444.

Nichols, A. B., Gabrieli, C. F., Fenoglio, J. J. and Esser, P. D. (1984), Quantification of relative coronary arterial stenosis by cinevideodensitometric analysis of coronary arteriograms, *Circulation* **69**(3), 512–522.

Nichols, W. W. and O'Rouke, M. F. (2005), *McDonald's blood flow in arteries : theoretical, experimental and clinical principles*, London : Hodder Arnold.

Niki, N., Kawata, Y., Satoh, H. and Kumazaki, T. (1993), 3D imaging of blood vessels using X-ray rotational angiographic system, *IEEE Conference Recordings Nuclear Science Symposium and Medical Imaging Conference* **3**, 1873–1877.

Oktar, S. O., Yücel, C., Karaosmanoglu, D., Akkan, K., Ozdemir, H., Tokgoz, N. and Tali, T. (2006), Blood-flow volume quantification in internal carotid and vertebral arteries: comparison

of 3 different ultrasound techniques with phase-contrast MR imaging, *American Journal of Neuroradiology* **27**(2), 363–369.

Orlowski, P., Noble, J., Ventikos, Y., Byrne, J. and Summers, P. (2008), Image-based simulation of brain arteriovenous malformation hemodynamics, *Biomedical Imaging: From Nano to Macro (ISBI)* pp.676–679.

Ovitt, T. W., Christenson, P. C., Fisher, H. D., Frost, M. M., Nudelman, S., Roehrig, H. and Seeley, G. (1980), Intravenous Angiography using Digital Video Subtraction x-Ray-Imaging System, *American Journal of Roentgenology* **135**(6), 1141–1144.

Padayachee, T. S., Reidy, J. F., King, D. H., Reeves, M. and Gosling, R. G. (1983), Femoral artery flow and pain during lumbar aortography: comparison of ionic and non-ionic contrast media., *Clinical Radiology* **34**(1), 79–85.

Pappas, T. and Lim, J. (1988), A new method for estimation of coronary artery dimensions in angiograms, *IEEE Transactions on Acoustics, Speech, and Signal Processing* **36**(9), 1501–1513.

Parker, D. L., Pope, D. L., Bree, R. V. and Marshall, H. W. (1987), Three-dimensional reconstruction of moving arterial beds from digital subtraction angiography, *Computers and Biomedical Research* **20**(2), 166–185.

Perktold, K. and Peter, R. (1990), Numerical 3D-simulation of pulsatile wall shear stress in an arterial T-bifurcation model, *Journal of Biomedical Engineering* **12**(1), 2–12.

Perktold, K., Hofer, M., Rappitsch, G., Loew, M., Kuban, B. and Friedman, M. (1998), Validated computation of physiologic flow in a realistic coronary artery branch, *Journal of Biomechanics* **31**(3), 217–228.

Planiol, T. and Pourcelot, L. (1973), Doppler effect study of the carotid circulation, *Proceedings. of the 2nd World Congress on Ultrasonics in Medicine* pp.104–111.

Polak, J. F., Dobkin, G. R., O'Leary, D. H., Wang, A. M. and Cutler, S. S. (1989), Internal carotid artery stenosis: accuracy and reproducibility of color-Doppler-assisted duplex imaging., *Radiology* **173**(3), 793–798.

Pugh, N. D. (1996), Haemodynamic and rheological effects of contrast media: the role of viscosity and osmolality, *European Radiology* **6**, 13–15.

Pugh, N. D., Sissons, G. R. and Ruttley, M. (1992), The effect of iodixanol, a new isotonic contrast agent, on femoral blood flow in man., *Clinical Radiology* **45**(4), 243–245.

Redaelli, A., Rizzo, G., Arrigoni, S., Di-Martino, E., Origgi, D., Fazio, F. and Montevecchi, F. (2002), An assisted automated procedure for vessel geometry reconstruction and hemodynamic simulations from clinical imaging, *Computerized Medical Imaging and Graphics* **26**(3), 143–52.

Reiber, H. J. C., Booman, F., Tan, H., Slager, C., Schwubiers, J., Gerbrands, J. and Meester, G. (1978), A cardiac image analysis system: Objective quantitative processing of angiograms, *Computers in Cardiology* pp.239–242.

Rhode, K., Ennew, G., Lambrou, T., Hawkes, D. and Seifalian, A. (2001), The measurement of blood flow from dynamic digital x-ray images using a weighted optical flow algorithm: validation in a moving-vessel flow phantom, *in Medical Image Understanding and Analysis*.

Rhode, K., Lambrou, T., Seifalian, A. and Hawkes, D. (2002), In-vitro validation of a novel model-based approach to the measurement of arterial blood flow waveforms from dynamic digital X-ray images, *Proceedings SPIE Medical Imaging* **4683**, 286–296.

Rhode, K. S., Lambrou, T., Hawkes, D. J. and Seifalian, A. M. (2005), Novel approaches to the measurement of arterial blood flow from dynamic digital X-ray images, *IEEE Transactions on Medical Imaging* **24**(4), 500–513.

Rubin, E. (2001), *Rubins Pathology: Clinincopathologic Foundations of Medicine*, Lippincott Williams & Wilkins.

Rutishauser, W., Simon, H., Stucky, J. P., Schad, N., Noseda, G. and Wellauer, J. (1967), Evaluation of Roentgen cinedensitometry for flow measurement in models and in the intact circulation, *Circulation* **36**(6), 951–963.

Sapirstein, L. A. (1956), Fractionation of the cardiac output of rats with isotopic potassium, *Circulation Research* **4**(6), 689–692.

Satomura, S., Nimura, Y. and Yoshtda, T. (1960), Ultrasonic doppler cardiograph, *Proceedings of the 3rd International Conference on Medical Electronics* pp.249–253.

Schalij, M. J., Geldof, M. J. A., Zwet vander, P. M. J., Vel de vander, E. T., Nagtegaal, E. M., Manger Cats, V., C., R. J. H. and Bruschke, A. V. G. (1994), *Progress in Quantitative Coronary Arteriography*, Kluwer Academic Publishers, Chapter On-line Assessment of myocardial flow reserve, pp.173–189.

Schmitt, H., Grass, M., Rasche, V., Schramm, O., Haehnel, S. and Sartor, K. (2002), An X-ray-based method for the determination of the contrast agent propagation in 3-D vessel structures, *IEEE Transactions on Medical Imaging* **21**(3), 251–262.

Schmitt, H., Grass, M., Suurmond, R., Köhler, T., Rasche, V., Hähnel, S. and Heiland, S. (2005), Reconstruction of blood propagation in three-dimensional rotational X-ray angiography (3D-RA), *Computerized medical imaging and graphics* **29**(7), 507–520.

Schröder, J., Keller, H., Terwey, B. and Mittmann, U. (1981), Haemodynamic effects of intraarterial contrast injections, *RöFo : Fortschritte auf dem Gebiete der Röntgenstrahlen und der Nuklearmedizin* **135**, 143–151.

Seidel, G., Kaps, M. and Gerriets, T. (1995), Potential and limitations of transcranial color-coded sonography in stroke patients, *Stroke* **26**(11), 2061–2066.

Seifalian, A. M., Hawkes, D. J., Colchester, A. C. and Hobbs, K. E. (1989), A new algorithm for deriving pulsatile blood flow waveforms tested using stimulated dynamic angiographic data, *Neuroradiology* **31**(3), 263–269.

Seldinger, S. I. (1953), Catheter replacement of the needle in percutaneous arteriography; a new technique, *Acta Radiolgica* **39**(5), 368–376.

Selzer, R. H., Hagerty, C., Azen, S. P., Siebes, M., Lee, P., Shircore, A. and Blankenhorn, D. H. (1989), Precision and reproducibility of quantitative coronary angiography with applications to controlled clinical trials. A sampling study, *Journal of Clinical Investigation* **83**(2), 520–526.

Sen, A., Lan, L., Doi, K. and Hoffmann, K. R. (1999), Quantitative evaluation of vessel tracking techniques on coronary angiograms, *Medical Physics* **26**(5), 698–706.

Sethian, J. A. (1996), A fast marching level set method for monotonically advancing fronts, *Proceedings of the National Academy of Sciences* **93**(4), 1591–1595.

Sherwin, S., Franke, V., Peiró, J. and Parker, K. (2003), One-dimensional modelling of a vascular network in space-time variables, *Journal of Engineering Mathematics* **47**, 217 – 250.

Shmueli, K. (1983), Estimation of blood vessel boundaries in X-ray images, *Optical Engineering* **22**, 110–116.

Shpilfoygel, S. D., Close, R. A., Jahan, R., Duckwiler, G. R. and Valentino, D. J. (1998), Modified distance-density methods for instantaneous angiographic blood-flow measurement, *Proceedings SPIE Medical Imaging* (1), 242–252.

Shpilfoygel, S. D., Close, R. A., Valentino, D. J. and Duckwiler, G. R. (2000), X-ray videodensitometric methods for blood flow and velocity measurement: A critical review of literature, *Medical Physics* **27**(9), 2008–2023.

Silverman, N. R. and Rosen, L. (1977), Arterial blood flow measurement: assessment of velocity estimation methods, *Investigative Radiology* **12**(4), 319–324.

Singer, J. R. (1978), NMR diffusion and flow measurements and an introduction to spin phase graphing, *Journal of Physics E: Scientific Instruments* **11**(4), 281–291.

Skidmore, R. and Woodcock, J. P. (1978), Physiological significance of arterial models derived using transcutaneous ultrasonic flowmeters, *Journal of Physiology* **277**, 29–30.

Smith, M. A. (1990), The measurement and visualisation of vessel blood flow by magnetic resonance imaging, *Clinical Physics and Physiological Measurement* **11**(2), 101–123.

Spears, J. R., Sandor, T., Als, A. V., Malagold, M., Markis, J. E., Grossman, W., Serur, J. R. and Paulin, S. (1983), Computerized image analysis for quantitative measurement of vessel diameter from cineangiograms, *Circulation* **68**(2), 453–461.

Spiller, P., Jehle, J., Politz, B. and Schmiel, F. (1982), A digital x-ray image processing system for measurement of phasic blood flow in coronary arteries, *in Computers in Cardiology*, pp.223–226.

Spiller, P., Schmiel, F. K., Pölitz, B., Block, M., Fermor, U., Hackbarth, W., Jehle, J., Körfer, R. and Pannek, H. (1983), Measurement of systolic and diastolic flow rates in the coronary artery system by x-ray densitometry, *Circulation* **68**(2), 337–347.

Steinman, D. A., Poepping, T. L., Tambasco, M., Rankin, R. N. and Holdsworth, D. W. (2000), Flow patterns at the stenosed carotid bifurcation: effect of concentric versus eccentric stenosis., *Ann Biomed Eng* **28**(4), 415–423.

Steinman, D., Milner, J., Norley, C., Lownie, S. and Holdsworth, D. (2003), Image-based computational simulation of flow dynamics in a giant intracranial aneurysm, *American Journal of Neuroradiology* **24**(4), 559–566.

Stewart, G. N. (1893), Researches on the circulation time in organs and on the influences which affect it: parts I.-III, *Journal of Physiology* **15**(1-2), 1–89.

Stoeter, P., Prey, N., Hoffmann, C., Büdingen, H. J. and Bergleiter, R. (1984), Doppler-sonographic examination of the arterial flow in the carotid and supratrochlear arteries during carotid angiography., *Neuroradiology* **26**(3), 199–207.

Sun, Y. (1989), Automated identification of vessel contours in coronary arteriograms by an adaptive tracking algorithm, *IEEE Transactions on Medical Imaging* **8**(1), 78 – 88.

Suryan, G. (1951), Nuclear resonance in flowing liquids, *Proceedings of the Indian Academy of Sciences* **33**, 107–111.

Swanson, D. K., Kress, D. C., Pasaoglu, I., Hegge, J. O. and Kroncke, G. M. (1988), Quantitation of absolute flow in coronary artery bypass grafts using digital subtraction angiography, *Journal of surgical research* **44**(4), 326–335.

Takahashi, T., Korenaga, T. and Shen, F. (1990), A numerical solution for the dispersion in. laminar flow through a circular tube, *Canadian Journal of Chemical Engineering* **68**, 191–196.

Taylor, G. (1953), Dispersion of soluble matter in solvent flowing slowly through a tube, *Proceedings of the Royal Society of London. Series A - Mathematical an physical science* **219**(1137), 186–203.

Tenjin, H., Asakura, F., Nakahara, Y., Matsumoto, K., Matsuo, T., Urano, F. and Ueda, S. (1998), Evaluation of intraaneurysmal blood velocity by time-density curve analysis and digital subtraction angiography, *American Journal of Neuroradiology* **19**(7), 1303–1307.

The Arteriovenous Malformation Study Group (1999), Arteriovenous Malformations of the Brain in Adults, *The New England journal of medicine* **340**(23), 1812–1818.

Tomandl, B., Hastreiter, P., Eberhardt, K., Rezk-Salama, C., Nimsky, C. and Buchfelde, M. (1999), The kissing vessel-artifact: a problem occurring in the visualization of intracranial aneurysms using volume rendering and virtual endoscopy, *Radiology* **213**, 311.

Underwood, J. (2004), *General and systematic pathology*, Edinburgh : Churchill Livingstone.

University of Arkansas for Medical Science (2008), Coiling of Aneurysms, http://www.uams.edu/Radiology/info/clinical/aneurysm/.

Voigt, K., Stoeter, P. and Petersen, D. (1975), Rotational cerebral roentgenography. I. Evaluation of the technical procedure and diagnostic application with model studies., *Neuroradiology* **10**(2), 95–100.

Waechter, I., Bredno, J., Hermans, R., Weese, J., Barratt, D. C. and Hawkes, D. J. (2008a), Evaluation of model based blood flow quantification from rotational angiography, *in SPIE Medical Imaging*.

Waechter, I., Bredno, J., Hermans, R., Weese, J., Barratt, D. C. and Hawkes, D. J. (2008b), Model-based blood flow quantification from rotational angiography, *Medical Image Analysis* **12**(5).

Waechter, I., Bredno, J., Weese, J., Barratt, D. C. and Hawkes, D. J. (2008c), Using Flow Information to Support 3D Vessel Reconstruction From Rotational Angiography, *Medical Physics* **7**.

Wahle, A., Oswald, H. and Fleck, E. (1996), 3D heart-vessel reconstruction from biplane angiograms, *IEEE Computer Graphics and Applications* **16**(1), 65 – 73.

Walker, M. F., Souza, S. P. and Dumoulin, C. L. (1988), Quantitative flow measurement in phase contrast MR angiography, *Journal of Computer Assisted Tomography* **12**(2), 304–313.

Wankling, P. F., Perry, R. A., Seth, A., Hunt, A. C., Escaned, X., Newell, J. A. and Shiu, M. F. (1990), An objective computer system for the quantification of artery stenoses, *International Journal of Cardiac Imaging* **5**(2-3), 85–92.

Wicks, D. (1989), Intravascular blood flow measurement by quantitative cineangiography image analysis, PhD thesis, University of Manchester.

Wiegert, J. (2006), Scattered radiation in cone-beam computed tomography: analysis, quantification and compensation, PhD thesis, RWTH Aachen.

Williams, E. (1930), The induction of electromotive forces in a moving liquid by a magnetic field, and its application to an investigation of the flow of liquids, *Proceedings of the Physical Society* **42**, 466–478.

Wink, O., Kemkers, R., Chen, S. Y. and Carroll, J. D. (2003), Intra-procedural coronary intervention planning using hybrid 3-dimensional reconstruction techniques, *Academic Radiology* **10**(12), 1433–1441.

Wink, O., Niessen, W. and Viergever, M. (2004), Multiscale vessel tracking, *IEEE Transactions on Medical Imaging* **23**(1), 130–133.

Wolf, G. L., Shaw, D. D., Baltaxe, H. A., Kilzer, K. and Kraft, L. (1978), A proposed mechanism for transient increases in arterial pressure and flow during angiographic injections., *Investigative Radiology* **13**(3), 195–199.

Wollschlager, H., Lee, P. and Zeiher, A. (1985), Improvement of quantitative angiography by exact calculation of radiological magnification factors, *Computers in Cardiology* pp.483–486.

Womersley, J. (1955), Method for the calculation of velocity, rate of flow and viscous drag in arteries when the pressure gradient is known, *Journal of Physiology-London* **127**(3), 553–563.

Wyatt, D. (1984), Blood flow and blood velocity measurementin vivo by electromagnetic induction, *Medical and Biological Engineering and Computing* **22**(3), 193–211.

Wyatt, D. G. (1968), The electromagnetic blood flowmeter, *J Sci Instrum* **1**(12), 1146–1152.

Xu, X. Y. (2001), Image-Based Modeling of Blood Flow in the Human Cardiovascular System, *in Advances in Biomechanics*, pp.214–219.

Yerushalmi, S. and Itzchak, Y. (1976), Angiographic methods for blood flow measurements, *Medical Progress Through Technology* **4**(3), 107–115.

Young, S., Movassaghi, B., Weese, J. and Rasche, V. (2003), 3D vessel axis extraction using 2D calibrated X-ray projections for coronary modeling, *Proceedings of the SPIE* **5032**, 1491–1498.

Zhao, S. Z., Xu, X. Y., Hughes, A. D., Thom, S. A., Stanton, A. V., Ariff, B. and Long, Q. (2000), Blood flow and vessel mechanics in a physiologically realistic model of a human carotid arterial bifurcation, *Journal of Biomechanics* **33**(8), 975–984.

Zwaan, M., Helden, J. V. and Weiss, H. D. (1999), Local effect of three nonionic contrast media on the arterial blood flow velocity during iliofemoral arteriography., *Investigative Radiology* **34**(1), 5–12.